



MINISTÉRIO DA CIÊNCIA, TECNOLOGIA E INOVAÇÃO
INSTITUTO NACIONAL DE PESQUISAS ESPACIAIS

sid.inpe.br/mtc-m21b/2015/01.30.19.09-TDI

**STUDY OF CORONAL MASS EJECTIONS AND THEIR
CORRESPONDING INTERPLANETARY STRUCTURES
USING COMBINED OBSERVATIONS OF COSMIC RAY
DETECTORS AND CORONAGRAPHS**

Carlos Roberto Braga

Doctorate Thesis of the Graduate Course in Space Geophysics, guided by Drs. Alisson Dal Lago, and Ezequiel Echer, approved in February 27, 2015.

URL of the original document:

<<http://urlib.net/8JMKD3MGP3W34P/3HS23EB>>

INPE
São José dos Campos
2015

PUBLISHED BY:

Instituto Nacional de Pesquisas Espaciais - INPE

Gabinete do Diretor (GB)

Serviço de Informação e Documentação (SID)

Caixa Postal 515 - CEP 12.245-970

São José dos Campos - SP - Brasil

Tel.:(012) 3208-6923/6921

Fax: (012) 3208-6919

E-mail: pubtc@sid.inpe.br

**COMMISSION OF BOARD OF PUBLISHING AND PRESERVATION
OF INPE INTELLECTUAL PRODUCTION (DE/DIR-544):****Chairperson:**

Marciana Leite Ribeiro - Serviço de Informação e Documentação (SID)

Members:

Dr. Gerald Jean Francis Banon - Coordenação Observação da Terra (OBT)

Dr. Amauri Silva Montes - Coordenação Engenharia e Tecnologia Espaciais (ETE)

Dr. André de Castro Milone - Coordenação Ciências Espaciais e Atmosféricas
(CEA)

Dr. Joaquim José Barroso de Castro - Centro de Tecnologias Espaciais (CTE)

Dr. Manoel Alonso Gan - Centro de Previsão de Tempo e Estudos Climáticos
(CPT)

Dr^a Maria do Carmo de Andrade Nono - Conselho de Pós-Graduação

Dr. Plínio Carlos Alvalá - Centro de Ciência do Sistema Terrestre (CST)

DIGITAL LIBRARY:

Dr. Gerald Jean Francis Banon - Coordenação de Observação da Terra (OBT)

Clayton Martins Pereira - Serviço de Informação e Documentação (SID)

DOCUMENT REVIEW:

Simone Angélica Del Ducca Barbedo - Serviço de Informação e Documentação
(SID)

Yolanda Ribeiro da Silva Souza - Serviço de Informação e Documentação (SID)

ELECTRONIC EDITING:

Marcelo de Castro Pazos - Serviço de Informação e Documentação (SID)

André Luis Dias Fernandes - Serviço de Informação e Documentação (SID)



MINISTÉRIO DA CIÊNCIA, TECNOLOGIA E INOVAÇÃO
INSTITUTO NACIONAL DE PESQUISAS ESPACIAIS

sid.inpe.br/mtc-m21b/2015/01.30.19.09-TDI

**STUDY OF CORONAL MASS EJECTIONS AND THEIR
CORRESPONDING INTERPLANETARY STRUCTURES
USING COMBINED OBSERVATIONS OF COSMIC RAY
DETECTORS AND CORONAGRAPHS**

Carlos Roberto Braga

Doctorate Thesis of the Graduate Course in Space Geophysics, guided by Drs. Alisson Dal Lago, and Ezequiel Echer, approved in February 27, 2015.

URL of the original document:

<<http://urlib.net/8JMKD3MGP3W34P/3HS23EB>>

INPE
São José dos Campos
2015

Cataloging in Publication Data

Braga, Carlos Roberto.

B731s Study of coronal mass ejections and their corresponding interplanetary structures using combined observations of cosmic ray detectors and coronagraphs / Carlos Roberto Braga. – São José dos Campos : INPE, 2015.

xliv + 282 p. ; (sid.inpe.br/mtc-m21b/2015/01.30.19.09-TDI)

Thesis (Doctorate in Space Geophysics) – Instituto Nacional de Pesquisas Espaciais, São José dos Campos, 2015.

Guiding : Drs. Alisson Dal Lago, and Ezequiel Echer.

1. Interplanetary medium. 2. Solar-terrestrial interactions. 3. Galactic cosmic ray 4. Coronal mass ejections. 5. Magnetic clouds. I.Title.

CDU 523.9:524.1

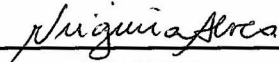


Esta obra foi licenciada sob uma Licença [Creative Commons Atribuição-NãoComercial 3.0 Não Adaptada](https://creativecommons.org/licenses/by-nc/3.0/).

This work is licensed under a [Creative Commons Attribution-NonCommercial 3.0 Unported License](https://creativecommons.org/licenses/by-nc/3.0/).

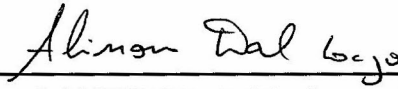
Aprovado (a) pela Banca Examinadora
em cumprimento ao requisito exigido para
obtenção do Título de **Doutor(a)** em
**Geofísica Espacial/Ciências do Ambiente
Solar-Terrestre**

Dra. Maria Virgínia Alves



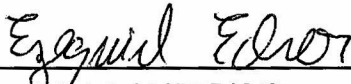
Presidente / INPE / SJCampos - SP

Dr. Alisson Dal Lago



Orientador(a) / INPE / São José dos Campos - SP

Dr. Ezequiel Echer



Orientador(a) / INPE / SJCampos - SP

Dr. Alexandre Alvares Pimenta



Membro da Banca / INPE / SJCampos - SP

Dr. Nelson Jorge Schuch



Membro da Banca / INPE / Santa Maria - RS

Dr. Sergio Ricardo Dasso



Convidado(a) / IAFE/UBA / Buenos Aires - AR

Dr. Caius Lucius Selhorst



Convidado(a) / UNIVAP / São José dos Campos - SP

Este trabalho foi aprovado por:

maioria simples

unanimidade

Aluno (a): **Carlos Roberto Braga**

São José dos Campos, 27 de Fevereiro de 2015

To my family

ACKNOWLEDGMENTS

Thanks to the supervisors Dr Alisson Dal Lago and Dr Ezequiel Echer for discussions that substantially improved the results since the first draft plots discussed in 2012. Also thanks to Dr Nelson Jorge Schuch for supervising me since 2004 when I started my engagement in scientific research.

Thanks to Prof Kazuoki Munakata for supervising me during a one-year visit to Shinshu University, in Matsumoto (Japan) between August 2013 and August 2014. The face-to-face discussions done during this period strongly improved the analysis of cosmic ray data.

Thanks to the scholarship from FAPESP (*Fundação de Amparo à Pesquisa do Estado de São Paulo*) under projects numbers 2012/05436-9 and 2013/02712-8. In addition, thanks to CAPES (*Coordenação de Aperfeiçoamento de Pessoal de Nível Superior*) scholarship provided through the Graduate Program in Space Geophysics from INPE during the initial 21 months of my Doctorate.

In this Thesis the coronal images were obtained by the Large Angle Spectrometric Coronagraph instrument (LASCO), constructed by a consortium consisting of the Naval Research Laboratory (Washington DC, USA), the Max-Planck Institute for Solar System Research (currently in Göttingen, Germany, formerly known as Max-Planck Institute for Aeronomie in Katlenburg, Lindau, Germany), the *Laboratoire d'Astronomie Spatiale* (Marseille, France), and the Space Research Group at the University of Birmingham (Birmingham, United Kingdom). LASCO is one of a complement of instruments on the Solar Heliospheric Observatory satellite (SOHO) build in an international collaboration between the European Space Agency (ESA) and National Aeronautics and Space Administration (NASA).

Beyond the coronal images used here from LASCO, this Thesis also uses data from Sun Earth Connection Coronal and Heliospheric Investigation (SECCHI). This instrument was produced by an international consortium of the Naval Research Laboratory (USA), Lockheed Martin Solar and Astrophysics Lab (USA), NASA Goddard Space Flight Center (USA), Rutherford Appleton Laboratory (UK), University of Birmingham (UK), Max-Planck Institute for Solar System Research (Germany), *Centre Spatiale de Liège* (Belgium), *Institut d'Optique Theorique et Appliquee* (France), *Institut d'Astrophysique Spatiale* (France).

This Thesis used algorithms from the Coronal Segmentation Technique (CORSET) originally developed by Dr Guillermo Stenborg and Dr Norberto Goussies. We thank Dr Guillermo Stenborg for sharing the algorithms in 2010.

This Thesis used data from the Global Muon Detector Network (GMDN), a joint project of the Shinshu University (Japan), University of Delaware (USA), Nagoya University (Japan), National Institute for Space Research (Brazil), Federal University of Santa Maria (Brazil), Australian Antarctic Division (Australia), University of Tasmania (Australia) and University of Kuwait (Kuwait). Thanks to all the collaborators from the GMND that made the possible the installation and operation of the GMDN: Dr. N. J. Schuch, Prof. K. Munakata, Dr. T. Kuwabara, Prof. C. Kato, Prof. M. Tokumaru, Prof. J. W. Bieber, Prof. P. Evenson, Prof. M. L. Duldig, Prof. J. E. Humble, Dr. A. Dal Lago, Dr. E. Echer, Dr. M. Rockenbach da Silva, Prof. H.K. Al Jassar, Prof. M. M. Sharma and Prof. I. Sabbah.

Data from three neutron monitors from Bartol Research Institute (University of Delaware) is used here. These detectors are supported by the National Science Foundation.

In this Thesis, we use data from the Advanced Composition Explorer (ACE) spacecraft. We thank ACE Magnetic Field Experiment (MAG) and Solar Wind Electron, Proton, and Alpha Monitor (SWEPAM) instruments teams and the ACE Science Center for providing the ACE data. We acknowledge use of NASA/GSFC's Space Physics Data Facility's OMNIWeb service, and OMNI data.

Thanks to Rafael Rodrigues Souza de Mendonça for correcting the muon data by the atmospheric temperature and pressure effects. Also thanks for the discussions and suggestions during all steps of the development of this Thesis.

A special thanks to my parents (Léo and Isonia) and my sister (Carina), which always supported my studies and gave all the support I needed.

Thanks to teachers and professors that I had since I first entered school, in 1993. This acknowledgment goes for those that worked hard wishing a better future for students.

Thanks for the evaluation committee of this Thesis for careful reading and suggestions to improve this work: Dr Maria Virginia Alves, Dr Alisson Dal Lago, Dr Ezequiel Echer, Dr Alexandre Alvares Pimenta, Dr Nelson Jorge Schuch, Dr Sergio Ricardo Dasso and Dr Caius Lucius Selhorst.

ABSTRACT

This Thesis aims to study coronal mass ejections (CMEs) and their interplanetary counterparts (ICMEs) using remote sensing observations from the solar corona, interplanetary in situ data and observations from ground-based cosmic ray detectors. CMEs have a central role on the Sun-Earth relationships because they are one of the main sources of geomagnetic disturbances. We have started the analysis by using a list of magnetic clouds (MCs) observed in the Earth-vicinity from 2008 to 2011. After probing the interplanetary structure, we identified the CMEs ejected in appropriate time and direction to produce each magnetic cloud. The CME propagation directions were studied thanks to the simultaneous observations of the solar corona from three viewpoints: one from the LASCO (Large Angle and Spectroscopic Coronagraph) and two others from SECCHI (Sun Earth Connection Coronal and Heliospheric Investigation). We developed a new methodology to track the CMEs in 3D combining pseudo-automatic tracking by texture with triangulation and tie-pointing analysis. For each CME analyzed, we estimated the tridimensional speed (magnitude and direction) using the new method and compared the results with previous works. Combining observations of four ground-based cosmic ray (muon) detectors, we deduced the cosmic ray density gradient during each magnetic cloud period and the overall position of the MC center. In some cases, we fit a model of cosmic ray distribution inside magnetic clouds to the observed data and deduced further properties of the MCs, such as orientation and diameter. Finally, for each case, the results derived in the solar corona were compared with those derived from cosmic ray observations.

**ESTUDO DE EJEÇÕES SOLARES E SEUS CORRESPONDENTES INTERPLANETÁRIOS UTILIZANDO
OBSERVAÇÕES CONJUNTAS DE DETECTORES DE RAIOS CÓSMICOS DE SUPERFÍCIE E
CORONÓGRAFOS**

RESUMO

O objetivo desta Tese é estudar ejeções coronais de massa (conhecidas pela sigla CME, da expressão em Língua Inglesa, *coronal mass ejections*) e suas correspondentes estruturas interplanetárias usando observações de sensoriamento remoto da coroa solar, dados de campo magnético e plasma *in situ* do meio interplanetário e observações de detectores de raios cósmicos instalados na superfície da Terra. As CMEs têm um papel central na relação Sol-Terra porque elas são uma das principais causadoras de tempestades geomagnéticas. Iniciou-se a análise desta Tese a partir de uma lista de nuvens magnéticas observadas entre 2008 e 2011 nas vizinhanças da Terra. Uma vez caracterizadas as estruturas interplanetárias, identificaram-se as CMEs ejetadas no período e direção apropriados para produzir cada uma das nuvens magnéticas. A direção das CMEs pode ser estudada graças a observação simultânea da coroa solar a partir de três pontos de observação distintos: um proveniente do instrumento LASCO (*Large Angle and Spectroscopic Coronagraph*) e outros dois do SECCHI (*Sun Earth Connection Coronal and Heliospheric Investigation*). Desenvolveu-se um novo método para rastrear as CMEs em três dimensões usando o rastreamento pseudo-automático por textura, triangulação e pontos de amarra. Para cada CMEs, estimou-se a velocidade tridimensional (tanto a magnitude como a direção) usando o novo método e, nos casos já abordados em trabalhos anteriores, compararam-se os resultados. Por outro lado, combinando-se observações de quatro detectores de raios cósmicos (múons), deduziu-se o gradiente da densidade dos raios cósmicos para todos os casos de nuvens magnéticas observadas e, por conseguinte, estimou-se a sua posição geral. Em alguns casos, ajustou-se um modelo da distribuição dos raios cósmicos no interior da nuvem magnética com os dados observados e deduziram-se outras propriedades da nuvem magnética, como orientação e diâmetro. Finalmente, para cada caso, resultados obtidos na coroa solar foram comparados com aqueles deduzidos por observações de raios cósmicos.

LIST OF FIGURES

	<u>Page</u>
Figure 1.1 - An example of a coronal mass ejection observed by LASCO-C3 onboard SOHO spacecraft.....	3
Figure 1.2 - A three-part structured CME showing the characteristic bright leading edge, dark void, and bright core. This event was observed by the LASCO/C2 coronagraph on 2000/12/10. The visible solar disc is represented by the white circle, while the larger dark disc shows the coronagraph occulter.	5
Figure 1.3 - An example of the change in the shape of a CME as it evolves. Two different timings of the same CME ejected in 2007/08/31 are illustrated. The first timing is in the SECCHI-COR1 field-of-view (the left two columns) and the second in the SECCHI-COR2 COR2 field-of-view (the right two columns) coronagraphs. Both A (second and fourth columns) and B (first and third columns) STEREO spacecraft images are shown. In all panels, the visible solar disc is represented by the white circle, while the larger dark disc shows the coronagraph occulter.....	5
Figure 1.4 - Two arbitrary particles (represented by the green and red circles) from the solar corona (represented in orange). These particles receive light from the photosphere of the Sun (represented by the orange circle) and reemit it. Some of the reemission (black dashed lines) is seen by some observer (black eye). The reemission is maximum in the plane indicated by each arrow close to the red and green points. The geometric representation of all points in space where the emission is maximum forms a sphere that is called Thomson's sphere (whose projection in the ecliptic plane is shown in black).....	7
Figure 1.5 - The orbits of the twin STEREO spacecraft seen in the ecliptic plane by an observer located north of this plane. On the left, the trajectory is represented by an inertial Sun centered coordinate system. On the right, the Sun-Earth line (represented in yellow) is fixed to show the increasing distance from the Earth.....	9
Figure 1.6 - The graduated cylindrical shell (CGS), a geometric model used to represent a CME that has flux rope structure.....	11

Figure 1.7 - Example of the application of the CGS method to a CME observed on 2010/04/03 at 10:39 UT. The image on the left corresponds to SECCHI-COR2A, the central image corresponds to LASCO-C2 and the right one to SECCHI-COR2B. The green structure superposed in each image shows the projection of the CGS model in each coronagraph FOV. In this example, the CME is directed toward the Earth (and LASCO-C2). Both SECCHI coronagraphs see the CME as a limb CME.....	12
Figure 1.8 - The magnetic field lines of a magnetic cloud in the interplanetary medium between the Sun (represented in yellow) and the Earth (the green point).	14
Figure 1.9 - The cosmic ray air shower.....	17
Figure 1.10 - The location of the four detectors that form the Global Muon Detector Network.....	19
Figure 1.11 - A vertical cross section of a detector of the GMDN, except for Kuwait. Each detector is formed by two layers; each one has an array of detection boxes (Figure 1.12). In between the two layers, there is a 5 cm lead layer that absorbs the soft component of the cosmic ray. The four straight lines represent four sample muon arriving at the detector. Each of these muons will be computed in a different directional channel, as described in the text.	21
Figure 1.12 - Diagram of the internal configuration of a detection box for the detectors of the GMDN, except for Kuwait.	22
Figure 1.13 - Diagram of the hodoscope installed at the University of Kuwait. Each tube is a proportional counter. The top and second layers form an upper pair, while the third and bottom layers form a lower pair.	23
Figure 1.14 - An example of the trajectory of the cosmic ray particles deflected by the geomagnetic field using a simulation code from Bobik et al. (2003). Each trajectory shows a cosmic ray particle (proton) with different energy from each other: (a) 20 GeV , (b) 60 GeV and (c) 180 GeV.....	24
Figure 1.15 - The cosmic ray density inside a MC at the beginning (A) and end (B) of a simulation performed and described by Munakata et al. (2006). The maximum cosmic ray density is represented by the light colors.....	26

Figure 3.1 - The count rate observed by the vertical directional channels for the conventional (black lines) and new (red lines) correlation system using one-hour integration times.	33
Figure 3.2 - The count rate observed by the vertical directional channels for the conventional (black lines) and new (red lines) correlation system using ten-minute integration times.	34
Figure 3.3 - One example of the muon count rate before and after the removal of the atmospheric influence due to the temperature and pressure effects. The data shown here is from the conventional correlation system. The violet curve refers to the data uncorrected for neither temperature effect nor pressure effects. The red curve refers to data corrected only for the pressure effect. The black curve indicates data corrected for both atmospheric temperature and pressure effects. The data processing from these corrections was done in collaboration with Mendonça (2015).	36
Figure 3.4 - An illustration of the anisotropy vector in the interplanetary medium and the anisotropy vector observed in the Earth’s surface. The orange circle represents the Earth seen from above.	37
Figure 3.5 - The coupling coefficients calculated for Hobart (upper row) and Kuwait (lower row) detectors. The columns, from left to right, represent the coupling coefficients c_{01} , c_{11} and s_{11} , respectively.	42
Figure 3.6 - The coupling coefficients calculated for Nagoya (upper row) and São Martinho da Serra (lower row) detectors. The columns, from left to right, represent the coupling coefficients c_{01} , c_{11} and s_{11} , respectively.	43
Figure 3.7 - Cartesian components of the anisotropy vector in the GSE coordinate system calculated using the new correlation system. The black line refers to data before the removal of the Compton-Getting effect and the red curve after its removal. An arbitrary period from 2011/10/22 to 2011/10/27 is shown here.	49
Figure 3.8 - The $\mathbf{B} \times \nabla n$ drift. Left side figure: each circle is a cosmic ray (positive charge) spinning due to the magnetic field \mathbf{B} . The particle density at the top is smaller than in the bottom. Right side figure is a “zoom” of the scenario on the left; the 3 arrows indicate the 3 sample particles rotation. As there are more	

particles in the bottom, a current (drift) will be formed following the direction of rotation of the particles in the bottom.....	51
Figure 3.9 - An explanation of the $\mathbf{B} \times \nabla n$ drift and the anisotropy vector drift in the Sun-Earth medium. Notice that the anisotropy and drift are pointing in opposite directions.	51
Figure 3.10 - Comparison of the anisotropy vector calculated in integration times of one hour (red) and ten minutes (black) using data from the new correlation system and already corrected for Compton-Getting effect.....	53
Figure 3.11 - Comparison of the gradient vector calculated in integration times of 1 hour (red) and 10 minutes (black) using data from the new correlation system.	54
Figure 3.12 - The interplanetary magnetic field magnitude (first panel at the top) and its Cartesian components in the GSE coordinate system (remaining three panels). The hourly-averaged data is shown in red and the 10-minutes averaged is represented in black.	55
Figure 3.13 - The perpendicular fractional gradient calculated using the original hourly integration time (black curves) and using the 10-minute integration time. For the latter case, we calculated the average vector for each hourly period (red curve) using the six data points available in each period. The gray curves show the average plus or minus the standard deviation.	56
Figure 3.14 - An illustration of the cosmic ray gradient vector for two different positions of the magnetic cloud flux rope approximated in this case by a straight cylinder.	57
Figure 3.15 - Example of the cosmic ray isotropic intensity as a function of the normalized distance from the cylinder axis x.	59
Figure 3.16 - The cosmic ray cylinder at three different hypothetical positions. In each position the vectors \mathbf{PE} and \mathbf{P} used in the model are shown (see text for details). The position at the center of the picture corresponds to the time t_C when the cylinder is closest to the Earth. The cylinder velocity vector is supposed to be coincident with solar wind velocity \mathbf{v}_{SW} indicated in the figure.	60
Figure 3.17 - Comparison of the results from the current work (upper panel) and those from Kuwabara et al. (2009) (lower panel) for the x component of the fractional gradient. The observed data is indicated by the curve with asterisks in the	

upper panel and with the bold curve with circles in the lower panel. The curves without symbols show the data fit by the model.....	62
Figure 3.18 - Comparison of the results from the current work (upper panel) and those from Kuwabara et al. (2009) (lower panel) for the x component of the fractional gradient. The observed data is indicated by the curve with asterisks in the upper panel and with the bold curve with circles in the lower panel. The curves without symbols show the data fit by the model.....	63
Figure 3.19 - Comparison of the results from the current work (upper panel) and those from Kuwabara et al. (2009) (lower panel) for the “x” component of the fractional gradient. The observed data is indicated by the curve with asterisks in the upper panel and with the bold curve with circles in the lower panel. The curves without symbols show the data fit by the model.....	63
Figure 4.1 - One example of the application of CORSET to track a CME in the SECCHI-COR2B FOV. The white line is the contour derived by CORSET.	66
Figure 4.2 - One example of the GLCM computation. (a) 4 x 4 image with four gray-tone values (0, 1, 2 and 3). (b) General form a GLCM for any image with four gray-tone values (0, 1, 2 and 3). #(i,j) stands for the number of times gray tones i and j have been neighbors (c)-(f) GLCM for different angles and distance of 1 pixel.....	69
Figure 4.3 - Example of a user-selected area (in red) for the CME on 2010/04/03 in the COR2B FOV. The image shown here is the difference of the first two images where the CME is visible in the FOV.	71
Figure 4.4 - Example of the user-selected area (red region) for the background associated to the CME on 2010/04/03 in the COR2B FOV. The image shown here is the difference of the two last images before the CME enters the FOV.....	72
Figure 4.5 - One example of the radial speed as a function of the angle (degrees, after rotation for the stereo baseline). The CME shown here was observed on 2011/09/05 by COR2B and it was tracked from 03:24UT to 05:39 UT.....	74
Figure 4.6 - Similar to Figure 4.5 but for a CME tracked from 2011/09/13 23:54 UT to 2011/09/14 02:54 UT by COR2A.....	75
Figure 4.7 - One example of an epipolar geometry used to do stereoscopy of the Sun (represented in yellow). The two observers are represented by two black	

dots. Between the Sun and the observers, a sample image taken by each one is shown. Each epipolar plane is represented by a rectangle in a different color. Here only five epipolar planes are shown, but as many as desired can be constructed. The intersection of these planes with the images forms the epipolar lines..... 77

Figure 4.8 - An example of a pair of stereoimages before (upper row) and after (lower row) the rectification process. Some sample epipolar lines are shown in each image (black lines). Notice that the epipolar lines became parallel after the rectification. Source: Loop & Zhang (1999). 78

Figure 4.9 - The graphical user interface of the Sunloop application tie-pointing tool on the leading edge of a sample CME observed on 2008/03/25. The tie-points locations are represented by the white crosses. The COR2B (A) image is on the left (right). Sunloop is available as part of the Solar Soft SECCHI software library (e.g., <http://www.lmsal.com/solarsoft/>). 80

Figure 4.10 - Tridimensional reconstruction of the leading edge of the CME observed in 2008/03/25 at five consecutive times shown in relation to the Sun (3D globe). The third reconstruction (represented in green) refers to the tie-points shown in Figure 4.9. The three colored straight lines (here, and in other 3D reconstruction figures in this Thesis) show the directions to STEREO B (violet), Earth (green), and STEREO A (red). Two viewpoints are shown, the left one is along the Sun-Earth line and the right one is along the propagation longitude. 81

Figure 4.11 - A diagram illustrating the selection of the apex of the CME (dashed black line) from the contours provided by CORSET (white contour) in each coronagraph image. The blue horizontal lines represent the epipolar lines. 82

Figure 4.12 - A screen dump of the “Sunloop/Tiepointer” tool showing the placement of automatic tie-points (black and white crosses on the CME leading edge contour). The white line shows the contour previously derived using CORSET (we modified the Sunloop code to allow the inclusion of the contours and the automatic determination of the tie-points to be used for 3D reconstruction). 83

Figure 4.13 - Diagram showing the main steps that need to be done when working with CORSET3D. 83

Figure 4.14 - One example of the difference of the reconstruction of the “apex” of the CME with the automatic tie-points derived using the CORSET contours in the Sunloop tool (right) and manually placing the tie-points in the Sunloop tool using the contour from CORSET only as a reference (left). Each line in a different color shows one of seven consecutive frames of a CME observed in 2008/12/12 between 10:07 and 13:07 UT. The Sun is represented by the 3D globe. The three colored straight lines (here, and in other 3D reconstruction figures) show the directions to STEREO B (violet), Earth (green), and STEREO A (red). This picture was made using the animator tool that is part of Sunloop application..... 85

Figure 4.15 - A simple model of a CME with spherical front (gray region) propagating approximately toward the Earth in the ecliptic plane with an angle β with respect to the Sun-Earth line. The STEREO A and B are supposed to be separated by the same angle θ . The dashed lines indicates the camera rays that are tangent to the CME model and, therefore, produce the brightest feature in the coronagraph FOV. Due to the DALE effect, the location calculated is the indicated by the red circle instead of the center of the CME. The illustration on the right details the geometry from the figure on the left.... 87

Figure 4.16 - The estimative of the error due to the DALE effect for the longitudinal propagation angle for $\beta = 10^\circ$ (black curve) and $\beta = 20^\circ$ (red curve). $\Delta\beta < 0$ indicates that the longitude estimated is smaller than the actual longitude. In this Figure we assume $a/R = 0.5$ 89

Figure 4.17 - The same than Figure 4.16 but assuming $a/R = 1.0$ 89

Figure 4.18 - The fractional error on the velocity of the CME due to the DALE effect supposing $a/R = 0.5$ and $\beta = 0^\circ$ (black), $\beta = 10^\circ$ (red) and $\beta = 20^\circ$ (green)..... 90

Figure 4.19 - The fractional error on the velocity of the CME due to the DALE effect supposing $a/R = 1.0$ and $\beta = 0^\circ$ (black), $\beta = 10^\circ$ (red) and $\beta = 20^\circ$ (blue).... 91

Figure 4.20 - A diagram of the Sun, showing lines of constant Stonyhurst heliographic longitude and latitude on the solar disk. The origin of the coordinate system

is at the intersection of the solar equator and the (terrestrial) observer's central meridian. Source: Thopson (2006).....	92
Figure 5.1 - Decrease (percentage) observed by each neutron monitor during each of the 18 magnetic clouds observed from 2008 to 2011. The date indicated in each bar indicates the beginning day of the magnetic cloud.....	95
Figure 6.1 - The interplanetary magnetic field and plasma parameters during a MC on 2008/12/17.	100
Figure 6.2 – The normalized cosmic ray count rate observed by the vertical directional channels of the GMND during the MC on 2008/12/17. The two vertical continuous lines indicate the beginning and end of the MC.	102
Figure 6.3 - The normalized cosmic ray count rate observed by three different neutron monitors (Delaware, Thule and McMurdo) throughout the MC on 2008/12/17. The two vertical dashed lines indicate the beginning and end of the MC.....	102
Figure 6.4 - The observation and modeling of cosmic ray depleted region associated to the magnetic cloud on 2008/12/17. The stair plot is the observed data and the line with diamonds is the modeling of the cosmic ray depleted region. The first panel, from top to bottom, shows the isotropic intensity. The remaining three plots show the orthogonal components of the fractional cosmic ray density gradient in the GSE coordinate system. The two vertical dashed lines correspond to the beginning and the end of the cosmic ray depleted region chosen by eye. These timings are indicated on top of the plot.	104
Figure 6.5 - A tridimensional representation of the cylinder derived from CRC model on 2008/12/17 at 10:00 UT. The Earth is located in the origin of the GSE coordinate system (represented by the three axis).....	105
Figure 6.6- The CME observed on 2008/12/12 on COR2A (left column) and COR2B (right column) FOVs. In this Figure, only the first three frames are shown.	109
Figure 6.7 - The CME observed on 2008/12/12 on COR2A FOV (left column) and COR2B FOV (right column). In this Figure, only the last three frames are shown.	110
Figure 6.8 - The height-time profile of the CME on 2008/12/12 on the COR2A FOV for the fastest moving position angle. A linear fit is shown and the speed calculated is indicated. This CME was tracked by CORSET from 11:07 UT to 14:37 UT.....	111

Figure 6.9 - The height-time profile of the CME on the COR2B FOV for the fastest moving position angle. A linear fit is shown and the speed calculated is indicated.	112
Figure 6.10 - The radial speed v_r of the CME front as a function of latitude and longitude (in HEEQ coordinate system). The black diamond indicates the center of the CME front.	113
Figure 6.11 - The direction of propagation for the CME on 2008/12/12. The blue points refer to the front track of the CME and the orange points to the back of the CME. On left panel, the results from the tangent-to-a-sphere method are shown. On the right, results from the triangulation method.	114
Figure 6.12 - Previous results from Liu et al. (2010) for the direction of propagation of the CME observed on 2008/12/12. Source: Liu et al. (2010).	116
Figure 6.13 - The interplanetary magnetic field and plasma parameters observed during a MC on 2009/02/04.	117
Figure 6.14 - The normalized cosmic ray count rate observed by the vertical directional channels of the GMND during the MC on 2009/02/04.	118
Figure 6.15 - The normalized cosmic ray count rate observed by three different neutron monitors (Delaware, Thule and McMurdo) during the MC ON 2009/02/04.	118
Figure 6.16 - The isotropic cosmic ray intensity and the orthogonal components of the cosmic ray fractional gradient during the MC period on 2009/02/04.	120
Figure 6.17 - The interplanetary magnetic field and plasma parameters during a MC on 2010/04/05.	122
Figure 6.18 - The normalized cosmic ray count rate observed by the vertical directional channels of the GMND during the MC on 2010/04/05.	124
Figure 6.19- The cosmic ray decrease observed by three different neutron monitors (Delaware, Thule and McMurdo) during the MC on 2010/04/05.	124
Figure 6.20 - The isotropic intensity and the orthogonal components of the gradient during the MC observation on 2010/04/05.	125
Figure 6.21 - The CME observed on 2010/04/03 in COR2A (left column) and COR2B (right column) FOVs. In this Figure, only the first three frames are shown.	127
Figure 6.22 - The CME observed on 2010/04/03 in COR2A (left column) and COR2B (right column) FOVs. In this Figure, only the last two frames are shown.	128

Figure 6.23 - The height-time profile of the CME on 2010/04/03 on the COR2A FOV for the fastest moving position angle. A linear fit is shown and the speed calculated in indicated. This CME was tracked by CORSET from 10:24 UT to 11:54 UT. ... 129

Figure 6.24 - The height-time profile of the CME on 2010/04/03 on the COR2B FOV for the fastest moving position angle. A linear fit is shown and the speed calculated is indicated. This CME was tracked by CORSET from 10:39 UT to 11:54 UT..... 130

Figure 6.25 - The radial speed v_r of the CME front as a function of latitude and longitude (in HEEQ coordinate system). The CME shown here was observed on 2010/04/03. The black diamond indicates the center of the CME front. 131

Figure 6.26 - The interplanetary magnetic field and plasma parameters during a MC on 2010/04/12. 134

Figure 6.27 - The cosmic ray decrease observed by three different neutron monitors (Delaware, Thule and McMurdo) during the MC on 2010/04/12. 135

Figure 6.28 - The cosmic ray decrease observed by the vertical directional channels of the GMND during the MC on 2010/04/12. 136

Figure 6.29 - The isotropic cosmic ray intensity and the orthogonal components of the cosmic ray fractional gradient during the MC period on 2010/04/12. 137

Figure 6.30 - The CME observed on 2010/04/08 on COR2A (left column) and COR2B (right column) FOVs. In this Figure, only the first three frames are shown. 140

Figure 6.31 - The CME observed on 2010/04/09 on COR2A (left column) and COR2B (right column) FOVs. In this Figure, only the fourth, fifth and sixth frames are shown. 141

Figure 6.32 - The radial speed of the CME front as a function of latitude and longitude (in HEEQ coordinate system). The CME shown here was observed on 2010/04/08. The black diamond indicates the center of the CME front. 143

Figure 6.33 - The projection of the GCS model (blue) of the elliptical flux rope model (in green) which is done using in situ data and the GCS model. Source: Colaninno (2012) 145

Figure 6.34 - The interplanetary magnetic field and plasma parameters during a MC observed on 2010/05/28. 146

Figure 6.35 - The CME observed on 2010/05/23 on COR2A (left column) and COR2B (right column) FOVs. In this Figure, only the first three frames are shown. 148

Figure 6.36 - The CME observed on 2010/05/23 on COR2A (left column) and COR2B (right column) FOVs. In this Figure, only the fourth, fifth and sixth frames are shown.	149
Figure 6.37 - The CME observed on 2010/05/24 on COR2A (left column) and COR2B (right column) FOVs. In this Figure, only the first three frames are shown.	150
Figure 6.38 - The radial speed of the CME front as a function of latitude and longitude (in HEEQ coordinate system). The CME shown here was observed on 2010/05/23. The black diamond indicates the center of the CME front.	151
Figure 6.39 - The radial speed of the CME front as a function of latitude and longitude (in HEEQ coordinate system). The CME shown here was observed on 2010/05/24. The black diamond indicates the center of the CME front.	152
Figure 6.40 - The normalized cosmic ray count rate observed by the vertical directional channels of the GMDN during the MC on 2010/05/28.	154
Figure 6.41 - The normalized cosmic ray count rate observed by three different neutron monitors (Delaware, Thule and McMurdo) during the MC on 2010/05/28.	155
Figure 6.42 - The observation and modeling of cosmic ray depleted region associated to the magnetic cloud on 2010/05/28. The stair plot is the observed data (from conventional correlation system) and the line with diamonds is the modeling of the cosmic ray depleted region. The first panel, from top to bottom, shows the isotropic intensity. The remaining three plots show the orthogonal components of the fractional cosmic ray density gradient in the GSE coordinate system. The two vertical dashed lines correspond to the beginning and the end of the cosmic ray depleted region chosen by eye. These timings are indicated on top of the plot.	156
Figure 6.43 - A tridimensional representation of the cylinder derived from CRC model on 2010/05/29 at 07:00 UT. The Earth is located in the origin of the GSE coordinate system (represented by the three axis).	157
Figure 6.44 - The interplanetary magnetic field and plasma parameters during a MC observed on 2010/08/04.	159
Figure 6.45 - The cosmic ray count rate observed by the vertical directional channels of the GMND during the MC on 2010/08/04.	160

Figure 6.46 - The cosmic ray decrease observed by three different neutron monitors (Delaware, Thule and McMurdo) during the MC on 2010/08/04.	161
Figure 6.47 - The isotropic cosmic ray intensity and the orthogonal components of the cosmic ray fractional gradient during the MC period on 2010/08/04.....	162
Figure 6.48 - The first earthward CME observed on 2010/08/01 on COR2A (left column) and COR2B (right column) FOVs.	164
Figure 6.49 - The second earthward CME observed on 2010/08/01 on COR2A (left column) and COR2B (right column) FOVs. In this Figure, only the first two frames tracked by CORSET are shown.	165
Figure 6.50 - The second earthward CME observed on 2010/08/01 on COR2A (left column) and COR2B (right column) FOVs. In this Figure, only the last two frames tracked by CORSET are shown.	166
Figure 6.51 - The three earthward directed CMEs identified by Liu et al. (2012). Source: Liu et al. (2012)	167
Figure 6.52 - The radial speed of the CME front as a function of latitude and longitude (in HEEQ coordinate system). This Figure corresponds to the first earthward CME observed on 2010/08/01. The black diamond indicates the center of the CME front.	169
Figure 6.53 - The radial speed of the CME front as a function of latitude and longitude (in HEEQ coordinate system). This Figure corresponds to the second earthward CME observed on 2010/08/01. The black diamond indicates the center of the CME front.	170
Figure 6.54 - The interplanetary magnetic field and plasma parameters during a MC observed on 2011/03/30.	172
Figure 6.55 - The CME observed on 2011/03/25 on COR2A (left column) and COR2B (right column) FOVs. In this Figure, only the first three frames are shown.	174
Figure 6.56 - The CME observed on 2011/03/25 on COR2A (left column) and COR2B (right column) FOVs. In this Figure, only the last two frames are shown here, the remaining are shown in Figure 6.55.....	175
Figure 6.57 - The time average radial speed of the CME front observed on 2011/03/25 as a function of latitude and longitude (in HEEQ coordinate system). The black diamond indicates the center of the CME front.	176

Figure 6.58 - The cosmic ray decrease observed by the vertical directional channels of the GMND during the MC on 2011/03/29. The vertical continuous lines correspond to the MC period suggested by the ICME catalog. 178

Figure 6.59 - The cosmic ray decrease observed by three different neutron monitors (Delaware, Thule and McMurdo) during the MC on 2011/03/29. The vertical continuous lines correspond to the MC period suggested by the ICME catalog. 179

Figure 6.60 - The observation and modeling of cosmic ray depleted region associated to the magnetic cloud in 2011/03/30 using the conventional correlation system. The stair plot is the observed data and the line with diamonds is the modeling of the cosmic ray depleted region. The first panel, from top to bottom, shows the isotropic CR intensity. The remaining three plots show the orthogonal components of the fractional cosmic ray density gradient in the GSE coordinate system..... 181

Figure 6.61 - The observation and modeling of cosmic ray depleted region associated to the magnetic cloud in 2011/03/30 using the conventional correlation system. The stair plot is the observed data and the line with diamonds is the modeling of the cosmic ray depleted region. The first panel, from top to bottom, shows the isotropic intensity. The remaining three plots show the orthogonal components of the fractional cosmic ray density gradient in the GSE coordinate system..... 182

Figure 6.62 - A tridimensional representation of the cylinder derived from CRC model on 2011/03/31 at 03:00 UT. The Earth is located in the origin of the GSE coordinate system (represented by the three axis)..... 183

Figure 6.63 - The projection of the GCS model (represented in blue and black) and elliptical flux rope model (in green). For the former, the blue outline is the maximum measured height. The black outline is the model projected to the height when the front crosses Earth. The dashed line is the axis at the center of the cavity. Source: Colaninno (2012). 184

Figure 6.64 - The interplanetary magnetic field and plasma parameters during a MC observed on 2011/05/28. 186

Figure 6.65 - The cosmic ray decrease observed by the vertical directional channels of the four muon detectors of the GMND during the MC on 2011/05/28.	187
Figure 6.66 - The cosmic ray decrease observed by three different neutron monitors (Delaware, Thule and McMurdo) during the MC on 2011/05/28.	188
Figure 6.67 - The cosmic ray gradient and omnidirectional intensity observed the GMDN during a MC observed on 2011/05/28.....	189
Figure 6.68 - The first earthward CME observed on 2011/09/06 on COR2A (left column) and COR2B (right column) FOVs.	190
Figure 6.69 - The second earthward CME observed on 2011/09/06 on COR2A (left column) and COR2B (right column) FOVs.	192
Figure 6.70 - The CME observed on 2011/09/08 on COR2A (left column) and COR2B (right column) FOVs.	193
Figure 6.71 - The CME observed on 2011/09/09 on COR2A (left column) and COR2B (right column) FOVs. In this Figure only the first three frames are shown.	195
Figure 6.72 - The CME observed on 2011/09/09 on COR2A (left column) and COR2B (right column) FOVs. In this Figure only the last two frames are shown.	196
Figure 6.73 - The interplanetary magnetic field and plasma parameters during a MC observed on 2011/09/10.	198
Figure 6.74 - The cosmic ray count rate observed by the vertical directional channels of the four muon detectors of the GMND during the MC on 2011/09/10.	199
Figure 6.75 - The cosmic ray decrease observed by three different neutron monitors (Delaware, Thule and McMurdo) during the MC on 2011/09/10.	200
Figure 6.76 - The cosmic ray isotropic intensity and orthogonal components of the gradient during the period of the MC (indicated by the vertical lines) observed on 2011/09/10.	201
Figure 6.77 - The interplanetary magnetic field and plasma parameters during a MC on 2011/09/17. The vertical lines indicate the magnetic cloud timing.	203
Figure 6.78 - The CME observed on 2011/09/14 in COR2A (left column) and COR2B (right column) FOVs. Only the first three frames are shown here. Notice that the images are rotated to the stereo baseline and that the north of the image is approximately pointing toward the bottom of the image.....	205

Figure 6.79 - The CME observed on 2011/09/14 in COR2A (left column) and COR2B (right column) FOVs. Only the fourth, fifth and sixth frame are shown here. Notice that the images are rotated to the stereo baseline and that the north of the image is approximately pointing toward the bottom of the image. 206

Figure 6.80 - The CME observed on 2011/09/14 in COR2A (left column) and COR2B (right column) FOVs. Only the last two frames are shown here. Notice that the images are rotated to the stereo baseline and that the north of the image is approximately pointing toward the bottom of the image..... 207

Figure 6.81 - The radial speed of the CME front observed on 2011/09/14 as a function of latitude and longitude (in HEEQ coordinate system). The black diamond indicates the center of the CME front. 208

Figure 6.82 - The cosmic ray decrease observed by the vertical directional channels of the four muon detectors of the GMND during the MC on 2011/09/17. 209

Figure 6.83 - The cosmic ray decrease observed by three different neutron monitors (Delaware, Thule and McMurdo) during the MC on 2011/09/17. 210

Figure 6.84 - The cosmic ray isotropic intensity and orthogonal components of the gradient during the period of the MC (indicated by the vertical lines) observed on 2011/09/17. 211

Figure 6.85 - The interplanetary magnetic field and plasma parameters during a MC on 2011/10/06. Within the thin vertical lines, there are three interplanetary structures. The thick vertical lines indicate the MC timing (disturbance #2). ... 213

Figure 6.86 - The CME observed on 2011/10/01 in COR2A (left column) and COR2B (right column) FOVs. Only the first three frames are shown here. Notice that the images are rotated to the stereo baseline and that the north of the image is approximately pointing toward the bottom of the image. Notice the presence of the another CME (located slightly northward) included in the boundary found by CORSET..... 215

Figure 6.87 - The CME observed on 2011/10/01 in COR2A (left column) and COR2B (right column) FOVs. Only the fourth, fifth and sixth frames are shown here. Notice that the images are rotated to the stereo baseline and that the north of the image is approximately pointing toward the bottom of the image. There is

another CME located slightly northward of the CME we are interested, but it is hard to distinguish them in the frames shown here.	216
Figure 6.88 - The CME observed on 2011/10/01 in COR2A (left column) and COR2B (right column) FOVs. Only the seventh and eighth frames are shown here. Notice that the images are rotated to the stereo baseline and that the north of the image is approximately pointing toward the bottom of the image. There is another CME located slightly northward of the CME we are interested, but it is hard to distinguish them in the frames shown here.	217
Figure 6.89 - The CME observed on 2011/10/02 in COR2A (left column) and COR2B (right column) FOVs. Only the first three frames are shown here. Notice that the images are rotated to the stereo baseline and that the north of the image is approximately pointing toward the bottom of the image.....	218
Figure 6.90 - The CME observed on 2011/10/02 in COR2A (left column) and COR2B (right column) FOVs. Only the last three frames are shown here. Notice that the images are rotated to the stereo baseline and that the north of the image is approximately pointing toward the bottom of the image.....	219
Figure 6.91 - The radial speed of the CME front observed on 2011/10/01 as a function of latitude and longitude (in HEEQ coordinate system). The black diamond indicates the center of the CME front.	221
Figure 6.92 - The radial speed of the CME front observed on 2011/10/02 as a function of latitude and longitude (in HEEQ coordinate system). The black diamond indicates the center of the CME front.	222
Figure 6.93 -The cosmic ray decrease observed by the vertical directional channels of the four muon detectors of the GMND during the MC on 2011/10/06.	224
Figure 6.94 - The cosmic ray decrease observed by three different neutron monitors (Delaware, Thule and McMurdo) during the MC on 2011/10/06.	224
Figure 6.95 - The cosmic ray isotropic intensity and orthogonal components of the gradient during the period of the MC and two other interplanetary structures. The vertical lines indicate the period since the beginning of the first structure until the end of the last one.....	225
Figure 6.96 - The interplanetary magnetic field and plasma parameters during a MC on 2011/10/25.	227

Figure 6.97 - The CME observed on 2011/10/22 in COR2A (left column) and COR2B (right column) FOVs. Only the first three frames are shown here. Notice that the images are rotated to the stereo baseline and that the north of the image is approximately pointing toward the bottom of the image.....	229
Figure 6.98 - The CME observed on 2011/10/22 in COR2A (left column) and COR2B (right column) FOVs. Only the last two frames are shown here. Notice that the images are rotated to the stereo baseline and that the north of the image is approximately pointing toward the bottom of the image.....	230
Figure 6.99 - The height-time profile of the CME on 2011/10/22 on the COR2A FOV for the fastest moving position angle. A linear fit is shown and the speed calculated in indicated. This CME was tracked by CORSET from 02:24 UT to 04:24 UT. ...	231
Figure 6.100 - The height-time profile of the CME on 2011/10/22 on the COR2B FOV for the fastest moving position angle. A linear fit is shown and the speed calculated in indicated. This CME was tracked by CORSET from 02:24 UT to 04:24 UT. ...	232
Figure 6.101 - The radial speed of the CME front as a function of latitude and longitude (in HEEQ coordinate system). The black diamond indicates the center of the CME front.	233
Figure 6.102 - The cosmic ray decrease observed by the vertical directional channels of the four muon detectors of the GMND during the MC on 2011/10/25.	234
Figure 6.103 - The cosmic ray decrease observed by three different neutron monitors (Delaware, Thule and McMurdo) during the MC on 2011/10/25.	235
Figure 6.104 - The observation and modeling of cosmic ray depleted region associated to the magnetic cloud in 2011/10/25 using data from the conventional correlation system. The stair plot is the observed data and the line with diamonds is the modeling of the cosmic depleted region. The first panel, from top to bottom, shows the isotropic intensity. The remaining three plots show the orthogonal components of the fractional cosmic ray density gradient in the GSE coordinate system. The two vertical dashed lines correspond to the beginning and the end of the cosmic ray depleted region chosen by eye. These timings are indicated on top of the plot.....	237
Figure 6.105 - The observation and modeling of cosmic ray depleted region associated to the magnetic cloud in 2011/10/25 using data from the new correlation	

system. The stair plot is the observed data and the line with diamonds is the modeling of the cosmic ray depleted region. The first panel, from top to bottom, shows the isotropic intensity. The remaining three plots show the orthogonal components of the fractional cosmic ray density gradient in the GSE coordinate system. The two vertical dashed lines correspond to the beginning and the end of the cosmic ray depleted region chosen by eye. These timings are indicated on top of the plot..... 238

Figure 6.106 - A tridimensional scale model of the cylinder derived from CRC model on 2011/10/25 at 08:00 UT using the conventional correlation system. The actual cylinder length used in the model is infinite. The Earth is located at the origin of the GSE coordinate system (represented by the three axes)..... 239

Figure 6.107 - The observation and modeling of cosmic ray depleted region associated to the magnetic cloud in 2011/10/25 using data from the conventional correlation system and imposing the latitude and longitude angles found by the MVA analysis. The stair plot is the observed data and the line with diamonds is the modeling of the cosmic ray depleted region. The first panel, from top to bottom, shows the isotropic intensity. The remaining three plots show the orthogonal components of the fractional cosmic ray density gradient in the GSE coordinate system. The two vertical dashed lines correspond to the beginning and the end of the cosmic ray depleted region chosen by eye. These timings are indicated on top of the plot..... 240

Figure 6.108 - The interplanetary magnetic field and plasma parameters during a MC at 2011/11/07. 242

Figure 6.109 - The cosmic ray count rate observed by the vertical directional channels of the four muon detectors of the GMND during the MC at 2011/11/07. The two vertical continuous lines indicate the beginning and end of the MC. 244

Figure 6.110 - The cosmic ray count rate observed by three different neutron monitors (Delaware, Thule and McMurdo) during the MC on 2011/11/07. The two vertical dashed lines indicate the beginning and end of the MC..... 245

Figure 6.111 - The isotropic cosmic ray intensity and the orthogonal components of the cosmic ray fractional gradient during the MC period on 2011/11/07..... 246

Figure 6.112 - The interplanetary magnetic field and plasma parameters during a MC on 2011/11/29.	248
Figure 6.113 - The cosmic ray count rate observed by the vertical directional channels of the four muon detectors of the GMND during the MC on 2011/11/29. The vertical lines indicate the period of the magnetic cloud.	249
Figure 6.114 - The cosmic ray count rate observed by three different neutron monitors (Delaware, Thule and McMurdo) during the MC on 2011/11/29.	250
Figure 6.115 - The isotropic cosmic ray intensity and the orthogonal components of the cosmic ray fractional gradient during the MC period on 2011/11/29. The error bars indicate the error calculated from the six data points calculated using integration time of 10 minutes.....	251
Figure 6.116 - The CME observed on 2011/11/26 in COR2A (left column) and COR2B (right column) FOVs. Notice that the images are rotated to the stereo baseline and that the north of the image is approximately pointing toward the bottom of the image.	253
Figure 6.117 - The height-time profile of the CME on 2011/11/26 in the COR2A FOV for the fastest moving position angle. A linear fit is shown and the speed calculated is indicated. This CME was tracked by CORSET from 07:39 UT to 08:54 UT.....	254
Figure 6.118 - The height-time profile of the CME on 2011/11/26 on the COR2B FOV for the fastest moving position angle. A linear fit is shown and the speed calculated is indicated. This CME was tracked by CORSET from 07:54 UT to 09:24 UT.....	255
Figure 6.119 - The radial speed of the CME front as a function of latitude and longitude (in HEEQ coordinate system). The black diamond indicates the center of the CME front.	256

LIST OF TABLES

	<u>Page</u>
Table 1.1 - Difference between the gradual and impulsive CMEs. Source: Sheeley et al. (1999)	13
Table 1.2 - The locations of each detector of the Global Muon Detector Network.	19
Table 3.1 - The main characteristics of each conventional directional channel for Nagoya detector.	30
Table 3.2 - The main characteristics of each conventional directional channel for Hobart detector.	30
Table 3.3 - The main characteristics of each conventional directional channel for Kuwait detector.	31
Table 3.4 - The main characteristics of each conventional directional channel for São Martinho da Serra detector.	31
Table 3.5- The coupling coefficient c_{01} calculated for the conventional correlation system. ...	39
Table 3.6 - The coupling coefficient c_{11} calculated for the conventional correlation system...	40
Table 3.7 - The coupling coefficient s_{11} calculated for the conventional correlation system....	41
Table 3.8 - The meaning of each term in Eq. 3.1.....	44
Table 4.1 - The average plus or minus one standard deviation GLCM for a CME in their first frame. These values were calculated using COR2B for the CMEs observed on 2010/04/03, 2010/04/08 and 2010/07/30.	70
Table 4.2 - The average plus or minus standard deviation GLCM for a CME in the last frame calculated using COR2B for the CME observed on 2010/04/03, 2010/04/08 and 2010/07/30. This depends of the expansion parameter used and it will be exactly the same GLCM of first frame when $Q=0$ (no expansion, see explanation in Section 4.5).	70
Table 4.3 - The average GLCM for the background using COR2B for the CME observed on 2010/04/03, 2010/04/08 and 2010/07/30.....	70
Table 4.4 - Comparison of the manual and automatic tie-points.	84
Table 5.1 - List of magnetic clouds analyzed in this Thesis.	93
Table 5.2 - The location of each Neutron Monitor Station.	95
Table 6.1 - The parameters of the MC observed on 2008/12/17.	105

Table 6.2 - Results of the latitude and longitude of the flux rope found by different methods.	107
Table 6.3 - Kinematic parameters of the CME derived using CORSET3D. The angles shown here are given in HEEQ coordinate system.....	113
Table 6.4 - Kinematic parameters of the CME on 2010/04/03. The angles shown here are given in HEEQ coordinate system.	130
Table 6.5 - Comparison of the speed derived for the CME observed on 2010/04/03 by different previous works and two automatic catalogs (indicated by an asterisk).....	133
Table 6.6 - The projected speed of the CME observed on 2010/04/08 on the COR2A and COR2B FOVs.....	142
Table 6.7 - Kinematic parameters of the CME derived using CORSE3D. The angles shown here are given in HEEQ coordinate system.....	143
Table 6.8 - The two CMEs associated to the MC observed in 2010/05/28.....	147
Table 6.9 - Kinematic parameters of the CME on 2010/05/23 and 2010/05/24. The angles shown here are given in HEEQ coordinate system.	152
Table 6.10 - Comparison of the speed derived for the CME observed on 2010/05/23 (CME #1) by different previous works and two automatic catalogs (indicated by an asterisk). ...	153
Table 6.11 - Comparison of the speed derived for the CME observed in 2010/05/24 (CME #2) by different previous works and two automatic catalogs (indicated by an asterisk). ...	153
Table 6.12 - Parameters of the cosmic ray cylinder model of the MC observed on 2010/05/28.	157
Table 6.13 - Kinematic parameters of the two earthward directed CMEs observed on 2010/08/01. The angles shown here are given in HEEQ coordinate system.....	170
Table 6.14 - Comparison of the direction and de-projected speed of the two earthward CMEs observed on 2010/08/01 derived using different methods (in HEEQ coordinates)..	171
Table 6.15 - Kinematic parameters of the CME on 2011/03/25. The angles shown here are given in HEEQ coordinate system.	176
Table 6.16 - The speed of the CME observed on 2011/03/25 on the COR2 A and COR2 B coronagraphs.	177
Table 6.17 - Parameters of the cosmic ray cylinder model of the MC observed on 2010/03/30.	180
Table 6.18 - Results of the minimum variance analysis (MVA) using SP and LP.	185

Table 6.19 - Kinematic parameters of the four CME ejected toward Earth from 2011/09/06 to 2011/09/09. The angles shown here are given in HEEQ coordinate system.	197
Table 6.20 - Kinematic parameters of the CMEs on 2011/09/14. The angles shown here are given in HEEQ coordinate system.	208
Table 6.21 - The list of three consecutive ICMEs on the beginning of October 2011. Source: ICME catalog from Richardson and Cane.....	212
Table 6.22 - The Earthward CMEs observed in association to the MC event on 2011/10/06..	220
Table 6.23 - Kinematic parameters of the CMEs on 2011/10/01 and 2011/10/02. The angles shown here are given in HEEQ coordinate system.....	223
Table 6.24 - Kinematic parameters of the CME on 2011/10/22. The angles shown here are given in HEEQ coordinate system.	233
Table 6.25 - Parameters of the cosmic ray cylinder model of the MC observed on 2011/10/25.	236
Table 6.26 - Kinematic parameters of the CME on 2011/11/26. The angles shown here are given in HEEQ coordinate system.	256
Table 7.1 – MCs (observed from 2008 to 2010) and characteristics of corresponding CMEs .	258
Table 7.2 – MCs (observed in 2011) and characteristics of corresponding CMEs	259
Table 7.3 - Parameters used when tracking each CMEs using CORSET that were compared to previous works.....	262
Table 7.4 - CME tracked by CORSET3D in this Thesis that could not be compared to previous works.....	263

LIST OF ABBREVIATIONS

AU	-	Astronomical Unit
CME	-	Coronal Mass Ejection
CORSET	-	Coronal Segmentation Tracking
CR	-	Cosmic Ray
CRC	-	Cosmic Ray Cylinder
EFR	-	Elliptical Flux Rope
FOV	-	Field-of-View
GCS	-	Graduated Cylindrical Shell
GMDN	-	Global Muon Detector Network
GSE	-	Geocentric Solar-Ecliptic
HEE	-	Heliocentric Earth Ecliptic
HEEQ	-	Heliocentric Earth Equator
ICME	-	Interplanetary Coronal Mass Ejection
IMF	-	Interplanetary Magnetic Field
LASCO	-	Large Angle Spectrometric Coronagraph
MC	-	Magnetic Cloud
MVA	-	Minimum Variance Analysis
SECCHI	-	Sun Earth Connection Coronal and Heliospheric Investigation
SOHO	-	Solar and Heliospheric Observatory
STEREO	-	Solar Terrestrial Relations Observatory

CONTENTS

	<u>Page</u>
1 INTRODUCTION	1
1.1 CMEs: first observation and definition.....	2
1.2 Thomson scattered light and the spectral components	6
1.3 The coronagraphs from SOHO and STEREO missions	8
1.4 Tridimensional reconstruction of CMEs.....	10
1.5 Propagation of CMES.....	12
1.6 Interplanetary coronal mass ejections and magnetic clouds.....	13
1.7 Cosmic rays: definition	14
1.8 Cosmic rays in the interplanetary medium and in the Earth's atmosphere	16
1.9 The Global Muon Detector Network (GMDN)	18
1.10 The cosmic ray arrival direction and the effects of the geomagnetic field.....	23
1.11 A model for cosmic ray distribution inside the magnetic cloud	25
2 OBJECTIVES.....	27
3 COSMIC RAYS (MUONS): FROM COUNT RATE TO COSMIC RAY DENSITY GRADIENT	29
3.1 The directional channels of the conventional and new correlation system	29
3.2 Removing the atmospheric effects on the muon count rate.....	34
3.3 The concept of the anisotropy vector.....	37
3.4 Calculation of the coupling coefficients.....	38
3.5 Calculation of the anisotropy vector.....	44
3.6 The Compton-Getting effect	47
3.7 The cosmic ray gradient	50

3.8	Recalculating the first order anisotropy vector and the cosmic ray gradient density using integration time of 10 minutes.....	52
3.9	A model of cosmic ray density inside the magnetic cloud.....	57
3.10	An additional model of cosmic ray density inside the magnetic cloud.....	61
3.11	Testing the model from Kuwabara et al. (2009)	61
4	DERIVING THE CORONAL MASS EJECTION KINEMATIC PARAMETERS.....	65
4.1	The CORSET	65
4.2	Why using CORSET instead of other manual or automatic catalogs?.....	66
4.3	Texture analysis.....	68
4.4	Detection of the CME: segmenting it from the background.....	71
4.5	Tracking the CME	72
4.6	Deriving the radial speed of a CME in a coronagraphic image	73
4.7	Starting stereoscopy: a tridimensional reconstruction using the epipolar constraint	76
4.8	One tool to reconstruct CMEs front.....	79
4.9	Combining CORSET and Sunloop.....	81
4.10	Are the results similar using manual and automatic tie-points?	84
4.11	Deriving the radial speed of the CME as a function of angle	85
4.12	The error estimative.....	86
4.13	Coordinates systems used in the solar corona	91
5	CRITERIA TO SELECT THE LIST OF EVENTS.....	93
5.1	List of magnetic clouds.....	93
5.2	Interplanetary magnetic field and solar wind plasma data	94
5.3	The cosmic ray decreases observed by neutron monitors	94
5.4	The cosmic ray analysis in previous works.....	96
5.5	Events discarded from the list.....	96
6	RESULTS.....	99

6.1	The magnetic cloud observed on 2008/12/17	99
6.1.1	The interplanetary medium	99
6.1.2	The cosmic ray observations and modeling	101
6.1.3	The origins in the solar corona	107
6.2	The magnetic cloud observed on 2009/02/04	116
6.2.1	The interplanetary medium	116
6.2.2	The cosmic ray observations and modeling	118
6.2.3	The origins in the solar corona	120
6.3	The magnetic cloud observed on 2010/04/05	121
6.3.1	The interplanetary medium	121
6.3.2	The cosmic ray observation.....	123
6.3.3	The origins in the solar corona	125
6.4	The magnetic cloud observed on 2010/04/12	133
6.4.1	The interplanetary medium	133
6.4.2	The cosmic ray observations	135
6.4.3	The origins in the solar corona	138
6.5	The magnetic cloud observed on 2010/05/28	145
6.5.1	The interplanetary medium	145
6.5.2	The origins in the solar corona	147
6.5.3	The cosmic ray observation and modeling.....	154
6.6	The magnetic cloud observed on 2010/08/04	158
6.6.1	The interplanetary medium	158
6.6.2	The cosmic ray observations	160
6.6.3	The origins in the solar corona	163
6.7	The magnetic cloud observed on 2011/03/30	171
6.7.1	The interplanetary medium	171

6.7.2	The origins in the solar corona	173
6.7.3	The cosmic ray observations and modeling	178
6.8	The magnetic cloud observed on 2011/05/28	185
6.9	The magnetic cloud observed on 2011/09/10	189
6.9.1	The origins in the solar corona	189
6.9.2	The interplanetary medium and the cosmic ray modulation	197
6.9.3	The cosmic ray observations	199
6.10	The magnetic cloud observed on 2011/09/17	201
6.10.1	The interplanetary medium	201
6.10.2	The origins in the solar corona	204
6.10.3	The cosmic ray observations and modeling	209
6.11	The magnetic cloud observed on 2011/10/06	211
6.11.1	The interplanetary medium	211
6.11.2	The origins in the solar corona	214
6.11.3	The cosmic ray observations	223
6.12	The magnetic cloud observed on 2011/10/24	226
6.12.1	The interplanetary medium	226
6.12.2	The origins in the solar corona	228
6.12.3	The cosmic ray observations and modeling	234
6.13	The magnetic cloud observed on 2011/11/07	241
6.14	The magnetic cloud observed on 2011/11/29	246
6.14.1	The interplanetary medium	246
6.14.2	The cosmic ray observations	249
6.14.3	The origins in the solar corona	251
7	DISCUSSION OF THE RESULTS	257
7.1	Earthward directed CMEs observed	257

7.2	Overall analysis of CORSET3D tracking results for each CME	260
7.3	Results from cosmic ray observation	263
7.4	Comparing the properties of CMEs and corresponding ICMEs.....	265
8	CONCLUSIONS	269
	REFERENCES	275

1 INTRODUCTION

The study of Sun-Earth relationships started more than a century and a half ago with the first association of a solar flare with geomagnetic phenomena by R. C. Carrington and R. Hodgson (CARRINGTON, 1859; HODGSON, 1859). Since the beginning of the space era and the development of scientific satellites and spacecraft, a huge amount of data has been collected, both *in situ* in the interplanetary medium and from remote sensing of the Sun. This allowed the observation, study and discovery of many solar and interplanetary phenomena that we know today.

Among these phenomena, coronal mass ejections (CMEs) and their corresponding structures in the interplanetary medium (known as ICMEs) are of great importance because they are directly responsible for geomagnetic storms (GOSLING et al., 1990). They cause most of the intense storms (GONZALEZ et al., 1999). Geomagnetic storms are perturbations in the magnetic field of the Earth that are linked with damages in many technological systems. Onboard satellites, memory devices may lose information (DUZELLIER, 2005). On the surface of the Earth, failures in telecommunication systems and blackouts in the electric power grid may happen (BOTELER et al., 1998). One way to prevent these damages is forecasting geomagnetic storms by studying the CMEs that caused them.

Depending on some characteristics, the CMEs may or may not cause a geomagnetic storm. First, we need to know the propagation direction of the CME close to the Sun to decide whether it is coming toward the Earth or not. When a CME is directed toward the Earth, the onset of the geomagnetic storm depends on the arrival time of the CMEs at the Earth. This arrival time ranges from tens to hundreds of hours and, for this reason, studying the CME speed is of central interest. Finally, a CME arriving at the Earth does not cause a geomagnetic storm if its magnetic configuration does not follow a specific pattern that enables enhanced solar wind-magnetosphere energy coupling through the magnetic reconnection mechanism (GONZALEZ et al., 1999). The magnetic configuration of the CMEs close to the Sun has never been observed *in situ* so far, but can be inferred using some reconstruction techniques (THERNISIEN et al., 2006). This magnetic configuration, however, is not necessarily kept constant while the CME propagates from the Sun to the Earth: sometimes the CMEs interact with other interplanetary

structures and their characteristics are changed (LUGAZ et al., 2012). Thus, it is necessary to study the magnetic configuration of the corresponding ICME close to the Earth.

The motivation to start this Thesis is trying to improve the answer to whether a CME will have the appropriate characteristics to cause a geomagnetic storm:

- is the CME coming toward the Earth?
- when will the ICME arrive at Earth?
- how is the magnetic configuration of the CME/ICME?

As there is no *in situ* data of the Sun so far, remote sensing is the key to study the Sun and the CMEs. As will be explained later in this Chapter, observations from more than one viewpoint started in 2006 allowing us to better study the propagation speed and direction of CMEs.

The magnetic configuration of ICMEs close to the Earth can be studied by analyzing the spatial and temporal variation of cosmic rays which are electrically charged particles arriving to Earth from outside the solar system. These particles are modulated by the magnetic structure of ICMEs when they are near the Earth, this allows us to study ICMEs. The observation of these particles was also highly improved in 2008 (OKAZAKI et al., 2008).

1.1 CMEs: first observation and definition

The first observation of a CME was made in December 14th 1971 by the spacecraft Orbiting Solar Observatory 7 (OSO-7) and the term was mentioned for the first time by Gosling et al. (1975).

The definition of a CME is:

an observable change in coronal structures that (1) occurs on a timescale between a few minutes and several hours and (2) involves the appearance of a new, discrete, bright white-light feature in the coronagraph field of view (HOWARD et al., 1997, p. 18).

Notice that the definition above is very focused on the observations. Mierla et al. (2010) describe a definition more focused on the physical processes:

CMEs are enormous eruptions of magnetized plasma expelled from the Sun into the interplanetary space, over the course of hours to days (MIERLA et al., 2010, p. 203).

The detection of CMEs in white light requires an instrument called coronagraph. Such an instrument is pointed toward the Sun but does not take the direct light incident from the solar disk because the coronagraph blocks it with an occulting disk. The observation of a coronagraph is equivalent to observing the Sun during a full eclipse. The light observed by coronagraphs is called Thomson-scattered light (described in more details in the Section 1.2). These instruments can be installed in observatories both on the ground and onboard a spacecraft. Nowadays, there are at least two coronagraphs in operation: one onboard the Solar and Heliospheric Observatory, hereafter SOHO (1996-now) and another onboard the twin Solar Terrestrial Relations Observatory, hereafter STEREO (2006-now). There are also a few ground-based coronagraphs such as the Mirror Coronagraph for Argentina (MICA). An example of a CME viewed by SOHO is shown in Figure 1.1.

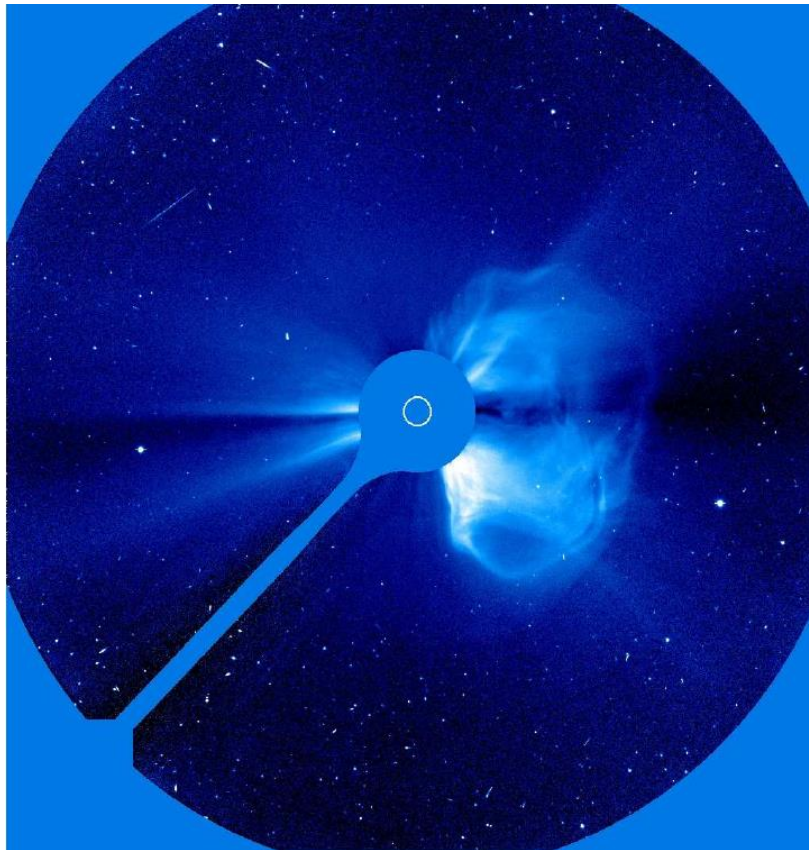


Figure 1.1 - An example of a coronal mass ejection observed by LASCO-C3 onboard SOHO spacecraft.
Source: <http://sohowww.nascom.nasa.gov/> (2010).

The frequency of CME observation depends strongly on the phase of the 11-year solar cycle: while during solar minimum around one is observed per day, nearly five per day are observed at

solar maximum (ST CYR et al., 2000; GOPALSWAMY et al., 2006). The mass carried lies in the range of 10^{14} to 10^{16} g (VOURLIDAS et al., 2010). The transverse size of a CME can cover from a fraction up to more than a solar radius, and the ejection speed is in the range from hundreds to thousands of km/s. It is a consensus that a CME is associated with a release of magnetic energy in the solar corona, but its relation to the flare phenomenon is controversial (GOSLING, 1993). Even big flares have no associated CME in about 40% of the cases (ANDREWS, 2003).

A CME have a variety of shapes and there are some attempts to classify them. Howard et al. (1985) classified the CMEs in 10 different categories taking into account their morphology. More recently, Vourlidas et al. (2013) classified the CMEs into five observation-based categories:

- Flux-rope: CMEs that exhibit a clear three-part structure: a bright leading edge, a dark void (also called cavity) and a bright core (ILLING; HUNDHAUSEN, 1986; HOWARD et al., 1985), as displayed in Figure 1.2. These CMEs are considered to have embedded magnetic flux ropes. This category agrees very well with CMEs classified as “structured CMEs” by Cremades (2005);
- Loop: CMEs with a bright and filamentary loop but without core and/or cavity;
- Jet: narrow CMEs with width of less than about 40° lacking a sharp front, detailed sub-structure, or circular morphology;
- Outflow: similar than the jets but wider;
- Failed: events that are very bright in the corona close to the Sun but that disappear while they move outward;
- Unknown: events that cannot be classified in any of the other categories mainly due to poor observational data.

The morphology of CMEs is subject of much debate, because of ambiguities from the line-of-sight projection effects and the optical thickness of CMEs. Other point is that the shape of some CMEs may change with time in the coronagraph field-of-view making the morphological classification even more complicated (MIERLA et al., 2009). One example is shown in Figure 1.3.

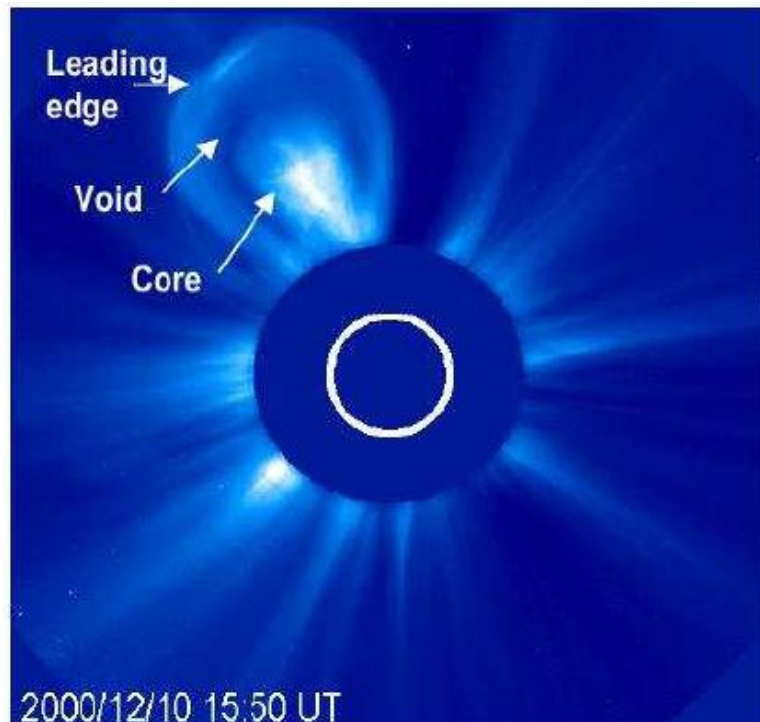


Figure 1.2 - A three-part structured CME showing the characteristic bright leading edge, dark void, and bright core. This event was observed by the LASCO/C2 coronagraph on 2000/12/10. The visible solar disc is represented by the white circle, while the larger dark disc shows the coronagraph occulter.
Source: Cremades (2005).

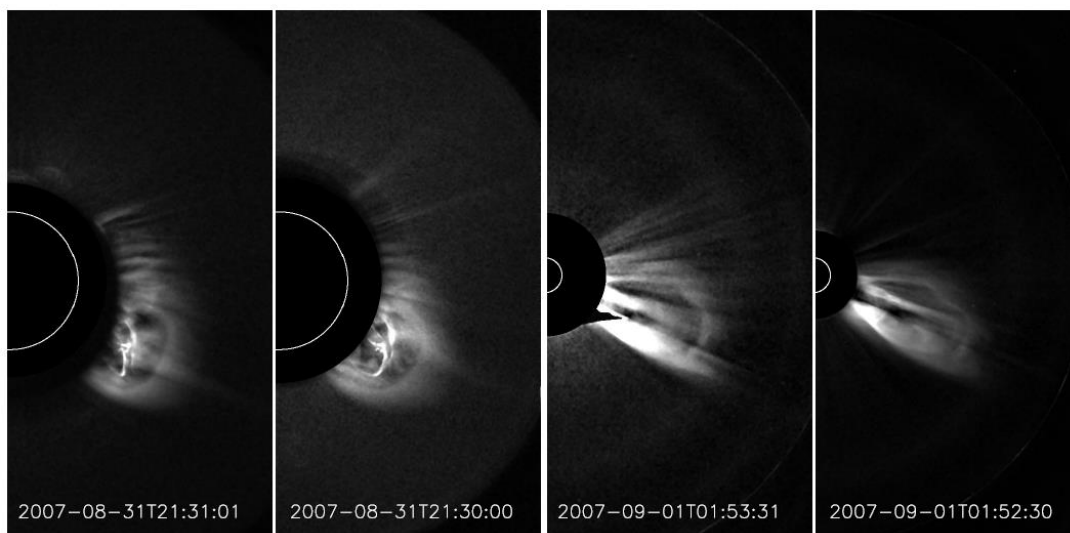


Figure 1.3 - An example of the change in the shape of a CME as it evolves. Two different timings of the same CME ejected in 2007/08/31 are illustrated. The first timing is in the SECCHI-COR1 field-of-view (the left two columns) and the second in the SECCHI-COR2 COR2 field-of-view (the right two columns) coronagraphs. Both A (second and fourth columns) and B (first and third columns) STEREO spacecraft images are shown. In all panels, the visible solar disc is represented by the white circle, while the larger dark disc shows the coronagraph occulter.
Source: adapted from Mierla et al. (2009).

Regarding shape of CMEs in a given coronagraph field-of-view, there are some terms frequently used: halo, semi (or partial) halo and limb CMEs. Halo CMEs are those with an apparent width of about 360° in a coronagraph field-of-view (HOWARD et al., 1982). They are directed parallel or anti-parallel to the Sun-observer line. The partial halo CMEs are those which apparent width lower than 360° but at least about 180° . Their propagation direction is almost parallel to the observer-Sun line. We call limb CMEs those with apparent width smaller than 180° that are ejected almost perpendicularly to the Sun-observer line. It is important to emphasize that a given CME can be seen as a halo from a given observation point and as a semi halo or limb from a different point of view.

1.2 Thomson scattered light and the spectral components

The white light emission of the solar corona originates from the Thomson scattering of the photospheric light into free coronal electrons. The brightness we see in any coronagraph image is related to the density of free electrons in a given region (MINNAERT, 1930). The electromagnetic waves hit the free electrons in a plasma and accelerate them. The electrons will then release radiation in the plane perpendicular to the incident wave. This plane is called reemission plane. If an observer is located in a position that his/her line of sight is parallel to the reemission plane, the observed brightness will be maximum. If the line-of-sight is perpendicular, the observer does not see any brightness (BILLINGS, 1996).

When the electron is relatively close to the Sun, the reemission plane is parallel to the line-of-sight. However, when the electron is significantly distant from the Sun, the reemission plane is no longer parallel to the observer (see Figure 1.4, the red arrow represents the reemission plane). The points that have reemission plane parallel to a given observer produce a spherical shell. This sphere is called Thomson's sphere (VOURLIDAS; HOWARD, 2006). One example of an electron located on the Thomson's sphere is shown in Figure 1.4 by the green points.

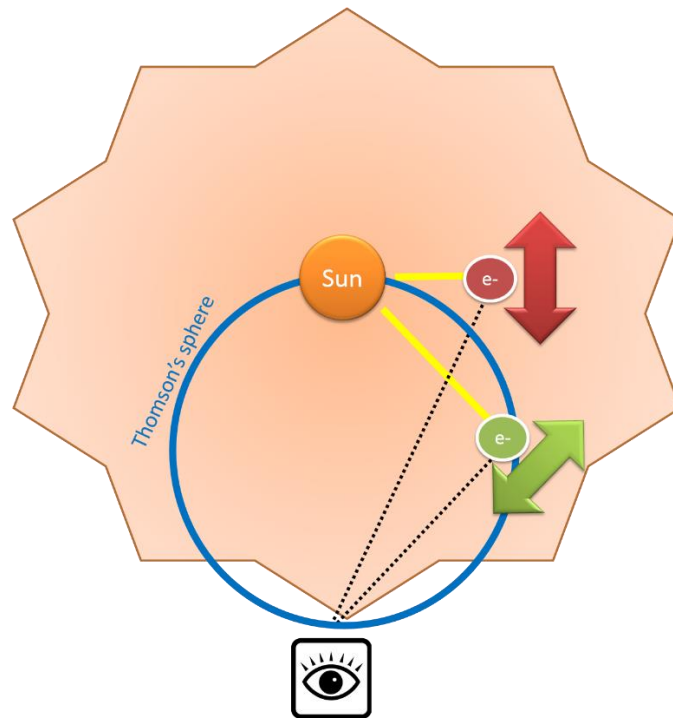


Figure 1.4 - Two arbitrary particles (represented by the green and red circles) from the solar corona (represented in orange). These particles receive light from the photosphere of the Sun (represented by the orange circle) and reemit it. Part of the reemission (black dashed lines) is seen by some observers (black eye). The reemission is maximum in the plane indicated by each arrow close to the red and green points. The geometric representation of all points in space where the emission is maximum forms a sphere that is called Thomson's sphere (whose projection in the ecliptic plane is shown in black).

A coronagraph observes the solar corona by blocking the direct light incident from the solar photosphere. It should ideally observe only the white light coming from the corona. Beyond some small contribution from the undesired direct photospheric light, the coronagraphs observe brightness due to two spectral components: the *kontinuerlich* (K) and the Fraunhofer (F). The "K" component comes from the solar corona but the "F" component does not. Therefore, it needs to be removed.

The "K" component is due to photospheric light scattered by free electrons in the corona. This component has a continuous spectrum and is partially polarized. This emission is optically thin and what we see in the coronagraph is the integrated emission along the line-of-sight. The "F" component comes from the photospheric light scattered by dust and it is unpolarized. Its contribution increases with the increment of the distance from the Sun and cannot be ignored after five solar radii if someone is interested in calculating the electron density from the brightness of the coronagraph images (HAYES et al., 2000). Usually the "F" component is almost

constant with time (changes only in a period of days) while the “K” component is very dynamic (changes from hour to hour).

1.3 The coronagraphs from SOHO and STEREO missions

The Solar and Heliospheric Observatory (SOHO) was launched in 1995 and it is located along the Sun-Earth line in the point of equilibrium between the gravity of the Earth and the Sun (L1 Lagrangian Point), about 1.6×10^6 km distant from the Earth (HOWARD et al., 1997). The Large Angle Spectrometric Coronagraph (LASCO) is one of the instrument sets onboard SOHO. It consists of three white-light coronagraphs, called C1, C2 and C3. Together the instruments cover from 1.1 to 30 solar radii (BRUECKNER et al., 1995). Almost 20 years after the launch, LASCO-C2 and LASCO-C3 are still in operation.

The Solar-Terrestrial Relations Observatory (STEREO) is a set of two identical spacecraft, one located ahead and the other behind the Earth when taking into consideration the orbit around the Sun. Both spacecraft are located at about 1 Astronomical Unit (AU) distant from the Sun. The spacecraft ahead is referred as STEREO A and the one behind as STEREO B. The orbits of both spacecraft (Figure 1.5) are such that the angle between each one and the Earth (with origin in the Sun) increases about 45 degrees per year (DUNHAM et al., 2009). When they were launched, in the end of 2006, the angle was close to zero. After 4 years, the angle was about 90 degrees. In the meantime, the front side of the Sun was observed from two viewpoints. By the end of 2014 the angle is close to 180° and they are remote sensing the backside of the Sun.

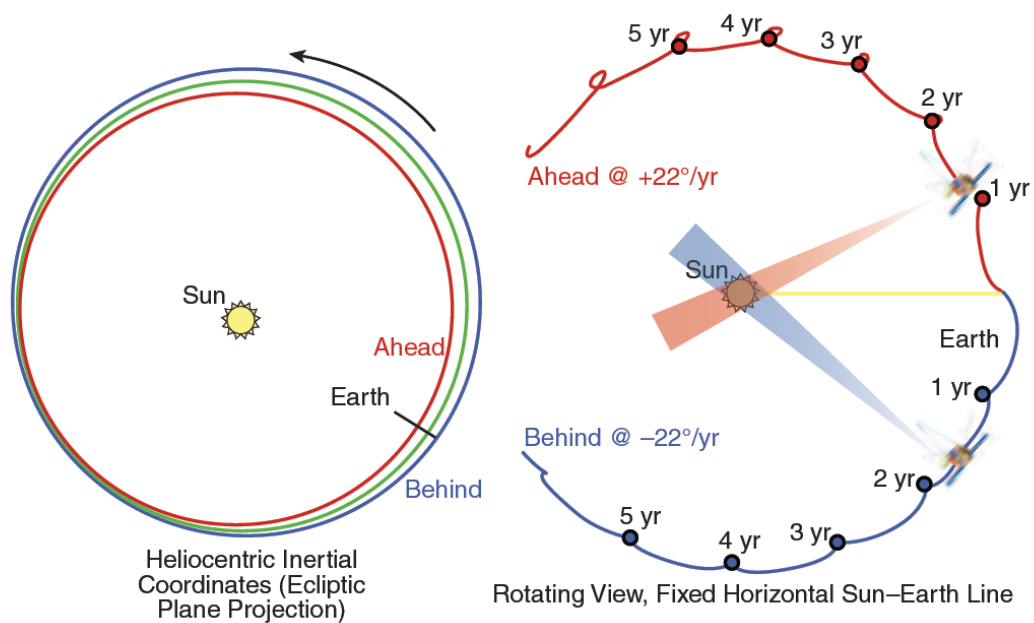


Figure 1.5 - The orbits of the twin STEREO spacecraft seen in the ecliptic plane by an observer located north of this plane. On the left, the trajectory is represented by an inertial Sun centered coordinate system. On the right, the Sun-Earth line (represented in yellow) is fixed to show the increasing distance from the Earth.

Source: Dunham et al. (2009).

Among other instruments onboard STEREO, the CMEs can be studied using a set of five instruments called “Sun Earth Connection Coronal and Heliospheric Investigation” (SECCHI). The acronym was chosen as a reference to the Italian astrophysicist Angelo Secchi (1818-1878), one of the pioneers to photograph the Sun during eclipses (HOWARD et al., 2008).

SECCHI has three types of instruments. One is an extreme ultraviolet (EUV) telescope that allow us to study the solar chromosphere and the solar corona up to 1.7 solar radii. This instrument is known as EUVI. The second type is a white-light coronagraph, which is of primary interest in this Thesis. Each one of the twin STEREO spacecraft has two coronagraphs, called COR1 and COR2. Together they cover the corona from 1.4 to 4 solar radii and from 2.5 to 15 solar radii, respectively. They are very similar to the C2 and C3 coronagraphs from the LASCO instrument. The reason to split the observation range in two instrument is the high brightness gradient in this range. The third type of instruments is called Heliospheric Imager (HI) and covers the corona from 15 to more than 200 solar radii (HOWARD et al., 2008).

1.4 Tridimensional reconstruction of CMEs

The first studies of CMEs in three dimensions started in close timing to the beginning of the STEREO mission because it was the first mission to allow simultaneous observations of the solar corona from more than one viewpoint (HOWARD et al., 2008).

There are several methods to reconstruct CMEs in 3D and, therefore, to derive their kinematic properties. These methods can be organized in three categories: a) those based in Thomson scattering properties; b) those based in epipolar geometry and tie-points; c) those based in forward modelling and inverse reconstruction. Each category is explained briefly in the next paragraphs.

The degree of polarization of Thomson-scattered light by coronal electrons is a function of the scattering angle between the direction of the incident light and the direction toward the observer (BILLINGS, 1966). In Figure 1.4, this is the angle between the yellow and black lines. By analyzing the ratio of polarized to unpolarized brightness, the scattering angle can be deduced and, as a consequence, the distance of the scattering location from the plane of the sky can be estimated (MORAN; DAVILA, 2004). All coronagraphs onboard LASCO and SECCHI take images with polarized brightness in three different orientations and can be used to do this analysis. The advantage of this method is that it does not need two viewpoints, therefore, it could be used before the STEREO/SECCHI era. More recently, it was applied independently to both STEREO spacecraft and the two results were compared to each other, providing an idea of the method uncertainty (MORAN et al., 2010)

Inhester (2006) introduced the application of epipolar geometry and tie pointing to CMEs. Tie-points are pair of points (one in each image taken from two different viewpoints) that correspond to the projection of the same object (or feature) in each image. Thanks to the epipolar geometry, the tie-points are constrained in a given line and finding them becomes easier. This methodology is used in this Thesis and it is described in Chapter 4.

The forward modeling techniques assumes a physical and/or geometric model of a CME. It is very frequent the use a physical model of a magnetic flux rope (the same physical model used in magnetic clouds, as explained in Section 1.6). The flux rope is then represented by the graduated cylinder shell (GCS) model. It consists of a tubular section attached to two cones that connect the main body of the CME to the solar surface (THERNISIEN et al., 2009). This structure

has free parameters that adjust both position and orientation (θ, ϕ, γ in the left side of the Figure 1.6), as well as size (c, a, α, δ on the right side of the same Figure) of the CME. Although many authors assume a flux rope for any CME studied, only about 40% of the CMEs follow the flux rope structure (see a discussion about this in Vourlidas et al., 2013).

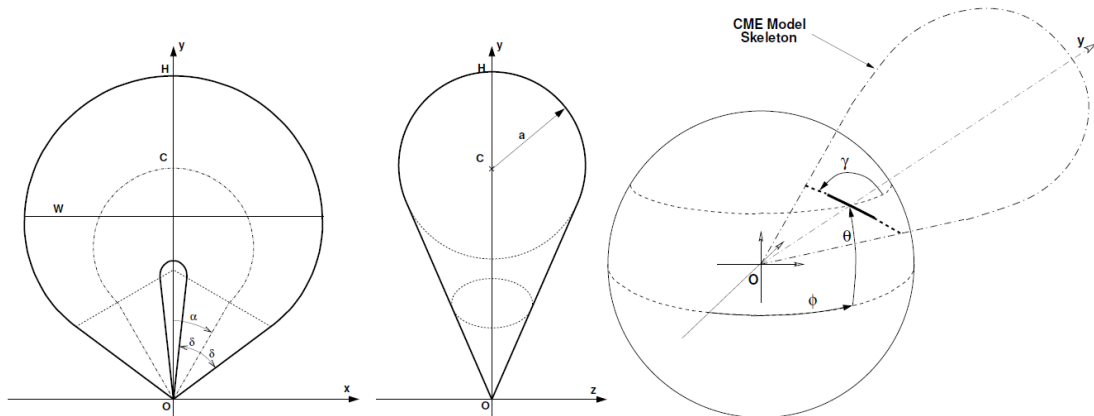


Figure 1.6 - The graduated cylindrical shell (CGS) model, a geometric model used to represent a CME that has flux rope structure.

Source: Thernisien et al. (2009)

Using the GCS model, the forward modelling fits the free parameters until the actual observed images from a coronagraph fit the projection of the CGS model over each coronagraph image. One example of the application of the CGS model for a given CME using combined observations from the two COR2A, COR2B and LASCO-C2 is shown in Figure 1.7.

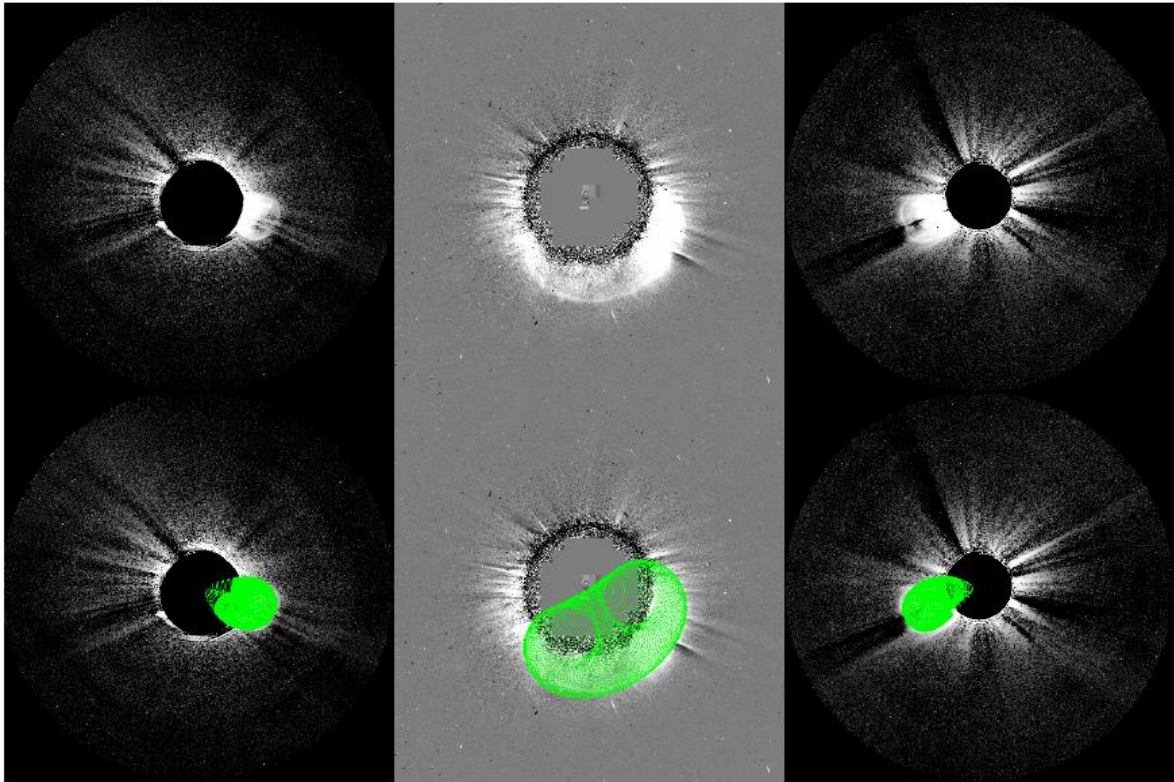


Figure 1.7 - Example of the application of the CGS method to a CME observed on 2010/04/03 at 10:39 UT. The image on the left corresponds to SECCHI-COR2A, the central image corresponds to LASCO-C2 and the right one to SECCHI-COR2B. The green structure superposed in in each image shows the projection of the CGS model in each coronagraph FOV. In this example, the CME is directed toward the Earth (and LASCO-C2). Both SECCHI coronagraphs see the CME as a limb.

Source: Colaninno (2012).

1.5 Propagation of CMES

After the CME reaches a given distance of about five solar radii from the Sun, the trend is that the fastest CMEs tend to be decelerated while the slowest ones tend to be accelerated. Gopalswamy et al. (2010) observed that, although initial CME speeds range from 124 to 1956 km/s, the speed of the corresponding structures in the interplanetary medium ranges from 320 km/s to 650 km/s. Sheeley et al. (1999), using coronagraph images from LASCO, found two kinds of CMEs according to their velocity and acceleration profiles: gradual and impulsive. The main differences between the two categories are shown in Table 1.1.

Table 1.1 - Difference between the gradual and impulsive CMEs. Source: Sheeley et al. (1999)

Parameter	Gradual CMEs	Impulsive
Initial speed	400-600 km/s	750-1000 km/s
Acceleration	Gradual between 3 and 40 m/s ²	Small or negative after 2 solar radii
Associated solar structures	Solar prominences	Solar flares

Source: Sheeley et al. (1999)

In principle there are three forces acting on CMEs after they reach a given distance from the Sun: the gravitational force, the electromagnetic Lorentz force and the “aerodynamic” drag due to the solar wind. The two first forces are considered negligible and the “aerodynamic” drag force is the strongest beyond a few solar radii (VRSNAK et al., 2013). This drag force is able to explain the results mentioned in the previous paragraph.

1.6 Interplanetary coronal mass ejections and magnetic clouds

The remnants of CMEs propagate in the interplanetary space and are called Interplanetary Coronal Mass Ejections (ICMEs). The need for a new term comes from the definition of CMEs that states that they are structures in the coronagraph field of view. ICME is the term mainly used hundreds of solar radii away from the Sun. It is frequently used while working with *in situ* data close to the Earth.

Magnetic clouds (MCs) are a special set of the ICMEs that have some special features associated to the presence of a magnetic flux rope structure. They are regions of increased magnetic field whose orientation varies slowly during their propagation in the interplanetary medium. The proton temperature is very low inside the structure (BURLAGA et al., 1981; BURLAGA, 1982; BURLAGA, 1995). The plasma pressure, dependent on the plasma temperature and density, is normally smaller than the magnetic pressure inside such structures. The ratio of the thermal pressure to the magnetic pressure is represented by the plasma beta parameter. This parameter is typically low ($\lesssim 0.1$) inside MCs due to the dominance of the magnetic field, the low proton temperature and the non-enhanced proton density (BURLAGA, 1990).

The geometry of a MC, when located at about 1 AU, is shown in Figure 1.8. Notice that the magnetic field of the cloud is axial at the center of the cylindrical cross section. As much as we move away from the center and close to the edge of the structure, the magnetic field becomes

less axial and highly poloidal. In this Figure, the “z” axis has the highest changes, ranging from negative to positive values. The “y” axis will oscillate between zero and negative values.

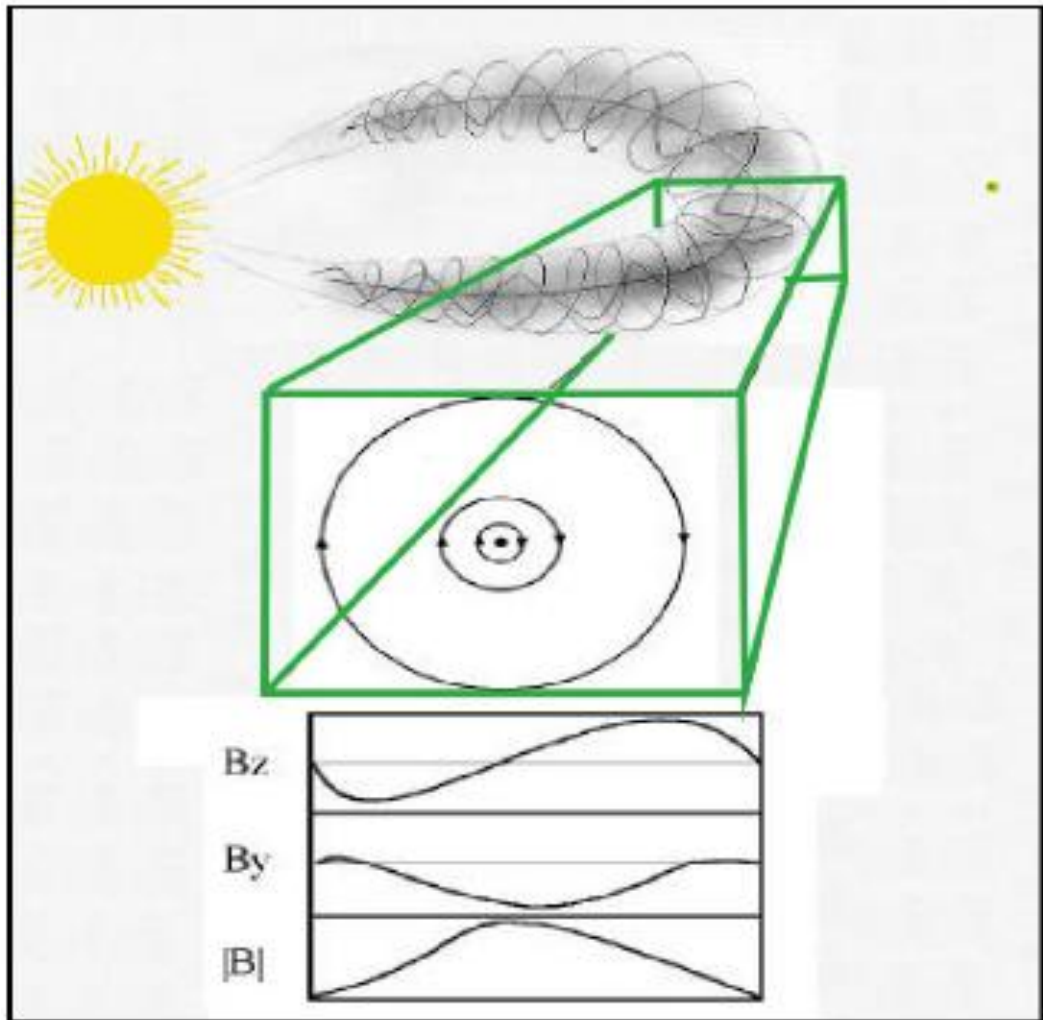


Figure 1.8 - The magnetic field lines of a magnetic cloud in the interplanetary medium between the Sun (represented in yellow) and the Earth (the green point).

Source: adapted from Dal Lago et al. (1999).

1.7 Cosmic rays: definition

A cosmic ray is a high energy particle – either an atomic nucleus or an electron– that travels throughout the Milky Way, including the solar system. Most of these particles come from sources outside the solar system and are known as galactic cosmic rays (GCRs). A few of them are originated in the Sun or outside the Milky Way. Cosmic ray particles that arrive at the top of

the Earth's atmosphere are called primaries; their collisions with atmospheric nuclei give rise to secondaries (FRIEDLANDER, 2014).

Cosmic rays are usually classified in three different groups depending on the place they come from and are accelerated: galactic, anomalous and solar cosmic rays (JOKIPII, 1997).

Anomalous cosmic rays are probably originated in the interaction between the solar wind with the interstellar medium. Neutral atoms streaming into the solar system become ionized. Later they move outward and encounter the solar wind termination shock where they are accelerated and gain energy. They are called anomalous because they produce a bump in the cosmic ray spectrum at about 100 MeV. Their energy ranges from 20-300 MeV/nucleon and their composition is mainly helium, nitrogen, oxygen, neon and protons (GIACALONE, 2010).

The solar cosmic rays are those particles originated and accelerated at the Sun either by solar flares and shock waves associated to CMEs. Their flux is highly anisotropic since particles are accelerated in the Sun and they are not significantly scattered in the interplanetary medium because the magnetic field is low. The solar cosmic ray flux is not constant with time, being higher in periods of a few minutes during solar flares or CMEs and negligible in the remaining period (JOKIPII, 2010).

The galactic cosmic rays (GCRs) are high energy particles originated from extrasolar sources within our galaxy. Although the source of GCRs has not been fully elucidated, supernova blast waves are thought to be one source. They are confined for millions of years in the interstellar magnetic field and they arrive in the heliosphere in a constant and isotropic way (JOKIPII, 2010). GCRs then cross the heliosphere and enter the Earth's atmosphere, where they are modulated both by the interplanetary magnetic field (which is related to solar activity) and by the geomagnetic field. Almost 90% of cosmic ray particles are protons, about 9% are helium nuclei, about 1% are electrons, and the remaining are heavier nuclei.

GCRs have energy up to 10^{21} eV. Those particles with energy lower than 1 GeV do not easily penetrate the solar system from outside because of the "sweeping-out" effect of the solar wind (GIACALONE, 2010). At energies up to tenths of GeV, they are highly modulated by the solar cycle (11 and 22 years) and the transient solar activity. When the particles arrive at the Earth, they enter in a region where the magnetic field is hundreds of times higher than in the

interplanetary space near the Earth where they might be reflected. Depending on the location of the Earth, cosmic rays need to have energy of at least 10 GeV to arrive at the surface.

In this Thesis, the data used consists only of GCRs with energy range centered at tens of GeV. This range is high enough so that particles can cross the magnetic field of the Earth and reach its surface. Furthermore, it is low enough to be modulated by interplanetary structures such as MCs.

1.8 Cosmic rays in the interplanetary medium and in the Earth's atmosphere

The passage of cosmic rays in the interplanetary medium can be explained by the combination of four major physical processes: diffusion, convection, drifts and adiabatic energy change. This theory was first introduced by E. Parker in 1965 (PARKER, 1965) and was complemented by Jokipii (1977) and others, especially in the drift topic.

Due to the diffusion, particles move from one place with higher density to another with smaller. Further, there are some directions where diffusion is more efficient than others. Since the particles are electrically charged, diffusion is higher in the direction parallel to the magnetic field lines. As an example, for cosmic rays with median rigidity of 60 GV, the parallel diffusion coefficient is three orders of magnitude higher than the perpendicular diffusion (MUNAKATA et al., 2006). Therefore, cosmic ray diffusion is highly anisotropic. In Mathematic terms, we express diffusion by the Laplace Operator, that is, the divergence of the gradient of a function. In order to include the anisotropy, we need to include a tensor inside the divergence.

The advection of the cosmic rays is due to the solar wind that sweeps particles away from the Sun. This effect will produce a higher count rate in the Sun-Earth direction away from the Sun when we compare to the remaining directions. The magnitude of this effect is proportional to the solar wind speed and proportional to the inverse of the particle speed. For particles with energy in the 10 GeV range, the convection produces an effect with an amplitude of about 0.6% (KANE, 1974). For the 60 GeV range, some studies show that the effect is about 0.2% (BRAGA, 2011).

The most important drift effects in the heliosphere are the curvature drift and the magnetic field gradient drift. The curvature drift comes from the centrifugal force of a particle while it is moving in a curved magnetic field. This drift points normally to the curvature plane. The magnetic field gradient drift is perpendicular both to the magnetic field direction and to the gradient direction.

This effect can be understood by the change in the Larmor radius of the particle before finishing a complete gyration cycle. When the particle enters a region with higher magnetic field, its Larmor radius becomes smaller.

The adiabatic energy change rises from the fact that the solar wind has radial divergence and the cosmic rays lose energy to the solar wind as they propagate inward the solar system. It also takes place inside an expanding flux rope, such as a magnetic cloud.

After crossing the heliosphere, cosmic rays enter in the Earth's atmosphere where their trajectory depends mainly on the geomagnetic field. They will hardly ever hit the ground but will collide (interact) with a nucleus of the air usually at an altitude of tens of kilometers producing an air shower (Figure 1.9). Among many other secondary particles generated by cosmic rays in the atmosphere, neutrons and muons are of special interest in this Thesis.

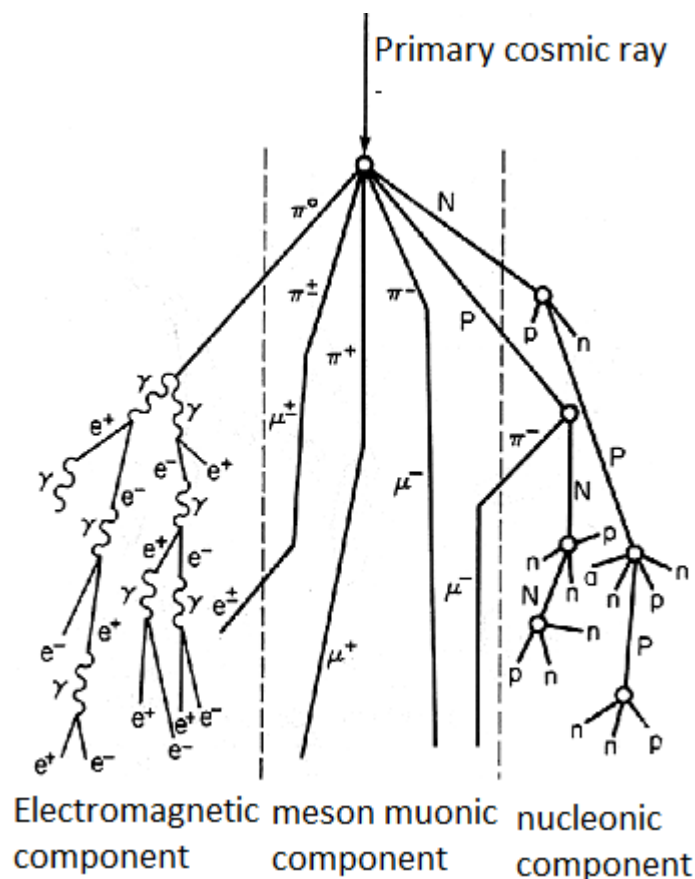


Figure 1.9 - The cosmic ray air shower.
Source: Otaola & Valdés-Galicia (1992).

Neutrons are generated by the interaction of primary GCRs with energy of ~ 10 GeV. Each secondary neutron carries part of the energy and then collides again with other atmospheric nuclei. The collision produces other new secondary neutrons. One can measure the secondary neutrons that reach the surface with neutron monitors. Because of multiple collisions, the incident direction of primary GCRs cannot be inferred from the observation of a single station (OKAZAKI, 2008).

Muons are generated by the interaction of primary GCRs with energy of ~ 50 GeV. The first interaction produces pions by the hadronic interaction with the atmospheric nuclei. These pions then generate other secondary particles again by colliding with the atmospheric nuclei or decaying into a muon and a neutrino in 29 ns. Some muons can reach the detector at the ground level, preserving the incident direction of GCRs. The lifetime of muons of $\sim 2.2 \times 10^{-6}$ s is elongated by several hundred times due to relativistic time dilatation. Therefore, ground-based muon detectors are able to observe them before they decay (OKAZAKI, 2008).

The observation of muons can be done both on the Earth's surface and below it. Thanks to the high mass of the detector and the necessary area to observe, there are no measurements of cosmic rays in the 50 GeV range onboard satellite and ground-based instruments are considered the state-of-the-art instruments for detecting this type of particles. (MCDONALD, 2000). The detectors installed in the Earth's surface have significant responses from ~ 10 GeV to several hundreds of GeV. Underground detectors cover a higher energy range up to ~ 1000 GeV. While the energy is increased, the modulation due to the solar activity and IMF decreases and underground muon detectors are less sensitive to those effects than ground-based detectors (DULDIG, 2000).

1.9 The Global Muon Detector Network (GMDN)

The cosmic rays (muon) data used in this Thesis comes from a set of four detectors that are installed as homogeneously as possible in the Earth's surface. They are known as the Global Muon Detector Network (GMDN) and the detectors are located in Nagoya (Japan), Hobart (Australia), São Martinho da Serra (Brazil) and Kuwait city (Kuwait), see Figure 1.10 and Table 1.2. In 1992, the network began as a two-hemisphere observation network using the detectors of Nagoya and Hobart. In March 2001, a small prototype detector was installed in São Martinho da Serra with 4 m² to fill a gap in directional coverage of the network over the Atlantic and Europe. In

December 2005, the detector in São Martinho da Serra had its area expanded to 28 m². On March 2006, a detector was installed in Kuwait City, completing the current configuration of the GMDN. Since then no more detectors were added but two of them had their area increased: in December 2010, the Hobart detector was upgraded to 16m² and in July 2012, the detector at São Martinho da Serra had its area increased to 32 m².

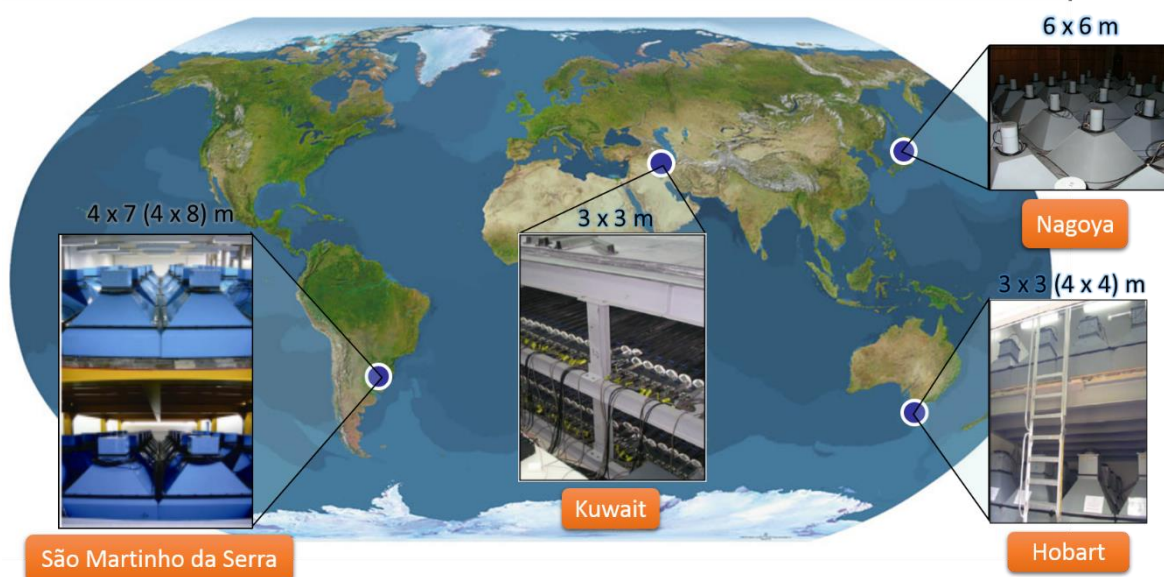


Figure 1.10 - The location of the four detectors that form the Global Muon Detector Network.
Background map source: <http://earthsatellitemaps.com/wp-content/uploads/2009/06/mapofearth.jpg>

Table 1.2 - The locations of each detector of the Global Muon Detector Network.

Detector	Nagoya	Hobart	São Martinho da Serra	Kuwait
Geographic coordinates	35.15° N, 136.97° E	43.00° S, 147.29° E	29.44° S, 53.81° W	29.37° N, 47.98° E
Altitude	77 m	65 m	488 m	19 m
Geomagnetic cutoff rigidity	11.5 GV	1.8 GV	9.3 GV	13.0 GV

The GMDN is a joint project of the Shinshu University and Nagoya University (Japan), University of Delaware (USA), National Institute for Space Research and Federal University of Santa Maria (Brazil), Australian Antarctic Division and University of Tasmania (Australia), and University of Kuwait (Kuwait).

Typically, the muon detectors are arranged in two or more trays generally disposed one over the other. Because the muons are relativistic, they cross all trays in a much shorter time than the latent detection time. A muon will hit one detector in each tray and, by comparing the relative position of the detectors in the tray, we can derive the direction of arrival.

An example of how the arrival direction is determined is shown in Figure 1.11. Suppose that the detector is aligned in the North-South direction and that four particles are arriving in the muon detector, one after the other (represented in the Figure by the four arrows). The particle shown in red will be computed as arriving from the vertical direction. The particle represented by the blue lines will be computed as arriving from the south direction because the particle crosses in the lower layer (tray) in a position southward when compared to a detector in the upper layer. If a particle is arriving from the south with a higher azimuth, such as the particle shown in green, it will be computed in a different directional channel. Depending on its azimuth range, it is computed as “South 2” or “South 3”.

Muon detectors produce electric pulses with duration of about 1 ms when they are hit by a particle (Figure 1.12). First, the muon hit a scintillator that, as a result, emits photons. A photomultiplier detects the photons and, by its turn, it produces electric pulses in its output. Both scintillators and photomultipliers are installed inside a closed iron box isolated from external sources of light. In this Thesis, we call this box as detection box.

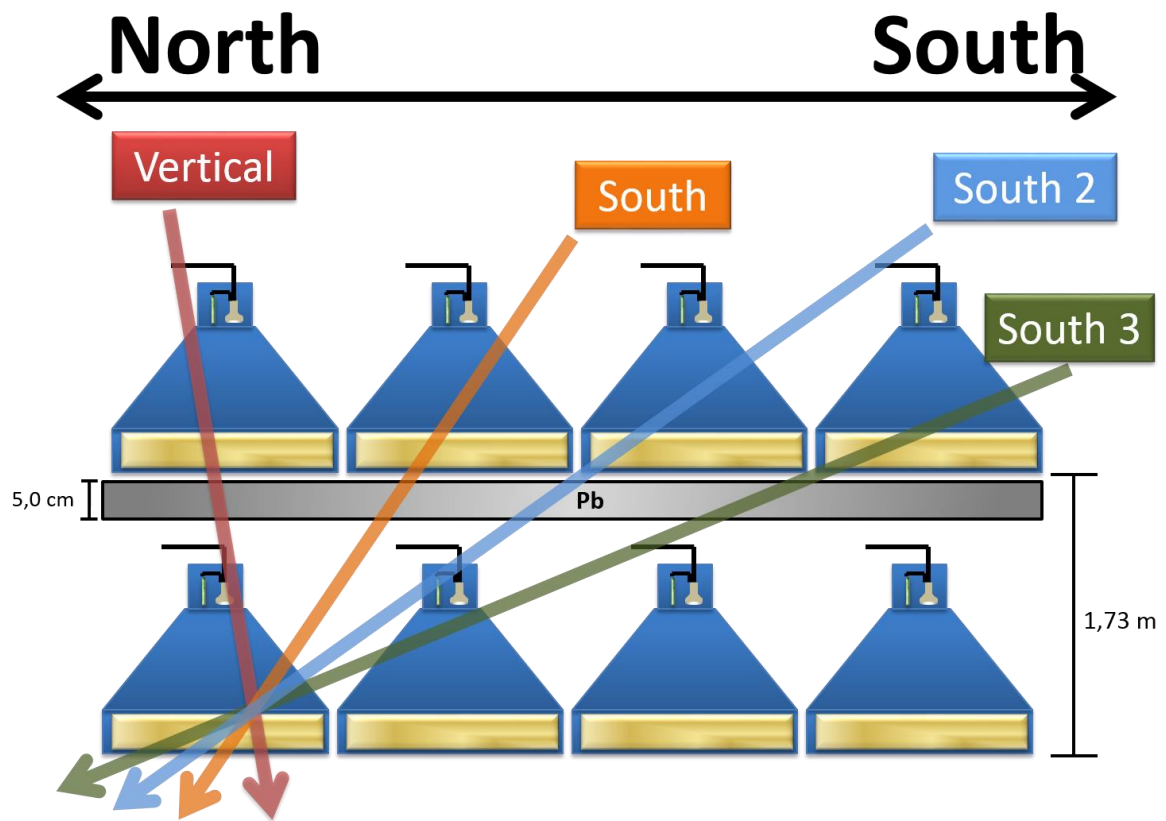


Figure 1.11 - A vertical cross section of a detector of the GMDN, except for Kuwait. Each detector is formed by two layers; each one has an array of detection boxes (Figure 1.12). In between the two layers, there is a 5 cm lead layer that absorbs the soft component of the cosmic rays. The four straight lines represent four samples muon arriving at the detector. Each of these muons will be computed in a different directional channel, as described in the text.

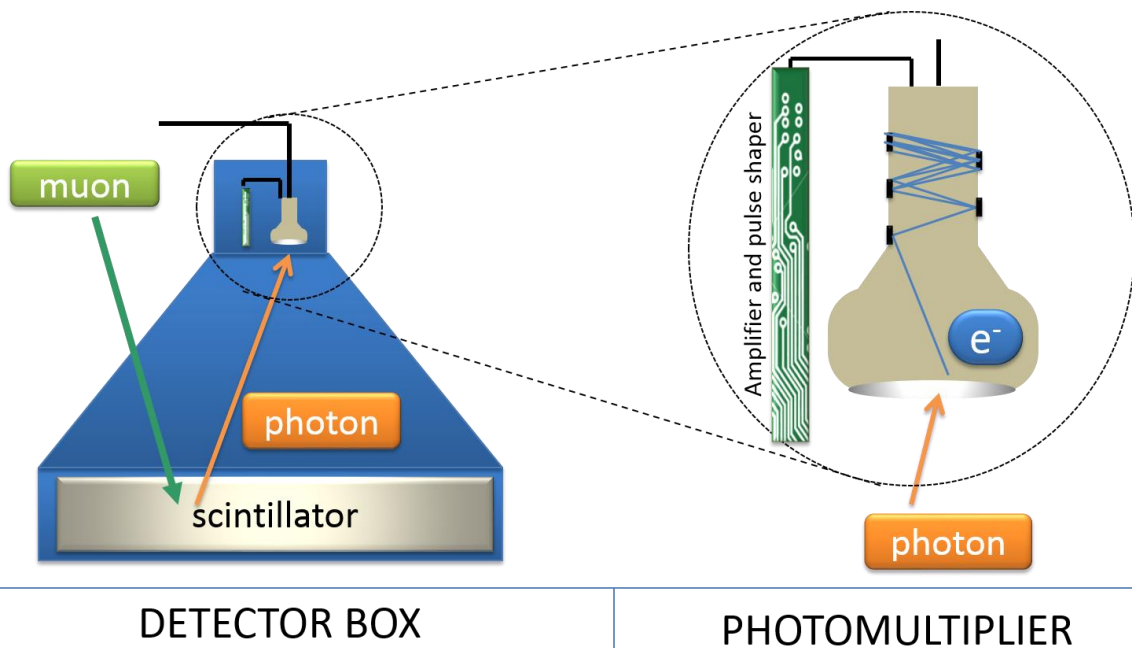


Figure 1.12 - Diagram of the internal configuration of a detection box for the detectors of the GMDN, except for Kuwait.

The detectors at Nagoya, Hobart and São Martinho da Serra consist of two horizontal layers of plastic scintillators, vertically separated by 1.73 m, with an intermediate 5 cm layer of lead to absorb the soft component radiation in the air (see Figure 1.11). Each layer comprises an array of 1 m² unit detectors, each one with a 0.1 m thick plastic scintillator viewed by a photomultiplier tube of 12.7 cm diameter. The only difference between them is the detection area.

The muon detector installed at Kuwait University, on the other hand, it is designed with neither plastic scintillators nor photomultipliers (Figure 1.13). It consists of four horizontal layers of 30 Proportional Counter Tubes (PCTs). Each PCT is a five-meter long cylinder with diameter of 10 cm. Along its axis, there is a 50 micron thick tungsten anode. Located above the detector, a 5 cm thick lead layer absorbs the soft component. The PCT axes are east-west geographically aligned (X) in the top and third layers and north-south aligned (Y) in the second and bottom layers. The top and second layers form an upper pair, while the third and bottom layers form a lower pair. The two pairs are separated vertically by 80 cm. Muon recording is triggered by the fourfold coincidence of pulses from all layers. The incident direction is identified from X-Y locations of the upper and lower PCT pairs (OKAZAKI et al., 2008).

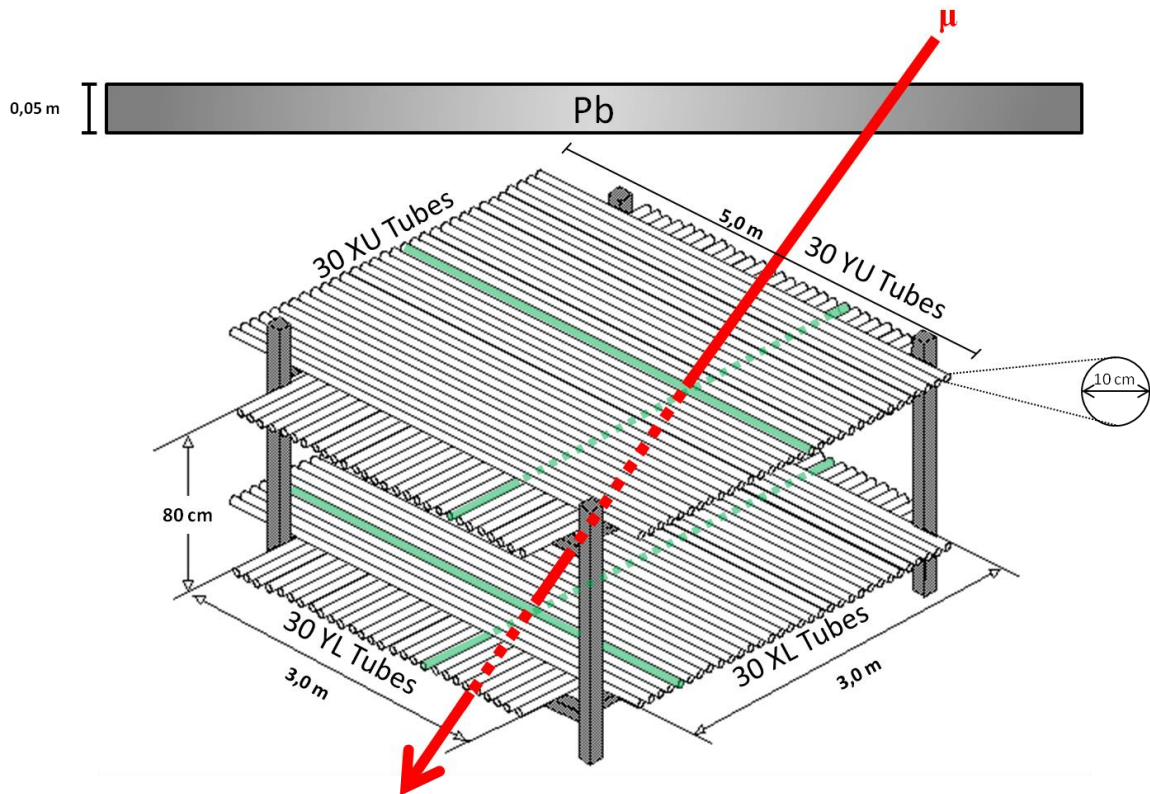


Figure 1.13 - Diagram of the hodoscope installed at the University of Kuwait. Each tube is a proportional counter. The top and second layers form an upper pair, while the third and bottom layers form a lower pair.

Source: K. Munakata (personal communication), 2013.

1.10 The cosmic ray arrival direction and the effects of the geomagnetic field

The muons observed by the GMDN keep the arrival direction of this originating primary cosmic ray and, in this way, observing the arrival direction of a muon allow us to know the arrival direction of the primary cosmic ray. This would be true if the Earth did not have its magnetic field.

The deflection due to the geomagnetic field is generally calculated using computer codes that take into account some model of geomagnetic field. In the case of the GMDN, the *International Geomagnetic Reference Field* (IGRF) from 1995 is used.

Using these codes, we are able to find the starting point of the particle's trajectory in the top of the atmosphere given the arrival point and direction of the detector on the surface of the Earth.

Solving this problem is equivalent of inverting the sign of the particle charge (from positive to negative) and the sign of the velocity vector (from toward to away from the Earth's surface) and interchanging the start and end of the trajectory (MCCRACKEN et al., 1962).

As an illustration of the trajectory of a cosmic ray particle, let us compare the trajectory of 3 protons with different energies arriving at the location of the São Martinho da Serra muon detector (Geographic latitude $29^{\circ}, 26', 24''$ South, geographic longitude $53^{\circ}, 48', 38''$ West, 488 m over the sea level). A detailed description of this simulation is available at Bobik et al. (2003). The trajectories calculated using the computer code are shown in Figure 1.14. For a given proton with energy of 180 GeV released from an altitude of 24 Earth radii, the deflection of the trajectory is approximately 7 degrees of longitude westward and one degree southward. The calculated geographic coordinates of the particle at the top of the atmosphere are (28.11° South, 46.25° West). As for the 60 GeV proton, the deflection was about 20° westward and 6° southward and the calculated coordinates are (23.76° South, 33° West). Finally, for the proton with lowest energy (20 GeV), the longitude deflection was 50° westward and 29° southward. The calculated coordinates at the top of the atmosphere are (0.03° South, 0.04° East).

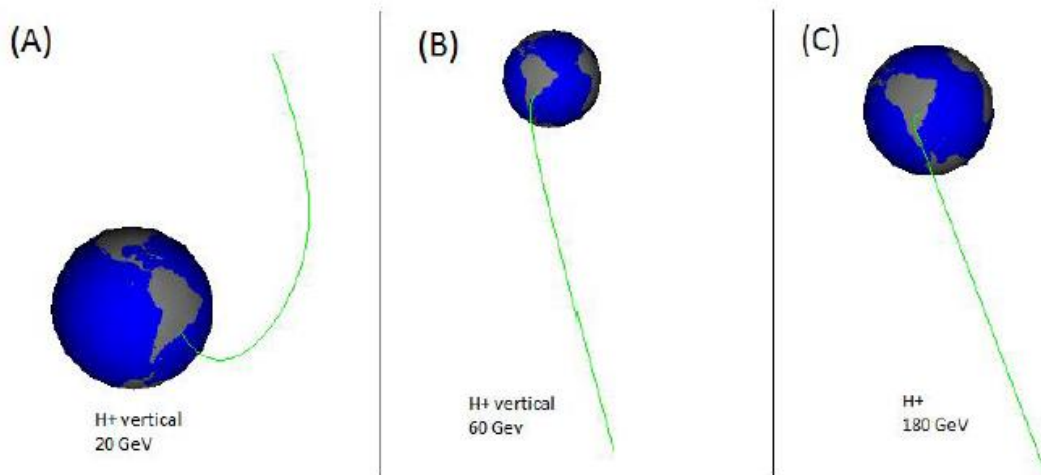


Figure 1.14 - An example of the trajectory of the cosmic ray particles deflected by the geomagnetic field using a simulation code from Bobik et al. (2003). Each trajectory shows a cosmic ray particle (proton) with different energy from each other: (a) 20 GeV , (b) 60 GeV and (c) 180 GeV.

It is clear from the simulation results that the higher the energy of the particle, the lower the deflection due to the geomagnetic field. Moreover, for the three particles shown here the

deflection was westward and toward the pole. The westward deflection can be explained by the dipolar configuration of the magnetic field pointing approximately to geographic north direction. The deflection toward the pole comes from the fact that the vertical component of the geomagnetic field increases as we get closer to the pole. In this way, the component of the geomagnetic field perpendicular to the particle trajectory decreases.

1.11 A model for cosmic ray distribution inside the magnetic cloud

Using the cosmic ray transport equation, Munakata et al. (2006) calculated the distribution of cosmic ray density inside a MC structure. Taking into account the cosmic ray density decrease observed by Kuwabara et al. (2003) during a MC, the model supposes a cosmic ray intensity decrease inside it. Taking into account the flux rope structure of a magnetic cloud, a cylinder shape was taken as an approximation. The density was supposed to be axis symmetric. The model also supposed that the cylinder is expanding as time passes to be in agreement with results from *in situ* observation.

Since the MC is originated from a CME, the structure should not have significant cosmic ray density right after the ejection from the Sun. In the simulation, the density at the start time was set to zero (left side of Figure 1.15). The cosmic rays enter the magnetic cloud flux rope structure by diffusion since the density outside is much higher than inside. Due to the magnetic configuration of the MC, the diffusion is perpendicular to the magnetic field lines. This process tends to increase the cosmic ray density inside the cloud. Other physical process that needs to be taken into account is the adiabatic cooling, which is due to the expansion of the MC, which leads to cosmic ray density decrease inside the cloud. The resulting density distribution was found to be minimum in the center of the cylinder (right side of Figure 1.15).

This result is the theoretical basis for a model that allows reconstruction of the magnetic clouds using cosmic ray distribution inside it. This model is detailed in Chapter 3.

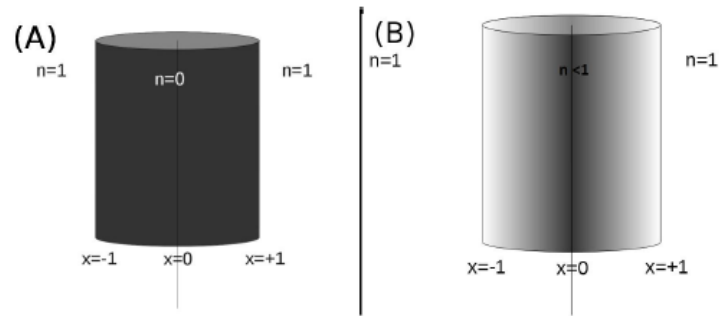


Figure 1.15 - The cosmic ray density inside a MC at the beginning (A) and end (B) of a simulation performed and described by Munakata et al. (2006). The maximum cosmic ray density is represented by the light colors.

2 OBJECTIVES

Since 2006, there are two different kinds of observational data to study the propagation of CMEs close to the Sun and its consequent magnetic clouds close the Earth. One is the observation of the solar corona performed by the twin STEREO spacecraft and the other is the Global Muon Detector Network (GMDN).

In general terms, this Thesis aims to understand the relation between a CME and its interplanetary counterparts close to the Earth. The main objectives are:

- To deduce the orientation of MCs by comparing data from the GMDN and a model of cosmic ray distribution inside a magnetic cloud from Munakata et al. (2006). The free parameters of the model (such as position of the magnetic cloud, orientation and radius) will be adjusted according to the observed data. The same methodology was applied by Kuwabara et al. (2009) for a set of events observed between 2001 and 2003 using a network of muon detectors much smaller than the current Global Muon Detector Network. This methodology has never been applied to newer events. This methodology is described in Chapter 3. Our objective here is to apply the methodology to MCs observed from 2006 up to 2011;
- To deduce the CMEs that caused the magnetic clouds studied in the topic above. For those CMEs, studying the speed of propagation applying the Coronal Segmentation Technique (CORSET, described in Chapter 4) and using data from coronagraphs onboard each of the twin STEREO spacecraft. CORSET has never been applied before for any extensive set of events from STEREO spacecraft. Goussies et al. (2010) studied only a set of five events using STEREO and Braga et al. (2013) studied a significant set of events (57) only for the LASCO-C3 onboard SOHO spacecraft.
- For any CMEs ejected up to 5 days before any MC, computing the direction of propagation. A new methodology introduced in this Thesis derives the direction of propagation and the real speed (free from projection speeds) using epipolar constraint and automatic tie-points derived from CORSET results. The motivation and advantages to use this new method are explained in Chapter 4.

This Thesis ultimately aims to identify the CMEs responsible for MCs observed near the Earth. Hence, this Thesis contributes to the forecasting of geomagnetic disturbances since they are dependent on the orientation of the magnetic field of the CMEs and its corresponding ICMEs.

3 COSMIC RAYS (MUONS): FROM COUNT RATE TO COSMIC RAY DENSITY GRADIENT

This Chapter describes the methodology to derive the cosmic ray density gradient in the interplanetary space close to the Earth. We start from the muon count rate observed by each one of the four detectors of the GMDN and then we derive cosmic ray anisotropy and gradient in the interplanetary space. These results, as well as a model of cosmic ray density inside a MC, are used latter in this Thesis to deduce the magnetic cloud orientations.

3.1 The directional channels of the conventional and new correlation system

As introduced in Section 1.9, the GMDN allow us simultaneous observations of cosmic ray particles arriving from different viewing directions thanks to the directional channels. In the GMDN detectors, the directional channels are computed in two independent electronic circuits that use different technologies. One is called conventional correlation system because it has been used for more than 40 years since the muon detector at Nagoya was installed, in the 1970s. The other was introduced by Yasue et al. (2003) and it is in operation for all detectors of the GMDN since May 2007. From then on, there is data available from both the conventional and new correlation system and both are used in this Thesis.

On the conventional correlation system, when a particle is detected simultaneously in one detector from the upper layer and in another from the lower layer, this particle may be computed in one of the directional channels arbitrarily defined. The directional channels include the vertical direction and the rose wind directions (north, south, east, west, northwest, northeast, southeast and southwest). The directions north, south, east and west are discriminated in two or three different zenith angle levels, depending on the size of the detector. In this way, up to 17 directional channels are formed for each detector. The construction of the directional channels is illustrated in Figure 1.11. The average count rate and statistical error and the median rigidity (calculated as explained in Section 1.10) are listed in Table 3.1, Table 3.2, Table 3.3 and Table 3.4.

Table 3.1 - The main characteristics of each conventional directional channel for Nagoya detector.

Directional channel	Average count rate (10^6 count rate per hour)	Error [%]	P_m [GV]
Vertical	2.984	0.06	59.5
North	1.352	0.09	64.5
South	1.334	0.09	62.7
East	1.330	0.09	66.6
West	1.364	0.09	61.8
Northeast	0.636	0.13	71.9
Northwest	0.667	0.12	66.7
Southeast	0.634	0.13	69.3
Southwest	0.655	0.12	65.7
North 2	0.646	0.12	83.1
South 2	0.635	0.13	80.6
East 2	0.616	0.13	88.1
West 2	0.654	0.12	79.4
North 3	0.187	0.23	105.5
South 3	0.186	0.23	103.9
East 3	0.182	0.23	113.1
West 3	0.188	0.23	103.0

Table 3.2 - The main characteristics of each conventional directional channel for Hobart detector.

Directional channel	Average count rate per hour (10^6 count rate per hour)	Error [%]	P_m [GV]
Vertical	1.471	0.08	54.6
North	0.621	0.13	59.0
South	0.586	0.13	59.0
East	0.608	0.13	59.0
West	0.600	0.13	59.0
Northeast	0.275	0.19	63.7
Northwest	0.274	0.19	63.7
Southeast	0.261	0.20	63.7
Southwest	0.261	0.20	63.7
North 2	0.207	0.22	75.3
South 2	0.197	0.23	75.3
East 2	0.200	0.22	75.3
West 2	0.203	0.22	75.3

Table 3.3 - The main characteristics of each conventional directional channel for Kuwait detector.

Directional channel	Average count rate per hour (10^4 count rate per hour)	Error [%]	Pm [GV]
Vertical	0.859	0.11	62.4
North	0.219	0.21	67.7
South	0.224	0.21	69.3
East	0.216	0.21	73.0
West	0.223	0.21	65.9
Northeast	0.064	0.39	77.6
Northwest	0.065	0.39	72.4
Southeast	0.065	0.39	81.4
Southwest	0.068	0.38	73.0
North 2	0.027	0.60	96.1
South 2	0.028	0.60	100.4
East 2	0.027	0.61	107.3
West 2	0.028	0.60	95.0

Table 3.4 - The main characteristics of each conventional directional channel for São Martinho da Serra detector.

Directional channel	Average count rate per hour (10^6 count rate per hour)	Error [%]	Pm [GV]
Vertical	3.025	0.06	55.6
North	1.222	0.09	59.9
South	1.260	0.09	59.1
East	1.438	0.08	61.6
West	1.451	0.08	58.3
Northeast	0.625	0.13	66.5
Northwest	0.639	0.13	62.8
Southeast	0.648	0.12	65.2
Southwest	0.651	0.12	62.3
North 2	0.420	0.15	75.7
South 2	0.433	0.15	74.1
East 2	0.579	0.13	78.7
West 2	0.592	0.13	73.1

On the new correlation system, one directional channel is computed for any possible zenith and azimuth angles from a given detector. For a detector such as Nagoya, constructed with an array of 6x6 detectors, 121 directional channels are computed. For the detector at São Martinho da Serra (9x4 detectors), 119 directional channels are possible. The directional channels are represented here by a pair of points where the first indicates the displacement of the particle in the east-west direction (east is positive) and the second indicates the displacement of the particle in the north-south direction (north is positive). In this way, the directional channels

corresponding to particles arriving from the vertical are called (0,0). Hereafter we will refer them as vertical directional channels from the new correlation system. For example, for the muon detector of São Martinho da Serra, particles arriving from the north direction and perpendicularly with the east-west direction are computed in the channels (0,1), (0,2) or (0,3), depending on the zenith angle range they have. Among the three channels mentioned, (0,1) has the lowest zenith angle and (0,3) has the highest zenith angle. For some detectors, a set of the directional channels has a very low count rate due to the high zenith angle and they are ignored in the analysis.

Sample plots using data regarded by the conventional and new vertical directional channels are shown in Figure 3.1 and Figure 3.2. One can notice that the count rate from both correlation systems of Hobart, Nagoya and São Martinho da Serra are very similar. These detectors are all constructed with scintillators and detection boxes with areas of 1 m by 1 m. For all of them, the new coincidence system exactly matches the conventional correction system. For the detector at Kuwait, however, there is a significant difference: it is constructed with Proportional Counter Tubes (PCTs) and the vertical directional channel of the new correlation system has a very small zenith angle range because the area of each element is 0.1 m by 0.1 m. As explained in Section 1.9, the PCTs have a diameter of only 0.1 m and this is the reason why the area of each element is reduced for Kuwait detector by a factor of 10 in each dimension. In order to keep similarity with the scintillation detectors, the conventional correlation system of Kuwait was reconstructed supposing a hypothetical element with area of 0.8 m by 0.8 m, allowing zenith angular range similar to the vertical channels of the conventional correlation system of the remaining detectors. For this reason, the count rate of the new correlation system of Kuwait is dramatically reduced when we compare it to the conventional correlation system. As a result, the statistical error increases. Notice in Figure 3.1 and Figure 3.2 the difference between the new and conventional vertical directional channels of Kuwait.

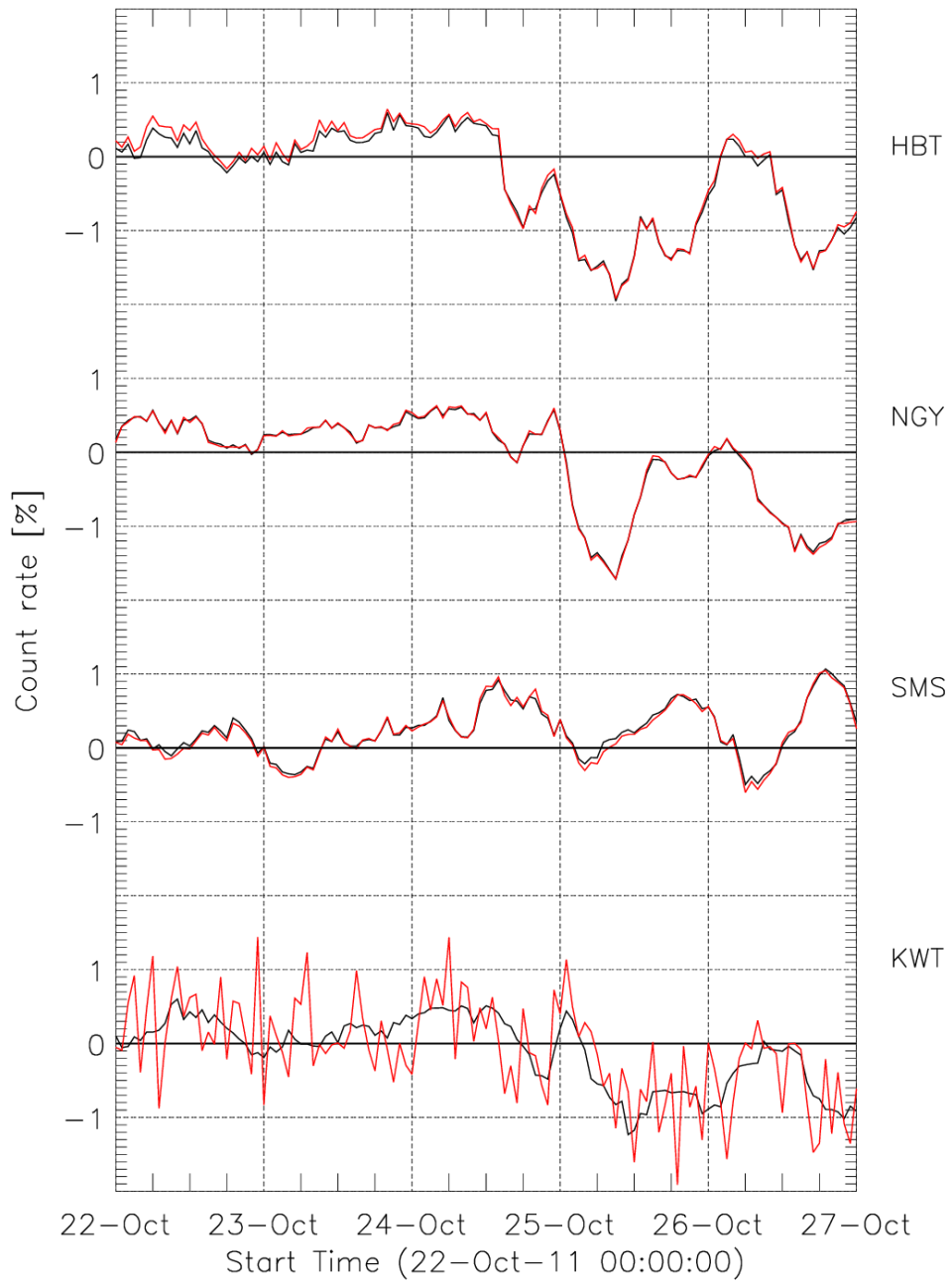


Figure 3.1 - The count rate observed by the vertical directional channels for the conventional (black lines) and new (red lines) correlation system using one-hour integration times.

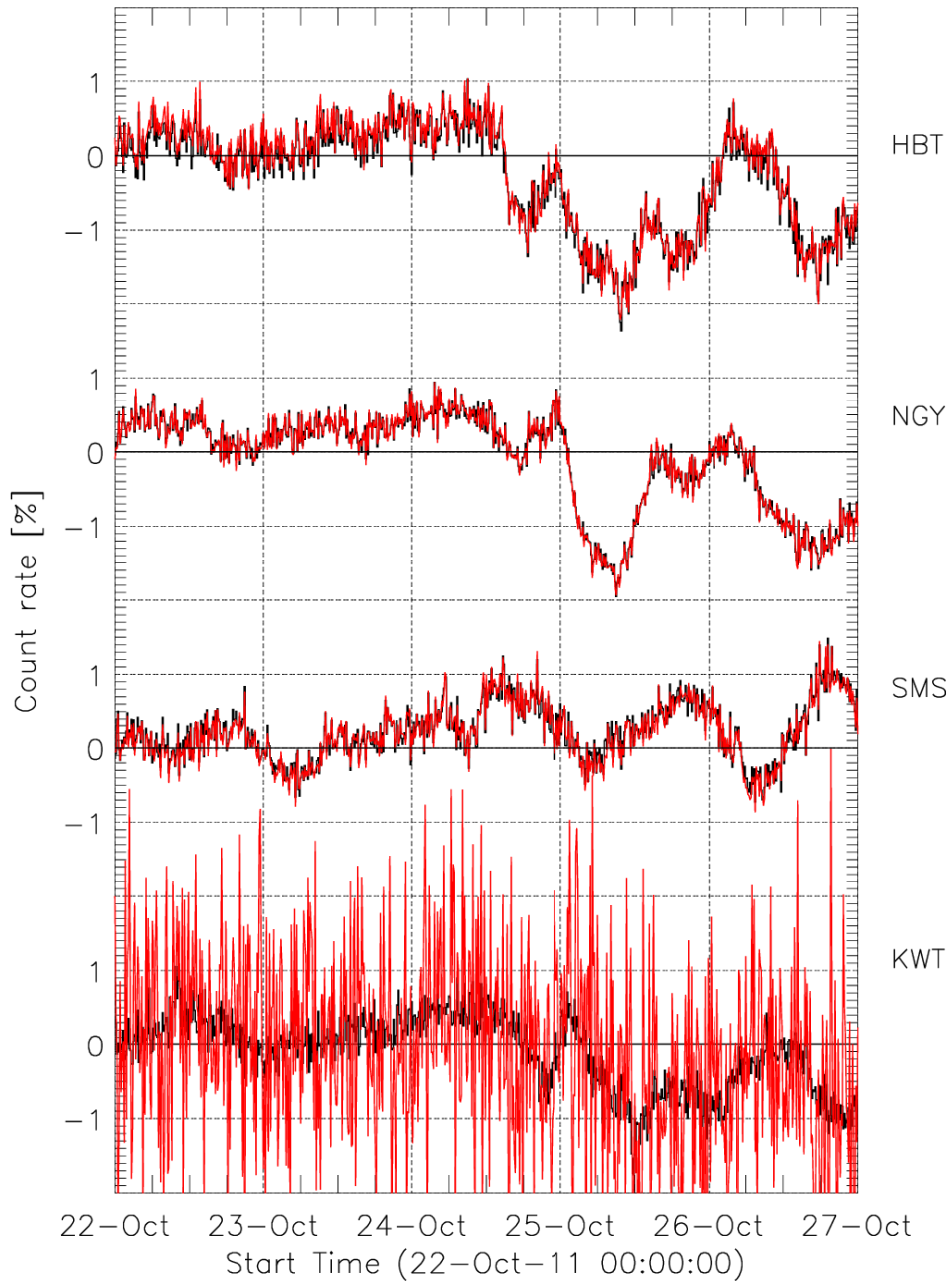


Figure 3.2 - The count rate observed by the vertical directional channels for the conventional (black lines) and new (red lines) correlation system using ten-minute integration times.

3.2 Removing the atmospheric effects on the muon count rate

The muon count rate observed at the surface of Earth depends on both the atmospheric pressure and temperature because the production and decay of these muons depend on those atmospheric conditions (DORMAN, 2004). Since we are interested in the primary cosmic ray

distribution, the atmospheric effects need to be removed from the observed data as much as possible.

The atmospheric pressure effect is basically anti-correlated with the muon count rate (SAGISAKA, 1986). Vieira et al. (2012) describes the application of this method for one detector of the GMDN in details. The same methodology is used in this Thesis.

The temperature effect for the GMDN was done in collaboration with Mendonça (2015)¹ using the mass-averaged temperature method. This method is based on determining the mass-averaged temperature in the atmosphere using a temperature profile and the distribution of mass in different parts of the atmosphere (BERKOVA et al., 2011). In other words, this method takes into account the temperature in all layers of the atmosphere (from the ground until the exosphere) and the weight of each layer depends on its atmospheric depth (MENDONÇA et al., 2013).

One example of the relative vertical count rate before and after the correction of both atmospheric effects is shown in Figure 3.3.

¹ R. R. S. de Mendonça. Correction of the atmospheric temperature effect observed by the Global Muon Detector Network. São José dos Campos, National Institute for Space Research, 2015. Private Communication.

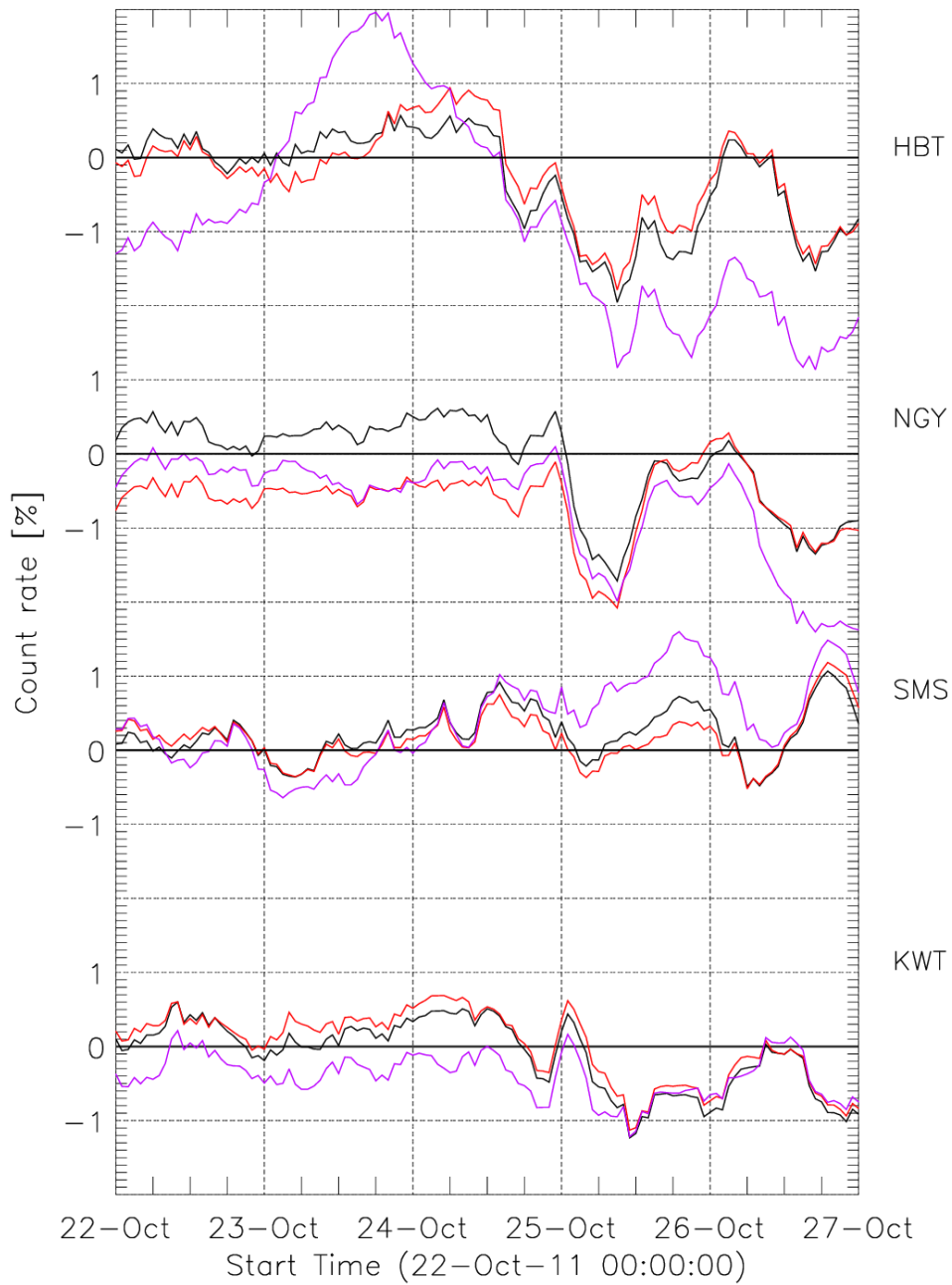


Figure 3.3 - One example of the muon count rate before and after the removal of the atmospheric influence due to the temperature and pressure effects. The data shown here is from the conventional correlation system. The violet curve refers to the data uncorrected for neither temperature effect nor pressure effects. The red curve refers to data corrected only for the pressure effect. The black curve indicates data corrected for both atmospheric temperature and pressure effects.

3.3 The concept of the anisotropy vector

Suppose that we have a cosmic ray anisotropy vector in interplanetary space and that it is stationary. We represent this anisotropy by a vector pointing toward the maximum cosmic ray intensity. This anisotropy $\xi^{interplanetary}$ produces a different anisotropy vector at the Earth's surface with smaller amplitude and with a different direction. Hereafter we call the former as ξ^{Earth} (see Figure 3.4). The relation between the anisotropy vectors can be expressed by a transformation matrix A . Each term of this matrix is called coupling coefficient and its calculation is explained in Section 3.4.

In this Thesis, we adopt a Cartesian coordinate system with origin in the center of the Earth. x and y directions lie on the equatorial plane of the Earth with x pointing away from the Sun (in other words, to midnight in local time) and y pointing toward dawn (6:00 in local time). The z direction completes the right-handed coordinate systems and points toward the Geographic North Pole. Hereafter, we refer this coordinate system simply as non-rotational geographic (hereafter, NRGeo) since it is similar to the geographic coordinate system but x and y axis do not follow the daily rotation of the Earth along the z axis.

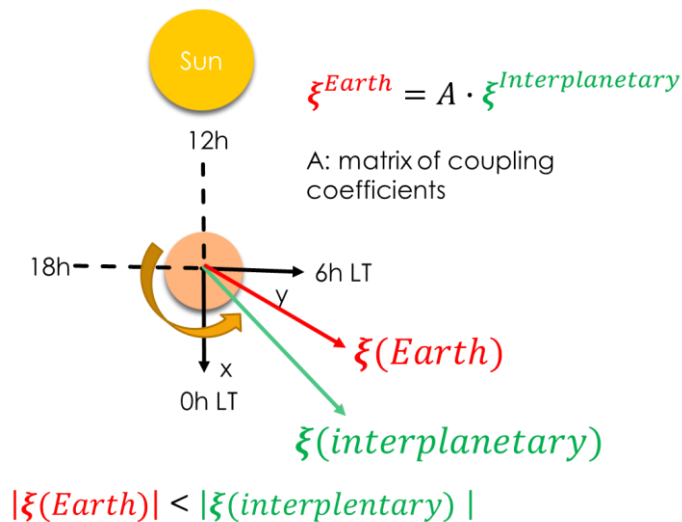


Figure 3.4 - An illustration of the anisotropy vector in the interplanetary medium and the anisotropy vector observed in the Earth's surface. The orange circle represents the Earth seen from above.

3.4 Calculation of the coupling coefficients

The coupling coefficients are a result of a mathematical calculation from Nagashima et al. (1971A, 1971B, 1971C, 1971D) that relates a given anisotropy in the interplanetary medium with its effect on a given directional channel of a detector taking into account its location (and consequent geomagnetic deflection), the declination and the rigidity spectrum.

Every directional channels of a muon detector has a coupling coefficient. Mathematically, each coupling coefficient is a complex number $c + is$ where $i = \sqrt{-1}$. Its magnitude ranges between 0 and 1. It represents the relative intensity ratio between a given modulation observed in the interplanetary medium and its corresponding effect observed by a directional channel of a muon detector at a given location on the surface of the Earth. The phase of the number represents the difference in the longitude of the viewing direction of a given directional channel and the longitude of the detector. This difference in longitude comes from effects such as the geomagnetic field deflection and declination/azimuth of the directional channel.

Following the notation from Nagashima et al. (1971A, 1971B, 1971C, 1971D), each coupling coefficient has a superscript and a subscript. The superscript of the coupling coefficients represents the order of the anisotropy. The subscript represents the order of the harmonic component observed on the surface of the Earth. In this Thesis, as well as in all previous works using data from the GMND (see the references from Rockenbach et al., 2014) we have calculated and used only the first order coupling coefficients c_0^1 , c_1^1 and s_1^1 .

For the conventional system, we have calculated the coupling coefficients in a similar way that was done by Da Silva (2009). The results are shown in Table 3.5, Table 3.6 and Table 3.7. Notice that we have calculated two different sets of coupling coefficients for Hobart detector. This was necessary due to the upgrade done on December 2010: its area was enlarged from $9m^2$ to $16m^2$ and the East-West direction of the detector was inclined 28° from the geographic East-West direction. Up to date, all publications using data from the GMDN did use data from before the upgrade in this detector. This work, on the other hand, uses data from 2008 to 2012, a period that spans from before to after the upgrade. We also calculated the coupling coefficients for each directional channel of the new correlation system (Figure 3.5 and Figure 3.6).

Table 3.5- The coupling coefficient c_0^1 calculated for the conventional correlation system.

Directional Channel	Hobart	Hobart	Kuwait	São	Nagoya
	(before upgrade)	(after upgrade)		Martinho da Serra	
Vertical	-0.52	-0.50	0.28	-0.26	0.30
North	-0.33	-0.28	0.56	0.04	0.48
South	-0.63	-0.69	-0.04	-0.51	0.06
East	-0.33	-0.42	0.29	-0.14	0.15
West	-0.64	-0.55	0.21	-0.36	0.43
North-east	-0.17	-0.20	0.53	0.12	0.32
North-west	-0.46	-0.32	0.52	-0.04	0.61
South-east	-0.45	-0.59	0.02	-0.37	-0.06
South-west	-0.75	-0.72	-0.13	-0.62	0.18
North 2	-0.11	-0.02	0.72	0.31	0.56
South 2	-0.66	-0.76	-0.31	-0.66	-0.17
East 2	-0.14	-0.30	0.25	-0.03	0.01
West 2	-0.67	-0.50	0.07	-0.39	0.47
North 3	-	-	-	0.44	0.60
South 3	-	-	-	-0.70	-0.34
East 3	-	-	-	0.03	-0.06
West 3	-	-	-	-0.37	0.48

Table 3.6 - The coupling coefficient c_1^1 calculated for the conventional correlation system.

Directional Channel	Hobart	Hobart	Kuwait	São	Nagoya
	(before upgrade)	(after upgrade)		Martinho da Serra	
Vertical	0.68	0.67	0.56	0.66	0.56
North	0.87	0.85	0.41	0.76	0.33
South	0.44	0.44	0.58	0.45	0.72
East	0.67	0.57	0.27	0.49	0.41
West	0.61	0.72	0.76	0.74	0.63
North-east	0.84	0.72	0.16	0.57	0.21
North-west	0.79	0.89	0.59	0.86	0.38
South-east	0.43	0.35	0.30	0.32	0.54
South-west	0.37	0.47	0.80	0.52	0.81
North 2	0.93	0.90	0.16	0.73	0.08
South 2	0.17	0.18	0.48	0.21	0.74
East 2	0.56	0.39	-0.02	0.28	0.22
West 2	0.46	0.65	0.77	0.70	0.57
North 3	-	-	-	0.66	-0.08
South 3	-	-	-	0.05	0.75
East 3	-	-	-	0.15	0.10
West 3	-	-	-	0.60	0.50

Table 3.7 - The coupling coefficient s_1^1 calculated for the conventional correlation system.

Directional Channel	Hobart	Hobart	Kuwait	São	Nagoya
	(before upgrade)	(after upgrade)		Martinho da Serra	
Vertical	0.34	0.33	0.45	0.41	0.46
North	0.20	0.34	0.31	0.38	0.49
South	0.44	0.31	0.57	0.43	0.40
East	0.59	0.61	0.69	0.66	0.68
West	0.05	0.02	0.11	0.09	0.16
North-east	0.46	0.61	0.57	0.62	0.69
North-west	-0.09	0.03	-0.05	0.06	0.23
South-east	0.67	0.57	0.77	0.67	0.63
South-west	0.17	0.00	0.26	0.13	0.10
North 2	0.06	0.33	0.13	0.32	0.46
South 2	0.49	0.25	0.60	0.42	0.30
East 2	0.75	0.77	0.78	0.80	0.78
West 2	-0.23	-0.28	-0.27	-0.24	-0.13
North 3	-	-	-	0.26	0.45
South 3	-	-	-	0.37	0.25
East 3	-	-	-	0.85	0.83
West 3	-	-	-	-0.49	-0.36

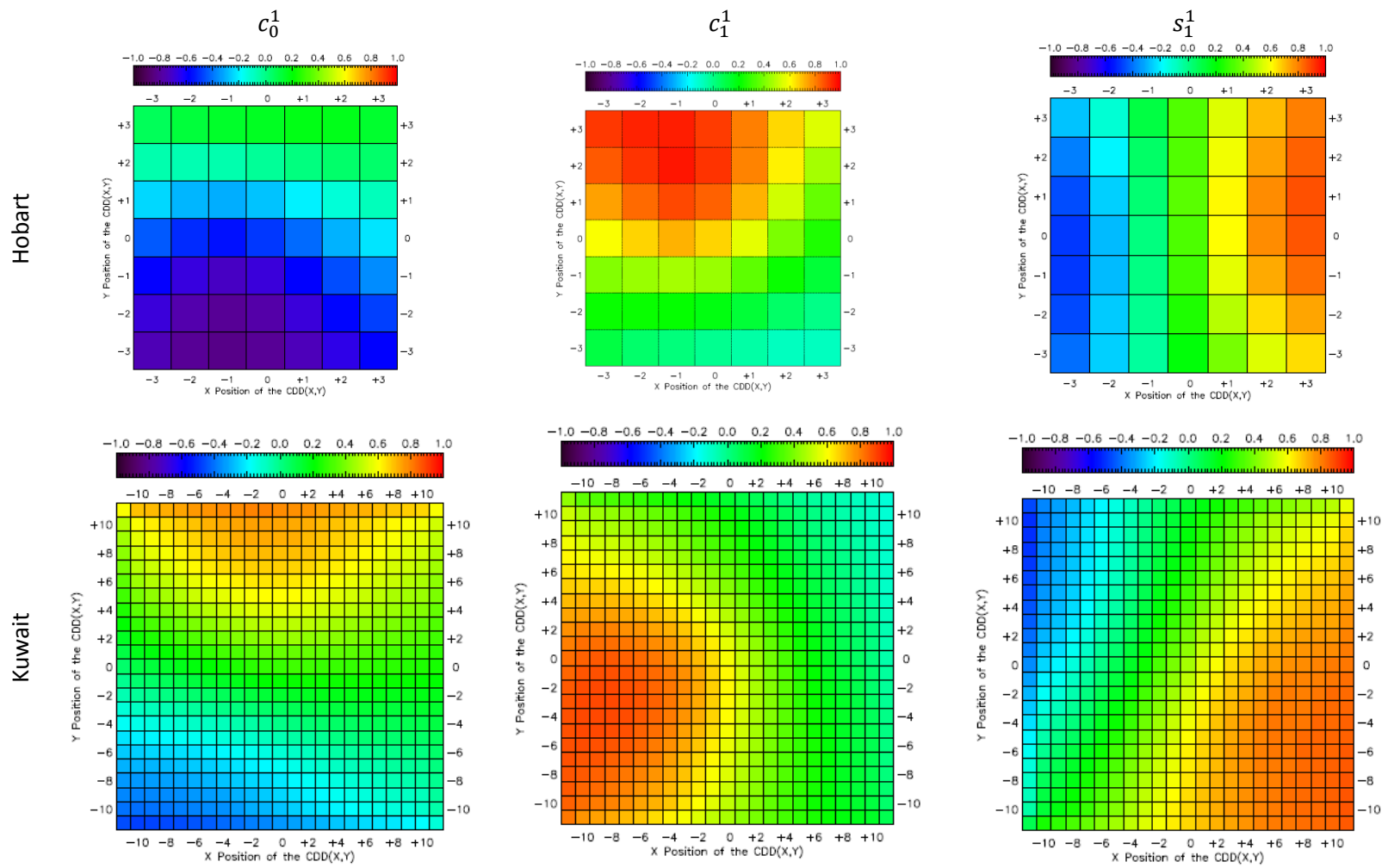


Figure 3.5 - The coupling coefficients calculated for Hobart (upper row) and Kuwait (lower row) detectors. The columns, from left to right, represent the coupling coefficients c_0^1 , c_1^1 and s_1^1 , respectively.

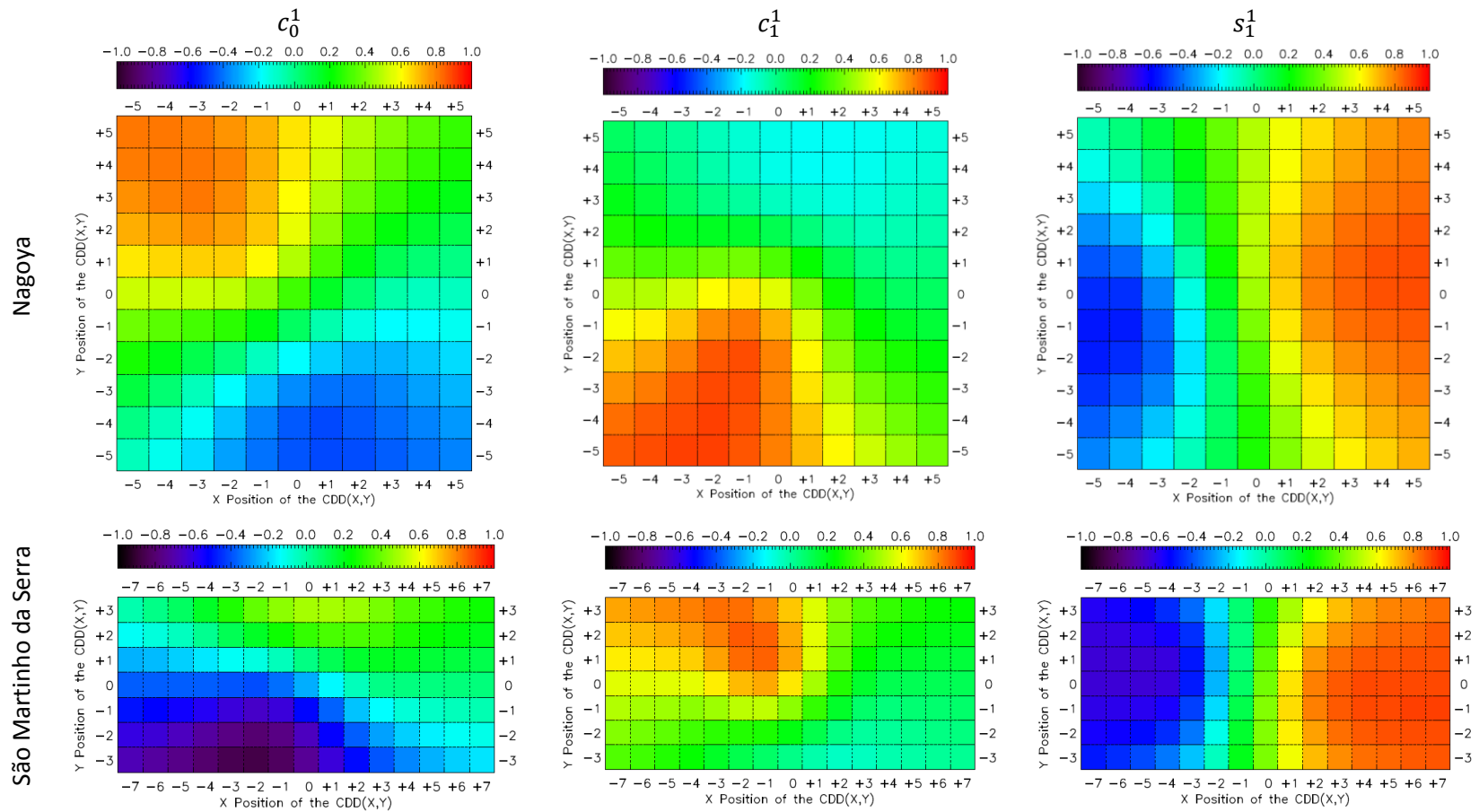


Figure 3.6 - The coupling coefficients calculated for Nagoya (upper row) and São Martinho da Serra (lower row) detectors. The columns, from left to right, represent the coupling coefficients c_0^1 , c_1^1 and s_1^1 , respectively.

3.5 Calculation of the anisotropy vector

Before starting the calculation of the anisotropy vector, all data were corrected for both the atmospheric pressure and temperature effects, as explained in Section 3.2. The data were also normalized to the average of each directional channel in a way to have it in percentage. Hereafter, we refer this data by cosmic ray intensity. After this, we started the calculation of the anisotropy vector. In this Thesis, we combine two methodologies.

One was introduced by Kuwabara et al. (2004) and was used for periods of a few days during magnetic clouds observation in the interplanetary medium. Hereafter, we identify the anisotropy vector calculated by this method as ξ^S . We fit the normalized count rate for each station i and directional channel j by the following equation:

$$I_{i,j}^{fit}(t) = I^0(t) + \xi_x^S(t)(c_{1i,j}^1 \cos \omega t_i - s_{1i,j}^1 \sin \omega t_i) + \xi_y^S(t)(s_{1i,j}^1 \cos \omega t_i + c_{1i,j}^1 \sin \omega t_i) + \xi_z^S(t)c_{1i,j}^0. \quad (3.1)$$

The meaning of each term in Eq. 3.1 is given in Table 3.8. By this equation, at each time, the intensity levels observed at detectors rotating with the Earth are transported into an isotropic component $I^0(t)$ plus the anisotropy vector $(\xi_x^S, \xi_y^S, \xi_z^S)$. Notice that the anisotropy is already in a coordinate system not rotating with the Earth that is suitable for studying the interplanetary medium. The information about the location of each detector are contained in the local time of each detector and in the coupling coefficients.

Table 3.8 - The meaning of each term in Eq. 3.1.

Term	Meaning
i	i -th cosmic ray detector
j	j -th directional channel
$I^0(t)$	The isotropic cosmic ray intensity
$c_{1i,j}^1$ and $s_{1i,j}^1$	First order coupling coefficients with daily periodicity
$c_{1i,j}^0$	First order coupling coefficients without periodicity
ω	The angular rotation speed of the Earth. $\omega = 2\pi/24$ (radian/hour)
t_i	The local time at the i -th cosmic ray detector
ξ_x^S	The x-component of the anisotropy in the NRGeo coordinate system
ξ_y^S	The y-component of the anisotropy in the NRGeo coordinate system
ξ_z^S	The z-component of the anisotropy in the NRGeo coordinate system
t	Universal time

This method has one drawback when we use it for periods such as one month or one year. If we take data from a period like this and normalize it by its average, sometimes the intensity level of one detector is significantly higher than the average for some days. It is unlikely that this difference is caused by interplanetary sources because the difference is kept constant during the rotation of the detector with the Earth. If it were from interplanetary origin, it would somehow show a daily variation due to the daily rotation of the detector. The reason for this difference is unknown, probably due to the difference between the atmospheric effects in the different detectors (OKAZAKI et al., 2008). Other possibility might be some instrumental effect. The consequence of this effect on the anisotropy vector is a spurious daily variation with high amplitude. If we take a shorter period to calculate the anisotropy (for example, only those days that produced the intensity difference), the normalization of the data will remove such intensity difference keeping all directional channels to a level close to zero. As a result, the spurious daily variation on the anisotropy vector will not be present.

To overcome this limitation, Okazaki et al. (2008) introduced another methodology that is suitable for longer periods such as one month or one year. Hereafter, the anisotropy vector calculated by this methodology is referred as ξ^l . It does not use the normalized cosmic ray count rate but rather it takes the difference between a given directional channel and the vertical channel of the same detector. To keep consistency, the coupling coefficients also need to be subtracted from its vertical:

$$\Delta c_{1i,j}^1 = c_{1i,j}^1 - c_{1i,1}^1 \quad (3.2)$$

$$\Delta s_{1i,j}^1 = s_{1i,j}^1 - s_{1i,1}^1 \quad (3.3)$$

$$\Delta c_{1i,j}^0 = c_{1i,j}^0 - c_{1i,1}^0. \quad (3.4)$$

Similarly, the primary cosmic ray median rigidity $P_{m i,j}$ also needs to be normalized. The expression used is:

$$\Delta P_{m i,j} = \frac{P_{m i,j} - P_{m i,1}}{P_{m 1,1}} \quad (3.5)$$

where $P_{m i,1}$ is the primary median rigidity of the vertical channel of the i -th detector and $P_{m 1,1}$ is the primary median rigidity of the vertical directional channel of Nagoya muon detector.

After this, we fit the observed cosmic ray count rate for each station i and directional channel j by the following equation:

$$\begin{aligned}
\Delta I_{i,j}^{fit}(t) = & I_{i,j}^{0''}(t) \Delta P_{m\ i,j} \\
& + \xi_x^l(t) (\Delta c_{1i,j}^1 \cos \omega t_i - \Delta s_{1i,j}^1 \sin \omega t_i) \\
& + \xi_y^l(t) (\Delta s_{1i,j}^1 \cos \omega t_i + \Delta c_{1i,j}^1 \sin \omega t_i) \\
& + \xi_z^l(t) \Delta c_{1i,j}^1.
\end{aligned} \tag{3.6}$$

If we assume that the atmospheric effects are the same for all directional channels of a given detector, this method automatically removes any atmospheric effect from the cosmic ray data. Unfortunately, the anisotropy vector calculated using this method is noisier than the one from Kuwabara et al. (2004) because the difference between two directional channels of a given detector is closer to zero than the actual intensity of a given directional channel.

Finally, we combine the results from both the methodology from Kuwabara et al. (2004) and Okazaki et al. (2008) using the following expression:

$$\xi(t) = [\xi^s(t) - \overline{\xi^s(t)}] + \overline{\xi^l(t)} \tag{3.7}$$

where

$$\overline{\xi^s(t)} = \frac{1}{24} \sum_{t-23}^t \xi^s(t) \tag{3.8}$$

and

$$\overline{\xi^l(t)} = \frac{1}{24} \sum_{t-23}^t \xi^l(t) \tag{3.9}$$

are the 24-hour trailing moving average of the anisotropy vectors. By these calculations, we take the lowest frequency component from the long-term anisotropy vector (last term on the right side of Eq. 3.7) and we remove the long-term anisotropy vector from the short-scale vector (term between brackets in the right side of Eq. 3.7).

We developed new IDL codes for calculating the anisotropy both in hourly basis and in 10-minutes basis. Previously the calculations were performed only in hourly basis using Fortran routines.

The methodology described in this section was used for all data observed by the GMDN in the period from 2008 to 2012. We have done this calculation using both the new and conventional correlation system. For the new correlation system, the directional channels with counting rate error higher than 1% were ignored, remaining 244 directional channels. For the conventional correlation system, all 56 directional channels were used.

3.6 The Compton-Getting effect

Up to the last section, all the calculations were performed in the NRGeo coordinate system (described in Section 3.3). From this section onwards, the anisotropy is used in the Geocentric Solar Ecliptic (GSE) coordinate system. This system is centered at the Earth and the xy plane is aligned with the Ecliptic Plane, a plane formed by the rotation of the Earth around the Sun; the x axis is aligned with the Earth-Sun line (point toward the Sun), the y axis points toward dusk and y axis points northward of the Ecliptic Plane. Notice that the GSE xy plane is not exactly correspondent to the NRGeo xy plane because the equator of the Earth is inclined in relation to the Ecliptic Plane. Moreover, the “ x ” and “ y ” axis are basically antiparallel to each other when comparing the two coordinate systems.

Following the original formulation from Gleeson & Axford (1968) and the previous works from Okazaki et al. (2008), we removed the Compton-Getting effect using the following expression:

$$\xi(t)_{(W)}^{GSE} = \xi(t)_{(E)}^{GSE} + (2 + \gamma)[\mathbf{v}_{sw}(t) - \mathbf{v}_E]/c \quad (3.10)$$

where the subscript (W) means the reference frame on the solar wind and the subscript (E) means the Earth frame of reference. $\xi(t)_{(W)}^{GSE}$ is free from the Compton-Getting effect since it is free from the change of solar wind speed with time. γ is the index of the GCR energy spectrum which we set to 2.7 following Okazaki et al. (2008). $\mathbf{v}_{sw}(t)$ is the solar wind velocity vector as a function of time, \mathbf{v}_E is the velocity vector of Earth’s orbital motion and c is the speed of the light. We use OMNI combined and definitive data averaged for multispacecraft interplanetary parameters. The data is time-shifted to the nose of the Earth’s Bow Shock. See more details about the data in the section “Interplanetary magnetic field data”.

The average solar wind velocity vector has a magnitude of hundreds of kilometers per second pointing roughly from the Sun to Earth. On the GSE coordinate system, this corresponds to a highly negative x component and negligible y and z components. If the solar wind speed is about 500 km/s, the contribution of the anisotropy effect will be about 0.8% in the x component. In y and z components, however, the effect is one order of magnitude smaller and can simply be ignored.

As for the Earth's orbital motion, we use a rough approximation of $\mathbf{v}_E = (0, -30, 0)$ km/s. The contribution from this term will be about 0.05% and, therefore, it is on the error range of the anisotropy vector and could simply be ignored in the analysis done here.

We calculated and removed the Compton-Getting effect from the anisotropy vector calculated for every hourly period between 2008 and 2012. As an example, we selected an arbitrary period to show the anisotropy vector before and after the Compton-Getting effect correction (Figure 3.7). Notice that the contribution is much larger in the x component than in the “ y ” and “ z ” components. There are some gaps on 2011/10/25 and 2011/10/26 in the anisotropy vector after Compton-Getting effect correction due to gaps in solar wind data.

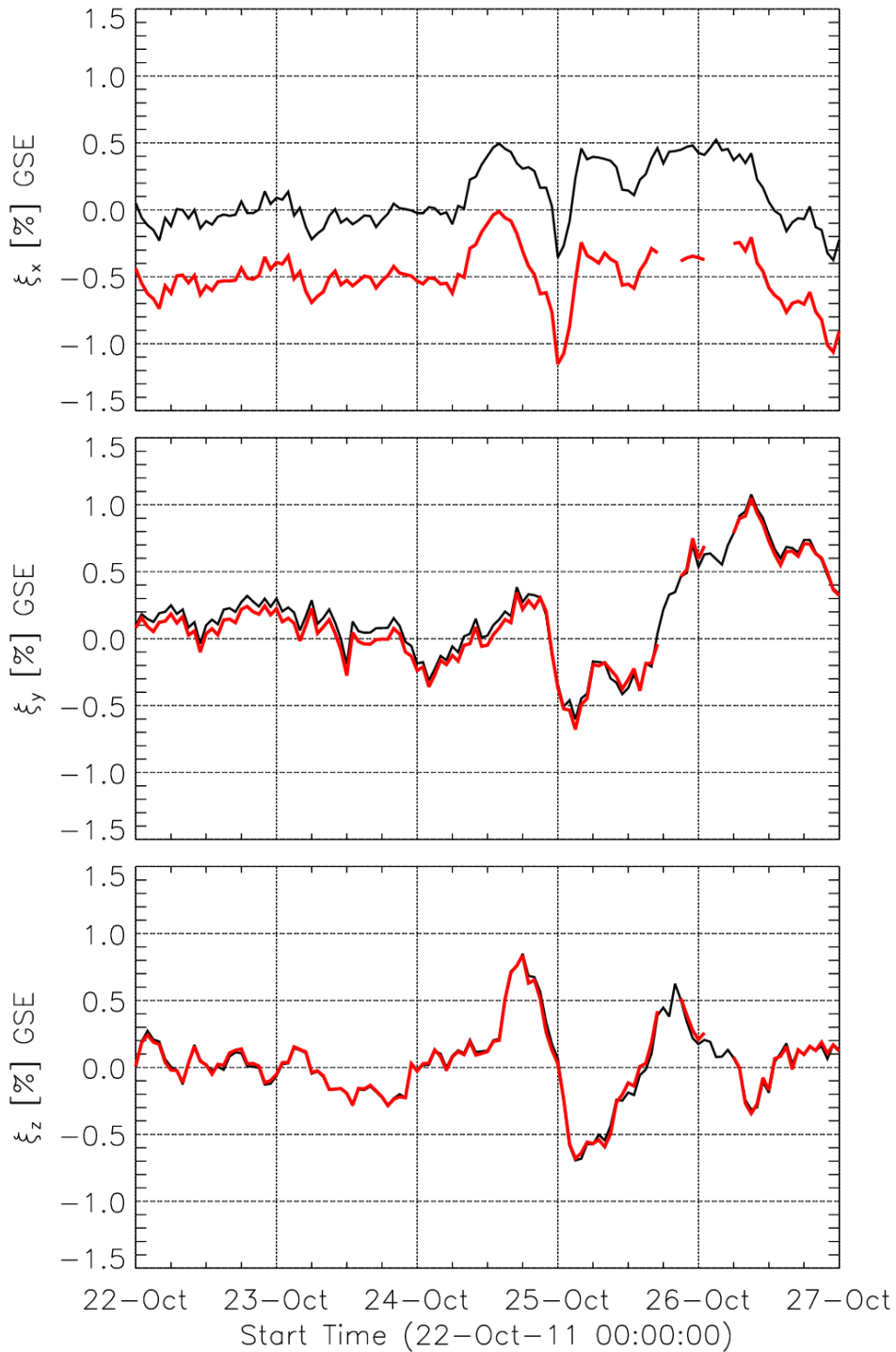


Figure 3.7 - Cartesian components of the anisotropy vector in the GSE coordinate system calculated using the new correlation system. The black line refers to data before the removal of the Compton-Getting effect and the red curve after its removal. An arbitrary period from 2011/10/22 to 2011/10/27 in shown here.

3.7 The cosmic ray gradient

Bieber & Evenson (1998), using data from a network of neutron monitors, observed enhanced cosmic ray anisotropy in periods associated to MCs and suggested that the cosmic ray anisotropy and interplanetary magnetic field \mathbf{B} are predominantly perpendicular to each other. Kuwabara et al. (2004, 2009) had obtained similar conclusions but using a network of muon detectors whose primary energy is higher than for neutron monitors. This result is used in this section to establish a mathematical expression to calculate the cosmic ray density gradient.

According to the cosmic ray transport equation, there are four sources of the enhanced anisotropy observed during MC periods: convection, perpendicular diffusion, parallel diffusion and the $\mathbf{B} \times \nabla n$ drift. If convection were the source of the anisotropy, the anisotropy would have its maximum pointing from the Sun to the Earth. It is clear for many years that this is not true (KANE, 1974). Since the component of the anisotropy parallel to \mathbf{B} is very small, we can dismiss parallel diffusion. The perpendicular diffusion is considered much smaller than the $\mathbf{B} \times \nabla n$ drift for energy range observed by neutrons monitors (see, for example, Bieber & Evenson, 1998). Therefore, we may conclude that the $\mathbf{B} \times \nabla n$ drift is the source of the anisotropy.

The drift $\mathbf{B} \times \nabla n$ occurs when we have a gradient of a given charged particle density in a direction perpendicular to the magnetic field, as illustrated in Figure 3.8 and Figure 3.9. Then we can write:

$$\mathbf{drift} = R_L \mathbf{b} \times \frac{\nabla n}{n} \quad (3.11)$$

where \mathbf{b} is the unit vector in the direction of the interplanetary magnetic field. Notice in Figure 3.9 that the drift and the anisotropy will have opposite sign, therefore:

$$\xi_{\perp}^{(W)} = -R_L \mathbf{b} \times \frac{\nabla n}{n}. \quad (3.12)$$

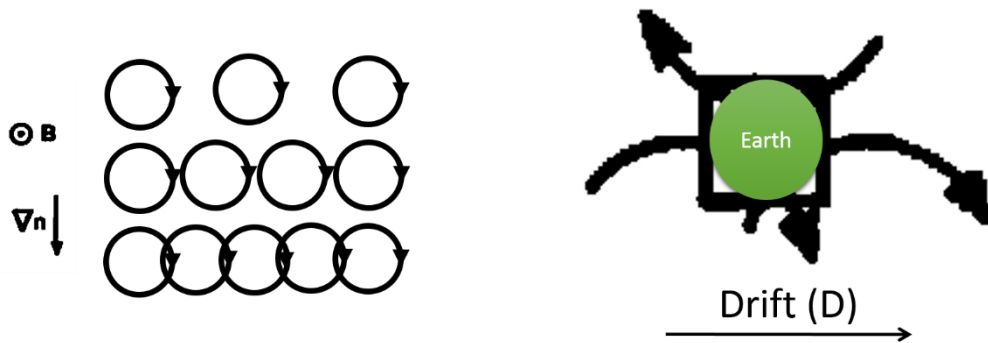


Figure 3.8 - The $\mathbf{B} \times \nabla n$ drift. Left side figure: each circle is a cosmic ray (positive charge) spinning due to the magnetic field \mathbf{B} . The particle density at the top is smaller than in the bottom. Right side figure is a “zoom” of the scenario on the left; the 3 arrows indicate the 3 sample particles rotation. As there are more particles in the bottom, a current (drift) will be formed following the direction of rotation of the particles in the bottom.

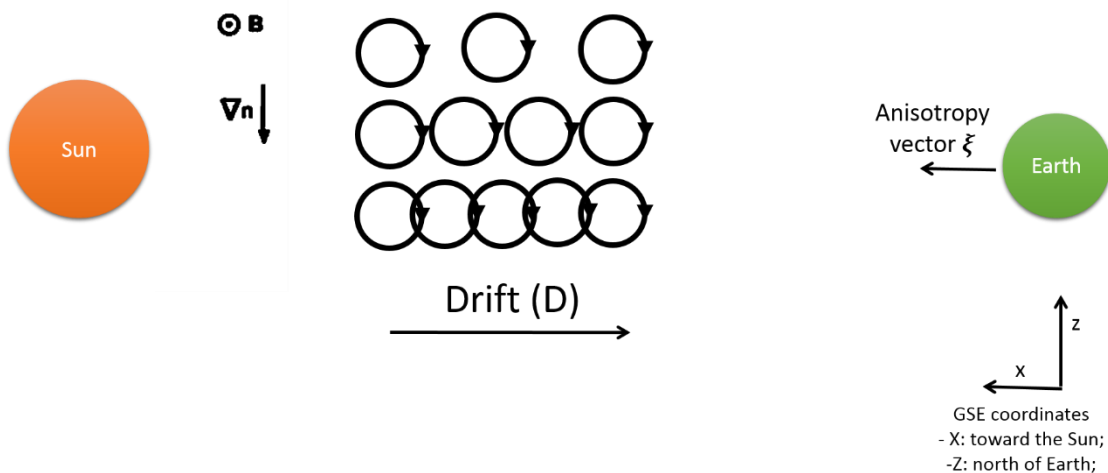


Figure 3.9 - An explanation of the $\mathbf{B} \times \nabla n$ drift and the anisotropy vector drift in the Sun-Earth medium. Notice that the anisotropy and drift are pointing in opposite directions.

The superscript (W) indicates the anisotropy in the solar wind frame of reference and the subscript \perp indicates that we are taken into account only the component perpendicular to the IMF. Due to the properties of the cross product, the anisotropy component parallel to the IMF is automatically neglected. In this way, we needed to check if the desired anisotropy is approximately perpendicular to the magnetic field. If this is not true and the anisotropy is almost parallel to the magnetic field direction, we cannot use this equation for calculating the gradient.

Using the cross product properties, we can write:

$$R_L \frac{\nabla n}{n} = \mathbf{b} \times \xi_{\perp}^{(W)}. \quad (3.13)$$

By using the Eq. 3.13, we have one expression to calculate the fractional cosmic ray gradient. For shortly, the term on the left hand side of Eq. 3.13 has its Cartesian components referred as g_x , g_y and g_z in the plots in this Thesis.

3.8 Recalculating the first order anisotropy vector and the cosmic ray gradient density using integration time of 10 minutes

The GMDN data analysis performed up to now used data with integration time of 1-hour since only this integration time was available for all detectors until 2006. Since 2007, after upgrades in all detectors of the GMDN, their data started to be recorded with integration time of 10-minutes. Although more than six years passed since this data is available, the data in integration times of 10 minutes have never been used before.

We made new code in Interactive Data Language (IDL) software to correct the pressure and temperature effects on the observed data in 10-minutes basis and, after this, calculating the anisotropy and the cosmic ray gradient. We selected an arbitrary period with significant anisotropy magnitude in 2011. An example of the comparison between the anisotropy vectors in both integration times is shown in Figure 3.10. Both anisotropy vectors have values very similar to each other. For the same arbitrary period, the gradient in both hourly and 10-minutes integration periods is shown in Figure 3.11. The difference between both gradient vectors is higher than the difference between both anisotropy vectors. The reason is the difference in the IMF vector in hourly and 10-minutes basis, which is clear in the last hours of 2011/10/24 and in the first hours of 2011/10/25 (Figure 3.12). We also calculated, for each hour, the average and standard deviation of the gradient using the six data points calculated using 10-minutes integration time (Figure 3.13). Notice that for vast majority of the points the standard deviation is much smaller than 0.1 and might be considered negligible since it is much smaller than the statistical error of the instrument.

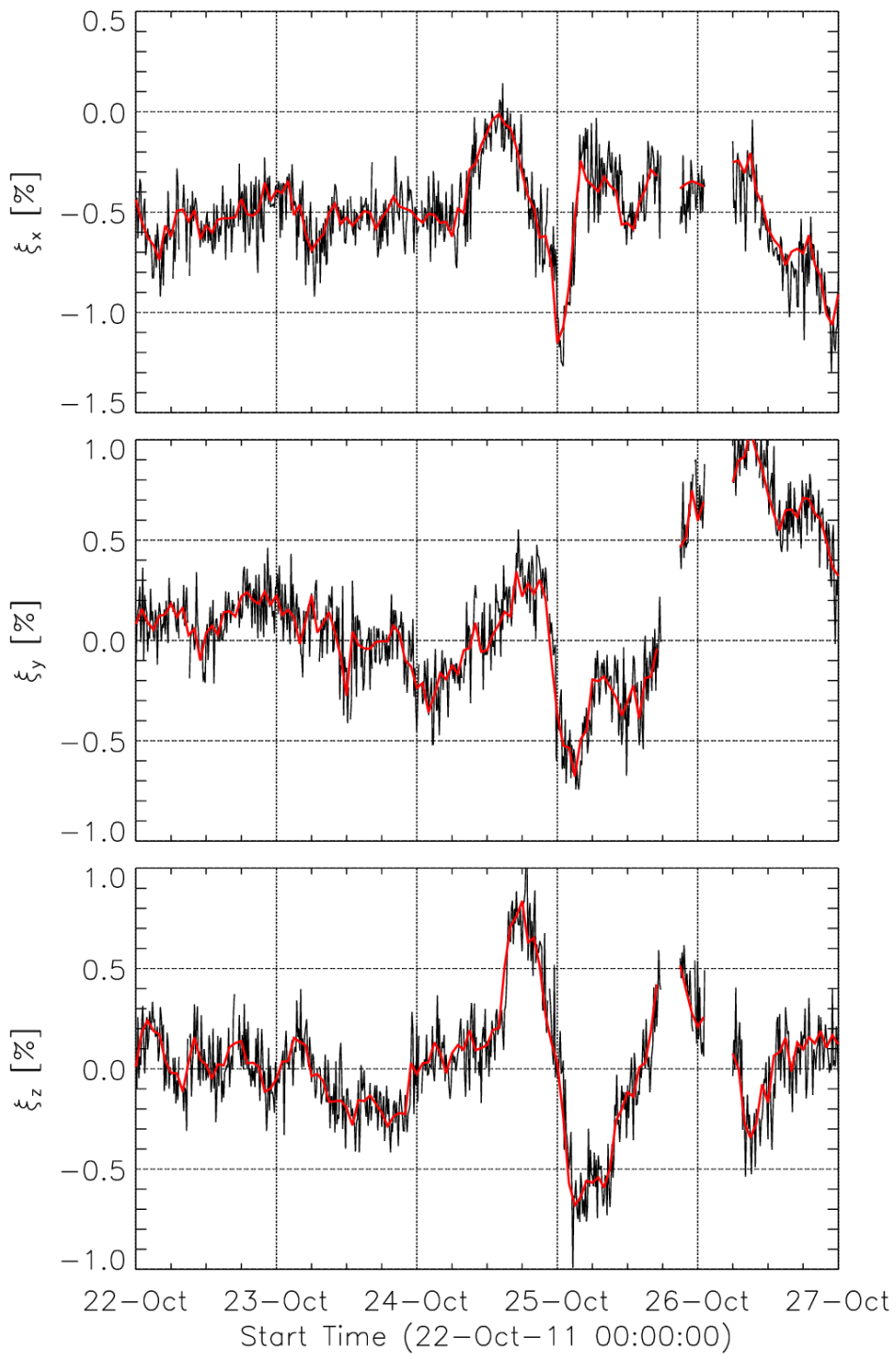


Figure 3.10 - Comparison of the anisotropy vector calculated in integration times of one hour (red) and ten minutes (black) using data from the new correlation system and already corrected for Compton-Getting effect.

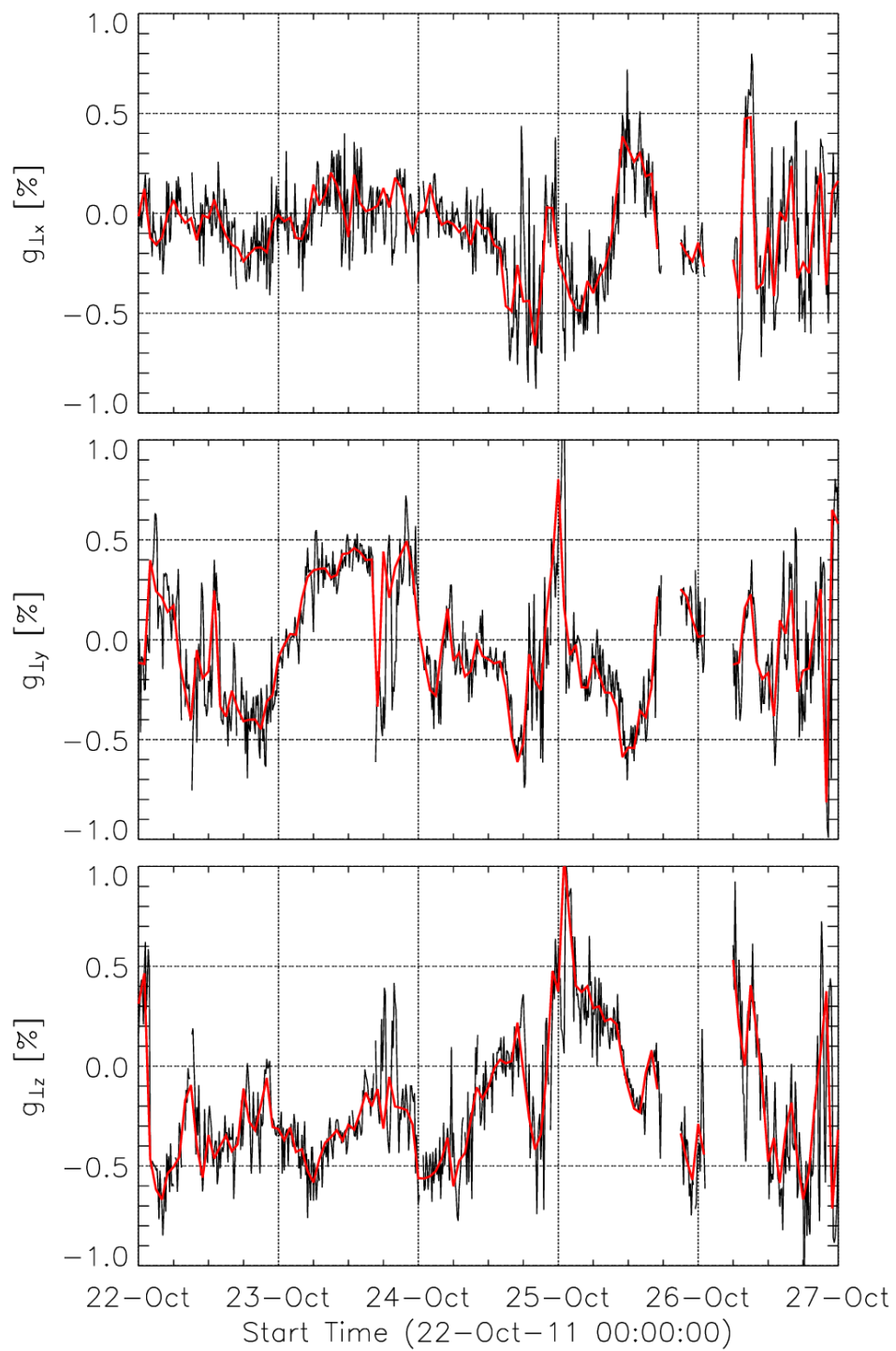


Figure 3.11 - Comparison of the gradient vector calculated in integration times of 1 hour (red) and 10 minutes (black) using data from the new correlation system.

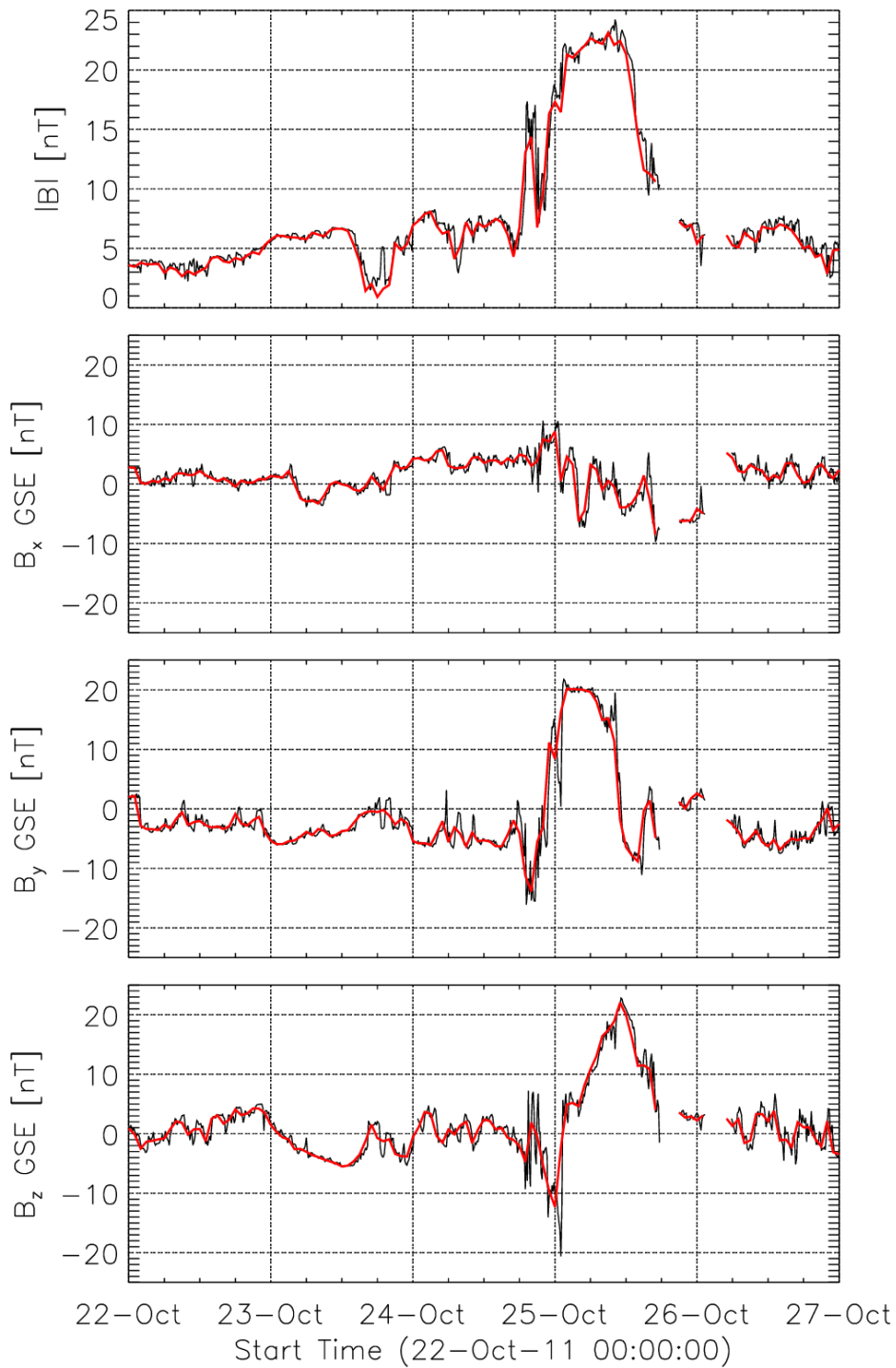


Figure 3.12 - The interplanetary magnetic field magnitude (first panel at the top) and its Cartesian components in the GSE coordinate system (remaining three panels). The hourly-averaged data is shown in red and the 10-minutes averaged is represented in black.

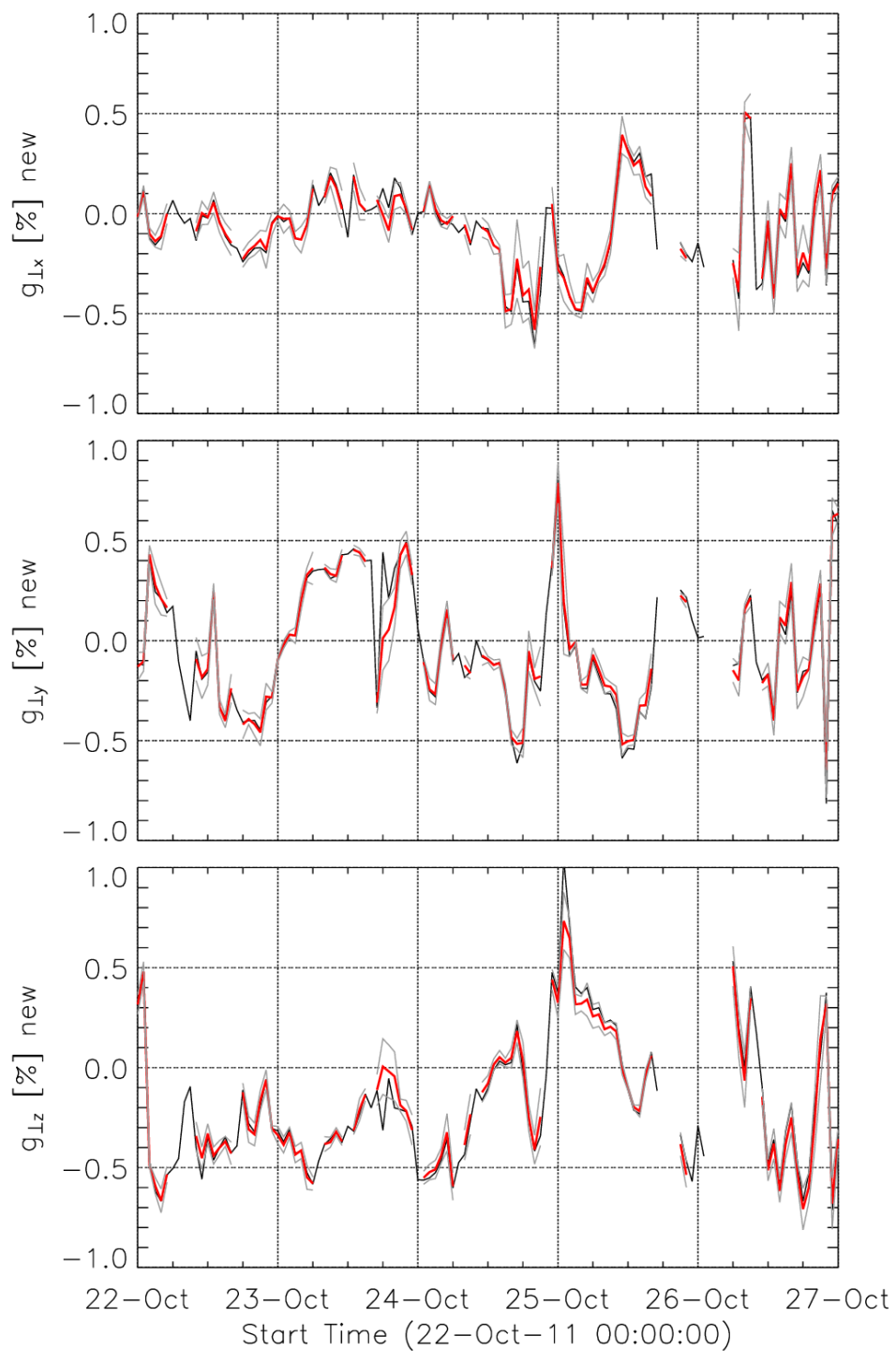


Figure 3.13 - The perpendicular fractional gradient calculated using the original hourly integration time (black curves) and using the 10-minute integration time as an estimate of the error (red curve). For the latter case, we calculated the average vector for each hourly period using the six data points available in each period. The gray curves show the average plus or minus the standard deviation.

3.9 A model of cosmic ray density inside the magnetic cloud

We use a model of an axisymmetric straight cylinder as a local approximation of a flux rope model of a magnetic cloud. The cylinder axis orientation is supposed to be constant during the magnetic cloud period. We assume the cylinder is moving with average solar wind velocity vector observed in the OMNI database during the magnetic cloud period. We do not use the hourly average because we are assuming that the cylinder is possibly expanding and, therefore, the velocity observed will be a superposition of the cylinder displacement as a whole plus the apparent speed due to the cylinder expansion. If this hypothesis were true, we would expect the solar wind speed profile to be gradually increasing inside a magnetic cloud if it is expanding. If the magnetic cloud were shrinking, the solar wind profile would be increasing.

We use the unit vector \mathbf{A} pointing above the ecliptic plane to represent the cylinder axis and the vector $\mathbf{P}_E(t)$ that at any time t points from the Earth to the closest point on the cylinder axis (see Figure 3.14). Notice that depending on the solar wind direction, a different portion of the cylinder will be closer to the Earth as time passes. The normalized distance from the cylinder center is defined as:

$$x(t) = \frac{|\mathbf{P}_E(t)|}{R(t)} \quad (3.14)$$

where $R(t)$ is the cylinder radius. Since we are using the cylinder from the time it touches the Earth for the first time until it leaves, it will have $0 \leq x \leq 1$.

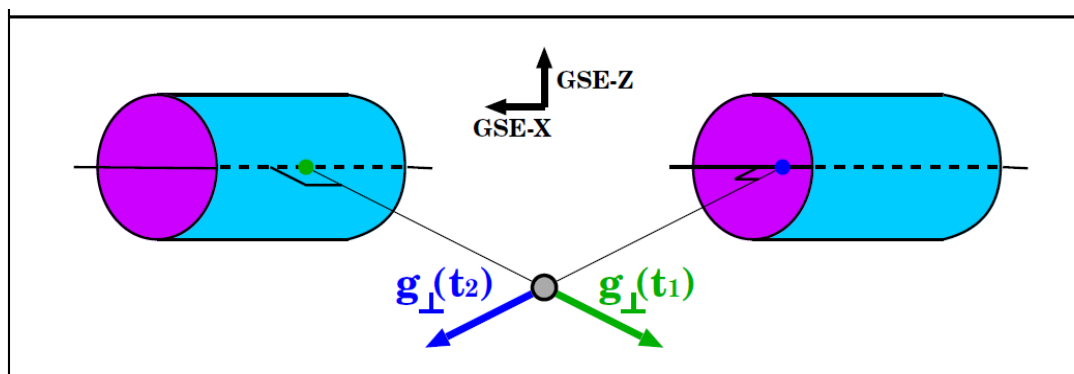


Figure 3.14 - An illustration of the cosmic ray gradient vector for two different positions of the magnetic cloud flux rope approximated in this case by a straight cylinder.

Source: Kuwabara (2005)

Munakata et al. (2006) calculated the numerical solution of the cosmic ray transport equation for the specific case of a magnetic cloud. According to that work, the cosmic ray fractional isotropic intensity I can be expressed as:

$$I(x) = \sum_{n=0}^{\infty} a_n x^n, \quad (3.15)$$

where

$$a_n = \begin{cases} \left(\frac{\Gamma}{n^2}\right) a_{n-2} & \text{for } n = 2, 4, 6, \dots \\ 0 & \text{for } n = 1, 3, 5, \dots \end{cases} \quad (3.16)$$

where Γ is a dimensionless parameter defined by:

$$\Gamma = \frac{2(2 + \gamma)}{3\kappa_0}. \quad (3.17)$$

Here γ is the cosmic ray power spectrum index, which we will assume to be 2.7. Here κ_0 is a dimensionless parameter given by:

$$\kappa_0 = \frac{\kappa_{\perp}(t)}{R(t) \cdot V_{ex}} \quad (3.18)$$

where $\kappa_{\perp}(t)$ is the perpendicular diffusion coefficient and V_{ex} is the cylinder radius increase rate (hereafter, expansion speed of the cylinder).

The expression in Eq. 3.15 then can be written as:

$$I(t) = a_0 \left\{ 1 + \frac{\Gamma}{4} x(t)^2 + \frac{\Gamma^2}{64} x(t)^4 + \frac{\Gamma^3}{2304} x(t)^6 + \dots \right\} \quad (3.19)$$

This expression expects an isotropic decrease with maximum in the cylinder axis ($x = 0$) and fractional isotropic decrease a_0 in the center of the cylinder. One example of the isotropic cosmic ray intensity as a function of position inside a magnetic cloud is shown in Figure 3.15. Notice that $0 < a_0 < 1$. For example, a 1% decrease corresponds to $a_0 = 0.99$.

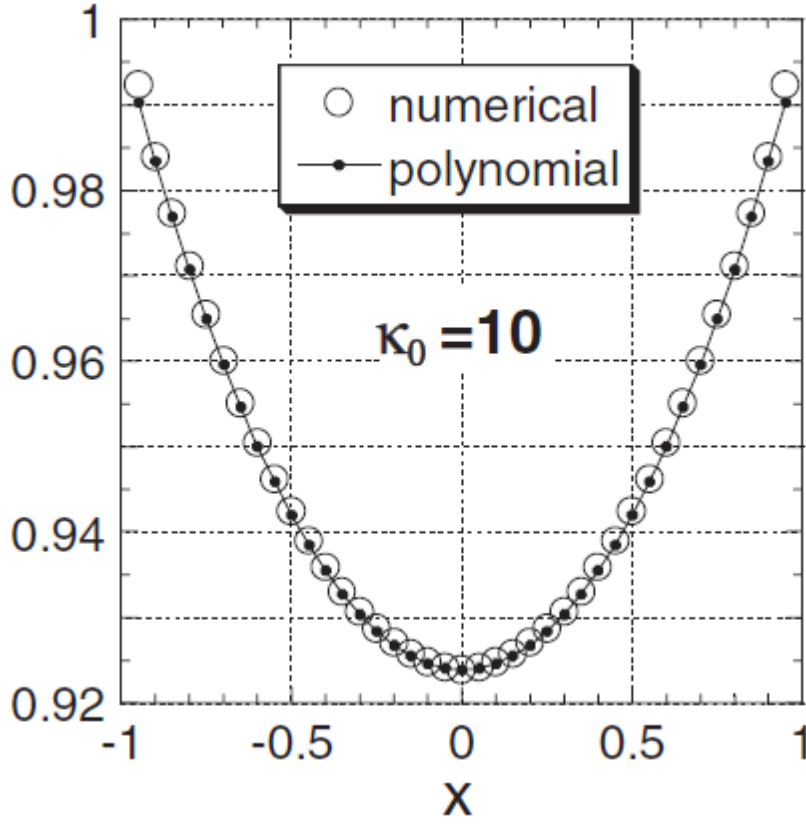


Figure 3.15 - Example of the cosmic ray isotropic intensity as a function of the normalized distance from the cylinder axis x .
Source: Munakata et al. (2006).

The cosmic ray isotropic intensity is minimum at the axis of the cylinder. In this way, the gradient of the cosmic ray isotropic intensity will always be perpendicular to the cylinder axis and pointing away from it. Notice that it is antiparallel to $\mathbf{P}_E(t)$. Using the expression of the fractional isotropic intensity, we may write the following expression for the cosmic ray fractional gradient:

$$\mathbf{g}^{exp}(t) = \frac{R_L}{R(t)} \frac{\nabla I(t)}{I(t)} \quad (3.20)$$

$$\mathbf{g}^{exp}(t) = -\frac{R_L}{R(t)} \frac{a_0}{I} \left\{ \frac{\Gamma}{2} x(t)^1 + \frac{\Gamma^2}{16} x(t)^3 + \frac{\Gamma^3}{384} x(t)^5 + \dots \right\} \frac{\mathbf{P}_E(t)}{|\mathbf{P}_E(t)|}. \quad (3.21)$$

Beyond the information about the expected cosmic ray gradient and isotropic intensity, we can make some geometric constraints to our model. Now we define the vector \mathbf{P}_0 which points from the Earth to the point where the magnetic cloud is closer to the Earth. This vector is illustrated in Figure 3.16. When the magnetic cloud is closer to the Earth (t_c) we have $\mathbf{P}_0 = \mathbf{P}_E(t_c)$.

Moreover, \mathbf{P}_0 is perpendicular both to the cylinder axis \mathbf{A} and to the solar wind velocity vector \mathbf{v}_{SW} . Therefore, we can write:

$$\mathbf{P}_0 = d \frac{\mathbf{A} \times \mathbf{v}_{SW}}{|\mathbf{A} \times \mathbf{v}_{SW}|} \quad (3.22)$$

where $d = x(t_C)$ is the distance from the Earth to the cylinder axis at the time t_C when the cylinder is closest to the Earth.

In the plane formed by the Earth and the solar wind velocity vector (see Figure 3.16), we define the vector $\mathbf{P}(t)$ which is given by:

$$\mathbf{P}(t) = \mathbf{P}_0 + \mathbf{v}_{SW}(t - t_C) \quad (3.23)$$

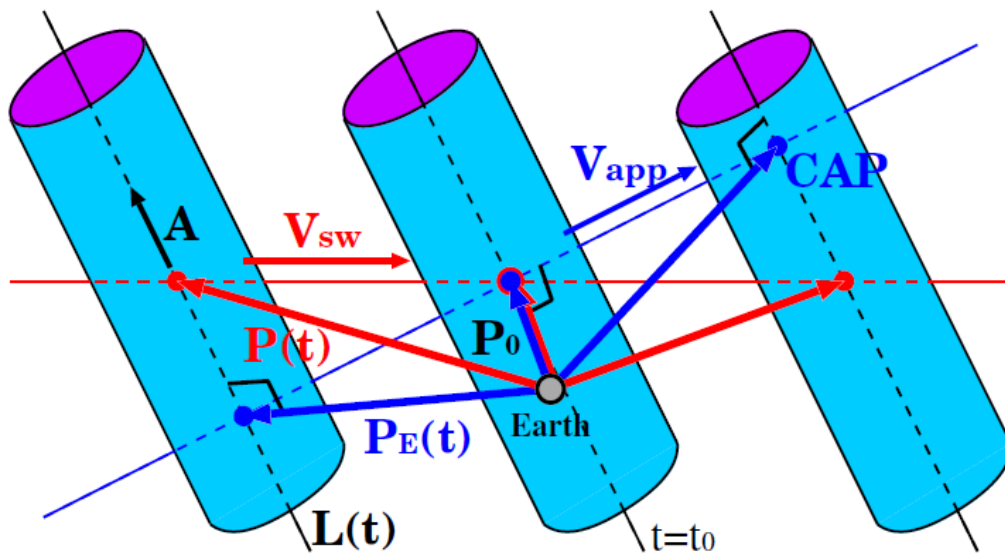


Figure 3.16 - The cosmic ray cylinder at three different hypothetical positions. In each position the vectors \mathbf{P}_E and \mathbf{P} used in the model are shown (see text for details). The position at the center of the picture corresponds to the time t_C when the cylinder is closest to the Earth. The cylinder velocity vector is supposed to be coincident with solar wind velocity \mathbf{v}_{SW} indicated in the figure.

Source: Kuwabara (2005)

Once we have an expression for $\mathbf{P}(t)$, we can find $\mathbf{P}_E(t)$ by subtracting from $\mathbf{P}(t)$ its projection into the cylinder axis \mathbf{A} .

$$\mathbf{P}_E(t) = \mathbf{P}(t) - (\mathbf{A} \cdot \mathbf{P})\mathbf{A} \quad (3.24)$$

We suppose that the cylinder radius will correspond to the position vector of the cylinder axis in the entrance and exit times of the cylinder. Therefore, we may write:

$$R(t_{out}) = |\mathbf{P}_E(t_{out})| \quad (3.25)$$

and

$$R(t_{in}) = |\mathbf{P}_E(t_{in})|. \quad (3.26)$$

where the subscripts *in* and *out* refer to the timing when Earth enters and leaves the cylinder, respectively. The cylinder radius increases linearly as a function of time with expansion speed given by:

$$V_{ex} = \frac{R(t_{out}) - R(t_{in})}{t_{out} - t_{in}}. \quad (3.27)$$

In this way, we are able to estimate the cylinder radius at any time inside the magnetic cloud period using the following expression:

$$R(t) = R(t_{in}) + V_{ex} \cdot (t - t_{in}). \quad (3.28)$$

3.10 An additional model of cosmic ray density inside the magnetic cloud

One additional model to deduce the cylinder of cosmic ray depleted region during a MC event was proposed by Kuwabara et al. (2004). Roughly speaking, it is similar to Kuwabara et al. (2009) except for two points: 1) it does not allow any expansion of the cylinder radius and 2) it does use a Gaussian distribution for the isotropic cosmic ray density decrease. Since the model from Kuwabara et al. (2009) can take into account the possibility of expansion, we did not apply the method for our new list of events. We only tested this model for the same MC studied in Kuwabara et al. (2004), observed on 2003/10/29. The results were similar to those from Kuwabara et al. (2004).

3.11 Testing the model from Kuwabara et al. (2009)

Before starting the application of the cosmic ray cylinder model from Kuwabara et al. (2009) in new events observed between 2008 and 2012, we wrote IDL codes using only the information on Kuwabara et al. (2009) and tested it for a very strong event observed in 2003/10/29. We fit the model to the same data used by Kuwabara et al. (2009) and the results are shown in Figure

3.17, Figure 3.18 and Figure 3.19. Notice that the results found are in good agreement with the reference.

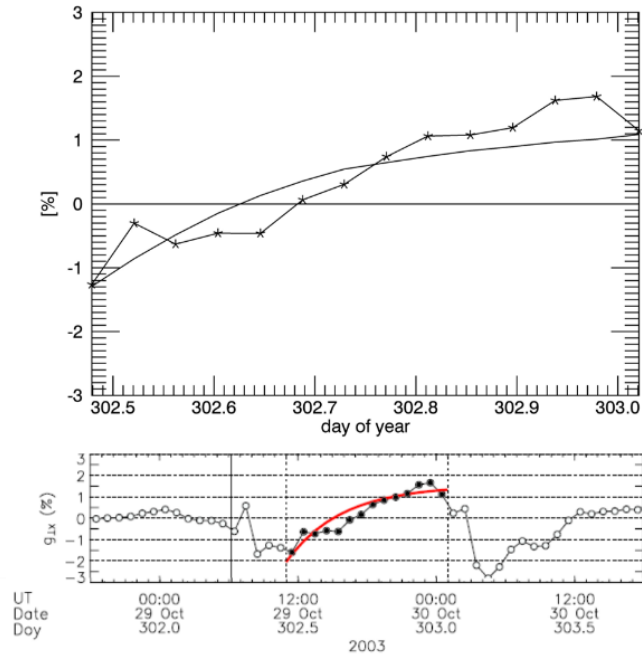


Figure 3.17 - Comparison of the results from the current work (upper panel) and those from Kuwabara et al. (2009) (lower panel) for the x component of the fractional gradient. The observed data is indicated by the curve with asterisks in the upper panel and with the bold curve with circles in the lower panel. The curves without symbols show the data fit by the model.

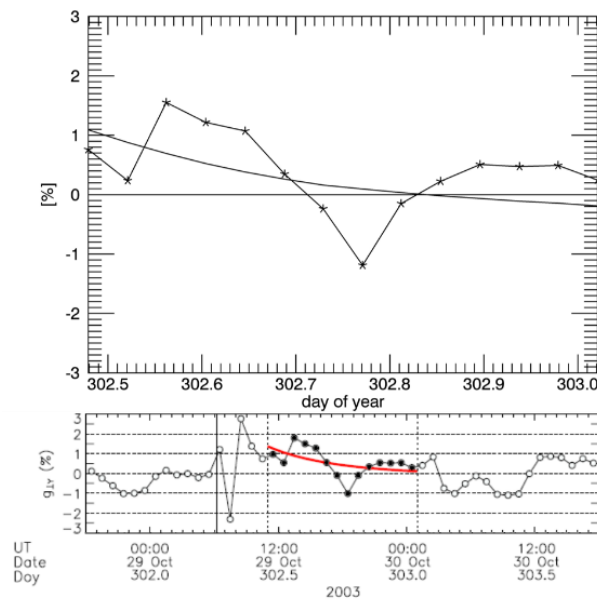


Figure 3.18 - Comparison of the results from the current work (upper panel) and those from Kuwabara et al. (2009) (lower panel) for the y component of the fractional gradient. The observed data is indicated by the curve with asterisks in the upper panel and with the bold curve with circles in the lower panel. The curves without symbols show the data fit by the model.

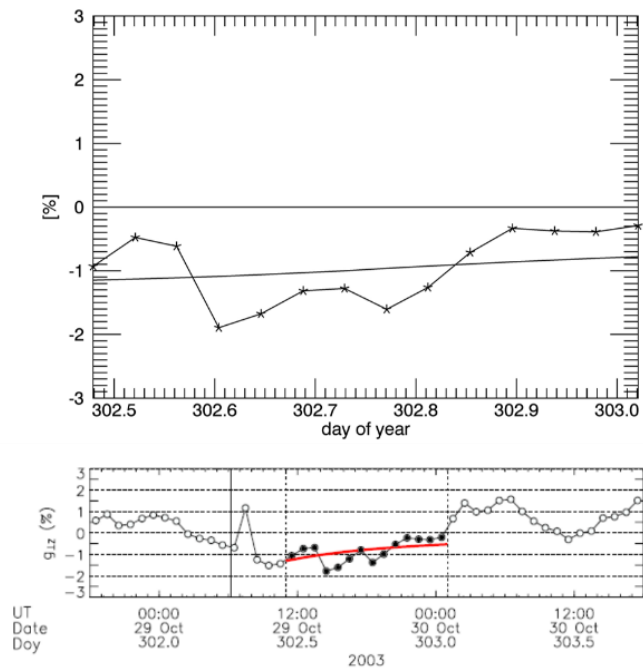


Figure 3.19 - Comparison of the results from the current work (upper panel) and those from Kuwabara et al. (2009) (lower panel) for the z component of the fractional gradient. The observed data is indicated by the curve with asterisks in the upper panel and with the bold curve with circles in the lower panel. The curves without symbols show the data fit by the model.

4 DERIVING THE CORONAL MASS EJECTION KINEMATIC PARAMETERS

This Chapter describes the methodology applied to process the images from the coronagraph SECCHI-COR2 onboard both the STEREO spacecraft. First, we explain briefly how the Coronal Segmentation Technique (CORSET) tracks CMEs and why it was chosen here among other methods. The result from CORSET is the identification of the CME boundary in each image. This boundary is then used to calculate the position of the CME and speed in each coronagraph field-of-view (FOV). Once this step is done, we start the methodology to derive the tridimensional parameters by combining the result from one coronagraph onboard STEREO A and the other onboard STEREO B. In this Thesis, we developed a new method that combines the results from CORSET, triangulation and tie-pointing. This methodology allows us to calculate the tridimensional speed and direction of propagation. Results from the application of this methodology are shown and discussed later, especially in Chapter 6.

4.1 The CORSET

The Coronal Segmentation Technique (CORSET) is a texture-based technique devised to isolate a CME from its background in a coronagraph FOV. CORSET is not a manual method to identify CMEs because a cursor is not used to define their boundaries. CORSET is also not an automatic method that is able to identify automatically the beginning and the end of the CME and find its boundary based only on some computer program. In CORSET, the user needs to define the period (a set of frames) where the CMEs are in the coronagraph FOV. In one of the images of the subset, an user-estimated sample area of the CME is also required. After this, the algorithm detects and tracks the event as it develops, by analyzing the texture of neighboring pixels to evaluate whether they belong to the CME feature or to the background. In this way, CORSET is neither a human-based manual method nor human-independent automatic method to track CMEs. It is a supervised (pseudo-automatic) procedure (GOUSSIES et al., 2010). One example of a CME tracked by CORSET is shown in Figure 4.1 where the continuous white line indicates the area considered to be the CME.

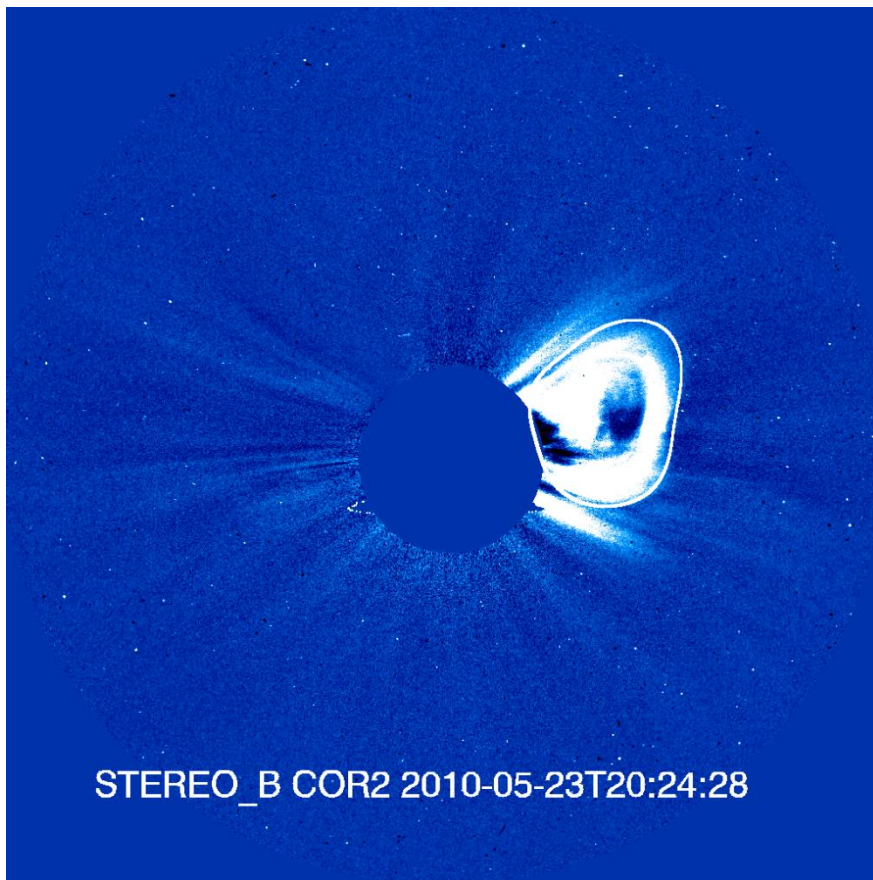


Figure 4.1 - One example of the application of CORSET to track a CME in the SECCHI-COR2B FOV. The white line is the contour derived by CORSET.

4.2 Why using CORSET instead of other manual or automatic catalogs?

There are some manual catalogs of CMEs available such as the SOHO CDAW catalog (YASHIRO et al., 2004). This catalog is available online at http://cdaw.gsfc.nasa.gov/CME_list/ and it contains information about all the CMEs observed in LASCO-C2 and LASCO-C3 FOV since the beginning of the SOHO mission (in 1996) up to date. For each image available, the CME is identified by an observer who defines the boundary of the CME using visual inspection. The criteria used to select the boundary of the CME is purely subjective. Once the CME is identified in all frames available, many kinematic properties are calculated such as angular width, speed, acceleration and mass. Due to the unclear criteria to select CMEs, there are discrepancies when we compare the SOHO CDAW catalog with other works that identified CMEs manually. For instance, Yashiro et al. (2004) identified 1084 CMEs between January 1996 and June 1998. St

Cyr et al. (2000), on the other hand, identified only 841 CMEs. Among the CMEs from the later work, 23 of them do not correspond to any CME identified by Yashiro et al. (2004).

There are many techniques used to track CMEs automatically as well as many catalogs. Among them we can cite the “Computed Aided CME Track” (CACTus) that autonomously detect CMEs in a sequence of images from both LASCO-C2, LASCO-C3 and SECCHI-COR2 by constructing height-time maps and using Hough transform to identify structures that are CMEs. This method is fully described in Robbrecht & Berghmans (2004) and the catalog is available online at <http://sidc.oma.be/cactus/>. Another fully automated catalog is the “Solar Eruptive Event Detection System” (SEEDS) available at <http://spaceweather.gmu.edu/seeds/> (OLMEDO et al., 2005; OLMEDO et al., 2008). This catalog includes both the coronagraphs LASCO-C2 and SECCHI-COR2.

The advantage of the automatic catalogs when compared to manual ones is that they are more objective because the criteria to detect CME are clearly written in an algorithm. There are many discrepancies when we compare different automated catalogs and when we compare them to manual inspection of CMEs. One reason for the discrepancies is that the catalogs do not have any criteria to distinguish two adjacent CMEs seen in the coronagraph FOV at the same time. Since the CMEs are optically thin, different CMEs or other coronal structures might be superposed. This point is one of the well-known limitations of CACTus: the impossibility to distinguish between different CMEs when they are observed in close timing and position. For an extensive discussion about the strength and weakness of CACTus, the reader is referred to Bonte et al. (2011). Other complication is that CMEs have a wide range of shapes (see explanation in Section 1.1) and therefore a unique fixed shape cannot be used as a constraint when tracking CMEs. Other drawback is the splitting of some CMEs in more than one CME when there is actually only one. As a result, part of the angular range is considered one event and the remaining part another. Thanks to this fact, automatic catalogs tend to have a higher number of events observed than the manual catalogs do.

The CORSET method has the advantage of being an objective method with explicit criteria to track CMEs and, even so, it is flexible in a way to avoid the limitation of fully automated catalogs. A detailed discussion about the usage of CORSET instead of other existing methods and a detailed comparison of results from different catalog and CORSET can be found in Braga et al. (2013).

In the following section, we briefly address the idea behind texture analysis. The reader is referred to Goussies et al. (2010) and references therein for the mathematical details behind CORSET.

4.3 Texture analysis

Texture analysis is one of the fundamental methods used to discriminate between a background and an object (HARALICK et al., 1973). This approach, alone or combined with other features (e.g., shape, brightness, motion, etc.), is commonly applied in computer vision to distinguish, characterize, and eventually extract objects in digital images (TRUCCO; VERRI, 1998).

Image texture is briefly defined as a function of the spatial variation of the pixel intensities (gray levels). It is assumed that the texture information of an image is contained in the overall spatial relationship that the gray levels in the image have to one another. Hence, Haralick et al. (1973) proposed the use of the so-called Gray Level Co-occurrence Matrix (GLCM) as a mean to capture and therefore characterize the texture of the different regions. In other words, the GLCM is a matrix that contains information about the distribution of the intensity levels inside the region. The elements of the GLCM are simply the relative frequencies of occurrence of pairs of grey-level values of pixels separated by a given distance in a certain direction. More specifically, this texture-content information can be specified by a matrix composed of the relative probabilities $P_{i,j}$ that two neighboring pixels separated by distance d in a given direction have gray levels i and j , respectively. Such gray-level matrices of spatial dependence frequencies are a function of (1) the angular relationship between the neighboring pixels and (2) the distance between them. One example of how a 4x4 GLCM is computed is shown in Figure 4.2 using distance of one pixel for four different directions. Notice that the matrix is symmetric and it will always be due to the definition.

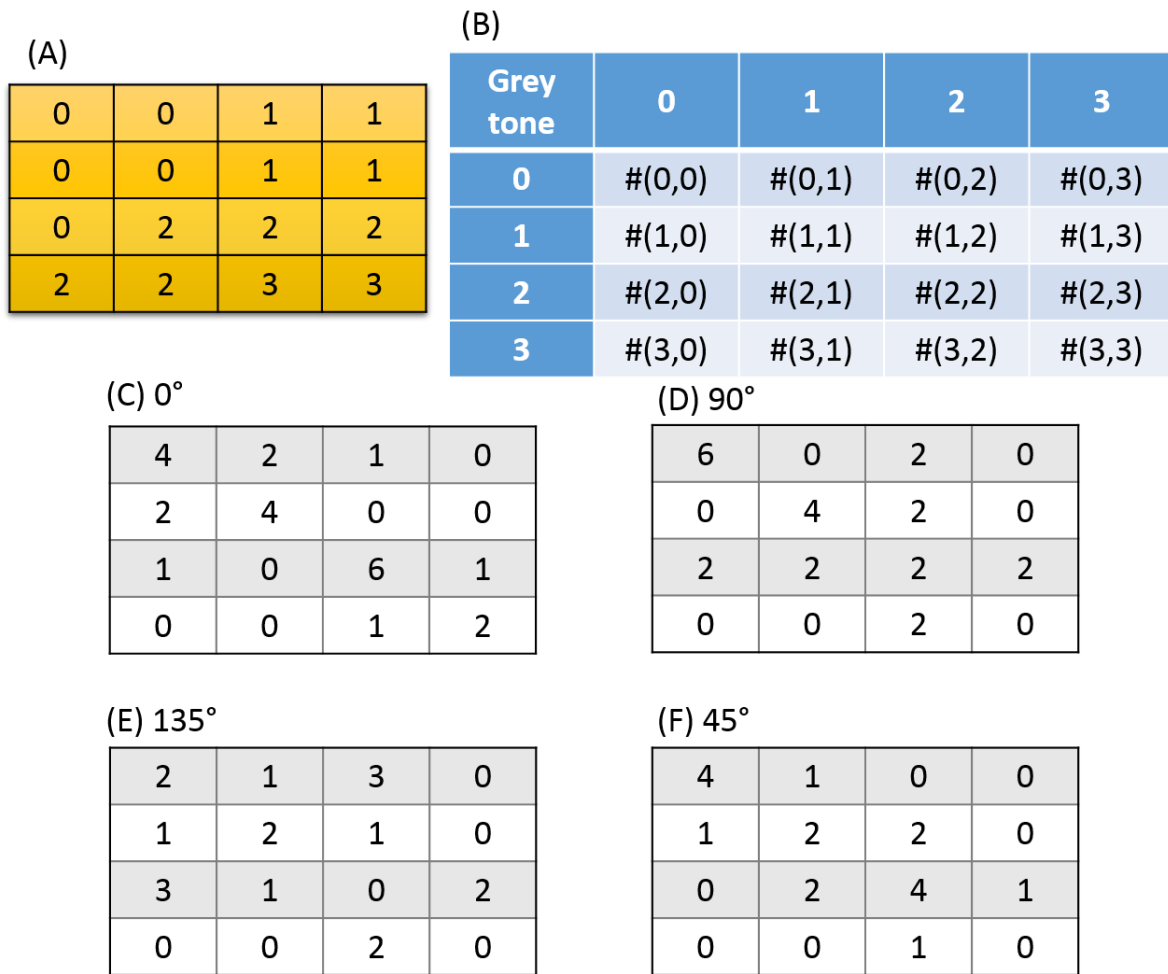


Figure 4.2 - One example of the GLCM computation. (a) 4 x 4 image with four gray-tone values (0, 1, 2 and 3). (b) General form a GLCM for any image with four gray-tone values (0, 1, 2 and 3). #(i,j) stands for the number of times gray tones i and j have been neighbors (c)-(f) GLCM for different angles and distance of 1 pixel.

In this Thesis, following the work from Goussies et al. (2010) and Braga et al. (2013), the GLCM were computed using distance of one pixel ($d = 1$) and direction of 45° (0° is the right side of the image and the angle increases counterclockwise) with four gray-tones (therefore the GLCM has 4x4 elements). Some examples of the GLCM for an arbitrary set of three CMEs and corresponding background analyzed in this Thesis for COR2B are shown in Table 4.1, Table 4.2 and Table 4.3. Each element of the tables corresponds to one element of the GLCM (as illustrated in Figure 4.2), except for one difference: $P_{i,j}$ is normalized by the sum of the matrix elements. More specifically, these tables show the average value plus or minus its standard

deviation calculated for the three GLCM available in each case. Results for COR2A were very similar and are omitted here.

Table 4.1 - The average plus or minus one standard deviation GLCM for a CME in their first frame. These values were calculated using COR2B for the CMEs observed on 2010/04/03, 2010/04/08 and 2010/07/30.

0.0103±0.0157	0.0189±0.0267	0.0000±0.0000	0.0000±0.0000
0.0189±0.0267	0.6191±0.2661	0.0152±0.0130	0.0001±0.0001
0.0000±0.0000	0.0152±0.0130	0.1752±0.1546	0.0101±0.0114
0.0000±0.0000	0.0001±0.0001	0.0101±0.0114	0.1069±0.1464

Table 4.2 - The average plus or minus standard deviation GLCM for a CME in the last frame calculated using COR2B for the CME observed on 2010/04/03, 2010/04/08 and 2010/07/30. This depends of the expansion parameter used and it will be exactly the same GLCM of first frame when Q=0 (no expansion, see explanation in Section 4.5).

0.0338±0.0344	0.0387±0.0297	0.0000±0.0000	0.0000±0.0000
0.0387±0.0297	0.7461±0.1155	0.0111±0.0117	0.0001±0.0001
0.0000±0.0000	0.0111±0.0117	0.0939±0.1229	0.0031±0.0041
0.0000±0.0000	0.0001±0.0001	0.0031±0.0041	0.0198±0.0243

Table 4.3 - The average GLCM for the background using COR2B for the CME observed on 2010/04/03, 2010/04/08 and 2010/07/30.

0.3125±0.0236	0.2016±0.0080	0.0000±0.0000	0.0000±0.0000
0.2016±0.0080	0.2840±0.0115	0.0001±0.0001	0.0001±0.0001
0.0000±0.0000	0.0001±0.0001	0.0000±0.0000	0.0000±0.0000
0.0000±0.0000	0.0001±0.0001	0.0000±0.0000	0.0000±0.0000

One can notice that there is a trend that the GLCM of the background to have higher elements with $i < 2$ and $j < 2$, in other words, with GLCM elements related to the lower gray-tones. The remaining terms are negligible. For the CME, the diagonal terms are higher, especially $P_{1,1}$ and $P_{2,2}$.

A GLCM of a CME depends on its brightness. For the CME on 2010/07/30, which has low brightness, the terms $P_{1,1}$ and $P_{3,3}$ are smaller than 0.03 for both COR2A and COR2B; the term $P_{2,2} \sim 0.9$. The CME on 2010/04/03, on the other hand, is much brighter and the terms $P_{1,1}$ and

$P_{3,3}$ are two times higher and $P_{2,2} < 0.8$. In spite of the fact that the 3 CMEs tested here CMEs have significant differences, they all have $P_{1,1} + P_{2,2} + P_{3,3} + P_{4,4} > 0.9$.

4.4 Detection of the CME: segmenting it from the background

Goussies et al. (2010) found that the GLCM for the CME features does not follow exactly a known probability density function and introduced a χ^2 statistical test to overcome the absence of a known probability density function. The test evaluates up to a certain level of significance whether the GLCM of a given pixel resembles that of the background or the foreground (CME).

To create the foreground model, the user must identify a region of interest (ROI), i. e., an approximate area comprising the CME feature, in the image where the event is first seen (Figure 4.3). Similarly, a region excluding the CME feature must be selected to identify the background (Figure 4.4). This procedure needs to be done by the user manually for each event of interest. The regions are defined by delineating with the computer mouse a contour around at least a part of the feature. The total area does not need to be selected.

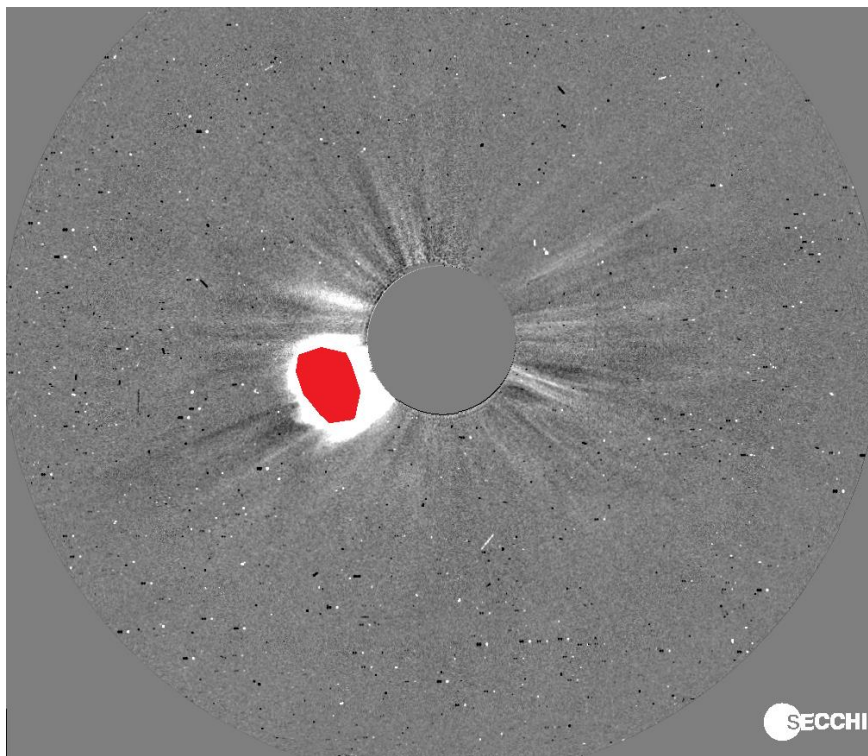


Figure 4.3 - Example of a user-selected area (in red) for the CME on 2010/04/03 in the COR2B FOV. The image shown here is the difference of the first two images where the CME is visible in the FOV.

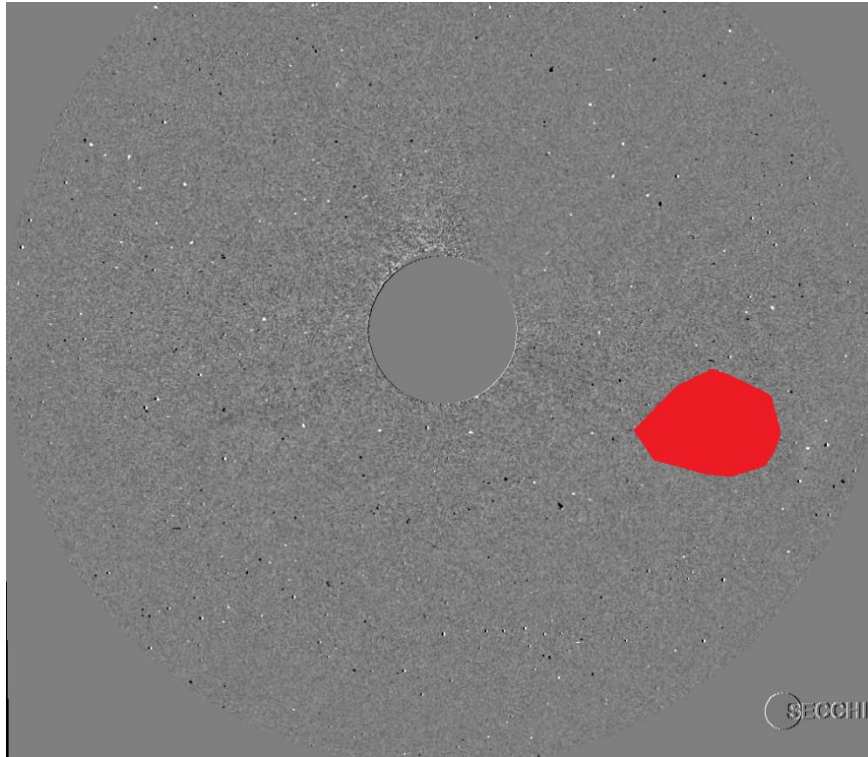


Figure 4.4 - Example of the user-selected area (red region) for the background associated to the CME on 2010/04/03 in the COR2B FOV. The image shown here is the difference of the two last images before the CME enters the FOV.

Note that the ROI can be arbitrarily selected as long as it is within the feature, i. e., it does not have to follow exactly the boundaries of the event. This presents an advantage with respect to human-based detection: despite the subjectivity involved in the determination of the initial boundaries, the CME feature in this first image is uniquely segmented based upon its texture characteristics.

4.5 Tracking the CME

Once the CME feature is segmented in the first frame, the region found is used as an initial guess for the following frame, and the detection procedure repeated. However, as mentioned in Goussies et al. (2010), some events, especially those that start with large speeds, do not keep a similar texture as they evolve, especially during their early development. To take into account the texture variability, the GLCM of the foreground is reevaluated in a region that corresponds to an isotropically expanded version of the region found in the previous frame, and only after this, the procedure is repeated. The degree of expansion is user-controlled. Briefly, if we call Z

the number of pixels comprising the region defined in frame $i - 1$, the extent of the expansion is calculated as Z/Q in each direction perpendicular to the boundary of the feature segmented, Q being a heuristically user-defined parameter between 1 and 60 ($Q = 0$ implies no expansion).

4.6 Deriving the radial speed of a CME in a coronagraphic image

Once we tracked a CME using CORSET, we have a region of the CME segmented for each frame on a given period that was manually selected. In principle, all frames where the CME is simultaneously present in the COR2A and COR2B FOV are used. From our experience with CORSET, we did not include in the analysis the frames in that the CME front already reached the outer limit of the coronagraph FOV. In some cases, the CME brightness is very low close to the outer boundary of the coronagraph and the result derived from CORSET is not consistent with the CME definition or only part of it is selected. These frames are removed from the analysis. Once the set of frames is defined, we start the calculation of the radial speed in each coronagraph FOV. Notice that the speed derived here is done independently in COR2A and COR2B data. Both speeds are not the tridimensional speed that is the main objective of this Thesis; they are only the projection of the speed in the plane-of-the sky.

For each frame, the distance to the center of the Sun's disk of each position angle is calculated. A height-time (HT) profile is then obtained for each angle. A linear speed is finally computed as the slope of a first order fit to the data points in the HT profiles. The result is a speed profile as a function of angle. Two examples of such plots are shown in Figure 4.5 and Figure 4.6.

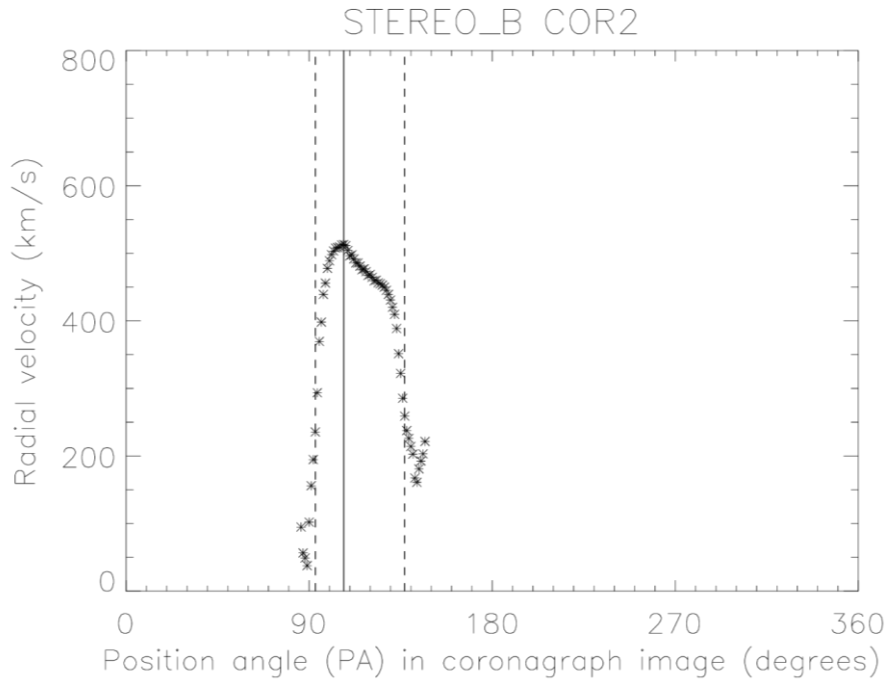


Figure 4.5 - One example of the radial speed as a function of the angle (degrees, after rotation for the stereo baseline). The CME shown here was observed on 2011/09/05 by COR2B and it was tracked from 03:24UT to 05:39 UT. The vertical dashed lines indicate the lateral boundaries of this region and the continuous line corresponds to the position angle of maximum radial speed.

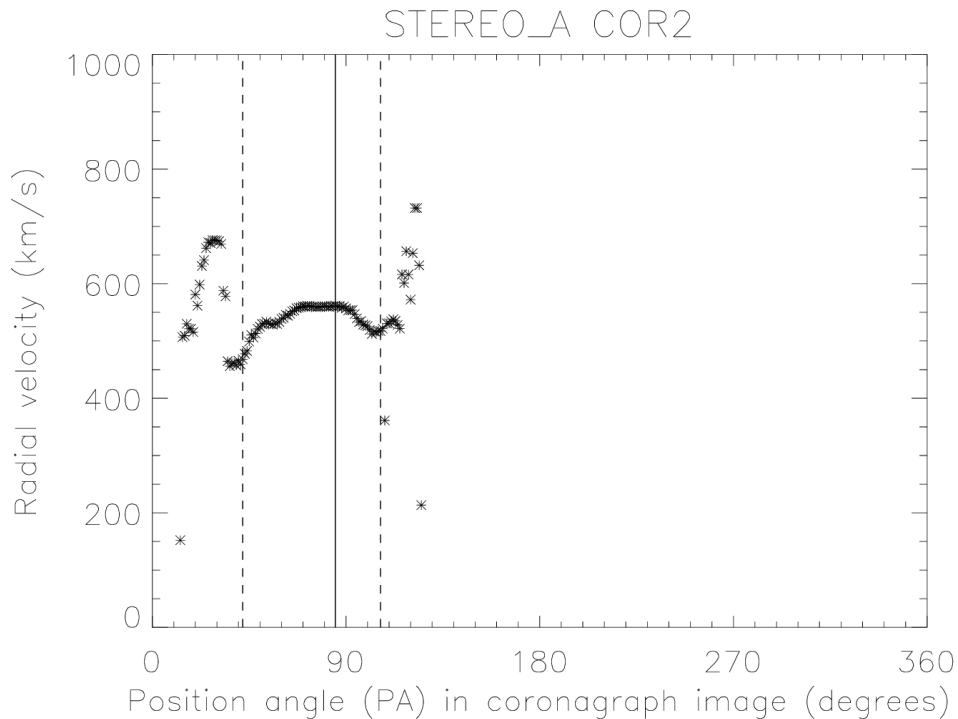


Figure 4.6 - Similar to Figure 4.5 but for a CME tracked from 2011/09/13 23:54 UT to 2011/09/14 02:54 UT by COR2A. The vertical dashed lines indicate the lateral boundaries of this region. For many events studied in this Thesis in COR2A FOV (the list of events is detailed in Chapter 5), it is common to observe peaks (i.e. relative high speeds) close to the angular limits of the CME (this is absent in Figure 4.5 but very clear in Figure 4.6). We manually inspected these measurements and confirmed that the peaks are spurious. Many velocity profiles also show steep increases in one lateral side and steep decreases on the other, as in Figure 4.5. The velocities in this range of the profile are also spurious. For that reason, the angular extent of the events was manually validated and the region considered appropriate was selected while the spurious parts were ignored. The vertical dashed lines in Figure 4.5 and Figure 4.6 indicate the lateral boundaries of this region. Within the appropriate range, the distribution of the radial speeds generally is smooth and frequently follows a parabolic-like curve. All the trends commented here were identified previously using data from LASCO-C3 FOV both in CORSET and the in CACTus catalog (BRAGA et al., 2013).

Once these steps are done, the maximum linear speed is selected among the manually validated region. In Figure 4.5 and Figure 4.6, it is indicated by the vertical continuous line. Notice that the maximum speed is not necessarily at the center of the CME angular range.

Since CORSET was never used before to derive the speed in COR2, the results we derived by this methodology are compared with previous works using different methodologies in order to check possible systematic errors. The results are shown in Chapter 6.

4.7 Starting stereoscopy: a tridimensional reconstruction using the epipolar constraint

Up to now the methodology described is used to derive the CME properties projected on a given coronagraph FOV. From this section on, the analysis described is about the tridimensional reconstruction (stereoscopy).

Stereoscopy consists on the reconstruction of surfaces starting from a pair of images from the same object but taken from different viewpoints. Each pair of images is called stereoimage. As human beings, we are used to see a 3D environment from the images formed in the focal plane of the eyes. We have a sense of deepness calibrated since the childhood and, when we see the two projections of an image in our eyes, we associate it immediately to the 3D object that we have in mind. Thus, the simple observation of two-dimensional projections of one tridimensional object is not enough. It is necessary to include additional information in order to reconstruct one object from its two projections (INHESTER, 2006).

In this Thesis, we take advantage of a special geometric constraint used in stereoscopy called epipolar constraint (illustrated in Figure 4.7). The line connecting the viewpoints is called stereo base line, which subtends the stereo base angle between the two main view directions. The position of the observers and any point to be studied in three dimensions define a plane, which is called epipolar plane. Since we have many points to be reconstructed we need to define a set of epipolar planes (INHESTER, 2006).

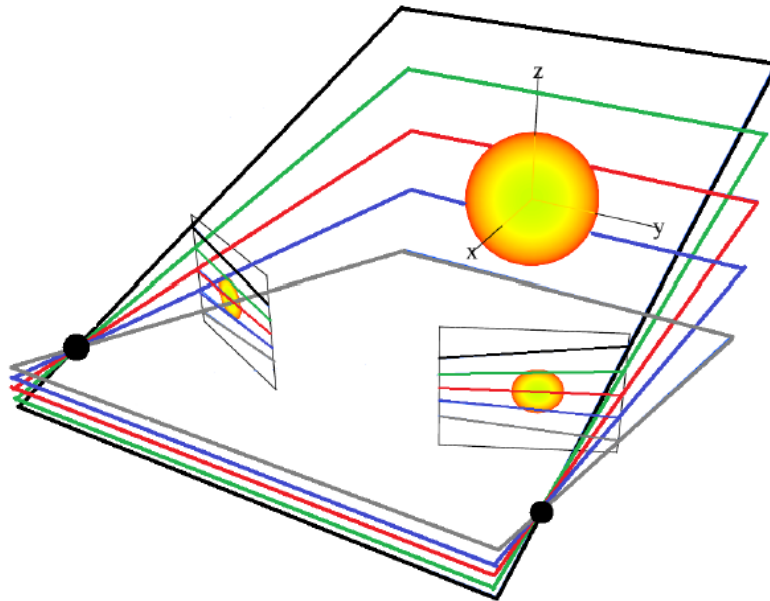


Figure 4.7 - One example of an epipolar geometry used to do stereoscopy of the Sun (represented in yellow). The two observers are represented by two black dots. Between the Sun and the observers, a sample image taken by each one is shown. Each epipolar plane is represented by a rectangle in a different color. Here only five epipolar planes are shown, but as many as desired can be constructed. The intersection of these planes with the images forms the epipolar lines.
 Source: Inhester (2006).

The intersection of any epipolar plane with the observer's image defines a line. Any of these lines is called an epipolar line. It is important to notice that the epipolar images depend on the position of both observers; any change in the position of one observer requires a new determination of the epipolar lines for all observers (INHESTER, 2006).

In order to make the reconstruction easier, it is desirable to have the epipolar lines mapped into horizontal lines. This corresponds to the case when both spacecraft would have their optical axes directed parallel to each other. When this is not the case, the images are processed in such a way that epipolar lines become parallel to each other and preferably horizontal, as illustrated in Figure 4.8. This process is called rectification.

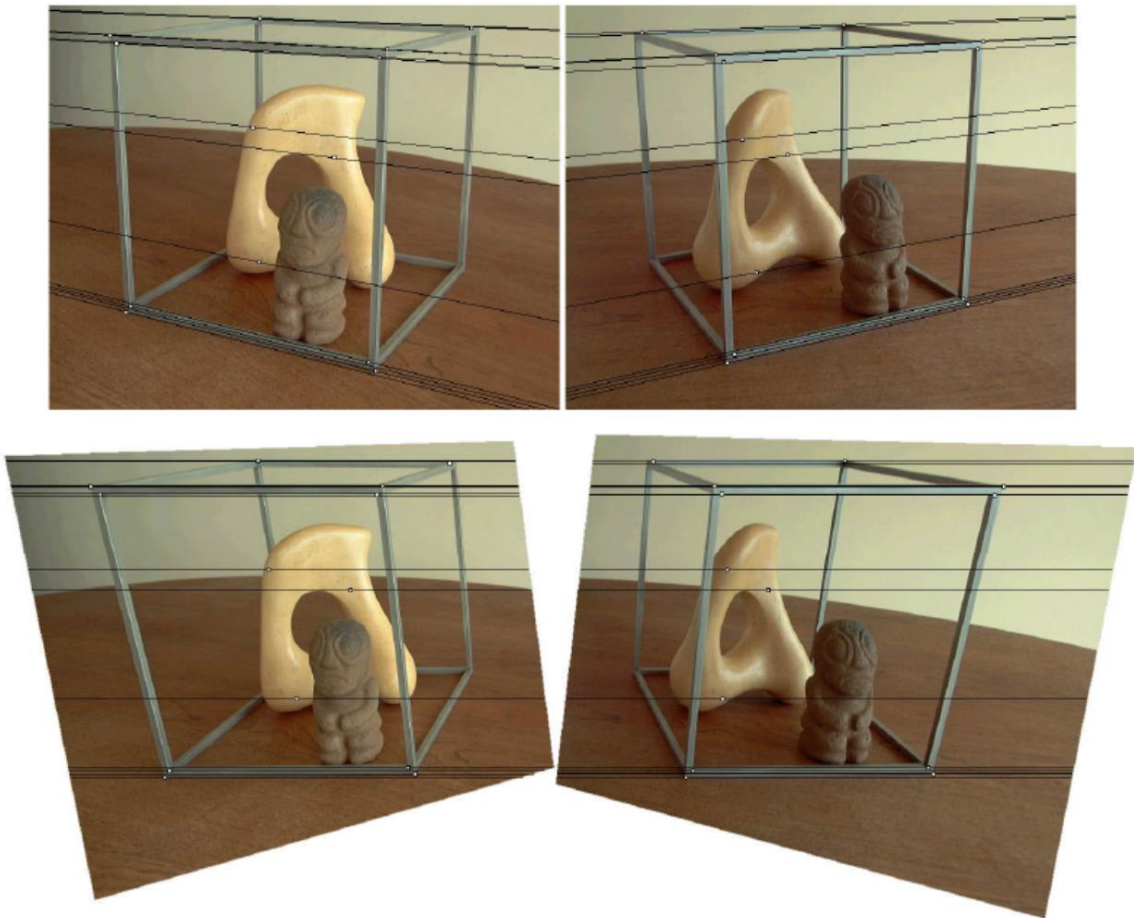


Figure 4.8 - An example of a pair of stereoimages before (upper row) and after (lower row) the rectification process. Some sample epipolar lines are shown in each image (black lines). Notice that the epipolar lines became parallel after the rectification. Source: Loop & Zhang (1999).

The fourth step consists in correctly matching the projections of a given object in one image in each of the stereoimages. Two hypotheses are implicit here: a) all the points to be reconstructed must be visible in both images and b) a given structure in space is seen in a similar way in both images (TRUCCO; VERRI, 1998).

Matching a given point in space over one epipolar line in both stereoimages is not trivial and it needs specific methodologies, depending how the object to be reconstructed is. Usually, the matching process is done manually by identifying corresponding points in a pair of stereoimages. The pair of points that correspond to the selection of the same feature in both stereoimages is called tie-point. Thanks to the epipolar constraint, the tie-points must lie in the same epipolar line and, therefore, the problem of matching is reduced from two-dimensions to one dimension.

4.8 One tool to reconstruct CMEs front

The CME front could be reconstructed using the forward fitting method such as the CGS method. Since we are using CORSET, that does not have any geometric constraint, it is desirable to use a reconstruction method that does not rely on such restriction. For this reason, we do not use the CGS model from Thernisien et al. (2009) in this work. Instead, we use the “Sunloop”, an application to perform the tie-pointing and triangulation using images from SECCHI developed by Liewer et al. (2009).

First, the images are preprocessed and slowly varying (monthly minimum) backgrounds are subtracted. This removes the contribution of the F-corona. The images are then scaled and corrected for the different distances of the two spacecraft from the Sun to make the plate scales identical. The difference in distance is about 10% in the later phase of STEREO mission. During some periods, especially in the first years of the mission, the difference is very small but it is corrected anyway. Using the epipolar constraint, the images are rectified in such a way that the horizontal lines in the images correspond to epipolar lines. Tie-points are then placed in each image using a cursor. Each position on an image defines a camera ray; the rays defined by the tie-points lie in an epipolar plane and, using triangulation, the location of the tie-pointed feature is the intersection of the two rays (LIEWER et al., 2011). One example of the application of the Sunloop is shown in Figure 4.9.

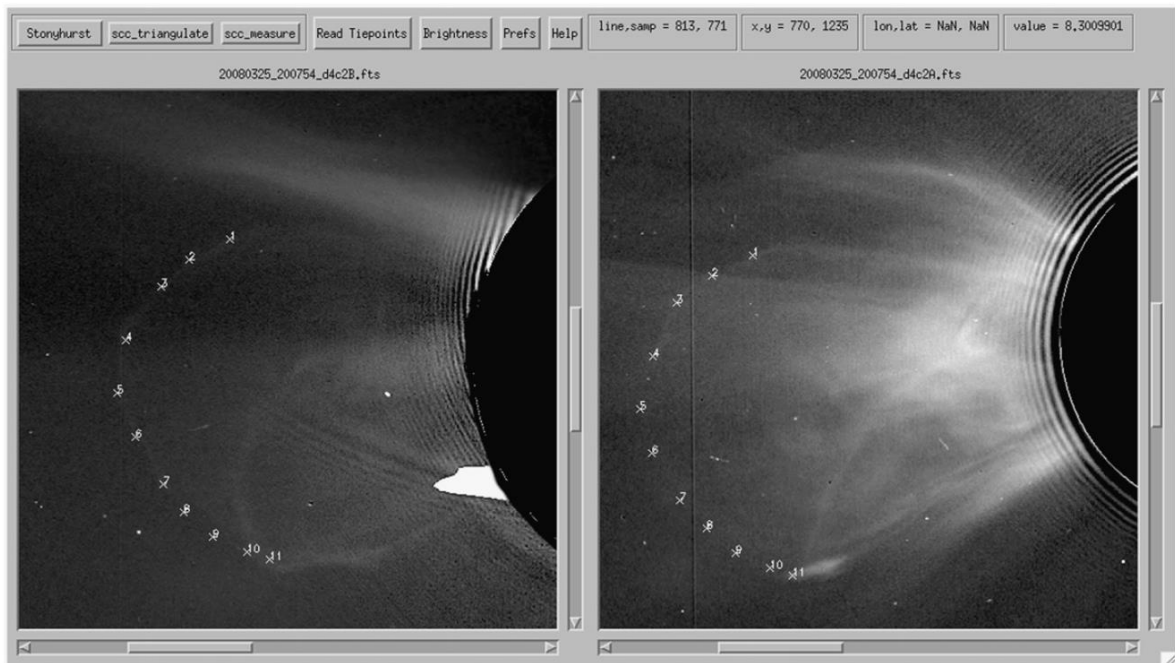


Figure 4.9 - The graphical user interface of the Sunloop application tie-pointing tool on the leading edge of a sample CME observed on 2008/03/25. The tie-points locations are represented by the white crosses. The COR2B (A) image is on the left (right). Sunloop is available as part of the Solar Soft SECCHI software library (e.g., <http://www.lmsal.com/solarsoft/>).

Source: Liewer et al. (2011).

After the tie-pointing is completed for all images where the CME is visible in the FOV, the results are shown in a visualization tool called Animator. The points obtained by triangulation are connected with straight-line segments to visualize the tridimensional reconstruction of the CME front (LIEWER et al., 2011). One example of such result is shown in Figure 4.10.

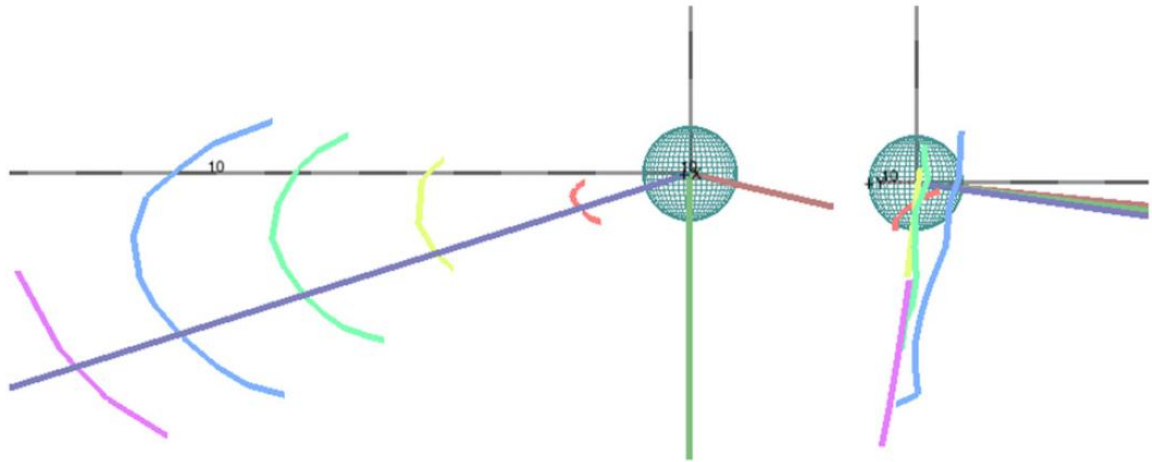


Figure 4.10 - Tridimensional reconstruction of the leading edge of the CME observed in 2008/03/25 at five consecutive times shown in relation to the Sun (3D globe). The third reconstruction (represented in green) refers to the tie-points shown in Figure 4.9. The three colored straight lines (here, and in other 3D reconstruction figures in this Thesis) show the directions to STEREO B (violet), Earth (green), and STEREO A (red). Two viewpoints are shown, the left one is along the Sun-Earth line and the right one is along the propagation longitude.

Source: Liewer et al. (2011).

From the set of leading edge reconstructions, the trajectory is determined by selecting, at each time, the point on the reconstructed edge furthest from the Sun (the apex of the front). The trajectory propagation direction is the average over the directions from the Sun to the apex for each time; the velocity is obtained from a linear fit to the true (3D) distance versus time data.

4.9 Combining CORSET and Sunloop

We introduce here a new methodology that combines CORSET and Sunloop. While CORSET is useful to define the boundary of the CME, the Sunloop method allows an interactive way to perform the triangulation and tie-pointing.

Sunloop could be used without any input from CORSET, using a set of tie-points defined by eye. An epipolar line constrains the tie-point in one dimension of the image. Hence, once a tie-point is defined in a given view, the corresponding tie-point in the other view is free (along the epipolar line) and needs to be defined by the user. The exactly same feature must be selected in each image of the pair by visual inspection. By doing this, the result will be subjective and will depend on user decision. In this Thesis, we aim to define a more objective way to define the CME boundaries and the tie-points that does not depend on visual inspection. Firstly, we

included only the boundary found by CORSET in Sunloop and defined the tie points according to the boundary shown. Although there are some minor differences in the results according to the pixel selected by the user, this approach is independent from user decision (this topic is explored in Section 4.10). It is, however, very time consuming and tedious. Finally, we constructed an algorithm to create the tie-points automatically using the contours for each stereoimage.

We suppose that each tie-point of the CME front contour (as defined by CORSET) in a given view corresponds to a tie-point in the corresponding image pair, which is defined by the intersection of the CME front contour in this image pair and the corresponding epipolar line (Figure 4.11).

Typically, the algorithm defines automatically from 50 to 200 tie-points in each COR2 image (2048 x 2048 pixels). We observed that the tie-points close to the lateral side of the CME produced inconsistent results, probably because they do not point to the same CME feature. For this reason, we arbitrarily choose an angular range where only the front of the CME is located and we ignore the points of the contour of the CME outside this region.

Once the set of matching tie-points pairs are defined in this automatic way, the Sunloop code calls the SolarSoft routine *ssc_triangulate* to perform the triangulation. Hereafter, we will call this methodology CORSET3D since it depends on the results from CORSET and it allows tridimensional reconstruction of the CME front. One example of the application of CORSET3D is shown in Figure 4.12.

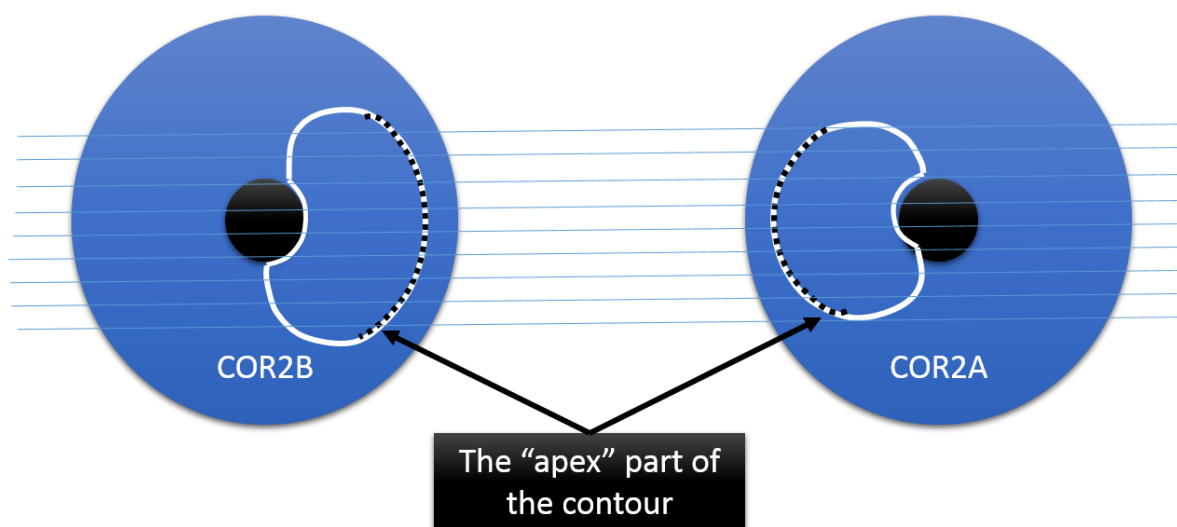


Figure 4.11 - A diagram illustrating the selection of the apex of the CME (dashed black line) from the contours provided by CORSET (white contour) in each coronagraph image. The blue horizontal lines represent the epipolar lines.

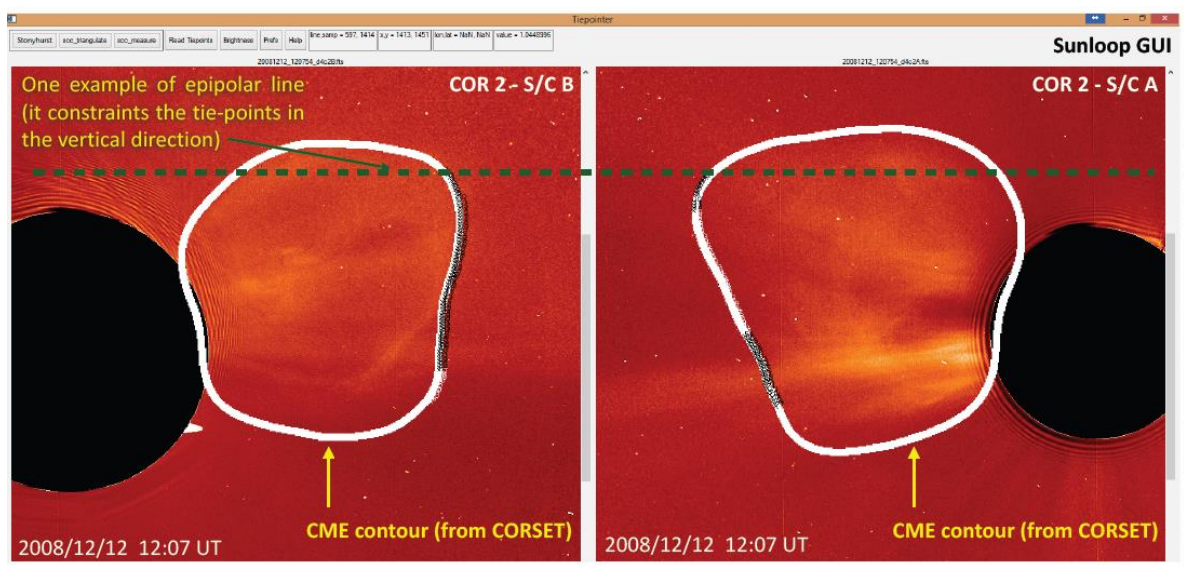


Figure 4.12 - A screen dump of the “Sunloop/Tiepointer” tool showing the placement of automatic tie-points (black and white crosses on the CME leading edge contour). The white line shows the contour previously derived using CORSET (we modified the Sunloop code to allow the inclusion of the contours and the automatic determination of the tie-points to be used for 3D reconstruction).

The diagram in Figure 4.13 wraps up the main steps that need to be done when using CORSET3D. The steps indicated in gray are performed independently on images from each coronagraph and they are based on CORSET (BRAGA et al., 2013). Those indicated in orange require two viewpoints and are based on the Sunloop method (LIEWER et al., 2011).

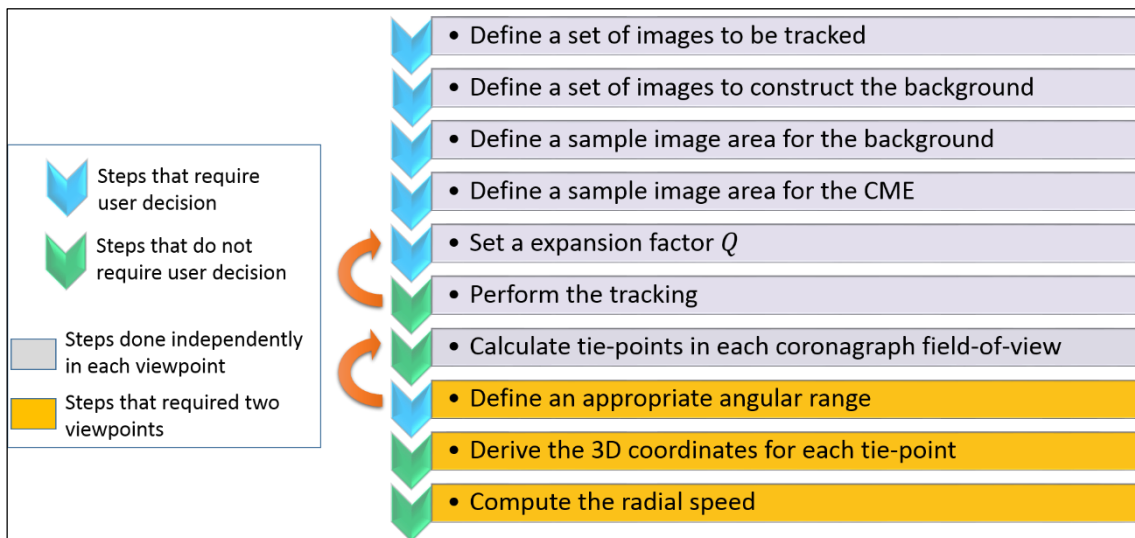


Figure 4.13 - Diagram showing the main steps that need to be done when working with CORSET3D.

4.10 Are the results similar using manual and automatic tie-points?

In this section we compare the results derived using CORSET3D with the use of Sunloop with tie-points placed manually. The contour derived by CORSET was placed over each coronagraph image inside the Sunloop Graphical User Interface (GUI) but the tie-points were created manually by using a cursor. The leading edge derived in each case is shown in Figure 4.14.

The differences found for a set of three CMEs tracked in shown is Table 4.4. The difference is very small for the speed and can be considered negligible. For the direction, the difference is up to 5 degrees.

Table 4.4 - Comparison of the manual and automatic tie-points.

Parameter	Method	2008/12/12	2009/10/27	2011/09/14
Speed	Automatic	341 km/s	173 km/s	525
	Manual	348 km/s	178 km/s	534
	Difference	7 km/s	5 km/s	9 km/s
Stonyhurst Longitude	Automatic	2°	3°	37°
	Manual	3°	4°	32°
	Difference	1°	1°	5°
Stonyhurst Latitude	Automatic	5°	7°	15°
	Manual	7°	6°	19°
	Difference	2°	1°	4°

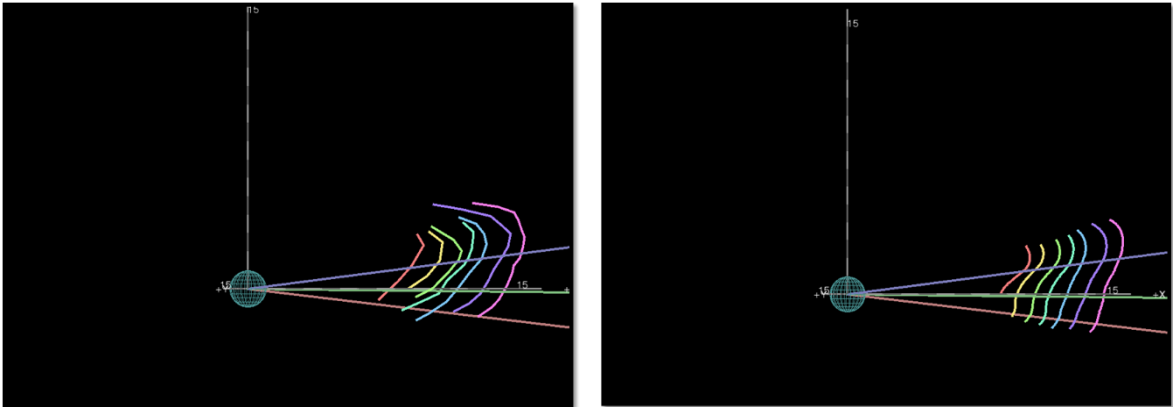


Figure 4.14 - One example of the difference of the reconstruction of the “apex” of the CME with the automatic tie-points derived using the CORSET contours in the Sunloop tool (right) and manually placing the tie-points in the Sunloop tool using the contour from CORSET only as a reference (left). Each line in a different color shows one of seven consecutive frames of a CME observed in 2008/12/12 between 10:07 and 13:07 UT. The Sun is represented by the 3D globe. The three colored straight lines (here, and in other 3D reconstruction figures) show the directions to STEREO B (violet), Earth (green), and STEREO A (red). This picture was made using the animator tool that is part of Sunloop application.

4.11 Deriving the radial speed of the CME as a function of angle

For each time that a coronagraph image is available (typically two or three times every hour) during the tracking time of a given CME ($t_1, \dots, t_i, \dots, t_n$), we have a couple of tie-points defined (generally from 10 to 50, depending on many factors such as the size of the CME and the distance from the Sun). For these points, we have the Cartesian and polar coordinates.

First, we find a range of latitudinal ($\theta_1, \dots, \theta_j, \dots, \theta_o$) and longitudinal ($\phi_1, \dots, \phi_k, \dots, \phi_p$) angles where all the frames of the CMEs have at least one tie-point. Inside this range, we define a radial line for every step of one degree of latitude j and longitude k . For each radial direction (θ_j, ϕ_k) for each frame t_i , we find the closest tie-point to the line and we define a new point with the same radial distance of the tie-point and the latitude and longitude from the radial direction. If the distance between the new point and the tie-point is too big (higher than an arbitrary limit of 300,000 km) we ignore this point. Radial distances defined in this way are a function of time and direction and will be represented by $r(t_i, \theta_j, \phi_k)$.

Using the new points created here, we calculate the instant speed for all consecutive frames for any possible radial direction using the following expression:

$$v_r(t_{i+1}, \theta_j, \phi_k) = \frac{r(t_{i+1}, \theta_j, \phi_k) - r(t_i, \theta_j, \phi_k)}{t_{i+1} - t_i} \quad \begin{array}{l} i = 2, \dots, n \\ j = 1, \dots, o. \\ k = 1, \dots, p \end{array} \quad (4.1)$$

We also calculated the speed averaged on time for each direction:

$$\bar{v}_r(\theta_j, \phi_k) = \frac{r(t_n, \theta_j, \phi_k) - r(t_1, \theta_j, \phi_k)}{t_n - t_1} \quad \begin{array}{l} j = 1, \dots, o \\ k = 1, \dots, p \end{array} \quad (4.2)$$

We also compute the group speed v_g of the CME front at each time t_i with $i > 1$ by the expression:

$$v_g(t_{i+1}) = \frac{1}{(o+1)(p+1)} \sum_{j=1}^o \sum_{k=1}^p v_r(t_{i+1}, \theta_j, \phi_k) \quad (4.3)$$

4.12 The error estimative

When every tie-point is determined in each image, due to the finite resolution of the image, there is an error in each image. The error on the resulting tridimensional point constructed from this tie-point is $ds/\sin(\gamma/2)$ where γ is the separation angle between the two STEREO spacecraft and ds is the error on each image along the epipolar line (MIERLA et al., 2010). When $\gamma = 90^\circ$ (January 2009), the error will be about $1.41ds$ and when $\gamma = 150^\circ$ (August 2010), it is $2ds$.

Other source of error that is uniquely present in the tie-pointing and triangulation is due to different appearing leading edges (DALE) effect. It comes from the fact that different coronagraphs may not see exactly the same leading edge of the CME. In this section, we apply a simple model to estimate the error due to the DALE effect developed by Liewer et al. (2011). The assumptions of the model are:

- The CME follows a model of spherical shell with radius a and with its sphere center distant R from the Sun, see Figure 4.15. The center of this CME forms an angle β with the Sun-Earth line;
- The CME is located in the ecliptic plane and the longitude of the propagation angle is close to the Sun-Earth line;

- Both STEREO spacecraft are located one Astronomical Unit distant from the Sun and at the same angle θ from the Sun-Earth line but at different sides. We further assume that $\beta < \theta$;
- The brightest features in the coronagraph will result from lines-of-sight with the longest path length through the CME. Since the tangent lines have the largest integrated electron density and thus higher intensity of Thomson scattered light, they are observed by the coronagraph;
- The coronagraphs can be interpreted as cameras at infinity, the camera rays are parallel to the spacecraft direction (represented by the dashed lines in Figure 4.15). This assumption is reasonable because when a CME is in the coronagraph FOV, the distance from the Sun is a few solar radii and the distance to the spacecraft is much higher, at about 200 solar radii.

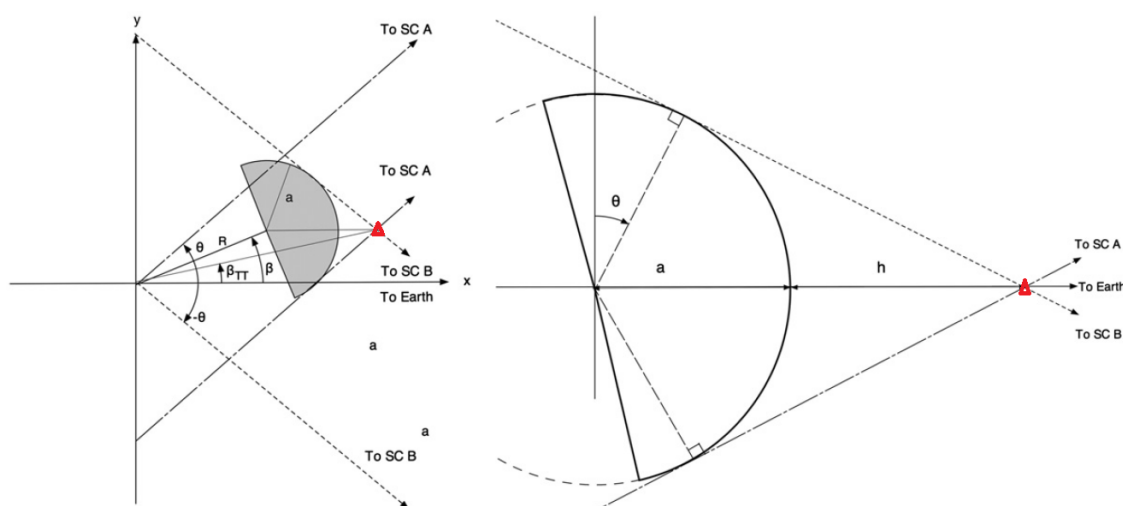


Figure 4.15 - A simple model of a CME with spherical front (gray region) propagating approximately toward the Earth in the ecliptic plane with an angle β with respect to the Sun-Earth line. The STEREO A and B are supposed to be separated by the same angle θ . The dashed lines indicates the camera rays that are tangent to the CME model and, therefore, produce the brightest feature in the coronagraph FOV. Due to the DALE effect, the location calculated is the indicated by the red circle instead of the center of the CME. The illustration on the right details the geometry from the figure on the left.

Source: Liewer et al. (2011).

According to this model, the resulting position of the CME front “apex” found by the triangulation and tie-pointing is represented in Figure 4.15 by the red triangle. Notice that this point is more distant from the Sun than the actual position of the “apex”.

According to the model from Liewer et al. (2011), when $\beta < \theta$ the angle calculated by the triangulated and tie-pointing β_{tt} is given by:

$$\tan \beta_{TT} = \frac{R \sin \beta}{R \cos \beta + a / \sin \theta} \quad (4.4)$$

The error of the propagation longitude is thus defined as $\Delta\beta = \beta_{TT} - \beta$ and it depends on the geometry of the CME (a, R), the separation angle between the STEREO spacecraft (θ) and the propagation direction of the CME (β).

In the present Thesis, the period of analysis ranges from December 2008 to December 2011. The separation angle of the STEREO spacecraft increases as time passes: it was 40° at the beginning and 105° at the end. The results from the application of Eq. 4.4 for $\beta = 10^\circ$ and $\beta = 20^\circ$ are shown in Figure 4.16 (supposing $a/R = 0.5$) and Figure 4.17 (supposing $a/R = 1.0$). According to these calculations, for a CME ejected approximately aligned with the Earth-Sun line, the systematic error is such that the longitude determined by triangulation and tie-pointing is smaller (close to the Sun-Earth line) than the true propagation longitude. Moreover, the error will be minimum when the CME is propagating close to the Sun-Earth line and will be maximum when it is directed toward one of the spacecraft.

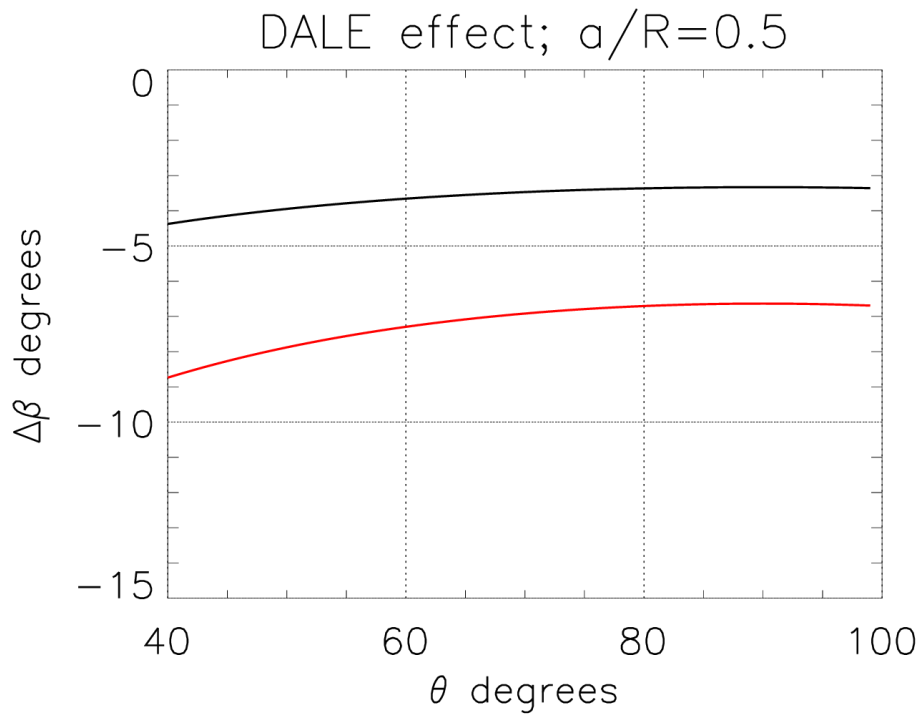


Figure 4.16 - The estimative of the error due to the DALE effect for the longitudinal propagation angle for $\beta = 10^\circ$ (black curve) and $\beta = 20^\circ$ (red curve). $\Delta\beta < 0$ indicates that the longitude estimated is smaller than the actual longitude. In this Figure we assume $a/R = 0.5$.

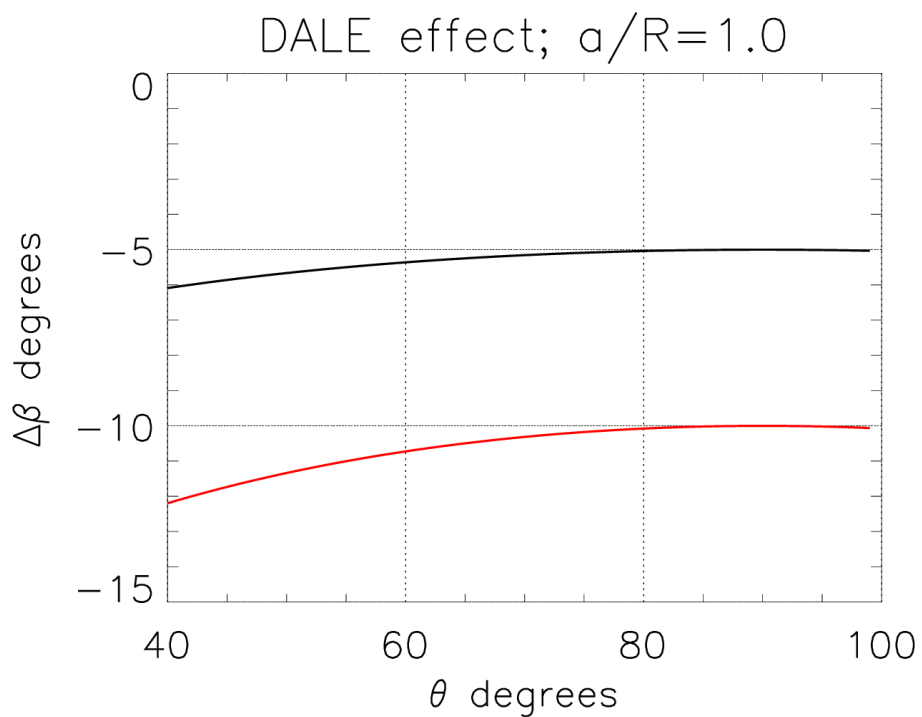


Figure 4.17 - The same than Figure 4.16 but assuming $a/R = 1.0$.

The DALE effect error was also computed for the velocity. As shown in Liewer et al. (2011), if a CME is propagating close to the Earth-Sun line, the fractional error in the velocity is given by:

$$\frac{\Delta v}{v} = \sqrt{\frac{1 + \frac{2a \cos \beta}{R \sin \theta} + \frac{a^2}{(R \sin \theta)^2}}{1 + a/R}} - 1. \quad (4.5)$$

We calculated the fractional error of the speed using Eq. 4.5 for the specific context of this Thesis: CME ejected approximately toward the Earth ($\beta = 0^\circ, \beta = 10^\circ, \beta = 20^\circ$) and $40^\circ < \theta < 100^\circ$. The results are shown in Figure 4.18 ($a/R = 0.5$) and Figure 4.19 ($a/R = 1$). Notice from both Figures that the speed derived tends to be higher than the actual speed. The error is highly dependent of the separation angle between the STEREO spacecraft and it is higher at the beginning of the mission and negligible when the separation angle is close to 90° .

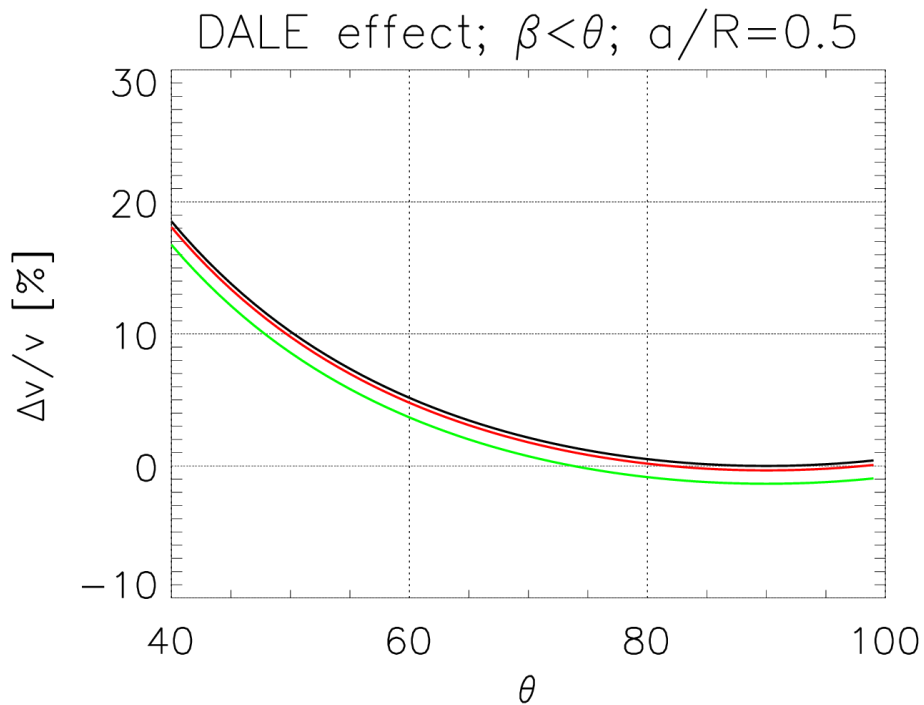


Figure 4.18 - The fractional error on the velocity of the CME due to the DALE effect supposing $a/R = 0.5$ and $\beta = 0^\circ$ (black), $\beta = 10^\circ$ (red) and $\beta = 20^\circ$ (green).

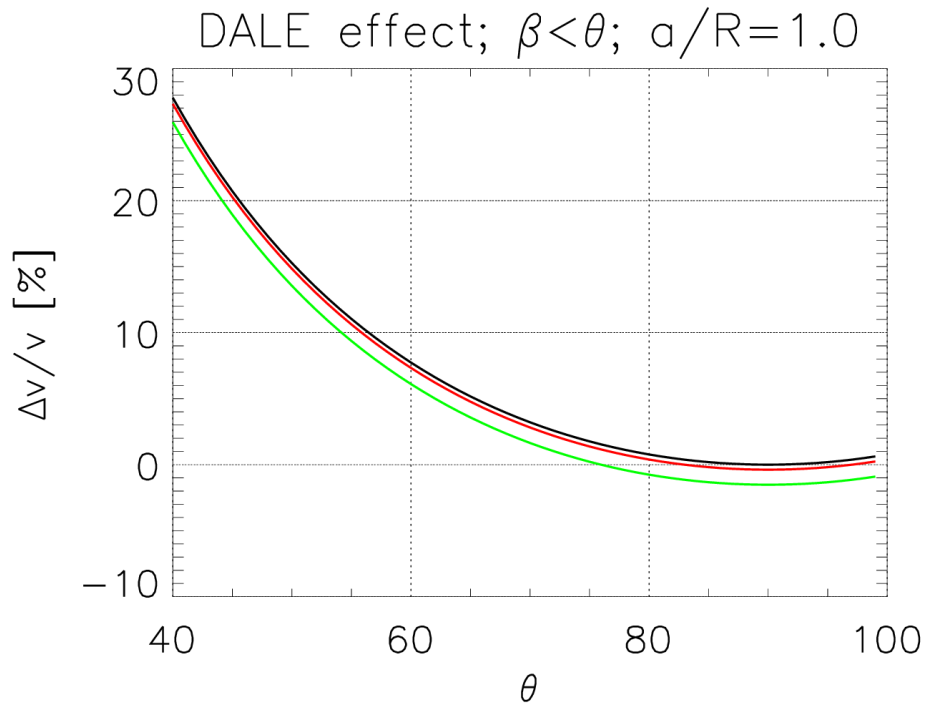


Figure 4.19 - The fractional error on the velocity of the CME due to the DALE effect supposing $a/R = 1.0$ and $\beta = 0^\circ$ (black), $\beta = 10^\circ$ (red) and $\beta = 20^\circ$ (blue).

4.13 Coordinates systems used in the solar corona

The coordinate system used in the interplanetary medium close to the Earth is the GSE, already introduced in Section 3.6. This coordinate system is geocentric, i. e., its origin is at the Earth and, therefore, it is not suitable when working with the solar corona.

Two coordinate systems are frequently used when working with the solar atmosphere. One is the Heliocentric Earth Equatorial (HEEQ) whose “x” is the intersection between solar equator and solar central meridian as seen from the Earth and “z” toward the North Pole of the solar rotation axis (HAPGOOD, 1992). The coordinates resulting from the conversion of the HEEQ coordinate system into polar coordinates is frequently called Stonyhurst heliographic coordinates (THOMPSON, 2006). The angles θ and ϕ are given in degrees with θ increasing toward Solar North and ϕ increasing toward the West limb of the Sun (Figure 4.20)

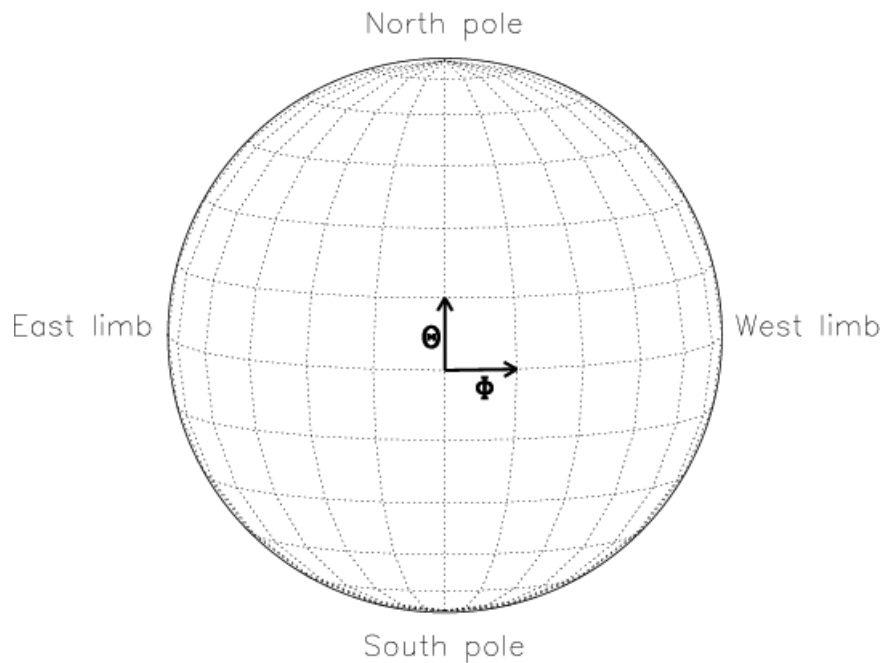


Figure 4.20 - A diagram of the Sun, showing lines of constant Stonyhurst heliographic longitude and latitude on the solar disk. The origin of the coordinate system is at the intersection of the solar equator and the (terrestrial) observer's central meridian. Source: Thompson (2006).

Other heliocentric coordinate system frequently used is the Heliocentric Earth Ecliptic (HEE) with “x” pointing from the Sun to the Earth and “z” toward ecliptic North Pole. The remaining axis completes the right-handed Cartesian triad and points approximately toward the West limb.

The results from this Thesis (Chapter 6) are displayed in HEEQ coordinates, except in those cases when a previous work has results in HEE.

5 CRITERIA TO SELECT THE LIST OF EVENTS

5.1 List of magnetic clouds

In this Thesis, we started our analysis from the ICMEs catalog from Richardson & Cane (2010) available and updated online at: http://www.srl.caltech.edu/ACE/ASC/DATA/level3/icme_table2.htm. We found 18 events from January 2008 to December 2011. The timing of the magnetic clouds are listed in Table 5.1.

Table 5.1 - List of magnetic clouds analyzed in this Thesis.

#	Beginning of the magnetic cloud period	End of the magnetic cloud period	Maximum magnetic field intensity [nT]	Maximum solar wind speed [km/s]
1	2008/12/17 03:00	2008/12/17 14:00	9	350
2	2009/02/04 00:00	2009/02/04 16:00	11	400
3	2009/10/29 05:00	2009/10/29 23:00	11	380
4	2010/02/07 18:00	2010/02/08 22:00	11	410
5	2010/04/05 12:00	2010/04/06 14:00	22	800
6	2010/04/12 01:00	2010/04/12 15:00	12	430
7	2010/05/28 19:00	2010/05/29 17:00	14	390
8	2010/08/04 10:00	2010/08/05 00:00	14	600
9	2010/12/28 03:00	2010/12/28 15:00	14	370
10	2011/02/04 13:00	2011/02/04 20:00	16	420
11	2011/03/29 23:00	2011/03/31 04:00	14	380
12	2011/05/28 05:00	2011/05/28 21:00	13	540
13	2011/09/10 03:00	2011/09/10 15:00	14	500
14	2011/09/17 14:00	2011/09/18 06:00	14	490
15	2011/10/06 12:00	2011/10/06 23:00	12	380
16	2011/10/24 22:00	2011/10/25 16:00	24	510
17	2011/11/07 17:00	2011/11/07 23:00	10	360
18	2011/11/29 00:00	2011/11/29 08:00	17	500
Average			14±4	456±108
Maximum			24	800
Minimum			9	350

5.2 Interplanetary magnetic field and solar wind plasma data

We used 1-minute averaged multispacecraft interplanetary magnetic field (IMF) and Plasma data time-shifted to the Nose of the Earth's Bow Shock taken from the OMNI database. The OMNI data used here is produced using data from two spacecraft: Wind and ACE (Advanced Composition Explorer). More information about the spacecraft are available at ACE Science Center (<http://www.srl.caltech.edu/ACE/>) and Space Physics Data Facility at the Goddard Space Flight Center (<http://pwg.gsfc.nasa.gov/wind.shtml>).

In each plot of IMF and plasma data in Chapter 6, we follow the same pattern. From top to bottom, the content of each panel is:

- 1) magnitude of the average IMF vector (nT);
- 2) "x" component of the magnetic field vector in GSE coordinate system (nT);
- 3) "y" component of the magnetic field vector in GSE coordinate system (nT);
- 4) "z" component of the magnetic field vector in GSE coordinate system (nT);
- 5) flow speed (km/s);
- 6) proton temperature (K);
- 7) proton density (cm^{-3});
- 8) plasma beta parameter (dimensionless).

The date and time of the beginning and end of each magnetic cloud are shown at the top part of each plot. In each time-series plot, the vertical continuous line indicates these timing. All time-series data plots show data starting one day before the beginning of the MC and ending one day after its end.

5.3 The cosmic ray decreases observed by neutron monitors

As commented in Chapter 1, neutrons are produced by primary cosmic rays with energy at about 10 GeV, a lower energy than the primary cosmic ray than originate the muons observed by the GMDN. Since neutron monitor data is highly modulated by magnetic clouds, we decided to include a brief analysis of some neutron data here.

In order to have an idea of the magnitude of the cosmic ray depleted region produced by each magnetic cloud we analyzed the cosmic ray decreases observed by three neutron monitors: McMurdo, Thule and Newark. The Bartol Research Institute from University of Delaware (<http://www.bartol.udel.edu/>) provides this data already corrected for the atmospheric pressure effect. The location of each neutron monitor is described in Table 5.2 and the decrease observed for each event is shown in Figure 5.1.

Table 5.2 - The location of each Neutron Monitor Station.

	Geographic Latitude	Geographic Longitude	Altitude
McMurdo, Antarctica	77.9° S	166.6° E	48 m
Thule, Greenland	76.5°N	68.7° W	26 m
Newark, Delaware, United States of America	39.7° N	75.7° W	50 m

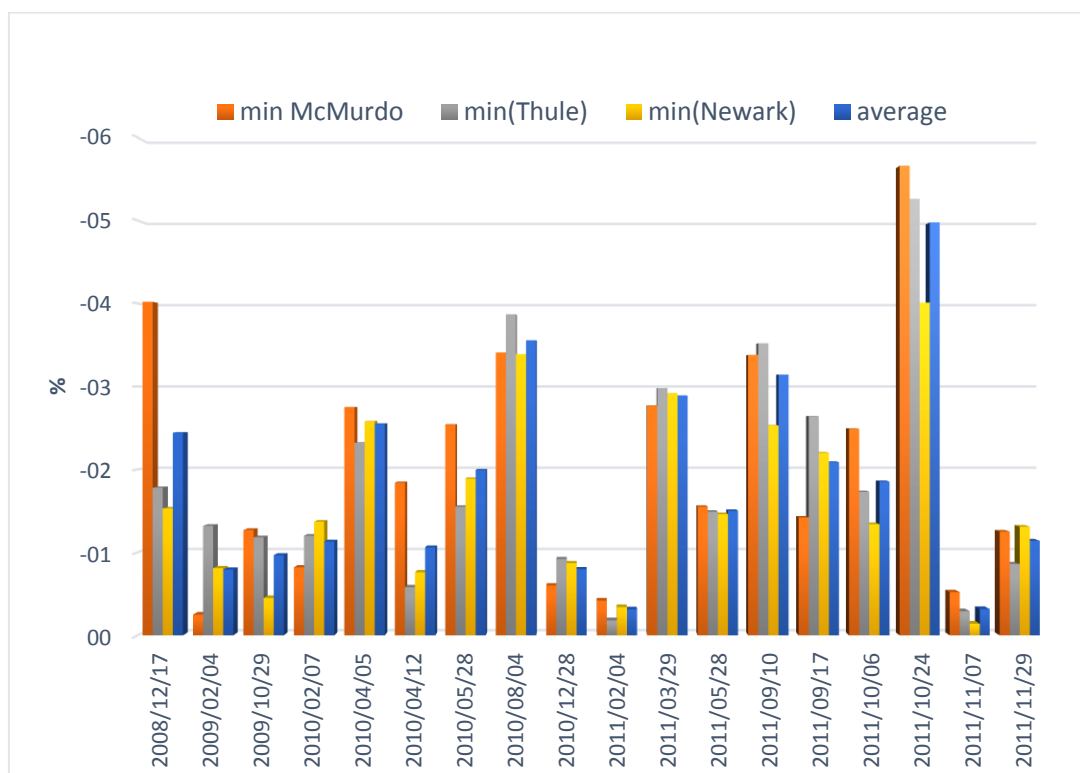


Figure 5.1 - Decreases (percentage) observed by each neutron monitor during each of the 18 magnetic clouds observed from 2008 to 2011. The date indicated in each bar indicates the beginning day of the magnetic cloud.

Since the energy range of primary cosmic ray is lower for neutron monitors than for muon detectors, the neutron decrease associated to a magnetic cloud is expected to have higher magnitude. While the maximum cosmic ray decreases observed by muon detectors do not exceed 2%, neutron monitor has decrease amplitude higher than 5%. For the neutron monitor data shown here, the highest decrease is observed during the event in 2011/10/24.

5.4 The cosmic ray analysis in previous works

This Thesis applied the same methodology from Kuwabara et al. (2009), which is an evolution of the methodology from Kuwabara et al. (2004). In general terms, the difference between them is that the article from 2009 takes into account the possibility of expansion of the magnetic cloud as times passes and the other does not, keeping the radius constant over time for a given event.

Kuwabara et al. (2004) analyzed only one event were the isotropic decrease was higher than 10% as observed by cosmic ray (muon) detectors. The event studied was the Halloween event in October 2003. Kuwabara et al. (2009) selected all the events observed between 2001 and 2003 that had isotropic decrease higher than 2%. It is important to notice that all the events studied here have magnitude smaller than 2% and, therefore, none of them would be selected by the criteria used in Kuwabara et al. (2009).

After the period analyzed by previous works, the GMDN was highly improved: a new detector was installed at Kuwait city; the muon detector at São Martinho da Serra was enlarged from 4 to 28 m² and the detector at Hobart was enlarged from 9 m² to 16 m².

One more difference is that the anisotropy vector was calculated using the methodology from Okazaki et al. (2008) that should have some advantages when compared to the anisotropy calculated previously. Other point is that Kuwabara et al. (2009) did not use correction of the atmospheric temperature effect, it corrected only the atmospheric pressure effect.

5.5 Events discarded from the list

There is a gap in the OMNI data during the MC period on 2009/10/29 and thus, the cosmic ray gradient cannot be determined. There are several data gaps in LASCO-C3 and COR2A and it is

not possible to determine if a CME is directed toward the Earth or not. We found a possible earthward directed CME but CORSET was not successful in tracking the CME on COR2 FOV.

On 2010/12/28, the data does not correspond to a MC signature and there is no clear decrease observed by neutron monitors nor muon detectors. It was possible to use CORSET to track the CME but results from CORSET3D were discarded: there was a high error in tie-pointing for this event because the separation of STEREO A and STEREO B is close to 180° and therefore the lines of sight of both spacecraft are almost parallel to each other. The analysis of the triangulation and tie-pointing had a very high error for this CME (up to 0.5 solar radii in the cases while up to 0.2 solar radii in the remaining). We considered this result spurious and discarded it.

The MC on 2011/02/04 does not have any gaps in the interplanetary data and the event seems to be a good example of a magnetic cloud with a high magnetic field intensity (23 nT) and low beta parameter. We identified the CME ejected on 2011/01/30 first seen at 12:36 UT as been earthward directed and as a source of the MC. However, there is gap in the coronagraph data from 2011/02/02 14:00 UT to 2011/02/04 00:00 UT and another CME might have been ejected toward the earth during this period. The results from CORSET3D for this event were also discarded because the separation angle between the STEREO spacecraft was 179° .

6 RESULTS

This Chapter describes the main results of this Thesis for all the 18 MC periods described before, except the four discarded in Section 5.5. For each event, a comprehensive analysis was made in order to identify the solar origins of the MC. In the interplanetary medium, we inspected the possibility of having more than one ICMEs associated to a given MC period. When possible, the cosmic ray cylinder (CRC) model was used to derive the magnetic cloud orientation and position. For some events, there are previous results from other authors. In those cases we compare the results as much as possible, taking into account that the difference between the methods used by other authors and explaining possible reasons of the discrepancies, when is this is the case.

6.1 The magnetic cloud observed on 2008/12/17

6.1.1 The interplanetary medium

The MC observed on 2008/12/17 (Figure 6.1) is a reasonable good example of a MC since many of the signatures are present inside its period, namely: a) the magnetic field is higher, reaching a level of 9 nT; b) the magnetic field has a smooth and wide rotation, particularly in its “z” axis; c) there are smaller fluctuations inside the MC; d) there is lower proton density; e) plasma beta parameter is smaller than 0.1 in a significant part of the MC and close to it on the remaining period.

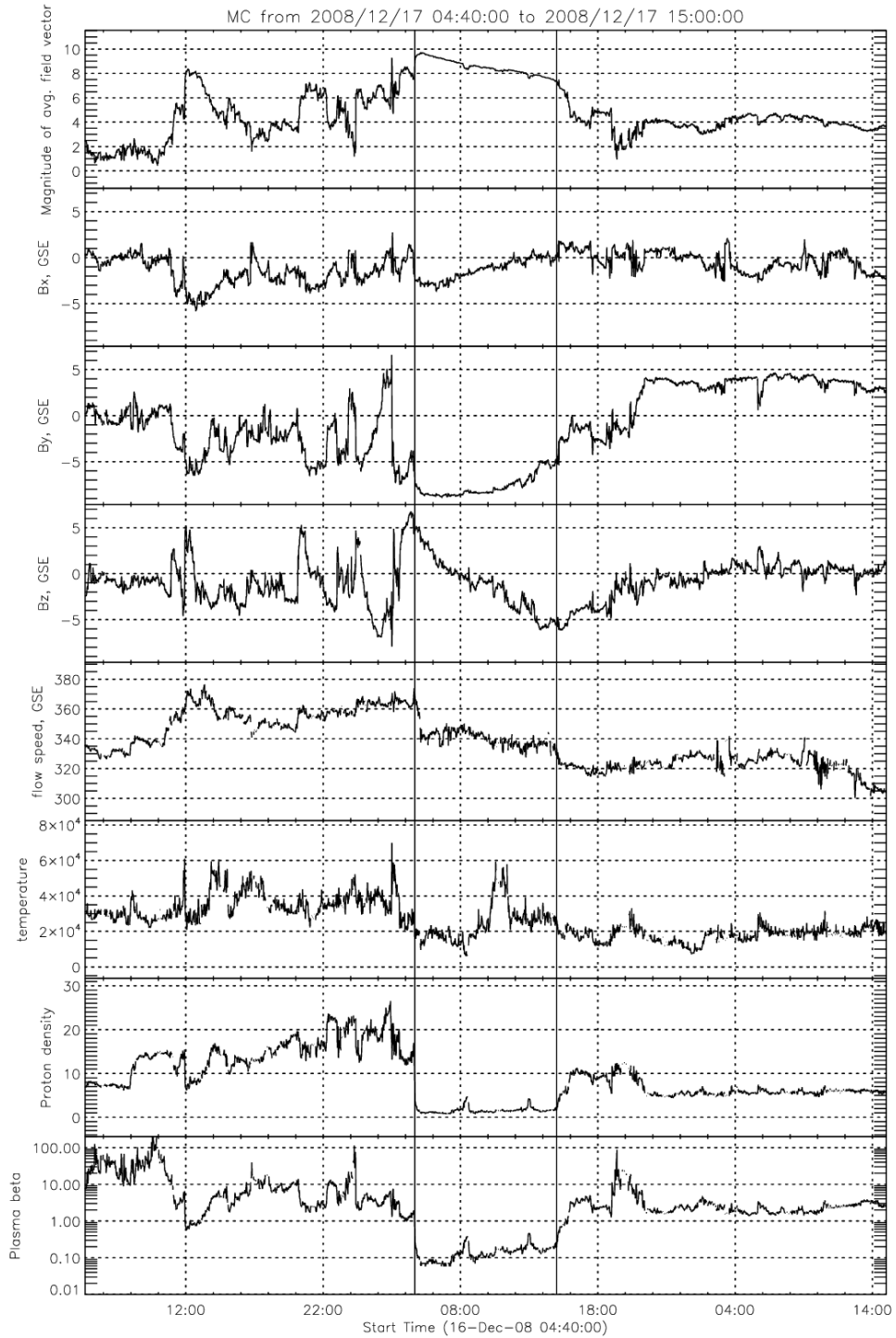


Figure 6.1 - The interplanetary magnetic field and plasma parameters during a MC on 2008/12/17.

The proton temperature, on the other hand, is not as low as expected for a magnetic cloud. The solar wind speed is very low inside the MC, ranging from 340 km/s at the beginning to 330 km/s

at the end. This solar wind time profile suggests a magnetic cloud with negligible expansion while the spacecraft crossed it.

There is simultaneous observations of both ACE and Wind spacecraft of this event. Both spacecraft data are very similar, except for the proton temperature data that is not available on ACE. According to the ICME catalog, this MC started at 03:00 and ended at 14:00 UT on 2008/12/17. In this Thesis, we consider a slightly different MC period starting at 04:40 and ending at 15:00. The beginning of the period was chosen due to 1) a clear reduction in proton density, 2) a reduction of the fluctuations of the magnetic field, 3) an increase of the magnetic field and 4) decrease in the beta parameter from more than 1.0 to less than 0.1. The end of the period can be identified observing the “x” and “y” components of the magnetic field and a quick increase in the beta parameter from ~ 0.2 to ~ 0.7 in a few minutes. The flow speed is reduced about 20 km/s at the beginning of the MC and reduced again ~ 20 km/s at the end. When looking to the temperature profiles, it is not very clear where the limits of the MC should be set.

There are no other MCs nor ICMEs observed in the interplanetary magnetic field and plasma data in the period up to 4 days before and after this MC. After this period, parameters are typical from a quiet period. There is some disturbance starting at about 12:00 UT on the day before the MC. There are some discontinuities before the MC. The magnetic field orientation suggests a toward sector (longitudinal angle between 90° and 180°) from at least four days before the MC until some hours after it ends. From then on, its orientation changes to away sector (longitudinal angle lying between 270° and 360°).

6.1.2 The cosmic ray observations and modeling

The cosmic ray (muon) detectors from the GMDN do not show a very significant cosmic ray decrease during the period of the current MC for any directional channels. The four vertical channels (from the conventional correlation system) are shown in Figure 6.2. Hobart detector observes the decrease with the highest amplitude. For comparison, we plot the time profiles of three neutron monitors (Delaware, Thule and McMurdo) during the same period. The decreases observed range between 1% and 2% during the period of the magnetic cloud (Figure 6.3).

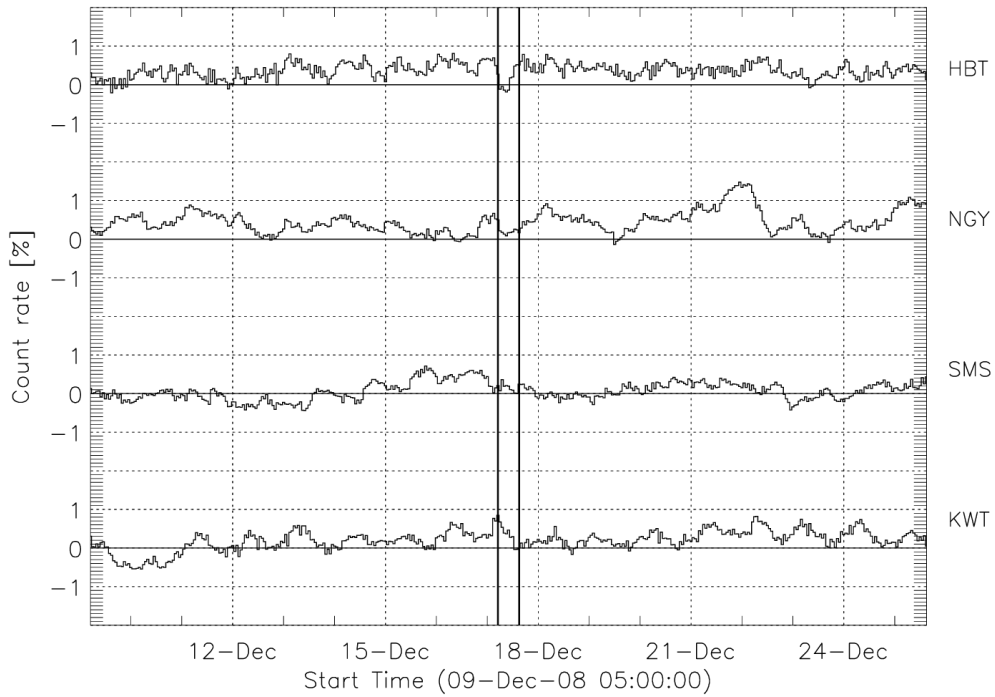


Figure 6.2 – The normalized cosmic ray count rate observed by the vertical directional channels of the GMND during the MC on 2008/12/17. The two vertical continuous lines indicate the beginning and end of the MC.

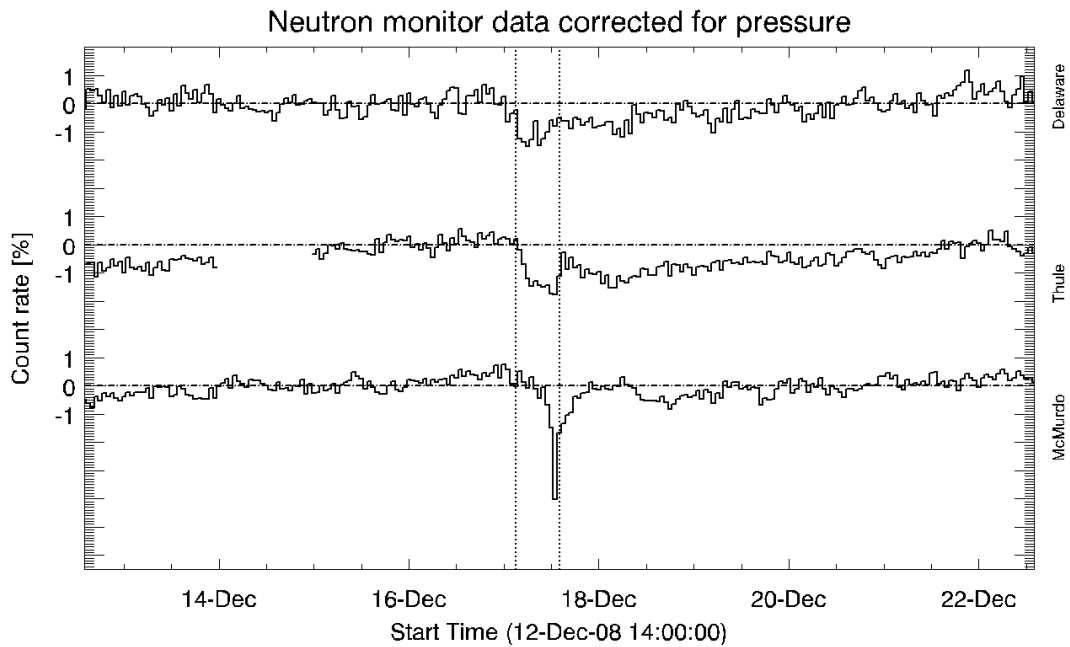


Figure 6.3 - The normalized cosmic ray count rate observed by three different neutron monitors (Delaware, Thule and McMurdo) throughout the MC on 2008/12/17. The two vertical dashed lines indicate the beginning and end of the MC.

We inspected the cosmic ray anisotropy vector direction in relation to the IMF direction and we noticed that, during the MC period, the component of the cosmic ray anisotropy perpendicular to the IMF is much higher than the parallel component. Therefore, the cosmic ray gradient calculated using Equation 3.13 is a good approximation of the total gradient.

The cosmic ray isotropic intensity and the orthogonal components of the fractional gradient during the MC are shown in Figure 6.4 (GSE coordinate system) and the three dimensional representation of the CRC is shown in Figure Figure 6.5. The first signature of a MC period is a decrease in the cosmic ray isotropic intensity followed by an increase to a similar level than before the beginning of the decrease. In this case, the amplitude of the decrease is about 0.2%, much smaller than the 2% minimum decrease amplitude chosen by Kuwabara et al. (2009). Although small, the decrease observed on the isotropic intensity fits very well the model.

The second signature that we expect to observe when a MC is approaching the Earth is a negative “x” component of the gradient in the beginning of the MC period followed by a gradual increase that ends up in positive values. This signature can be observed reasonably well, see second panel of Figure 6.4, from top to bottom.

The best fit of the model is compared with the observed data in Figure 6.4. We have done the best fit of the model using data from both the conventional and new correlation systems. The parameters derived using both datasets are shown in Table 6.1. Notice that there is some difference between the results. Since the isotropic intensity and the gradient are similar in both correlation systems, the differences illustrate how sensitive each parameter is to the data, i.e, to have an estimate of the error in each parameter.

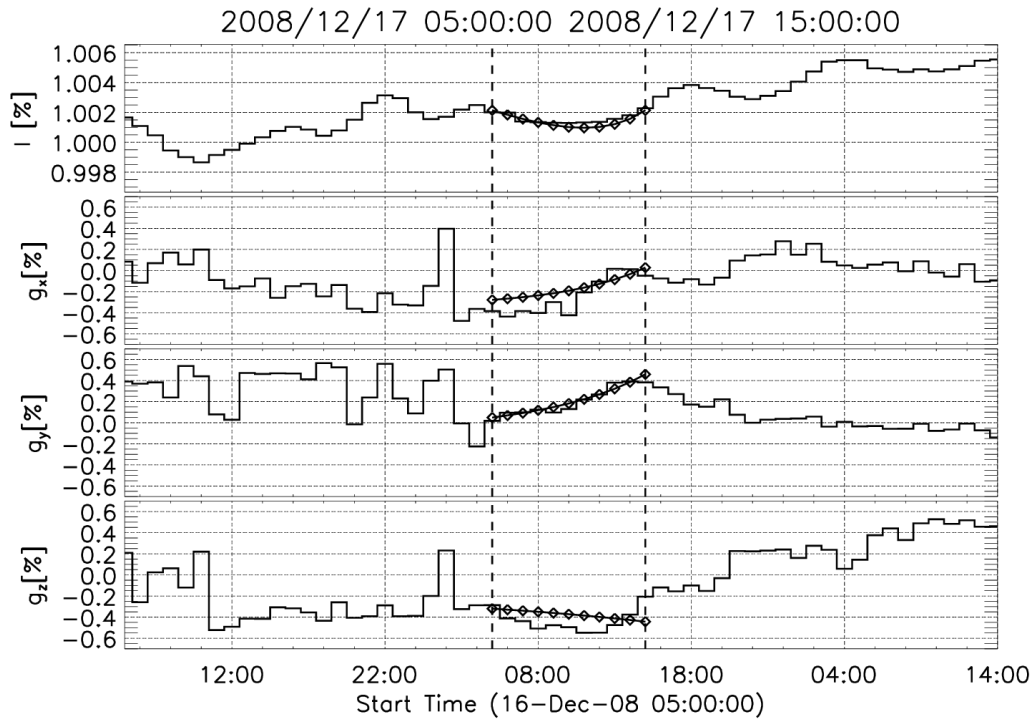


Figure 6.4 - The observation and modeling of cosmic ray depleted region associated to the magnetic cloud on 2008/12/17. The stair plot is the observed data and the line with diamonds is the modeling of the cosmic ray depleted region. The first panel, from top to bottom, shows the isotropic intensity. The remaining three plots show the orthogonal components of the fractional cosmic ray density gradient in the GSE coordinate system. The two vertical dashed lines correspond to the beginning and the end of the cosmic ray depleted region chosen by eye. These timings are indicated on top of the plot.

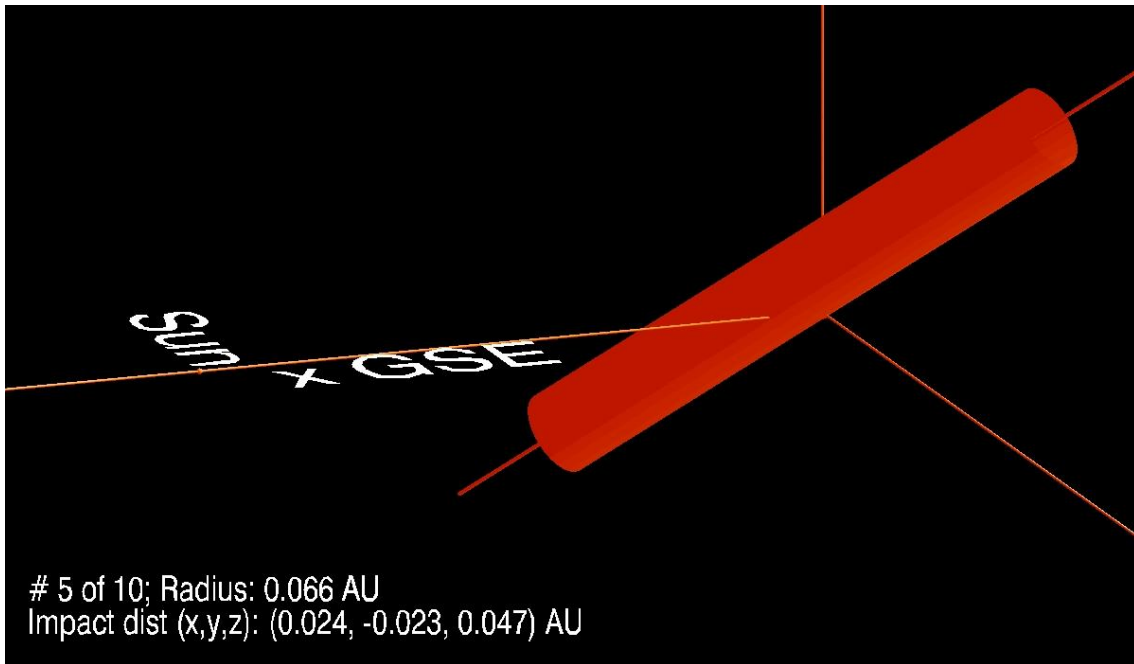


Figure 6.5 - A tridimensional representation of the cylinder derived from CRC model on 2008/12/17 at 10:00 UT. The Earth is located in the origin of the GSE coordinate system (represented by the three axis).

We can see that the “z” component of the gradient is always negative from 2008/12/16 10:00 UT until the next day at 20:00 UT. This behavior shows that the cosmic ray depleted region is located mainly above the ecliptic plane. Since the cosmic ray depleted region probably corresponds to the MC location, we may conclude that the MC is located more above the ecliptic plane than below it.

Table 6.1 - The parameters of the MC observed on 2008/12/17.

	Conventional correlation system	New correlation system
Beginning of the period	2008/12/17 05:00	2008/12/17 05:00
End of the period	2008/12/17 15:00	2008/12/17 15:00
Time with minimum cosmic ray isotropic intensity	2008/12/17 14:00	2008/12/17 10:00
Minimum cosmic ray isotropic intensity	0.996	0.993
Larmor radius (AU)	0.03	0.03
Latitude (degrees, GSE)	35°	41°
Longitude (degrees, GSE)	135°	120°
Impact distance (AU)	0.05	0.06
κ_0 (dimensionless)	122	89
Cylinder radius (AU)	0.06	0.07
Cylinder radius expansion speed (AU/hour)	-0.002	-0.003
Residue	0.008	0.011
Position at start [GSE coordinates, AU]	0.05, -0.01, 0.06	0.08, -0.02, 0.06
Position at end [GSE coordinates, AU]	-0.01, -0.04, 0.04	0.01, -0.04, 0.05

The model results suggest that the cylinder is shrinking as time passes. This fact might not necessarily indicate that the magnetic flux is shrinking. Probably the cosmic ray population increases inside the flux rope in a way that close to its outside boundary the density becomes similar to outside it. This hypothesis here is supported by the results from a simulation performed by Kubo & Shimazu (2010) for the 60 GeV cosmic rays inside a magnetic cloud. Their results suggest that the cosmic ray populates first the region closer to the outer boundary and, after this, the density in the innermost region starts increasing.

In a rough approximation, the cylinder diameter should be similar to the duration of the MC (in this case about 0.5 days) times the speed of the MC (which should be similar to the speed of the solar wind, about 300 km/s in this case). This simple calculation results in 0.09 AU. Liu et al. (2010) also analyzed this event and estimated the diameter of the MC to be 0.10 AU. The result found here using the conventional and new correlation system is 0.12 AU and 0.14 AU, respectively.

Looking to the interplanetary magnetic field and plasma data, we may suggest two causes of the very small cosmic ray isotropic density decrease. The first is the low intensity of the magnetic field with maximum of about 9 nT. The second might be the low solar wind speed and the long propagation time of the MC from the Sun to the Earth. According to previous works from Liu et al. (2010), this MC is the result of a CME ejected about 5 days before, in 2008/12/12. The cosmic ray intensity inside the cloud should increase as time passes due to perpendicular diffusion.

In order to compare the orientation angles, we also performed the Minimum Variance Analysis (MVA) using the period indicated in Table 6.1. The latitude and longitude found are shown in Table 6.2. The MVA was also done using a time offset of up to two hours before and after the beginning of the period indicated. In this way, the MVA was calculated 25 times for each case. The values indicated in the Table 6.2 are the averages plus or minus the standard deviations. In this event, the MVA calculations resulted in $\lambda_2/\lambda_3 > 2$ in 22 of the 25 cases. If we take into account the MVA standard deviation, the results from the MVA and CRC are similar to each other.

For the same event, Liu et al. (2010b) reconstructed the MC cross section using the Grad-Shafranov (GS) technique (HU; SONNERUP, 2002) and found a maximum axial field above the ecliptic plane with a tilt angle of 6°. The same reference, using the GCS model found the flux

rope to be 53° inclined with the ecliptic plane. These results are listed in Table 6.2. Notice that only the longitude has a reasonable agreement between all methods and the latitude of the Grad-Shafranov orientation is significantly different from the remaining results.

Table 6.2 - Results of the latitude and longitude of the flux rope found by different methods.

MVA		CRC -		CRC - new correlation system	GS from Liu et al. (2010B)	GCS from Liu et al. (2010B)
		conventional correlation system				
Latitude	single MVA	40°	35°	41°	6°	53°
	multiple MVA	$32 \pm 23^\circ$				
Longitude	single MVA	95°	135°	120°	95°	-
	multiple MVA	$101 \pm 31^\circ$				

6.1.3 The origins in the solar corona

We inspected the LASCO-C3 images from 2008/12/12 to 2008/12/16 in order to identify earthward directed CMEs that might be the solar source of this MC. We found only one halo CME which is observed on the first day analyzed (Figure 6.6). Beyond this CME, there are at least five limb CMEs and most of them with low brightness. By comparing the configuration of the limb CMEs with its observations in SECCHI, we confirmed that only the halo CME is earthward directed.

CORSET simultaneously tracked the CME on COR2A and COR2B FOV from 11:07 UT to 13:37 in six frames. The CME tracked in each frame is shown in Figure 6.6 and Figure 6.7. We used $Q = 0$ because the brightness of the CME does not change significantly with time in the six frames chosen in this analysis. For the foreground model (explained in Section 4.4), we used a sample region in the fourth frame. To our understanding, the front of the CME selected here is consistent with its definition. An internal portion of the CME in the STEREO A images are not selected because it has low brightness. This results from a subtraction of a bright structure in the background image. They come from the base image used to subtract every image to be tracked by CORSET: the base image has a bright structure. This structure changes the texture of the CME and CORSET becomes unable to track the CME in that region. This explains why the dark region in the CME is missed in the CORSET tracking. In COR2B, on the other hand, there is

no such structure in the base image and the CORSET tracked the inner part of the CME without any problem. Since we are interested in calculating the speed of the CME, this limitation does not affect the results because only the front side of the CME is used.

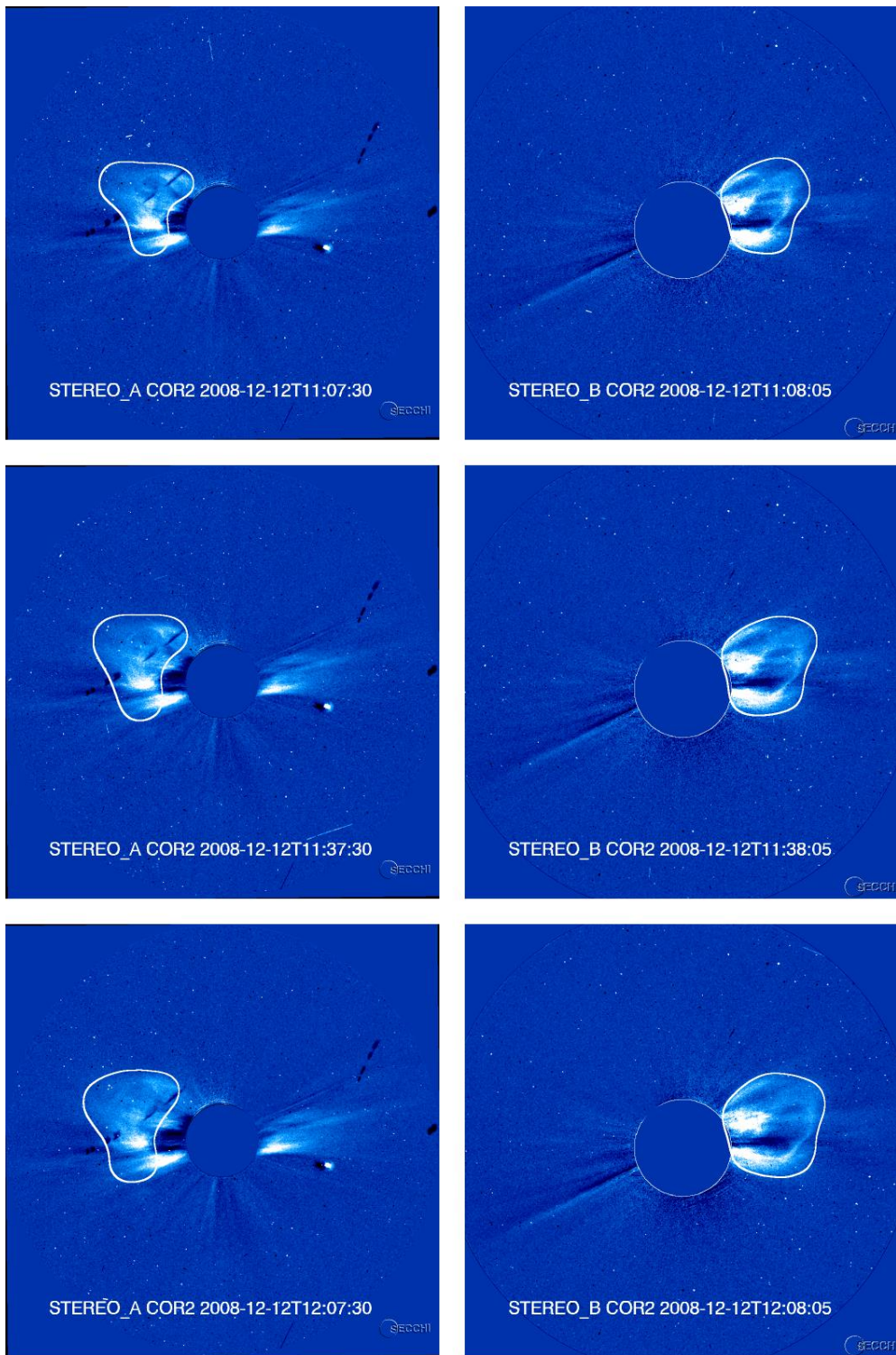


Figure 6.6- The CME observed on 2008/12/12 on COR2A (left column) and COR2B (right column) FOVs. In this Figure, only the first three frames are shown.

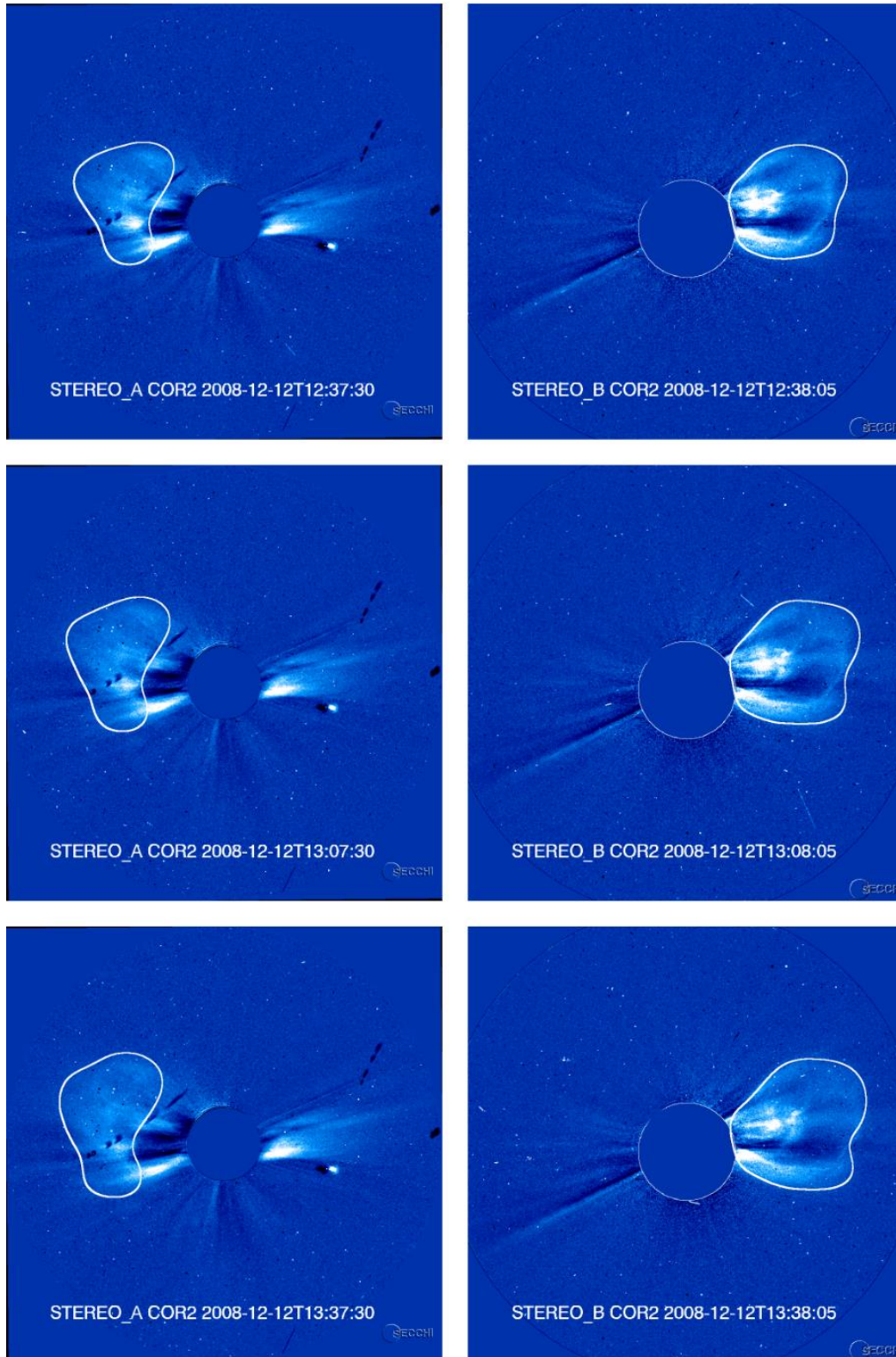


Figure 6.7 - The CME observed on 2008/12/12 on COR2A FOV (left column) and COR2B FOV (right column). In this Figure, only the last three frames are shown.

The height-time plot derived for the fastest moving part of the CME front in each coronagraph FOV is shown in Figure 6.8 and Figure 6.9. The resulting CME speeds derived using CORSET3D are shown in Figure 6.10.

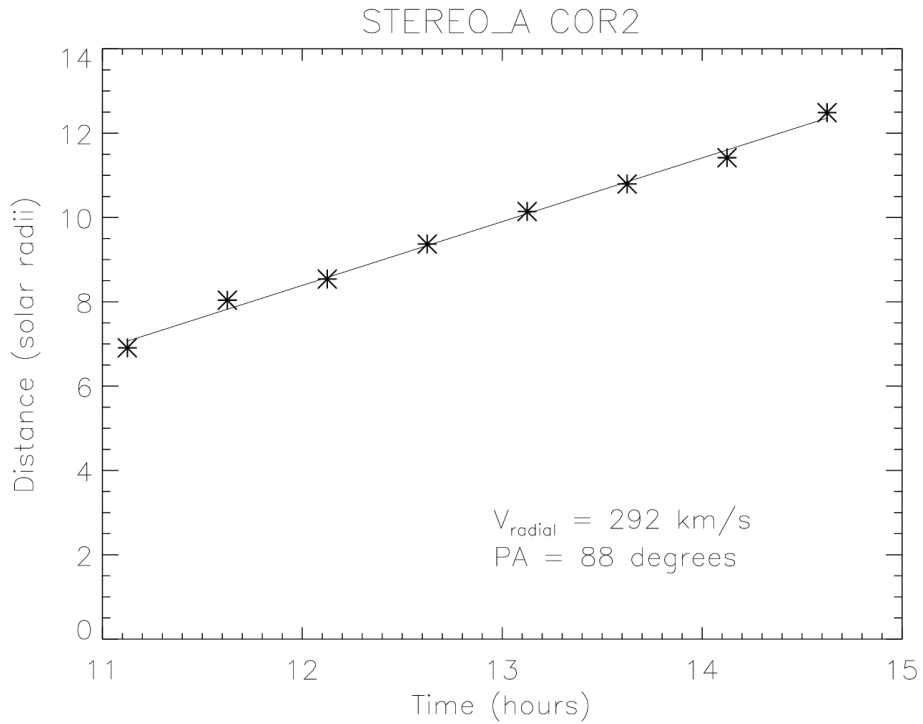


Figure 6.8 - The height-time profile of the CME on 2008/12/12 on the COR2A FOV for the fastest moving position angle. A linear fit is shown and the speed calculated is indicated. This CME was tracked by CORSET from 11:07 UT to 14:37 UT.

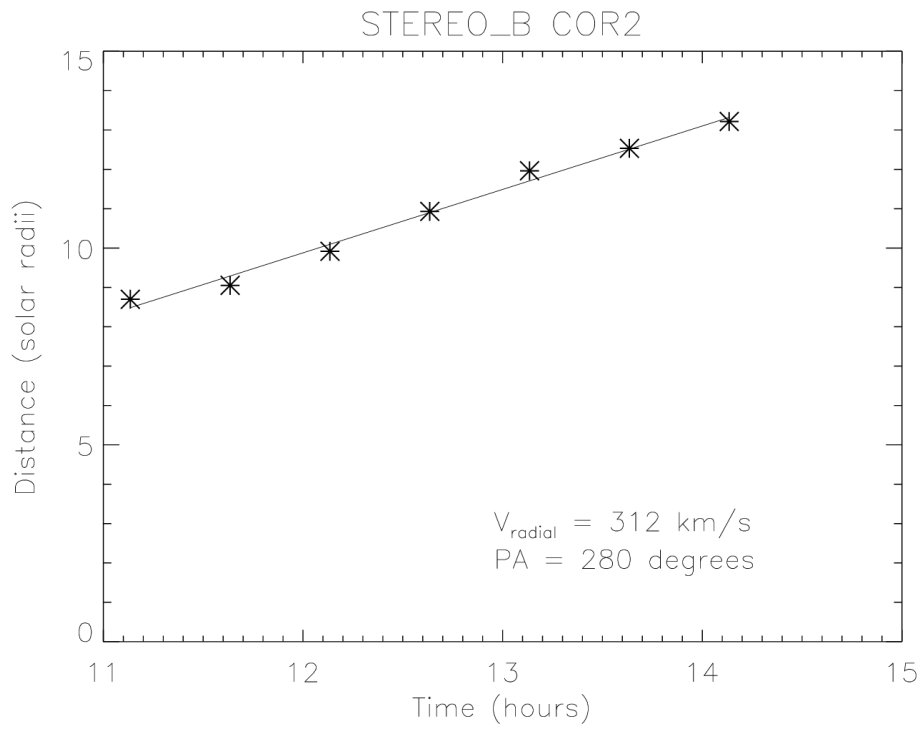


Figure 6.9 - The height-time profile of the CME on the COR2B FOV for the fastest moving position angle. A linear fit is shown and the speed calculated is indicated.

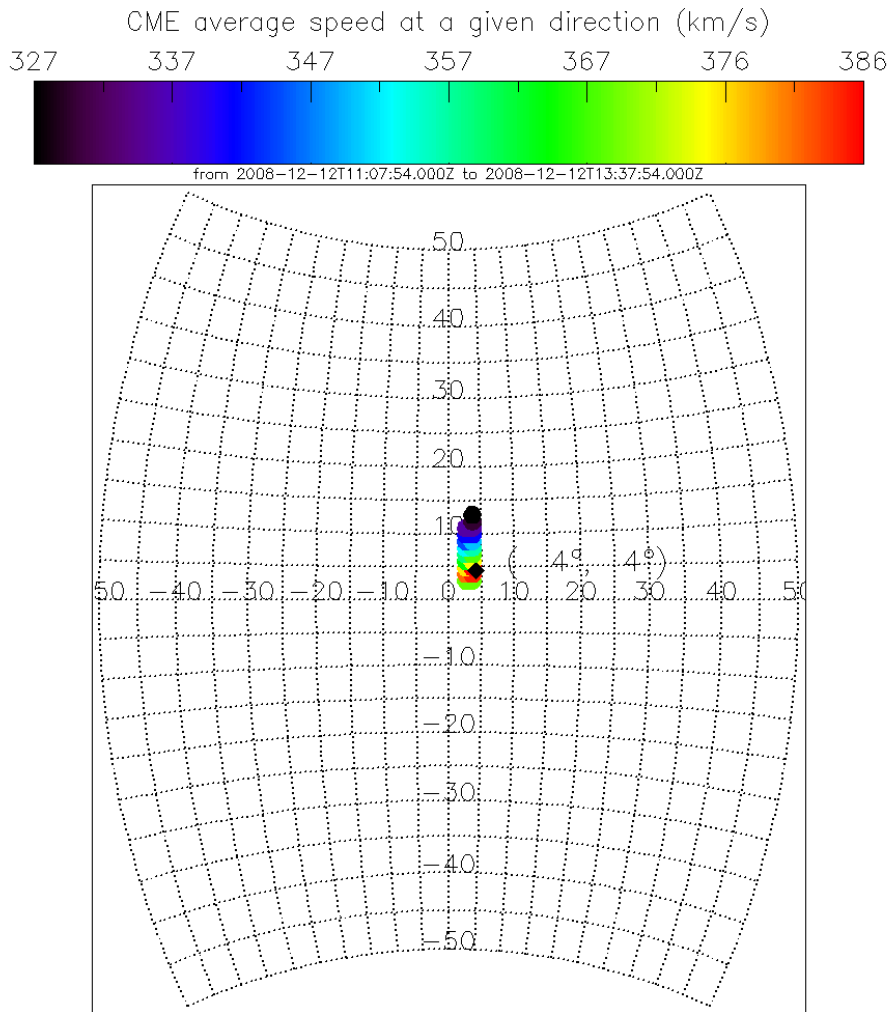


Figure 6.10 - The radial speed \bar{v}_r of the CME front as a function of latitude and longitude (in HEEQ coordinate system). The black diamond indicates the center of the CME front.

Table 6.3 - Kinematic parameters of the CME derived using CORSET3D. The angles shown here are given in HEEQ coordinate system.

Parameter	Result
Minimum and maximum latitudes	[-6°, 15°]
Minimum and maximum longitudes	[2°, 7°]
Group speed v_g averaged over time	357±19 km/s
Central direction of the CME averaged over time (longitude)	4°
Central direction of the CME averaged over time (latitude)	4°
Minimum value of $\bar{v}_r(\theta_j, \phi_k)$	327 km/s
Maximum value of $\bar{v}_r(\theta_j, \phi_k)$	386 km/s
Group speed as a function of time $v_g(t_{i+1})$	[266, 346, 480, 379, 253] km/s
Maximum error of the triangulation	0.1 solar radii

The direction of propagation with respect to the Sun-Earth line was calculated previously by Lugaz (2010) using triangulation and the tangent-to-a-sphere method in the Heliospheric Imager FOV. The second method “assumes that the measured part is not a single particle but a sphere (or a circle in the ecliptic plane) connected to the Sun at all times” (HOWARD; TAPPIN, 2009). The results were $3\pm 4^\circ$ for the first method and $8\pm 10^\circ$ for the second, respectively. The direction of propagation as a function of time is shown in Figure 6.11. Although both methods were done at further distances from the Sun, their results are in good agreement with the direction of propagation (longitude) estimated by CORSET3D (shown in Table 6.3).

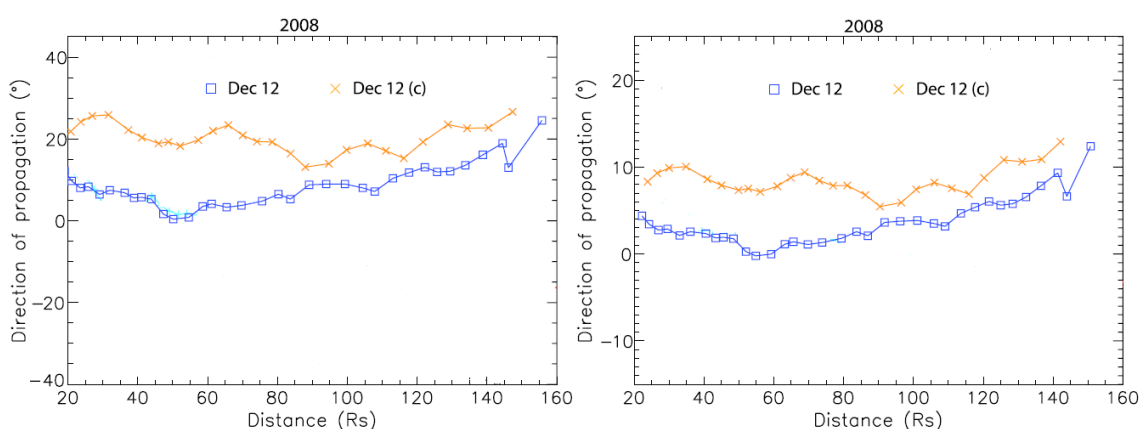


Figure 6.11 - The direction of propagation for the CME on 2008/12/12. The blue points refer to the front track of the CME and the orange points to the back of the CME. On the left panel, the results from the tangent-to-a-sphere method are shown. On the right, results from the triangulation method are shown. Source: modified from Lugaz (2010).

If we suppose that this CME propagates only radially after COR2 FOV until it reaches the Earth, it would be observed at the Earth with its center in the negative side of “y” axis GSE. This expectation is in agreement with the positions derived using the cosmic ray cylinder model (see the last two lines of Table 6.1). Furthermore, notice in Figure 6.10 that all the points of the radial speed derived here are located above the ecliptic plane (it corresponds to a few negative degrees of latitude in the HEEQ coordinate system). Again, if we suppose that the CME propagates only radially and that the front of the CME propagates as a unique structure, this result agrees with the cosmic ray cylinder model that found a MC located mainly above the ecliptic plane (see section 6.1.2).

A previous study from Liu et al. (2010) used triangulation in the COR2 FOV and in the Heliospheric Imager FOV and tracked the CME in its path from the Sun to the Earth for more than two days.

The results are reproduced in Figure 6.12. Each panel shows two structures identified in time-elongation maps constructed from running difference images along the ecliptic plane. These two structures (called “feature 1” and “feature 2” by the authors) represent only one CME, the same CME analyzed in this work. Error bars in Figure 6.12 were calculating by supposing a 10-pixel error in each instrument. This error was then propagated to elongation angle, distance and finally to speed units. The direction of propagation (shown in the upper panel) is calculated along the Sun-Earth line. Positive (negative) angles indicate positions westward (eastward) of the Sun-Earth line. Close to the Sun, the direction of propagation has good agreement with the results from this Thesis. As the ICME gets closer to the Earth (in the last hours of 2008/12/14 and in 2008/12/15), it is deflected eastward. If the CME propagates radially from this point up to the arrival at Earth, the trend is that it crossed the Earth eastward of the Sun-Earth line. The results from the cosmic ray cylinder, on the other hand, show the center of the cylinder westward on the Sun-Earth line, i.e., in the negative range of the “ γ ” axis. Another reference (LIU, DAVIES, *et al.*, 2010) found the propagation direction to be 8° above the ecliptic plane. These results agrees well with CORSET3D.

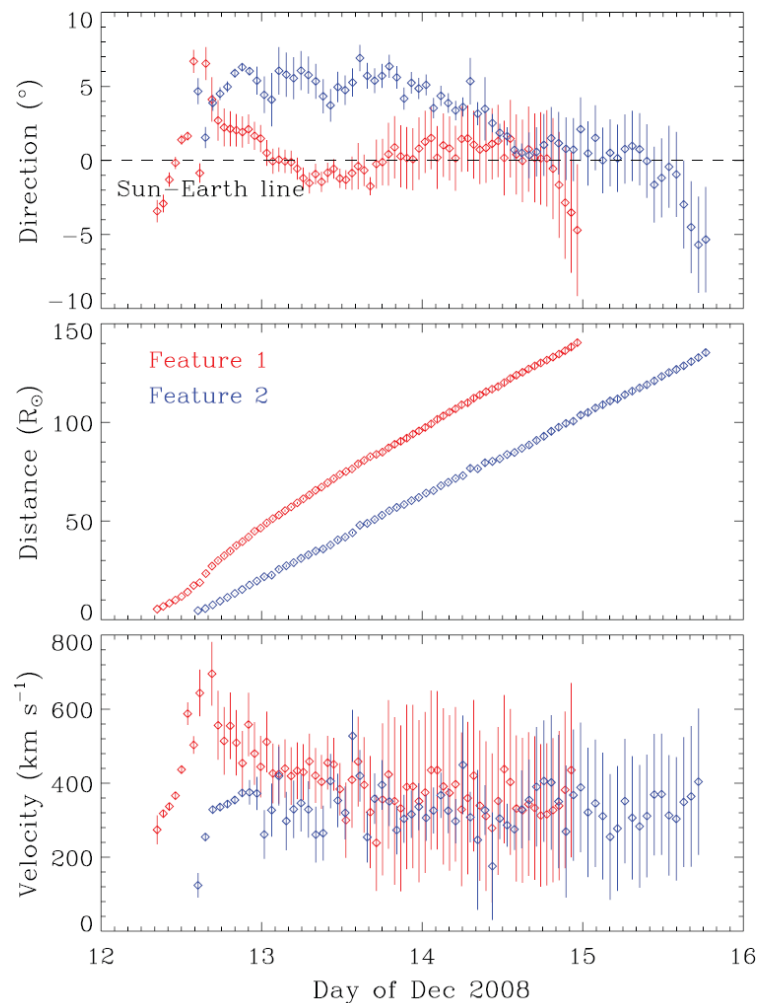


Figure 6.12 - Previous results from Liu et al. (2010) for the direction of propagation of the CME observed on 2008/12/12. Source: Liu et al. (2010).

6.2 The magnetic cloud observed on 2009/02/04

6.2.1 The interplanetary medium

The interplanetary magnetic field and plasma parameters for the MC observed on 2009/02/24 are shown in Figure 6.13. The vertical lines show the period indicated by the catalog, but it does not agree with our understanding that the magnetic cloud should have some reduction in the plasma beta parameter. It is close to the unity during the MC period while an ideal event should have it close to 0.1. The magnetic field intensity is rather small with maximum about 10 nT. The solar wind speed is low, not reaching 400 km/s. The only signature of a magnetic cloud here is a somehow smooth rotation of the magnetic field, mainly in the “y” and “z” components.

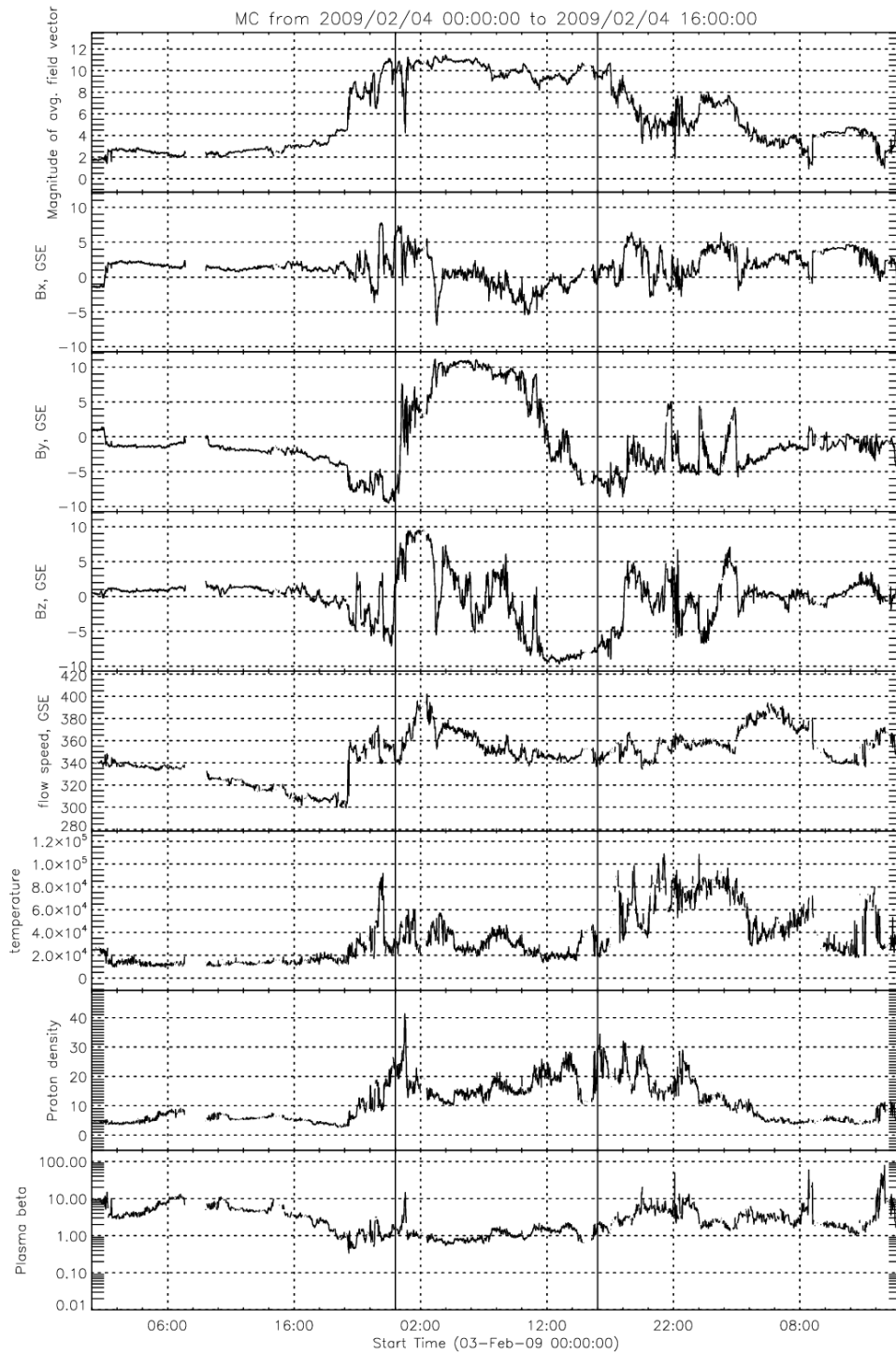


Figure 6.13 - The interplanetary magnetic field and plasma parameters observed during a MC on 2009/02/04.

6.2.2 The cosmic ray observations and modeling

Both the cosmic ray observed by the GMDN and the neutron monitors do not have a very expressive nor clear decrease during the magnetic cloud period (Figure 6.14 and Figure 6.15).

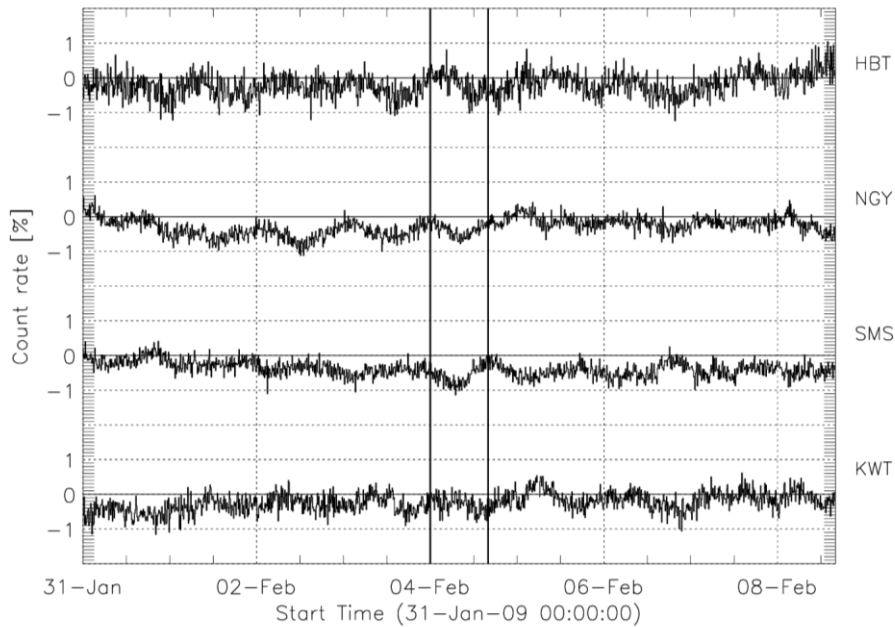


Figure 6.14 - The normalized cosmic ray count rate observed by the vertical directional channels of the GMND during the MC on 2009/02/04.

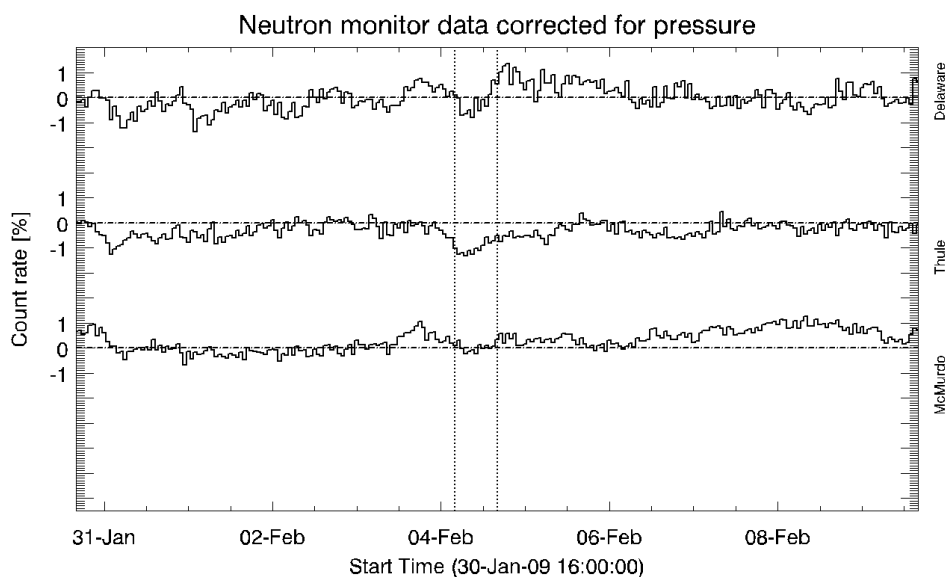


Figure 6.15 - The normalized cosmic ray count rate observed by three different neutron monitors (Delaware, Thule and McMurdo) during the MC ON 2009/02/04.

In the same way that was done in section 6.1.2, we inspected the cosmic ray anisotropy vector direction in relation to the IMF direction and we found that, during the MC period, the component of the cosmic ray anisotropy perpendicular to the IMF is much higher than the parallel component. Therefore, the cosmic ray gradient calculated using Eq. 3.13 is a good approximation of the total gradient.

When looking to the isotropic intensity, the first signature of a MC approaching the Earth is present here: the cosmic ray isotropy decrease is about 0.5% and it is very clear (Figure 6.16). We also expect the data to show a signature of a structure approaching the Earth in the “x” component, i.e., this component should increase with time. This signature, however, is not present here. In principle, the MC period we are using is not suitable for the application of the cosmic ray cylinder model. We tested it in this case and a completely different result is derived when we use both the new and conventional correlation system. Moreover, neither of them is consistent with a structure coming from the Sun and approaching the Earth. Since the “y” component of the gradient is significant, the results show a structure coming from the negative “y” axis. Moreover, they change dramatically when using the new and conventional correlation systems. For all these reasons, we conclude that the results found in this event using CRC model are spurious.

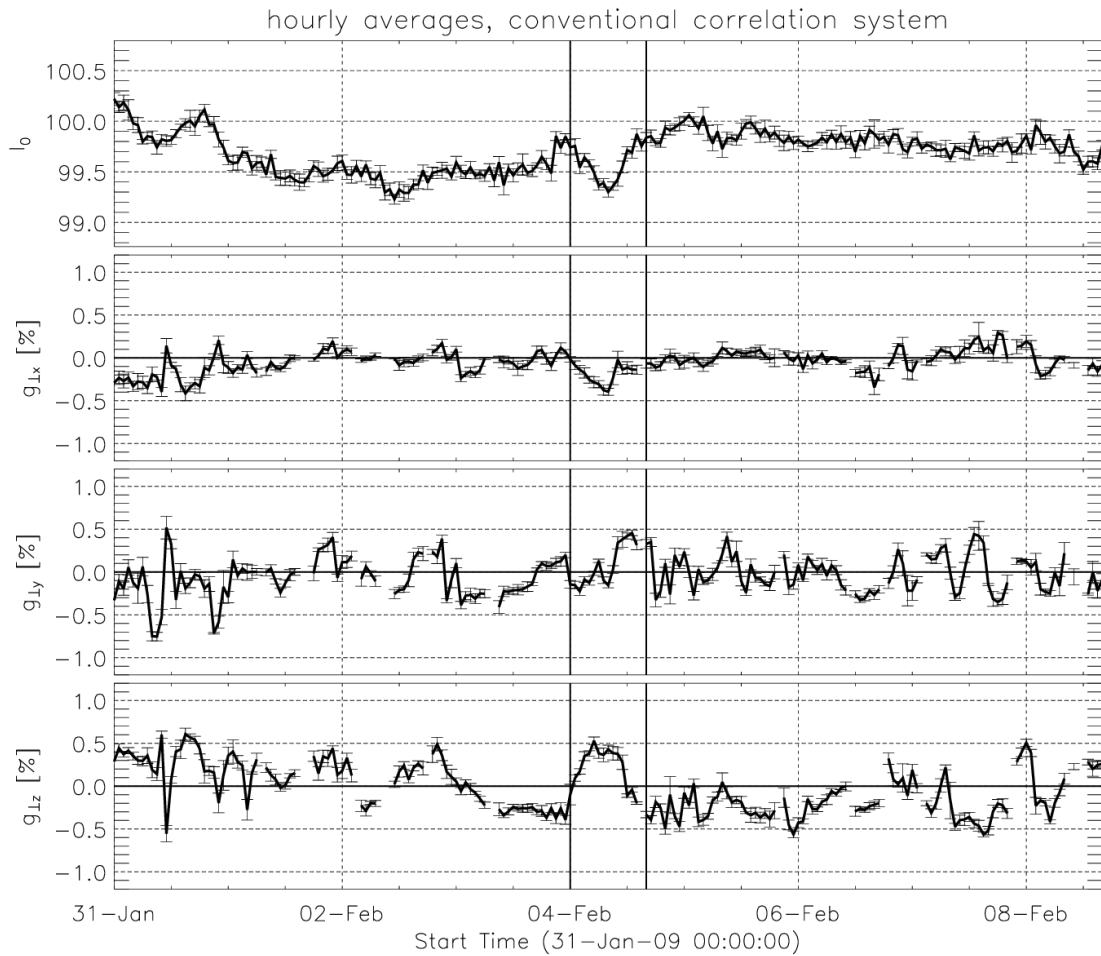


Figure 6.16 - The isotropic cosmic ray intensity and the orthogonal components of the cosmic ray fractional gradient during the MC period on 2009/02/04.

6.2.3 The origins in the solar corona

We inspected the coronagraph images from 2009/01/30 to 2009/02/03 in order to identify the CMEs possibly Earthward directed.

The LASCO-C3 data does not show any halo or partial halo CME during this period. There is a data gap from 2009/02/01 12:00 UT to 2009/02/01 20:00 UT but during this period there is data from the SECCHI coronagraphs and we did not identify any CME.

In this way, taking into account the observation from the interplanetary data, the cosmic ray modeling and the solar origins, it is very likely that there is no CME directed toward the Earth in this case and the interplanetary structure described as a MC by the catalog is probably not a MC.

6.3 The magnetic cloud observed on 2010/04/05

6.3.1 The interplanetary medium

In opposition to the MCs described in sections 6.1.1 and 6.2.1, this structure has a magnetic field peak intensity of more than 20 nT and peak solar wind speed of ~ 800 km/s (Figure 6.17). The orthogonal components of the magnetic field (GSE) show a maximum variation in the “y” axis which changes from about -20 nT to 0 nT. The minimum variation is in the “z” component, which changes less than 10 nT.

The IMF sector polarity is toward the Sun (angle between 270° and 360° GSE) for at least four days before and after the MC period. There is no other clear interplanetary structure observed and the IMF magnitude is ~ 5 nT outside the MC. The next significant increase in the IMF happens on 2010/05/11, about 6 days later than the current event.

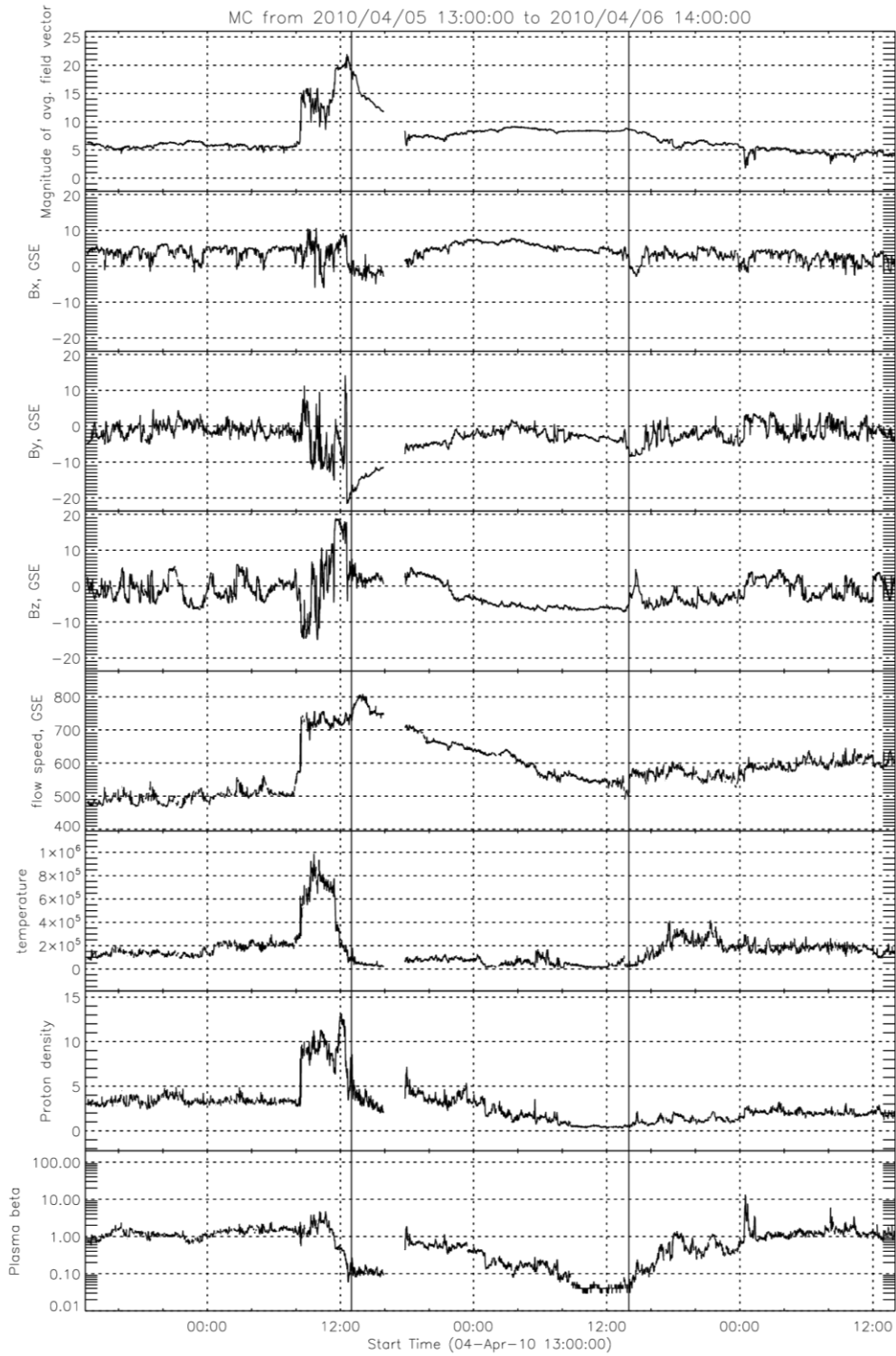


Figure 6.17 - The interplanetary magnetic field and plasma parameters during a MC on 2010/04/05.

This ICME is considered a “good” magnetic cloud (type 2) by the Richardson and Cane catalog because some sort of rotation in the magnetic field is observed. It has, however, some significant discrepancies from the ideal case:

(a) the magnetic field is high only during a period of less than 4 hours and it is quite low (lower than 10 nT) and stable in the remaining period;

(b) the plasma beta parameter is much higher than 0.1 during most of the duration of the MC. This is not the case in the very first hours of the magnetic cloud because in this period beta is close to 0.1.

6.3.2 The cosmic ray observation

The cosmic ray count rates observed by the GMDN do not have a common decrease among each other: while São Martinho da Serra does have a small decrease, others have some small increases (Figure 6.18). The cosmic ray count rates observed by the three neutron monitors used in this Thesis, on the other hand, show a decrease of about 2% during the ICME phase (Figure 6.19).

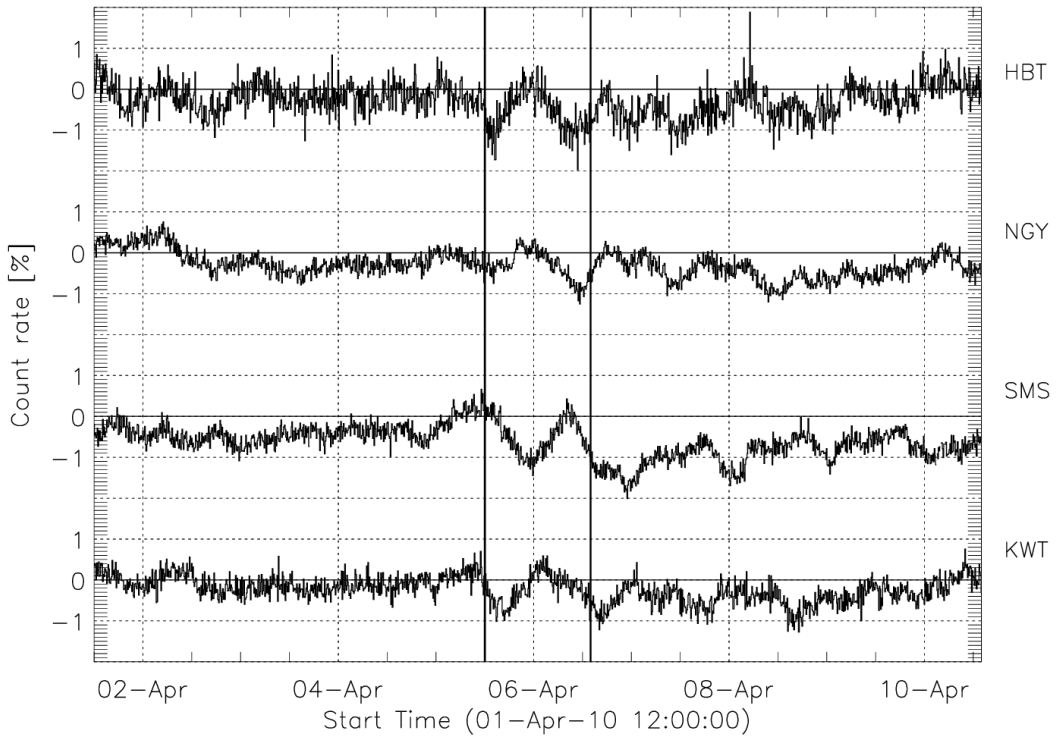


Figure 6.18 - The normalized cosmic ray count rate observed by the vertical directional channels of the GMND during the MC on 2010/04/05.

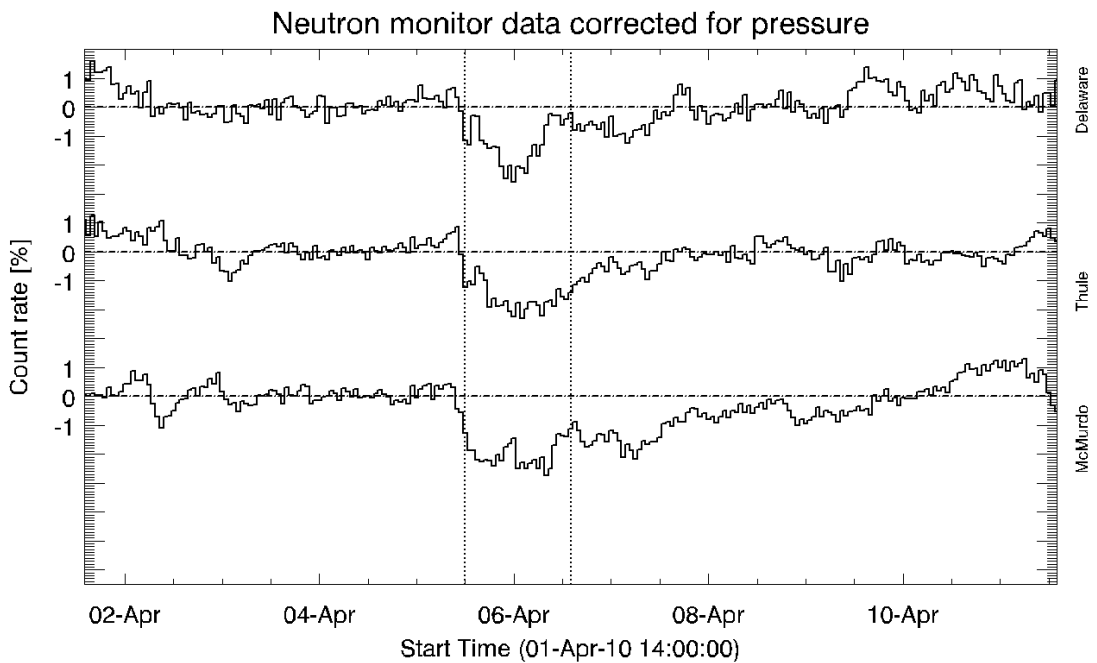


Figure 6.19- The cosmic ray decrease observed by three different neutron monitors (Delaware, Thule and McMurdo) during the MC on 2010/04/05.

The anisotropy parallel to the IMF is negligible in the period plotted. Therefore, the gradient calculated using Equation 3.13 is a good approximation of the total cosmic ray gradient and can be used in the current analysis.

We are not able to use the cosmic ray cylinder model even changing the time window used. The reasons are the absence of both signatures expected: there is no clear isotropic decrease and the “x” component of the gradient not consistent with a structure approaching the Earth (Figure 6.20).

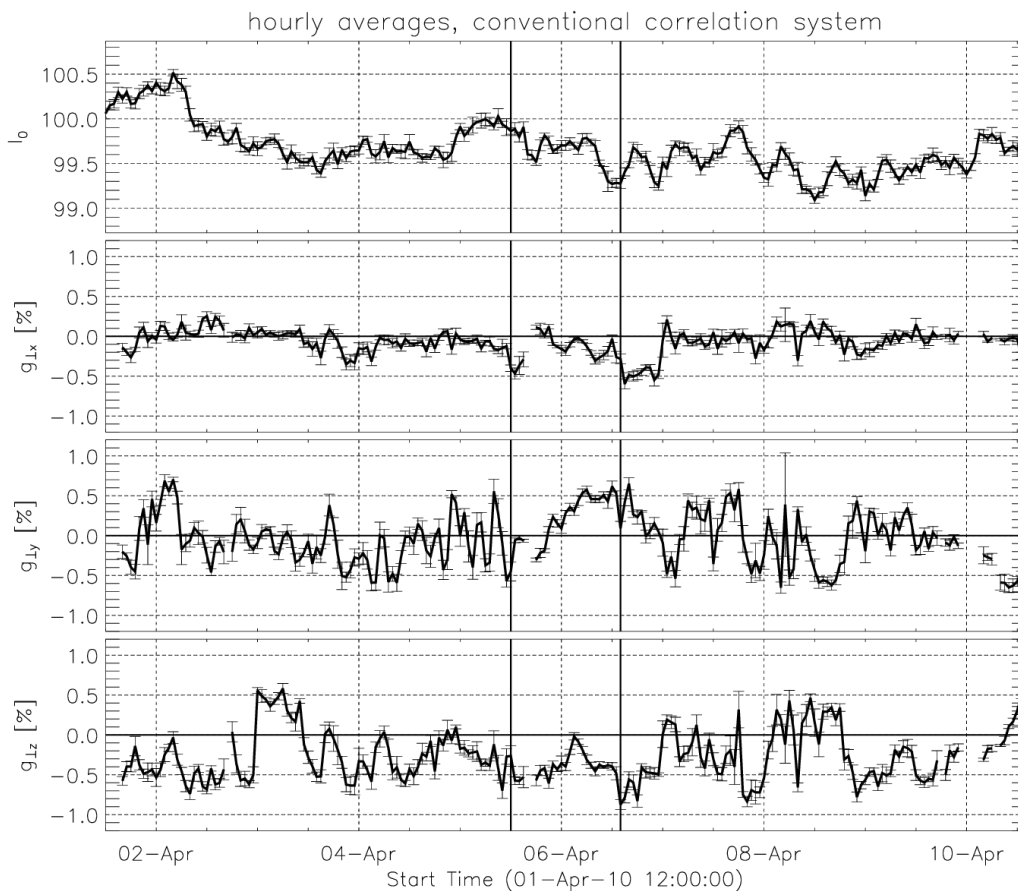


Figure 6.20 - The isotropic intensity and the orthogonal components of the gradient during the MC observation on 2010/04/05.

6.3.3 The origins in the solar corona

We inspected the LASCO-C3 images observed from 2010/04/01 0:00 UT to 2010/04/06 0:00 UT and we found only one halo CME on 2010/04/03 at about 11:00 UT. This CME was tracked in

both COR2 coronagraph between 10:39 UT and 11:54 UT using the default tracking parameter from Braga et al. (2013): the expansion factor Q was set at four. For the base image, we take the average of the images at 06:24 UT and 06:54 UT. The resulting region is shown in Figure 6.21 and Figure 6.22. The speed derived in each coronagraph (with projection effects) is indicated in Figure 6.23 and Figure 6.24. The results from CORSET3D are shown in Figure 6.25 and Table 6.4.

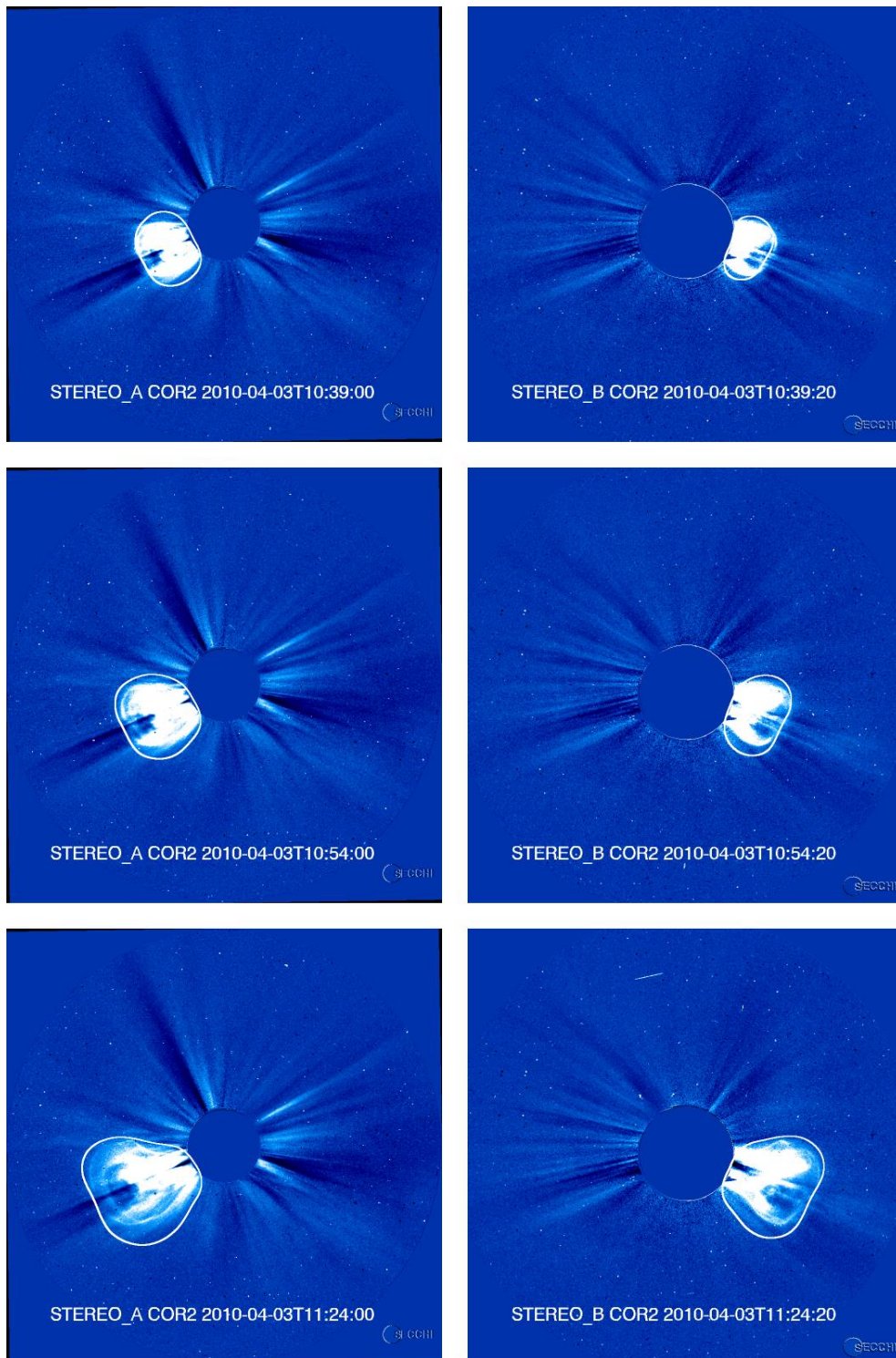


Figure 6.21 - The CME observed on 2010/04/03 in COR2A (left column) and COR2B (right column) FOVs. In this Figure, only the first three frames are shown.

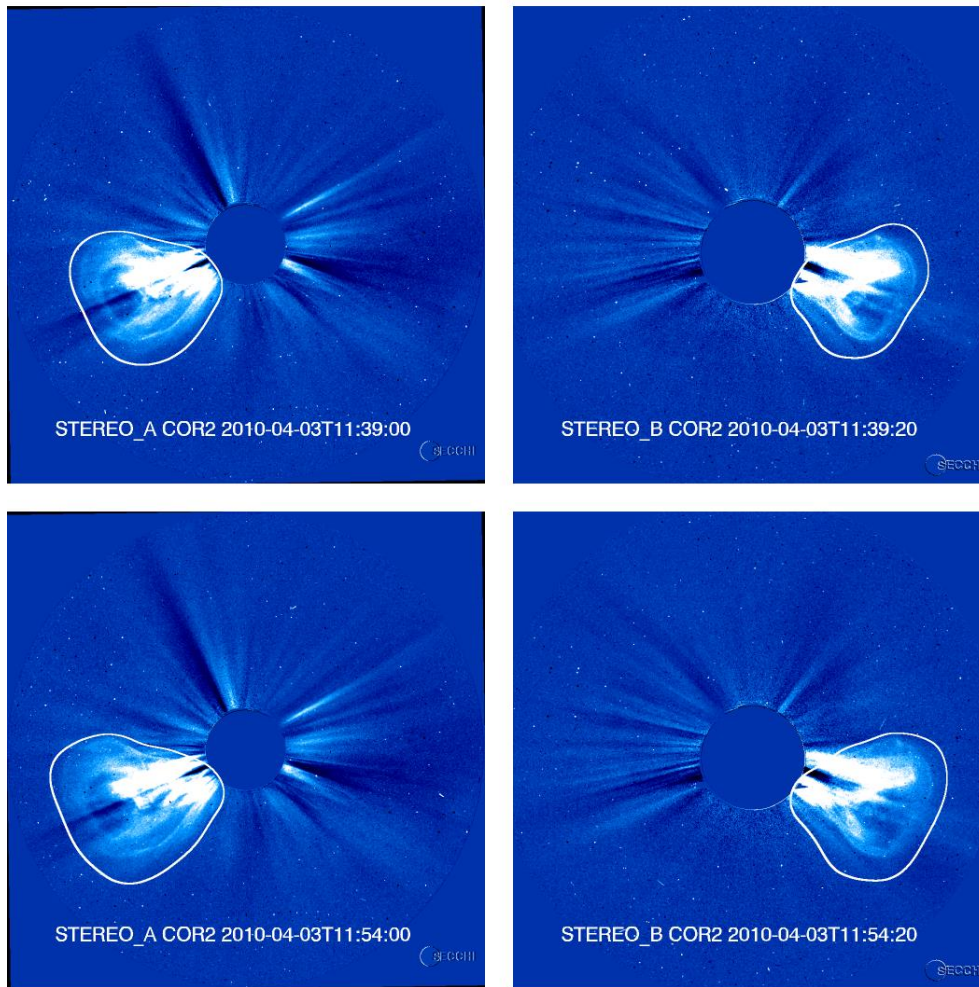


Figure 6.22 - The CME observed on 2010/04/03 in COR2A (left column) and COR2B (right column) FOVs. In this Figure, only the last two frames are shown.

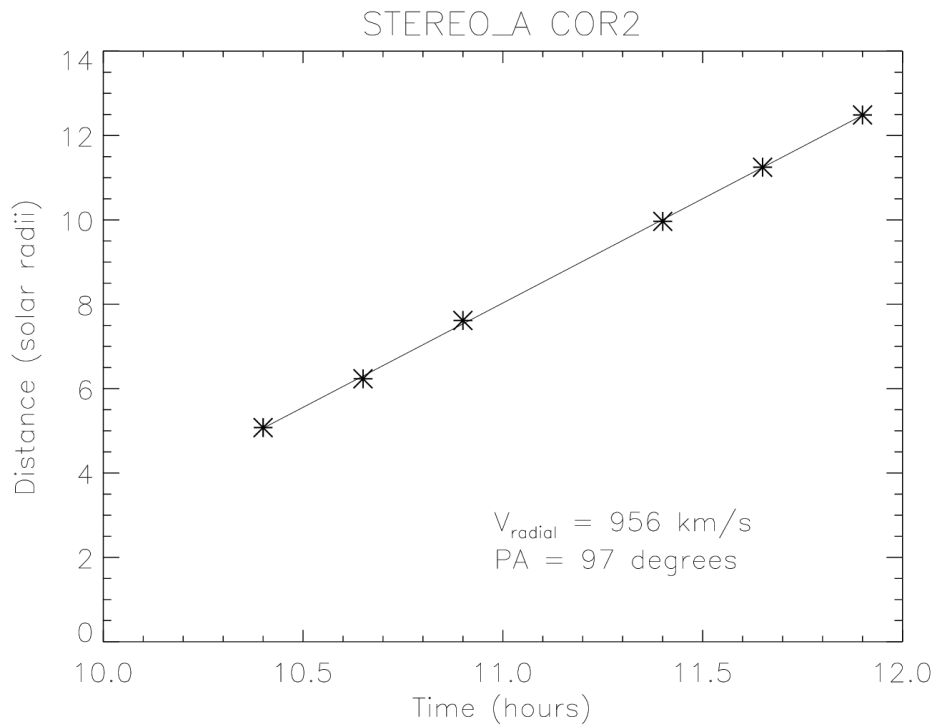


Figure 6.23 - The height-time profile of the CME on 2010/04/03 on the COR2A FOV for the fastest moving position angle. A linear fit is shown and the speed calculated in indicated. This CME was tracked by CORSET from 10:24 UT to 11:54 UT.

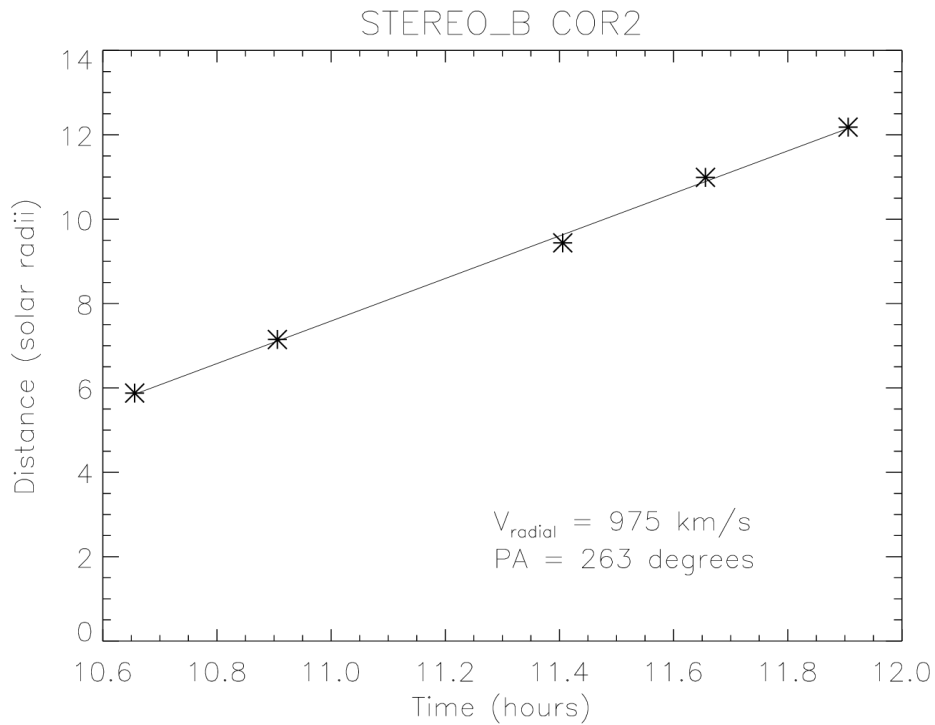


Figure 6.24 - The height-time profile of the CME on 2010/04/03 on the COR2B FOV for the fastest moving position angle. A linear fit is shown and the speed calculated is indicated. This CME was tracked by CORSET from 10:39 UT to 11:54 UT.

Table 6.4 - Kinematic parameters of the CME on 2010/04/03. The angles shown here are given in HEEQ coordinate system.

Parameter	Result
Longitude	$0 \pm 4^\circ$
Latitude	$-31 \pm 12^\circ$
Group speed v_g averaged over time	982 ± 5 km/s
Minimum value of time average radial speed $\overline{v_r}(\theta_j, \phi_k)$	965 km/s
Minimum value of time average radial speed $\overline{v_r}(\theta_j, \phi_k)$	989 km/s
Group speed as a function of time $v_g(t_{i+1})$	[1048, 872, 1046, 1070] km/s
Maximum error of the triangulation	< 0.1 solar radii

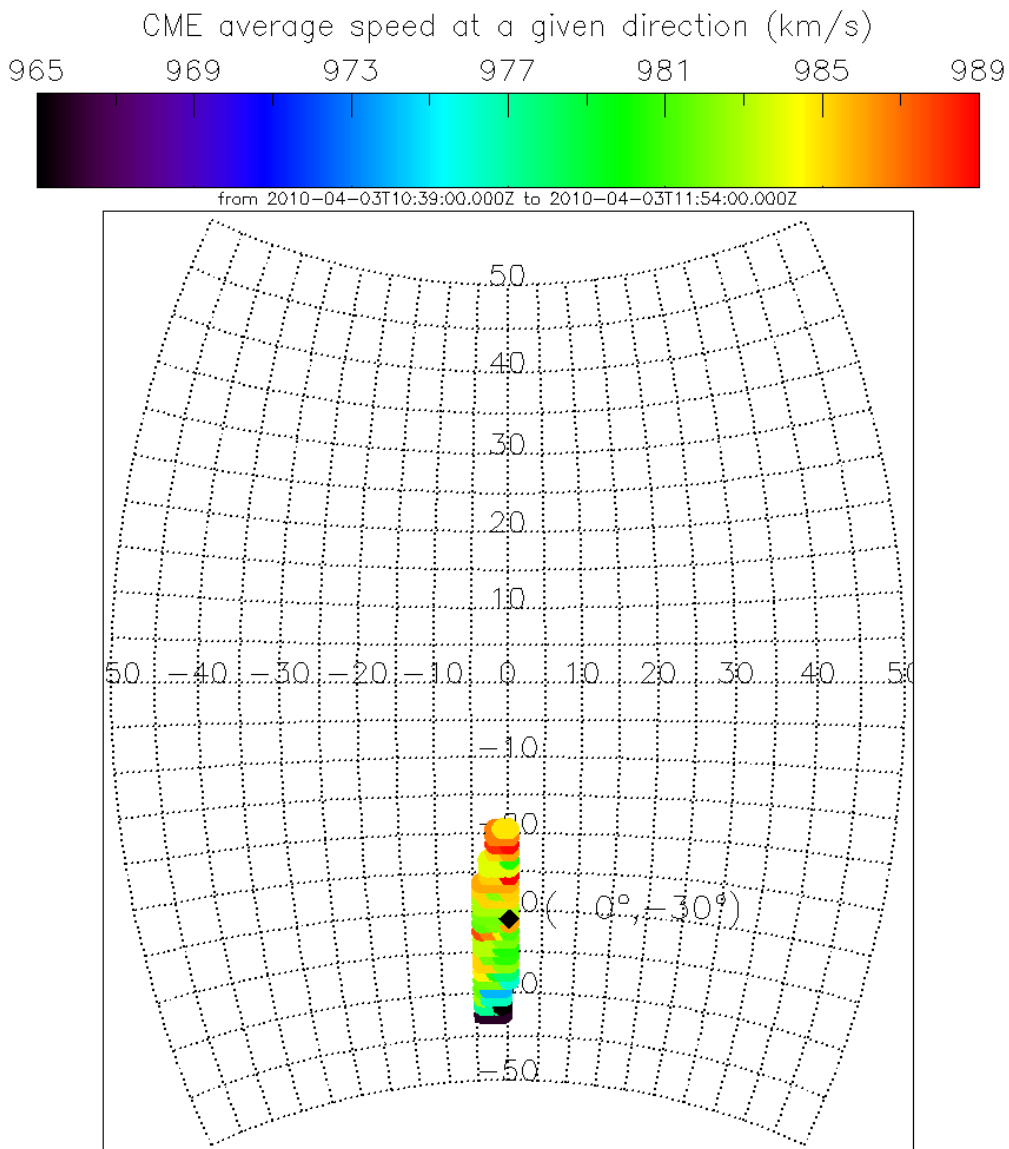


Figure 6.25 - The radial speed \bar{v}_r of the CME front as a function of latitude and longitude (in HEEQ coordinate system). The CME shown here was observed on 2010/04/03. The black diamond indicates the center of the CME front.

From CORSET3D results, the tridimensional average speed of the CME in the COR2 FOV is 984 km/s. Colaninno (2012) computed the apex of the GCS model and fit the height-time profile to multiple polynomial functions. The starting speed, computed at five solar radii, is similar to the result from this work. Rollett et al. (2012) studied this event using only the Heliospheric Imagers onboard STEREO, not using the observation from COR. They used two methods, the Fixed- Φ and Harmonic Mean. The first method was introduced by Sheeley et al. (1999) and it “assumes a radial propagation of a single plasma element along a straight line”. Although this result is

derived at distances much further from the Sun than in the CORSET3D analysis, the speed found is similar to the results from this Thesis if we take into account the error provided by the authors.

According to the results found from CORSET3D, this CME is directed significantly below the ecliptic plane (-29° in HEEQ, -22° in HEE). If the error of the triangulation method does not exceed 10° as estimated by Mierla et al. (2010), the CME should be directed at least about 10° toward south after taking into account the error. One possible source of error is that the region selected by CORSET3D does not correspond to the apex of the CME and corresponds only to a portion of it, ignoring some significant region. If these hypotheses were true, the results found by CORSET3D should not agree with previous works using different methods, but this is not the case. Colannino (2012) applied the CGS method at about 10 solar radii and found -19° of latitude (HEEQ). Other similar studies of this CME do not have any information about its latitudinal direction of propagation in coronagraphs FOV (ROLLETT et al., 2012; LIU et al., 2011). Liu et al. (2011) affirm that the source region of this CME is an active region located -25° of latitude.

The longitude of the CME propagation found using CORSET3D is -2° of the Sun-Earth line in a range up to 12 solar radii. Many previous papers also computed the longitude of the CME using different methods than CORSET3D. At 10 solar radii, Colannino (2012) found 6° using the CGS method. Another article computed the CME average longitude up to 16 solar radii and the result is 4° of longitude (MÖSTL et al., 2011). Other two articles extended the analysis at much further distances from the Sun including the observation from the Heliospheric Imagers. In the analysis of Liu et al. (2011) the direction of propagation is a function of time. Considering only the period covered by CORSET3D, the CME longitude starts at about -10° of longitude and gradually goes toward positive values, reaching about 10° at the end. At further distances from the Sun than studied here, the result from Liu et al. (2011) ranges mainly from 0° to 15° of longitude. Rollett et al. (2012), using exclusively the data from Heliospheric Imagers, got similar results using the Fixed- Φ method. The same authors also applied the Harmonic Mean method and the results are in disagreement with all the others mentioned here. In summary, the longitude found for this CME using CORSET3D seems to agree with most of previous works. The results commented here are listed in Table 6.5.

Table 6.5 - Comparison of the speed derived for the CME observed on 2010/04/03 by different previous works and two automatic catalogs (indicated by an asterisk).

Method and reference	COR2 A Speed	COR2 B Speed	De-projected speed	Latitude	Longitude	Details
CORSET3D (this Thesis)	956 km/s	975 km/s	984 km/s	- 22° (HEE)	-2° (HEE)	average up to 12 solar radii
CGS (Colaninno, 2012)	809 km/s	800 km/s	917 km/s	-19° (HEE)	6° (HEE)	average up to 10 solar radii
Triangulation (Liu et al., 2011)	-	-	[800-1000] km/s	-	[-10°, 15°] (HEE)	COR2, HI1 and HI2 FOVs
(Mostl et al., 2014)	-	-	829 km/s		4°	average up to 16.5 solar radii
Fixed- Φ (Rollett et al., 2012)	-	-	829 \pm 122 km/s	-	3° +- 4°	HI1 and HI2 FOVs
Harmonic Mean (Rollett et al. 2012)	-	-	829 \pm 122 km/s	-	-25° +- 10	HI1 and HI2 FOVs
CACTus (*)	833 km/s	833 km/s	-	-	-	COR2 FOV
SEEDS (*)	810 km/s	929 km/s	-	-	-	COR2 FOV

6.4 The magnetic cloud observed on 2010/04/12

6.4.1 The interplanetary medium

According to the ICME catalog, a MC was observed in the interplanetary medium from 2010/04/12 01:00 UT to 2010/04/12 15:00. The interplanetary data from OMNI is shown in Figure 6.26. This event has a maximum magnetic field intensity of 12 nT and the solar wind speed is always lower than 450 km/s. The beta parameter has some decrease during the MC period but it is much higher than 0.1. We slightly changed the period of the MC as indicated by the continuous vertical lines in Figure 6.26 in order to have a better agreement with the beta parameter and the IMF magnitude. The IMF is not smooth inside the magnetic cloud and the

orthogonal components have some small discontinuities. From the characteristics cited above, this event does not fill all the MC criteria.

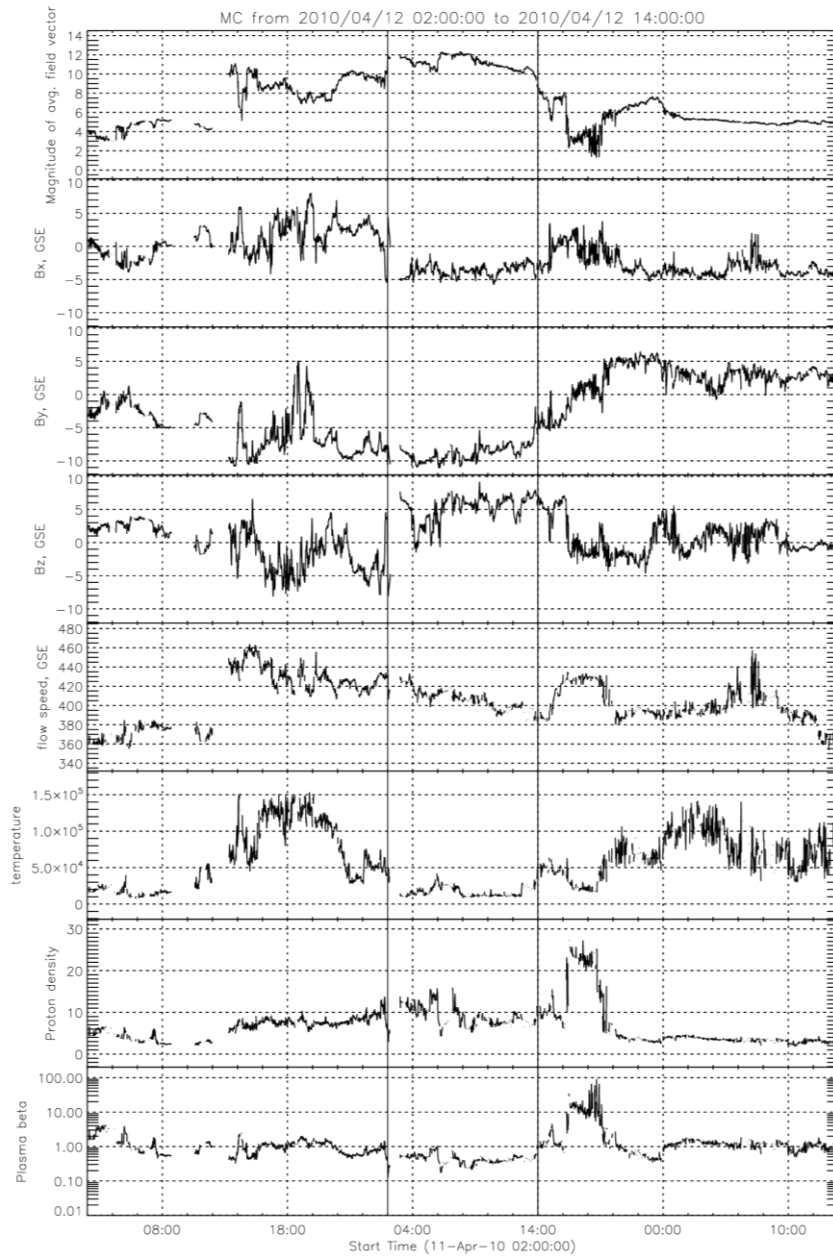


Figure 6.26 - The interplanetary magnetic field and plasma parameters during a MC on 2010/04/12.

From 2010/04/07 until the beginning of the MC, there is no ICME observed and the IMF is always lower than 5 nT, a typical value of a calm period. There is a shock at about 12:00 UT on 2010/04/08 and there is a sheath region between the shock and the beginning of the MC. There

also is a sector boundary in the interplanetary medium about 2 hours later the end of the MC period. The transition is from a sector toward the Sun (longitude of the IMF higher than 270°) to away from the Sun (longitude higher than 90°).

6.4.2 The cosmic ray observations

There is no clear decrease observed by the three neutron monitors during the MC period but there is a 1% decrease observed by McMurdo approximately half a day before probably due to the shock and/or sheath region, see Figure 6.27. The cosmic ray count rate from the GMDN does not have a common decrease for all stations (Figure 6.28).

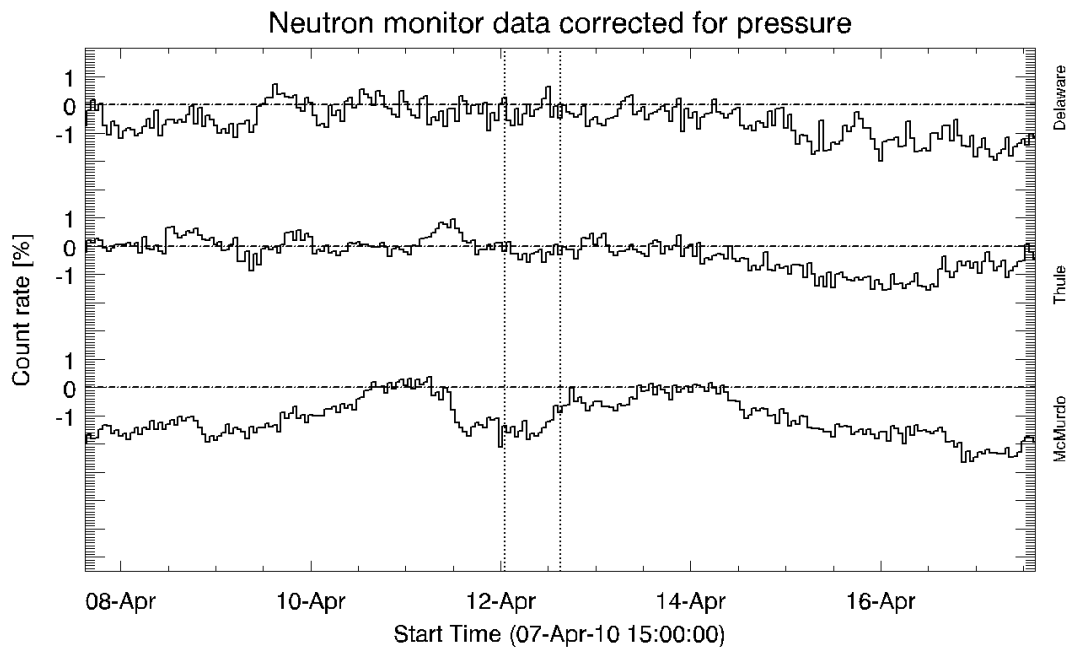


Figure 6.27 - The cosmic ray decrease observed by three different neutron monitors (Delaware, Thule and McMurdo) during the MC on 2010/04/12.

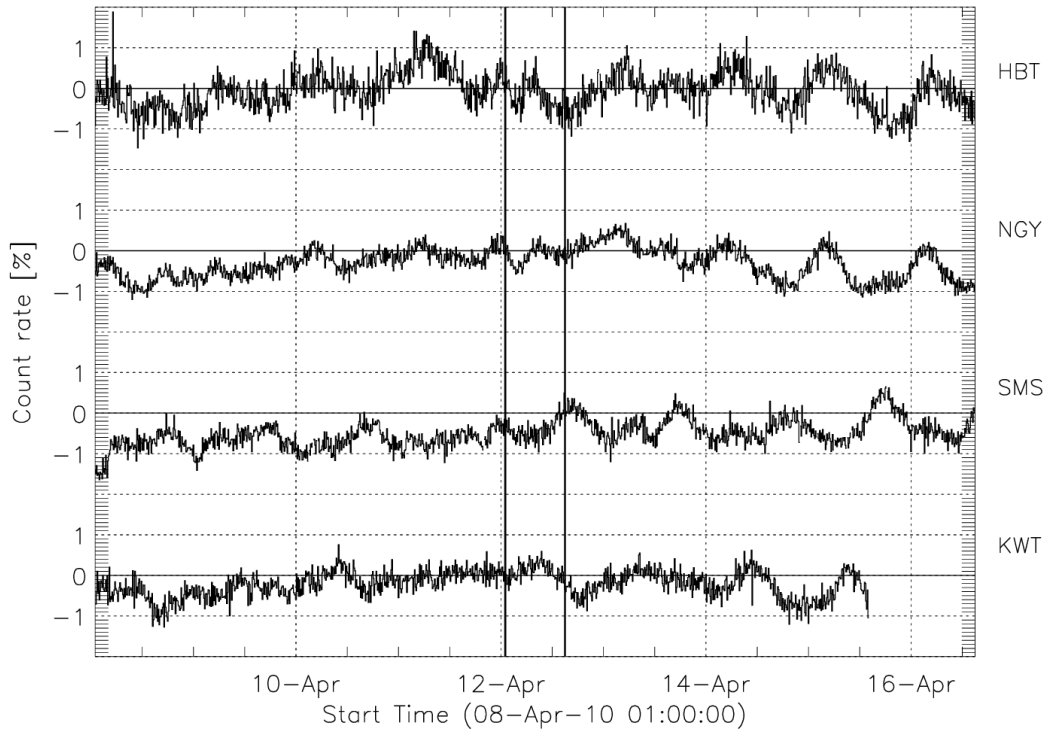


Figure 6.28 - The cosmic ray decrease observed by the vertical directional channels of the GMND during the MC on 2010/04/12.

Using the methodology described in Chapter 3, the resulting cosmic ray isotropic intensity has a decrease of about 0.5% (Figure 6.29). We calculated and compared the anisotropy components parallel and perpendicular to the IMF. From at least one day before the MC until its end, the perpendicular component is dominant and, thanks to this, the cosmic ray gradient calculated using Equation 3.13 is a good approximation of the total gradient.

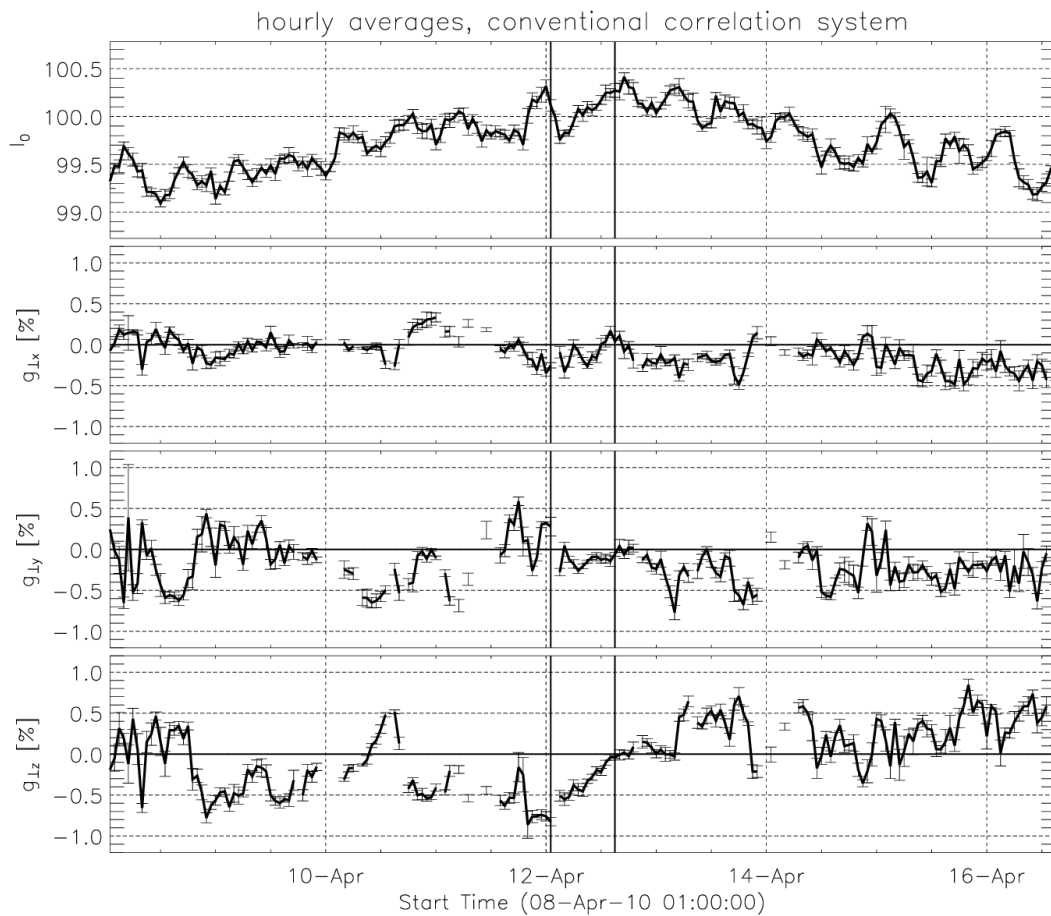


Figure 6.29 - The isotropic cosmic ray intensity and the orthogonal components of the cosmic ray fractional gradient during the MC period on 2010/04/12.

One explanation for the low cosmic ray count rate decrease might be the combination of low values of maximum IMF intensity (12 nT) and low solar wind speed (440 km/s). The "z" component of the cosmic ray gradient is mainly negative since the beginning of the plot until the end of the event. This fact suggests that some structure was modulating the cosmic rays before the period of the magnetic cloud, possibly another structure but not the MC, perhaps a shock and/or sheath region. This structure produced a decrease in the cosmic ray intensity above the ecliptic plane, therefore producing a maximum of the cosmic ray density below the ecliptic. The modeled cosmic ray cylinder moves mainly in the GSE "y" direction and with less amplitude in the GSE "x" direction. To our understanding, the CRC model result is not consistent with a magnetic cloud since it is not approaching the Earth and we discarded the results. One hypothesis here is that the cosmic rays observed by the GMDN in the period analyzed here are

modulated mainly by the sector boundary rather than by the MC. As a result, the model is actually reproducing a sector boundary region moving perpendicular to the Sun-Earth line.

6.4.3 The origins in the solar corona

According to the CDAW CME catalog (YASHIRO et al., 2004), there is only one halo CME observed by LASCO-C2 and LASCO-C3 from 2010/04/07 to 2010/04/11. We inspected the position angle of all CMEs on COR2A and COR2B FOVs and we conclude that the halo CME was ejected toward the Earth and no other CME propagates in the same direction.

The earthward CME was ejected on 2010/04/08 and was tracked using CORSET in six frames observed from 05:24 UT to 06:54 UT. We tested CORSET using the standard set of parameters but we notice that the area selected in the last frames included not only the CME but also part of the background. On the first frames, however, part of the CME was not selected. In this way, CORSET selected different features and different frames. This effect could lead to an erroneous idea of acceleration of this CME.

After testing other possibilities without proper CME identification, we adopted $Q = 0$, i.e., the region used to compute the GLCM has the size kept constant for all frames (more details about the expansion factor are explained in Section 4.5). When we set $Q = 0$ we do not use a sample area to compute the CME in the first frame because its texture can possibly be so different from the texture of the last one so that the latter is computed as a background by CORSET. As an illustration, we tested CORSET using a sample area on the first frame and the CME was identified correctly only on that frame. On the remaining, the area selected decreased as time passes so that the last one had a negligible area. This result was discarded because it certainly did not follow the CME definition. If the sample region to compute the texture is taken from the first frame, the GLCM of the last frame will have intermediate values between the background matrix and the CME matrix. As a result, the statistical test may consider parts of the CME as being background. If the sample region is taken from a frame close to end of the CME observation period, this possibility is reduced.

Finally, we kept $Q = 0$ and used a sample area of the CME taken from the fourth frame (in case of COR2A) and from the sixth frame (in case of COR2B). The result found is consistent with the definition of CME and seems to keep selection of the same feature of the CME as time passes.

As for the base image, we used the mean of a pair of frames observed up to one hour before the first CME observation in COR2. In the case of A, the pair is 02:54 and 03:24 and for B is 03:24 and 03:54. The result of the CME tracking using CORSET is shown in Figure 6.30 and Figure 6.31.

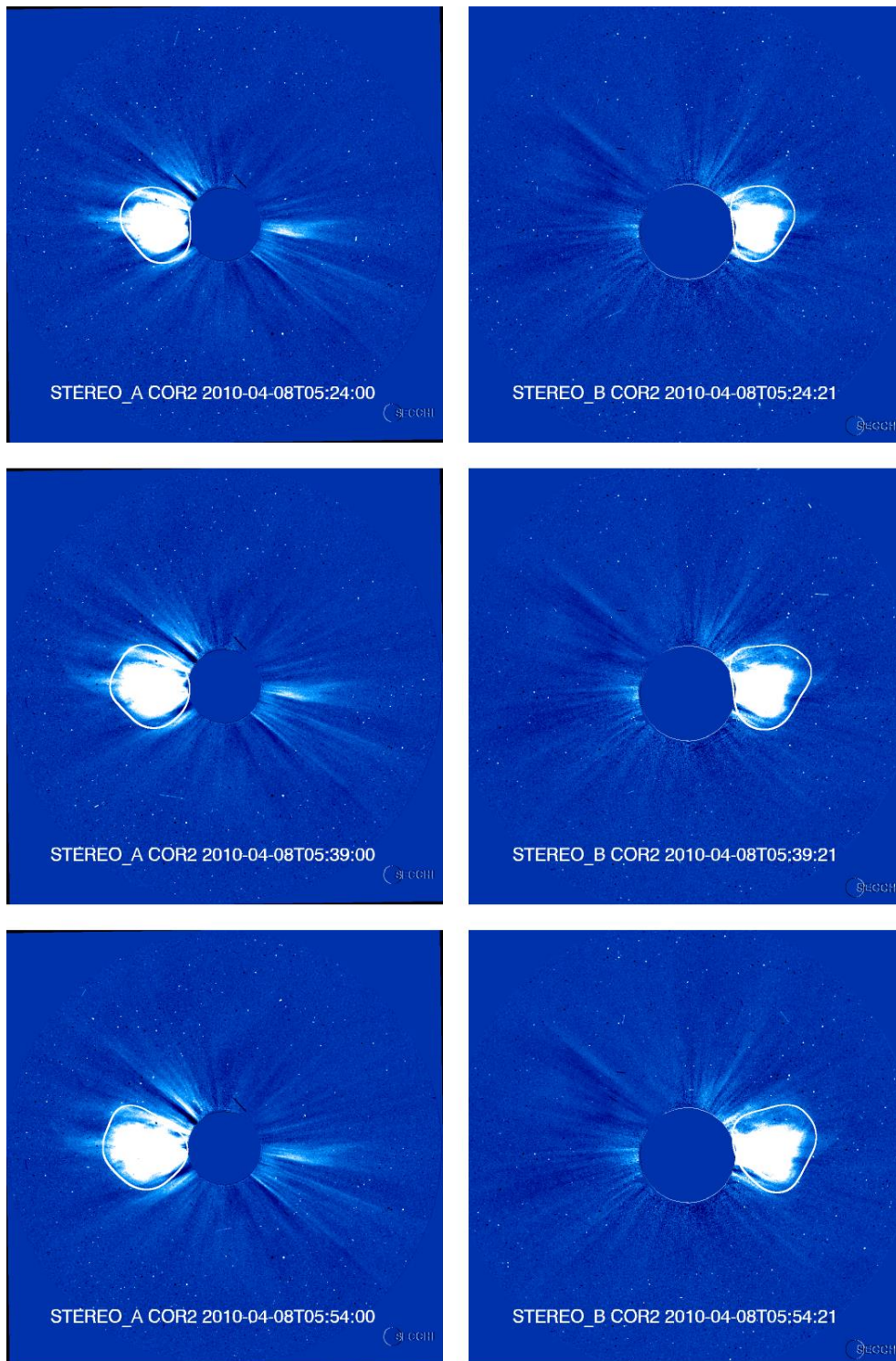


Figure 6.30 - The CME observed on 2010/04/08 on COR2A (left column) and COR2B (right column) FOVs. In this Figure, only the first three frames are shown.

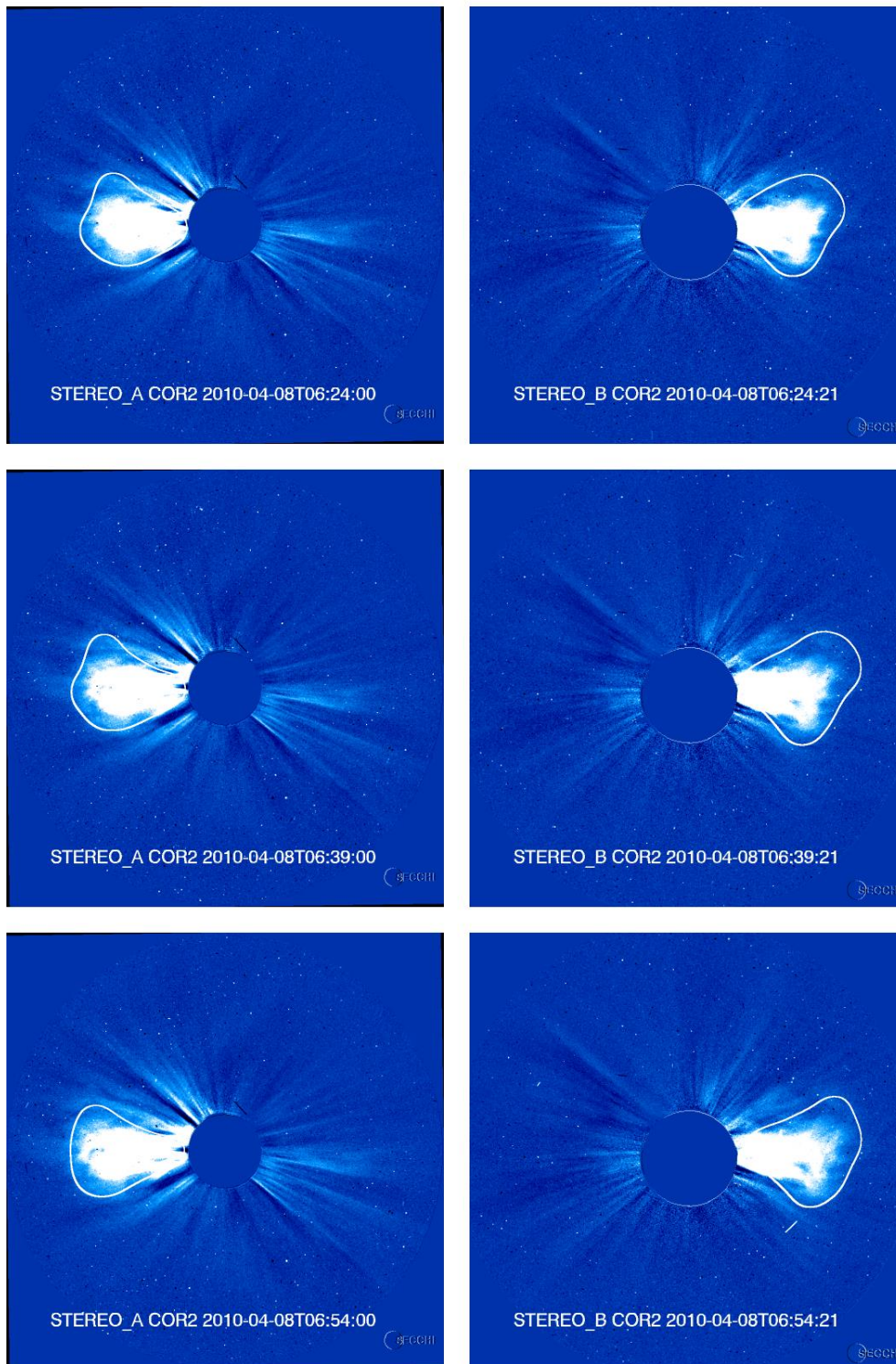


Figure 6.31 - The CME observed on 2010/04/09 on COR2A (left column) and COR2B (right column) FOVs. In this Figure, only the fourth, fifth and sixth frames are shown.

The results of the projected speed compared to previous works are shown in Table 6.6. All methods shown used a linear fit on the height-time profile produced only on COR2 FOV. Due to limitations of CORSET, the time window is smaller than the one used in other studies mentioned here: while we tracked the CME here for two hours, the automatic catalogs tracked it for more than three. According to Table 6.6, the trend is that the speed from CORSET tend to be higher than the remaining, except for CACTus. In the height-time profiles from CORSET, the linear fit produced is good. In those from SEEDs, we noticed that the first point in both coronagraphs do not fit with the remaining. As a result, speeds derived from the linear fit are smaller than they should be. From the remaining references, we do not have the height-time available.

Table 6.6 - The projected speed of the CME observed on 2010/04/08 on the COR2A and COR2B FOVs.

Method	COR2 A Speed	Time window	COR2 B Speed	Time window
CORSET	512 km/s	[05:24-07:24]	576 km/s	[05:24-07:24]
Colaninno (2012)	421 km/s	?	425 km/s	?
CACTus	520 km/s	[03:54-07:54]	543 km/s	[04:24-08:24]
SEEDS	478 km/s	[03:24-07:24]	492 km/s	[03:54-06:54]

The results from CORSET3D are shown in Figure 6.32 and Table 6.7. We noticed by the tie-points that this CME has maximum distance from the Sun in the portion with higher latitude. This trend is kept for any time available. For instance, on the last frame, the tie-point with highest latitude (4°) is 10.8 solar radii distant from the Sun while the tie-point in the other extreme portion (latitude of -15°) is 9.8 solar radii. Taken into account that the triangulation error is less than 0.1 solar radii for this case, the difference cannot be ignored.

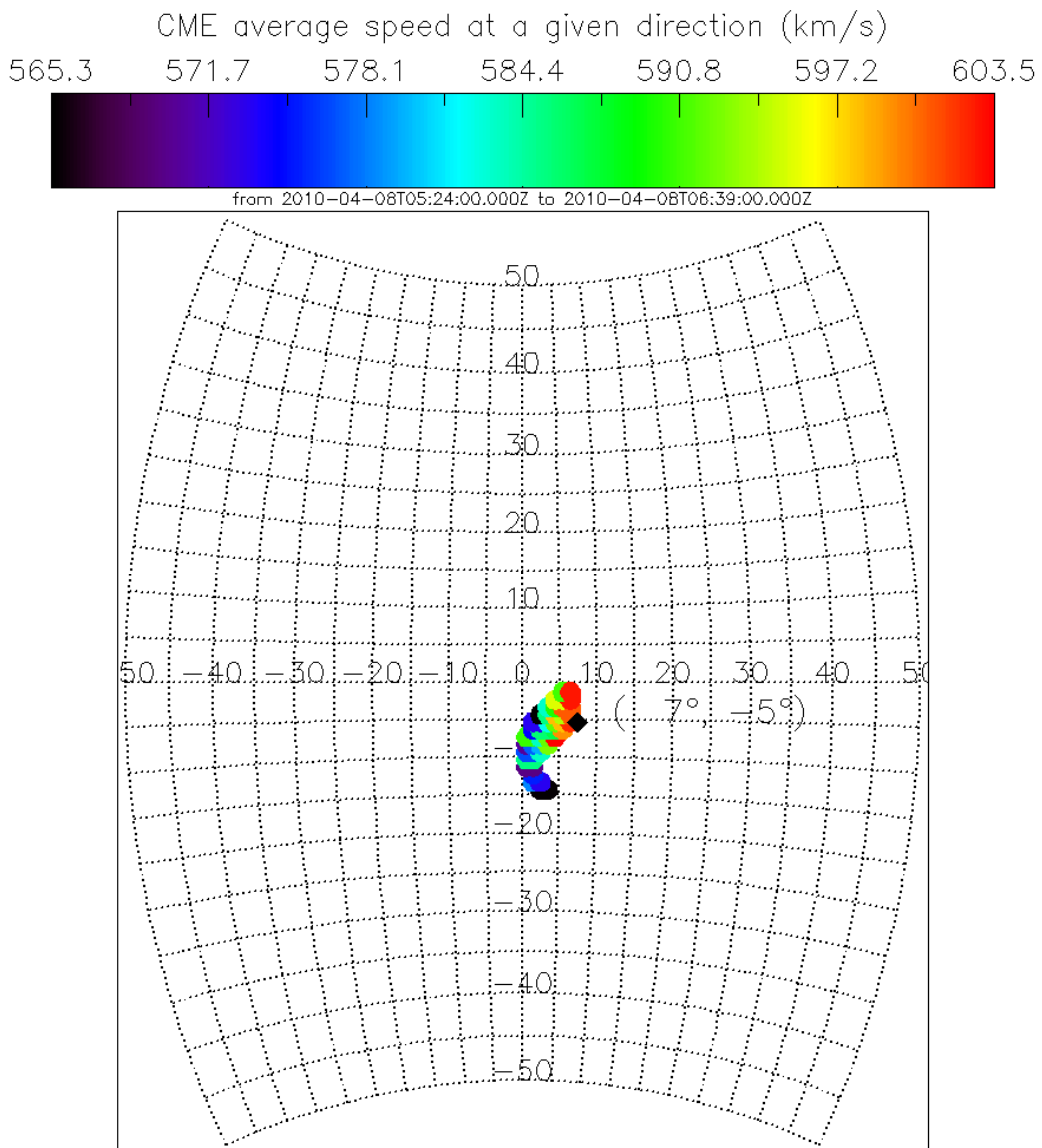


Figure 6.32 - The radial speed of the CME front as a function of latitude and longitude (in HEEQ coordinate system). The CME shown here was observed on 2010/04/08. The black diamond indicates the center of the CME front.

Table 6.7 - Kinematic parameters of the CME derived using CORSE3D. The angles shown here are given in HEEQ coordinate system.

Parameter	Result
Longitude	$7 \pm 7^\circ$
Latitude	$-5 \pm 9^\circ$
Group speed v_g averaged over time	590 ± 19 km/s
Minimum value of time averaged radial speed $\bar{v}_r(\theta_j, \phi_k)$	560 km/s
Maximum value of time averaged radial speed $\bar{v}_r(\theta_j, \phi_k)$	639 km/s
Group speed as a function of time $v_g(t_{i+1})$	[720, 385, 619, 656] km/s
Maximum error of the triangulation	0.1 solar radii

Using the GCS and forward modeling at 10 solar radii, Colaninno (2012) found -2° of longitude and -3° of latitude in the HEE coordinate system. Converting the result from CORSET3D to the same coordinate system, we have 7° of longitude and -4° of latitude. Although the difference in the direction of propagation is 9° of longitude, the results from both methods are in agreement with each other if we take into account the error estimated by Mierla et al. (2010). The de-projected speed we derived using CORSET3D (590 km/s), however, is significantly higher than the initial speed found by Colaninno (2012) which is 468.5 km/s.

As mentioned above, the CME has highest de-projected speed on its portion located at maximum latitude. This fact suggests, combined to the latitude observed close to the ecliptic, that the ICME/MC should be observed at Earth close to the ecliptic plane. The cosmic ray gradient calculated in Section 6.4.2 indicates some structure located mainly above the ecliptic plane. This is because the cosmic ray gradient is highly negative in the “z” direction (GSE coordinates) during the ICME period, suggesting that the cosmic ray depleted region is probably located mainly in the positive “z” direction (GSE coordinates).

The application of the GCS model close to the Earth vicinity also suggests that the ICME is located above the ecliptic plane (COLANINNO, 2012). This is shown in the second panel of Figure 6.33 (represented by the blue curve). The structure shown in green is the elliptic flux rope (EFF) model in the vicinity of the Earth calculated from in situ data. Both models are expected to produce similar results since they are done for a corresponding pair of CME and MC. However, “there is no similarity between the results of the GCS and the EFR for this CME” since “the size between the two models differs by an order of magnitude” and “the tilt of the models is different by 45° ” (COLANINNO, 2012). According to our observation from the in-situ data from interplanetary medium (Section 6.4.1), this event is not a good example of the magnetic cloud and, therefore, the application of flux rope model is expected to be worse than in the cases where the interplanetary structure does not follow the MC criteria strictly. The axis of the EFR model were found to be 0.02 AU and 0.01 AU. These values are quite small for a typical MC whose radius is expected to be 0.5 AU. Due to these two reasons, we believe that the results from the GCS model are more reliable than those from the EFR.

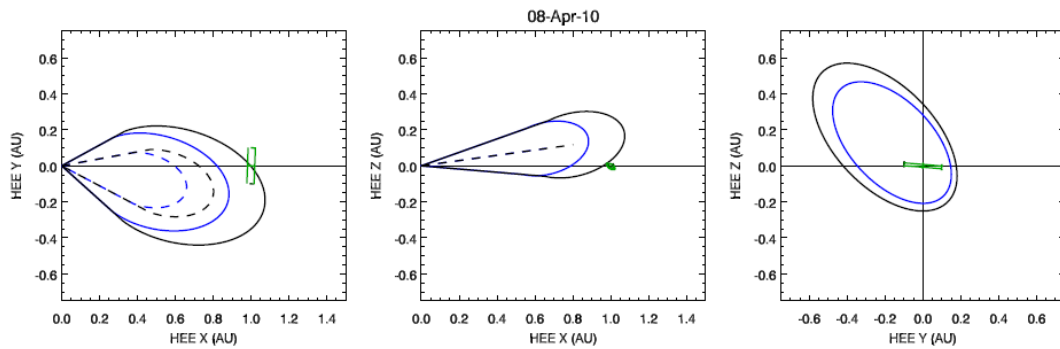


Figure 6.33 - The projection of the GCS model (blue) of the elliptical flux rope model (in green) which is done using in situ data and the GCS model. Source: Colaninno (2012)

6.5 The magnetic cloud observed on 2010/05/28

6.5.1 The interplanetary medium

The interplanetary magnetic field and plasma parameters for the MC observed on 2010/05/28 are shown in Figure 6.34. The two vertical continuous lines indicate the beginning and end of the structure. These limits are chosen according to the beta parameter. In this plot, the main signature of the magnetic cloud is the smooth and wide rotation of the magnetic field vector and the magnitude has a maximum of about 15 nT. Other signature of a MC is the low proton temperature inside it than outside. The plasma beta also shows a typical signature of a MC: its value is very close to 0.1 during most of the MC period. The solar wind during this MC is considerably slow (about 350 km/s).

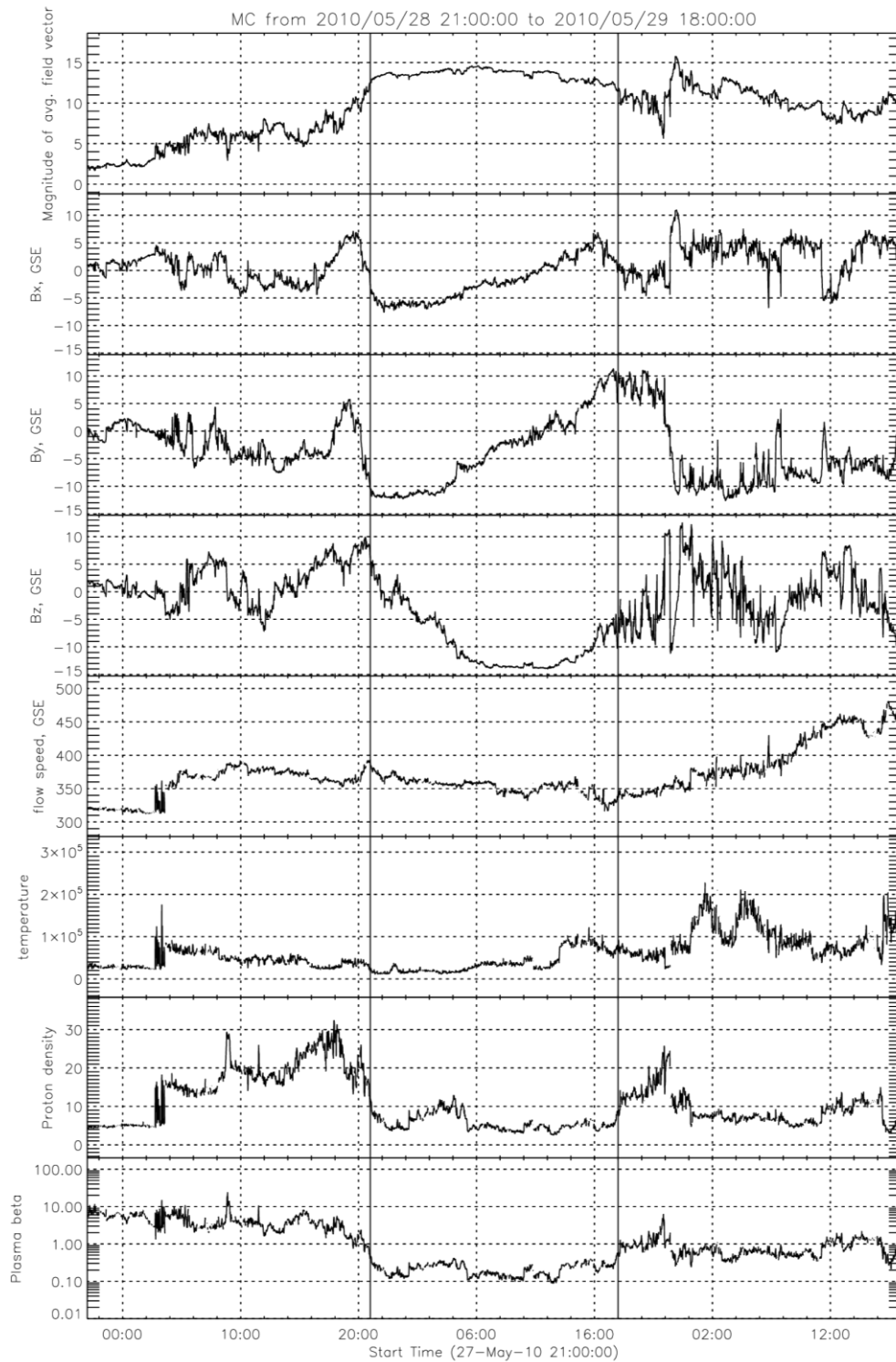


Figure 6.34 - The interplanetary magnetic field and plasma parameters during a MC observed on 2010/05/28.

A few days before the MC (2010/05/26), there is a sector boundary and the polarity changes from away to toward the Sun. Latter, there is a sheath structure observed (notice the discontinuity in the first hours of 2010/05/28). The IMF magnitude, the flow speed, the proton temperature and density increase during this period. After the MC period, the interplanetary medium does not have typical behavior of a calm period because the IMF is at relatively high levels. The structure following the MC does not have the characteristics of another MC. The IMF magnitude decreases only on 2010/05/31 when it reaches an average value of approximately 5 nT, a typical value of a calm period.

6.5.2 The origins in the solar corona

We inspected the LASCO-C3 images between 2010/05/23 0:00 UT to 2010/05/28 0:00 UT and found two halo CMEs. Then we inspected the coronagraph images from COR2A and COR2B to decide whether these CMEs were ejected toward or away from the Earth and we concluded that both are earthward directed. The first earthward CME was observed on 2010/05/23 and the second on 2010/05/24. See details in Table 6.8.

Table 6.8 - The two CMEs associated to the MC observed in 2010/05/28.

Parameter	CME #1	CME #2
Date	2010/05/23	2010/05/24
First observation at LASCO-C2	18:06	14:06
First frame tracked by CORSET on COR2 FOV	18:54	15:39
Last frame tracked by CORSET on COR2 FOV	20:39	16:24
Expansion parameter Q	4 (A); 8(B)	4
Number of frames tracked	6	3

The results of the CME tracking using CORSET are shown in Figure 6.35, Figure 6.36 and Figure 6.37. The images shown here were processed using a base difference image, in other words, we subtract a given common image (called base) from all the images of the analyzed period. Since the corona is very dynamic, we need to choose images from a period as close as possible to the beginning of the MC. If we choose an image where any CME is present it creates a region of a “ghost CME” (dark region due to the subtraction of the bright structure) which may prevent CORSET from identifying the CME satisfactorily.

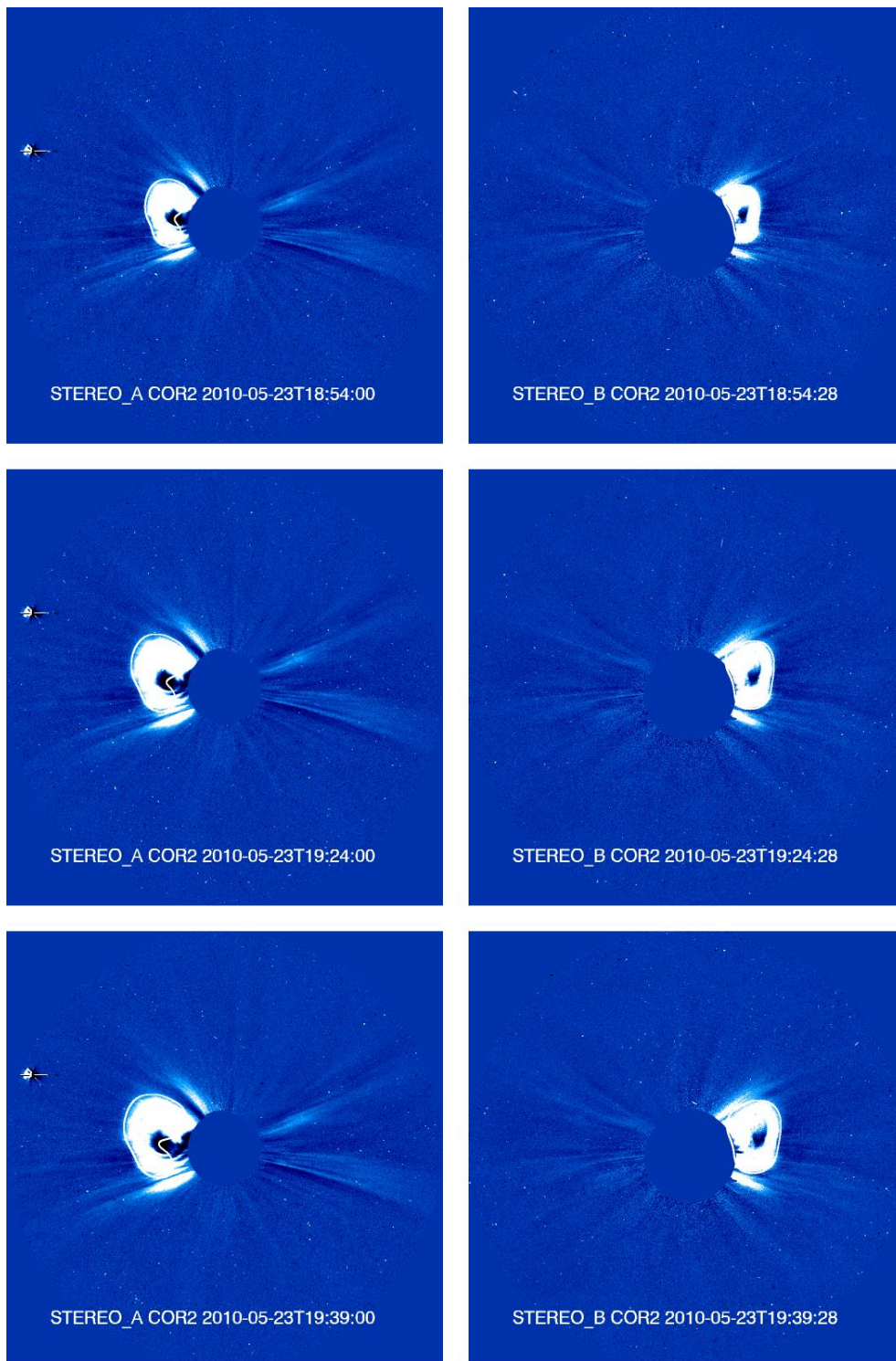


Figure 6.35 - The CME observed on 2010/05/23 on COR2A (left column) and COR2B (right column) FOVs. In this Figure, only the first three frames are shown.

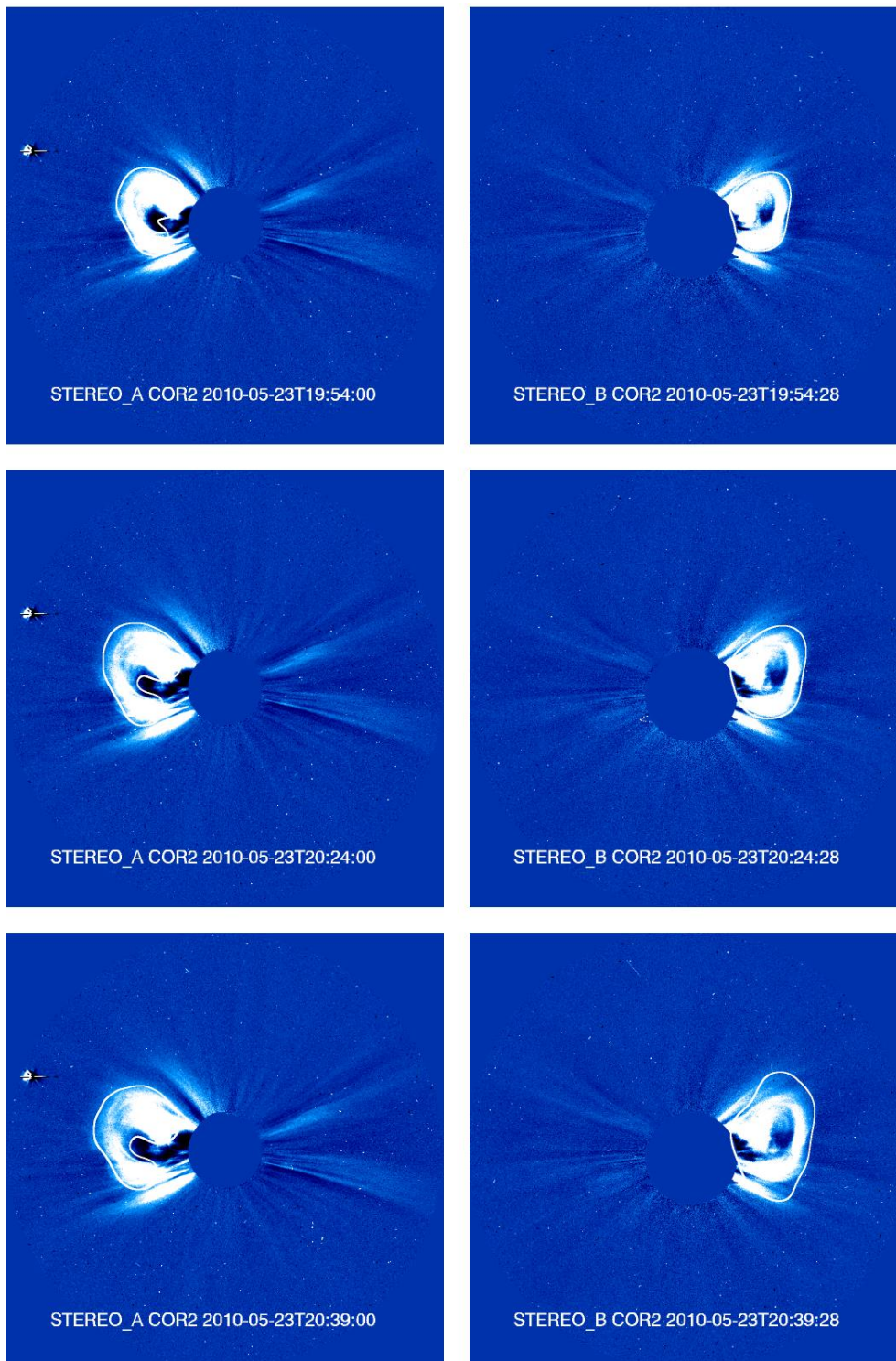


Figure 6.36 - The CME observed on 2010/05/23 on COR2A (left column) and COR2B (right column) FOVs. In this Figure, only the fourth, fifth and sixth frames are shown.

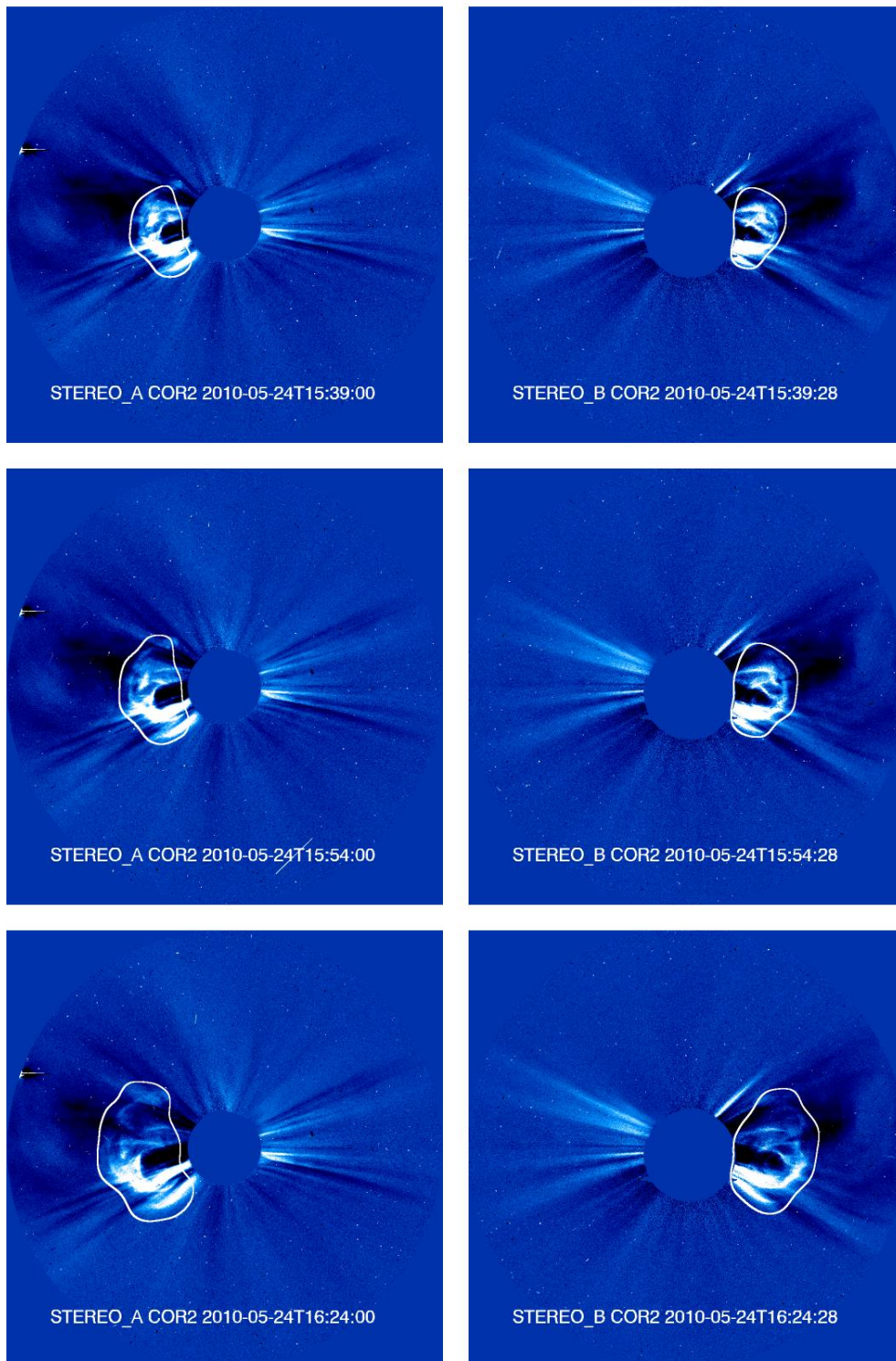


Figure 6.37 - The CME observed on 2010/05/24 on COR2A (left column) and COR2B (right column) FOVs. In this Figure, only the first three frames are shown.

The base image chosen here created a dark region close to the occulter and this resulted in inconsistent selection of the CME in the inside region. Since we take into account only the external shell of the CME, this error do not affect the results of neither the speed and direction estimations. The results of the radial speed of the CME, after the application of CORSET3D, are shown in Figure 6.38, Figure 6.39 and Table 6.9.

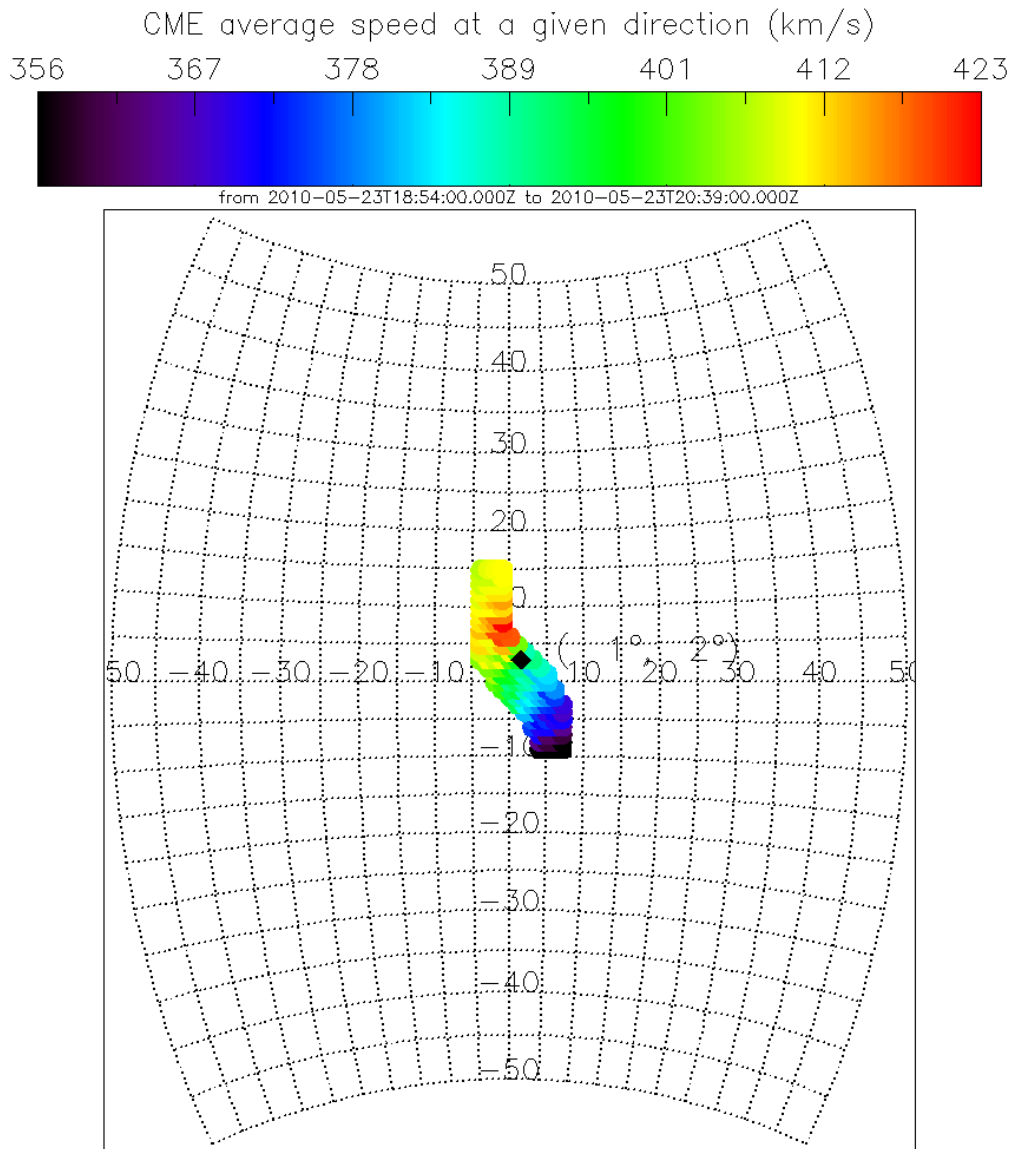


Figure 6.38 - The radial speed of the CME front as a function of latitude and longitude (in HEEQ coordinate system). The CME shown here was observed on 2010/05/23. The black diamond indicates the center of the CME front.

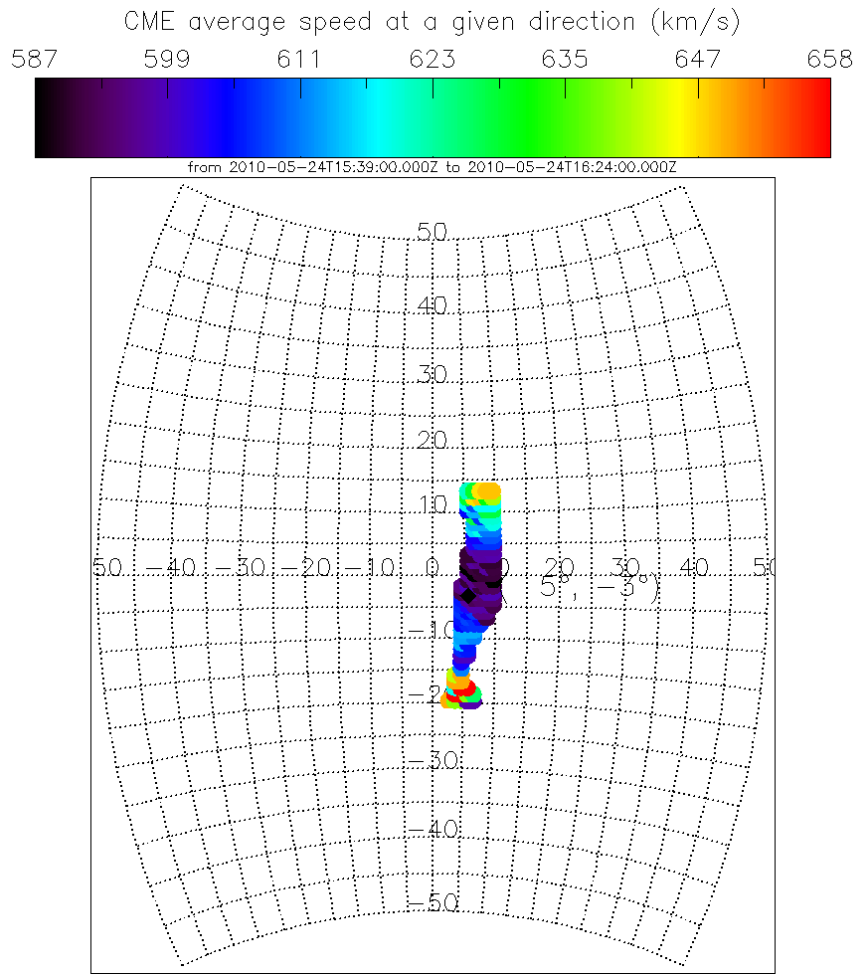


Figure 6.39 - The radial speed of the CME front as a function of latitude and longitude (in HEEQ coordinate system). The CME shown here was observed on 2010/05/24. The black diamond indicates the center of the CME front.

Table 6.9 - Kinematic parameters of the CME on 2010/05/23 and 2010/05/24. The angles shown here are given in HEEQ coordinate system.

Parameter	2010/05/23	2010/05/24
Minimum and maximum latitudes	[-10.0°, 15.8°]	[-20.4°, 14.0°]
Minimum and maximum longitudes	[-4.8°, 8.1°]	[0.7°, 10.6°]
Group speed v_g averaged over time	394±18 km/s	610±18 km/s
Central direction of the CME averaged over time (longitude)	2°	6°
Central direction of the CME averaged over time (latitude)	3°	3°
Minimum value of $\bar{v}_r(\theta_j, \phi_k)$	356 km/s	587 km/s
Maximum value of $\bar{v}_r(\theta_j, \phi_k)$	423 km/s	658 km/s
Group speed as a function of time $v_g(t_{i+1})$	[371, 364, 388, 393, 466] km/s	[661, 574] km/s
Maximum error of the triangulation	< 0.1 solar radii	< 0.1 solar radii

Lugaz et al. (2012) previously studied both CMEs analyzed here and their results are compared to those from CORSET3D in Table 6.10 (first CME) and Table 6.11 (second CME). Projected speed from automatic catalogs such as CACTus and SEEDs are also listed for comparison. These catalogs, unfortunately, do not have any study of the de-projected CME speed nor the direction of propagation. Colaninno (2012) did not include this event in her analysis because events with more than one CME earthward directed in the days preceding the ICME were ignored. Results derived using CORSET3D for the first CME are in good agreement with those from Lugaz et al. (2012) for both the speed and direction. For the second CME, there is a difference in the longitude angle of 19° which is higher than the estimated error or 10°.

According to the results found here and in Lugaz et al. (2012), the first CME, ejected less than 24 hours ahead of the second CME, has a significantly lower speed than the second CME. A simple calculation suggests that the second CME will reach the first before their arrival at Earth. By using observations from the Heliospheric Image, Lugaz et al. (2012) concluded that the CMEs interact with each other and that the propagation angle is changed after the collision: the first CME is deflected slightly eastward and the second westward of the Earth.

Table 6.10 - Comparison of the speed derived for the CME observed on 2010/05/23 (CME #1) by different previous works and two automatic catalogs (indicated by an asterisk).

Reference	COR2 A Speed	COR2 B Speed	3D speed	Latitude	Direction of propagation	Details
This work	393 km/s	467 km/s	413 km/s	4° S (HEE)	3° W (HEE)	Average up to 12 solar radii
Lugaz et al. (2012)	362 km/s	378 km/s	[300-400] km/s	0°S	10° W	CGS method at 9.5 solar radii
CACTus (*)	378 km/s	390 km/s	-	-	-	-
SEEDS (*)	363 km/s	365 km/s	-	-	-	Average up to 12 solar radii

Table 6.11 - Comparison of the speed derived for the CME observed in 2010/05/24 (CME #2) by different previous works and two automatic catalogs (indicated by an asterisk).

Reference	COR2 A Speed	COR2 B Speed	3D speed	Latitude	Direction of propagation	Details
This work	766 km/s	646 km/s	603 km/s	4° S (HEE)	7° W (HEE)	Average up to 12 solar radii
Lugaz et al. (2012)	650 km/s	650 km/s	[500-700] km/s	2°S	26° W	CGS method at 9.5 solar radii
CACTus (*)	480 km/s	No CME	-	-	-	-
SEEDS (*)	504 km/s	536 km/s	-	-	-	Average up to 12 solar radii

6.5.3 The cosmic ray observation and modeling

When inspecting the GMDN vertical count rate, the decrease during the MC period is not very clear because the count rate is not stable in the days before (Figure 6.40). On the other hand, the three cosmic ray neutron monitors used in this Thesis shown a decrease up to $\sim 2\%$ starting in close timing with the beginning of the MC, as shown in Figure 6.41. McMurdo has a sharp decrease (compared to the other two stations) followed by an increase and, right after, by another decrease.

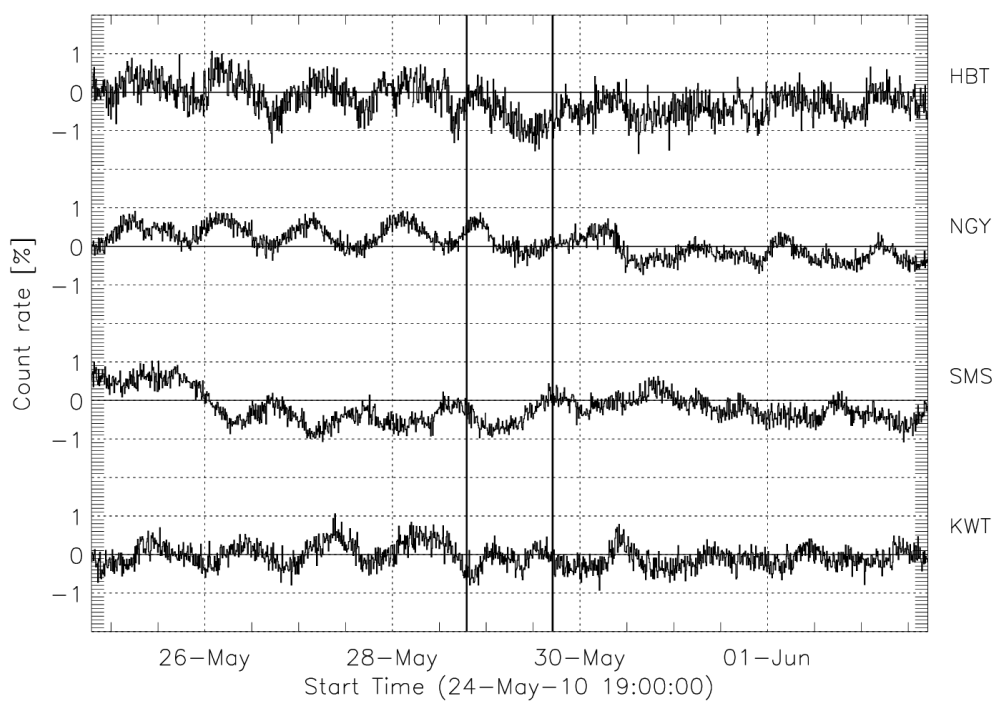


Figure 6.40 - The normalized cosmic ray count rate observed by the vertical directional channels of the GMDN during the MC on 2010/05/28.

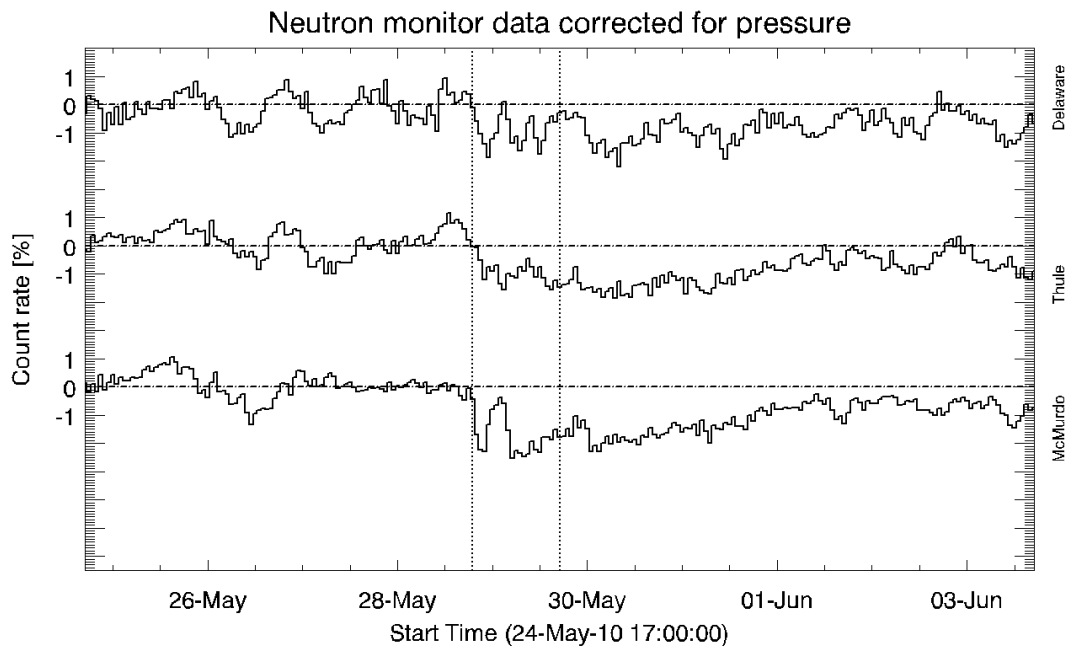


Figure 6.41 - The normalized cosmic ray count rate observed by three different neutron monitors (Delaware, Thule and McMurdo) during the MC on 2010/05/28.

We carefully compared the component of the anisotropy parallel to the IMF with the component perpendicular to the IMF and concluded that the first is much smaller than the second component. Therefore, we can consider the perpendicular component of the gradient as a good approximation of the total gradient and we may use the cylinder model with the perpendicular component of the gradient, i.e., we can use Eq. 3.3.

We selected a slightly different period for the cosmic ray cylinder model than the period shown in Figure 6.42 chosen using the interplanetary parameters: the last hour was removed because the isotropic intensity does not continue to increase in that hour and starts decreasing. The results of the model are shown in Figure 6.42 and Figure 6.43. Since the isotropic intensity must be similar at the beginning and end of the cosmic ray cylinder model, the inclusion of the last hour increases the residue when we use it in the model. The model was ran using the conventional and new correlation system and both results are shown in Table 6.12. If we change the beginning and at the end of the cosmic ray cylinder model period, the results do not change significantly or change less than the differences between the two columns of Table 6.12.

The cosmic ray gradient is always positive in the “y” component (Figure 6.42), this indicates that the cloud axis is always located in negative “y” axis. Notice, however, that the magnitude of the

“y” component (last row of Table 6.12) is never bigger than the cylinder radius indicating that the depleted region extends until the positive side of the “y” component, surrounding the Earth during all the period. This result is consistent with CME direction of propagation from this Thesis and from Lugaz et al. (2012) since both CMEs were ejected westward of the Earth and the resulting structure formed by the interaction should be located westward of the Earth.

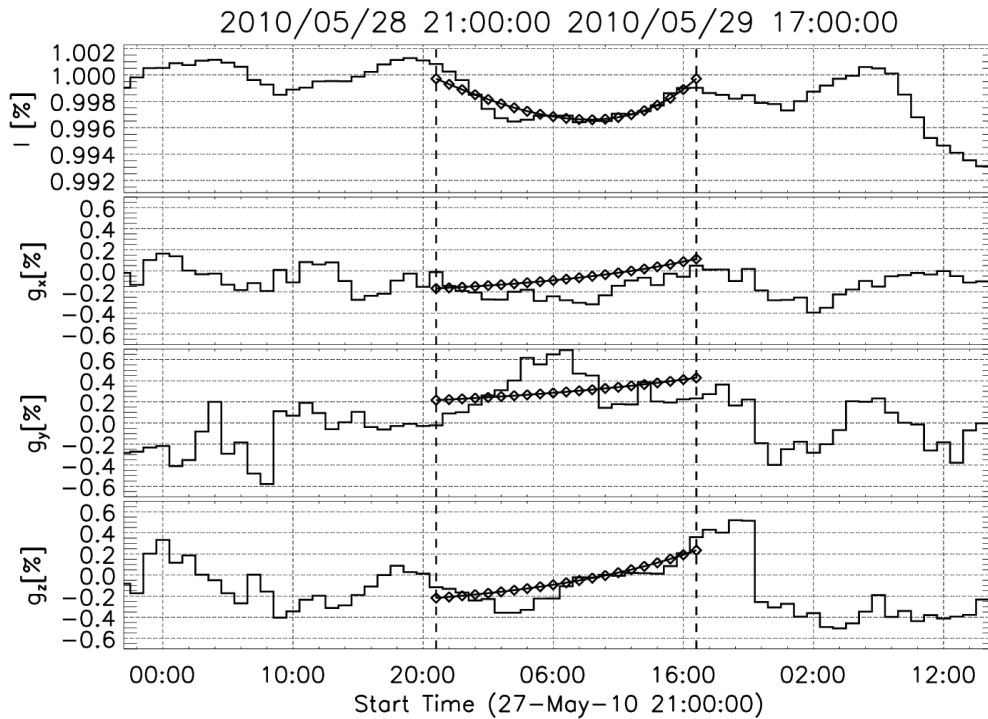


Figure 6.42 - The observation and modeling of cosmic ray depleted region associated to the magnetic cloud on 2010/05/28. The stair plot is the observed data (from conventional correlation system) and the line with diamonds is the modeling of the cosmic ray depleted region. The first panel, from top to bottom, shows the isotropic intensity. The remaining three plots show the orthogonal components of the fractional cosmic ray density gradient in the GSE coordinate system. The two vertical dashed lines correspond to the beginning and the end of the cosmic ray depleted region chosen by eye. These timings are indicated on top of the plot.

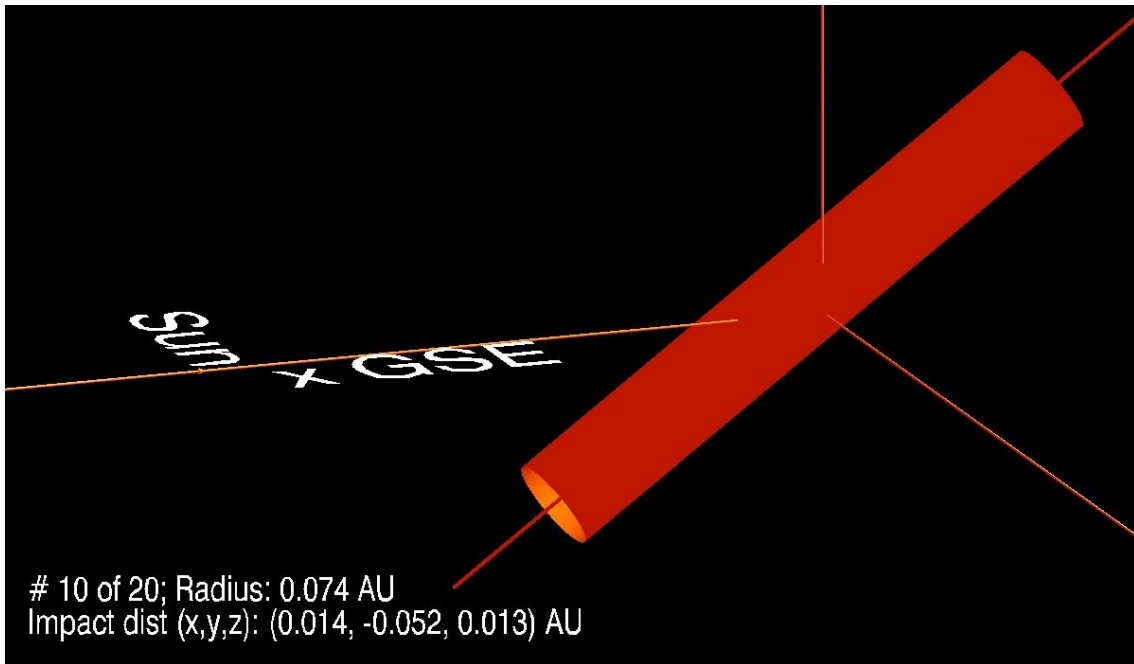


Figure 6.43 - A tridimensional representation of the cylinder derived from CRC model on 2010/05/29 at 07:00 UT. The Earth is located in the origin of the GSE coordinate system (represented by the three axis).

Table 6.12 - Parameters of the cosmic ray cylinder model of the MC observed on 2010/05/28.

Parameter	Conventional correlation system	New correlation system
Start period of analysis	2010/05/28 21:00:00	
End period of analysis	2010/05/29 17:00:00	
Time with minimum cosmic ray isotropic intensity	10:57	09:26
Minimum cosmic ray isotropic intensity	-0.7 %	-0.8 %
Larmor radius (AU)	0.02	0.02
Latitude (degrees, GSE)	33°	45°
Longitude (degrees, GSE)	186°	186°
Impact distance (AU)	-0.05	-0.04
κ_0 (dimensionless)	109	122
Cylinder radius (AU)	0.07	0.07
Cylinder radius expansion speed (AU/hour)	-0.001	-0.001
Residue	0.013	0.015
Position at the beginning [GSE coordinates, AU]	[0.04,-0.05, -0.05]	[0.06, -0.04, 0.05]
Position at the end [GSE coordinates, AU]	[-0.02,-0.05,-0.03]	[-0.03, -0.04, -0.03]

The radius of the flux-rope is found to be 0.11 AU by Lugaz et al. (2012) while the radius found by the cylinder model ranges from 0.09 AU (at the beginning) to 0.07 AU (at the end).

Lugaz et al. (2012) performed the Grad-Shafranov reconstruction and it shows a structure with main axis of 80° of latitude. The MVA using the same period of time than the cosmic ray cylinder

model (2010/05/28 21:00 UT to 2010/05/29 17:00 UT) results in latitude $\theta = 72^\circ$ and longitude $\phi = 71^\circ$ and ratio of $\lambda_2/\lambda_3 = 10.6$. Taking into account all the possible combinations shifting the beginning and end of the MC up to two hours, the results are $\theta = 68^\circ \pm 9^\circ$ and $\phi = 73^\circ \pm 32^\circ$ and in all cases $\lambda_2/\lambda_3 > 5$. If we use the period of the MC chosen from the interplanetary data (2010/05/28 21:00 UT to 2010/05/29 18:00 UT), the result is $\theta = 73^\circ$, $\phi = 95^\circ$ and $\lambda_2/\lambda_3 = 7.5$. In this way, the orientation of the cylinder found in this event using the CRC model is significantly different from results derived from other methods.

6.6 The magnetic cloud observed on 2010/08/04

6.6.1 The interplanetary medium

According to the ICME catalog (RICHARDSON, CANE, 2010) an ICME with MC characteristics was observed from 2010/08/04 10:00 to 2010/08/05 00:00, as shown in Figure 6.44. During this period, the plasma beta parameter is considerably lower than in the remaining period (close to 0.1). The IMF is higher than on the days before, it is quite smooth and shows some indication of rotation.

Approximately half a day before the MC, an interplanetary shock was observed on the last hours of 2010/08/03. This structure is very clear by the sudden increase in the IMF, flow speed, temperature and density. Within the shock and the MC, we can identify two regions with different behavior of the parameters. At the first hours, we see a region with high temperature. Right after, the temperature is strongly reduced and the IMF has some sort of rotation. This structure is not reported by the catalog but it has some signatures a MC. Its duration, however, is very short for a typical MC event.

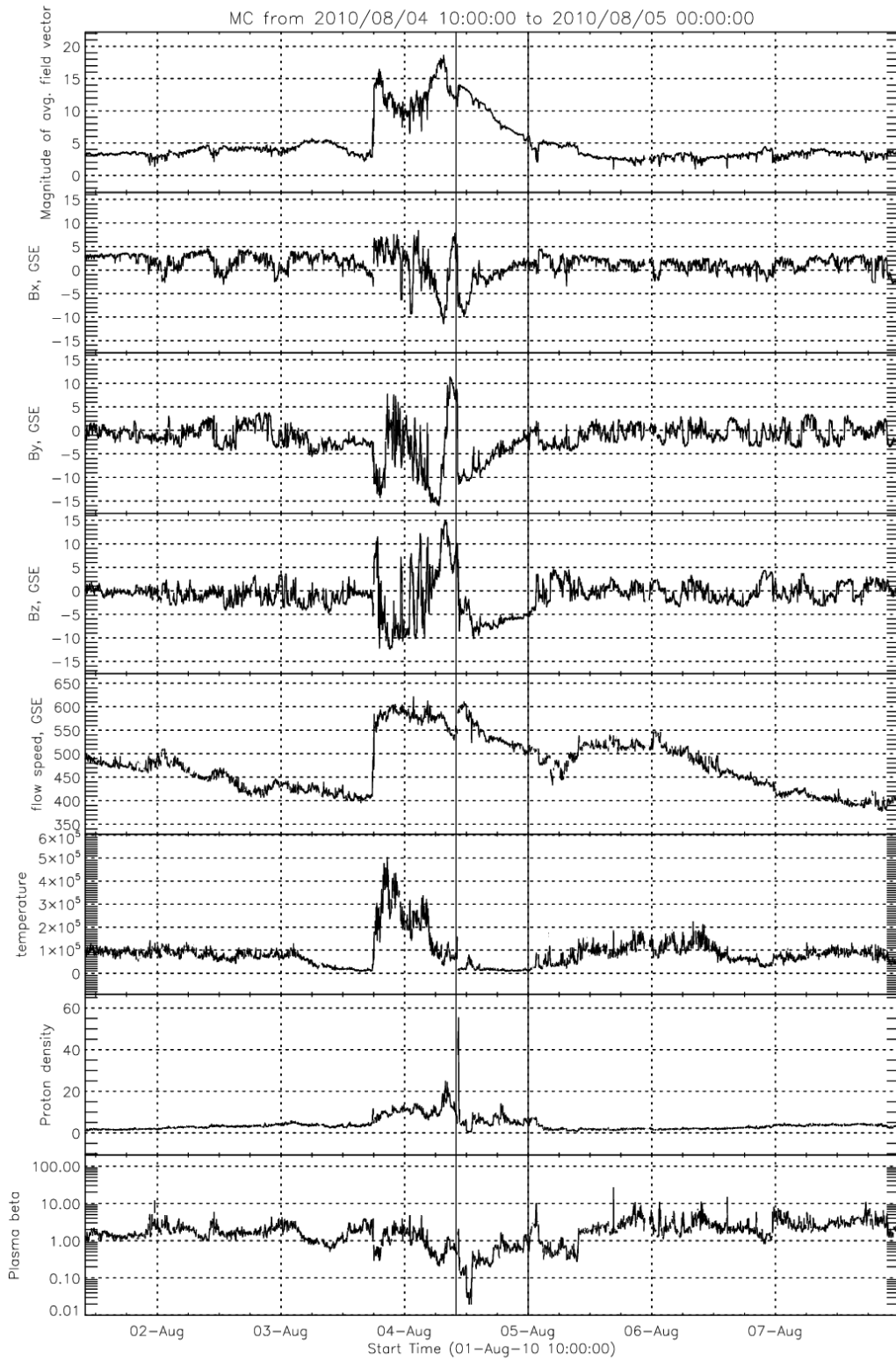


Figure 6.44 - The interplanetary magnetic field and plasma parameters during a MC observed on 2010/08/04.

6.6.2 The cosmic ray observations

The cosmic ray count rate observed both by the GMDN and by selected neutron monitors do not have a clear modulation before the interplanetary shock observation. The vertical directional channels of the GMDN have a count rate decrease with clearly different intensities: it is about 1% for Nagoya, São Martinho da Serra and Kuwait, but it is almost 2% for Hobart (Figure 6.45). For the three neutron monitors used here, the decrease is about 3% (Figure 6.46).

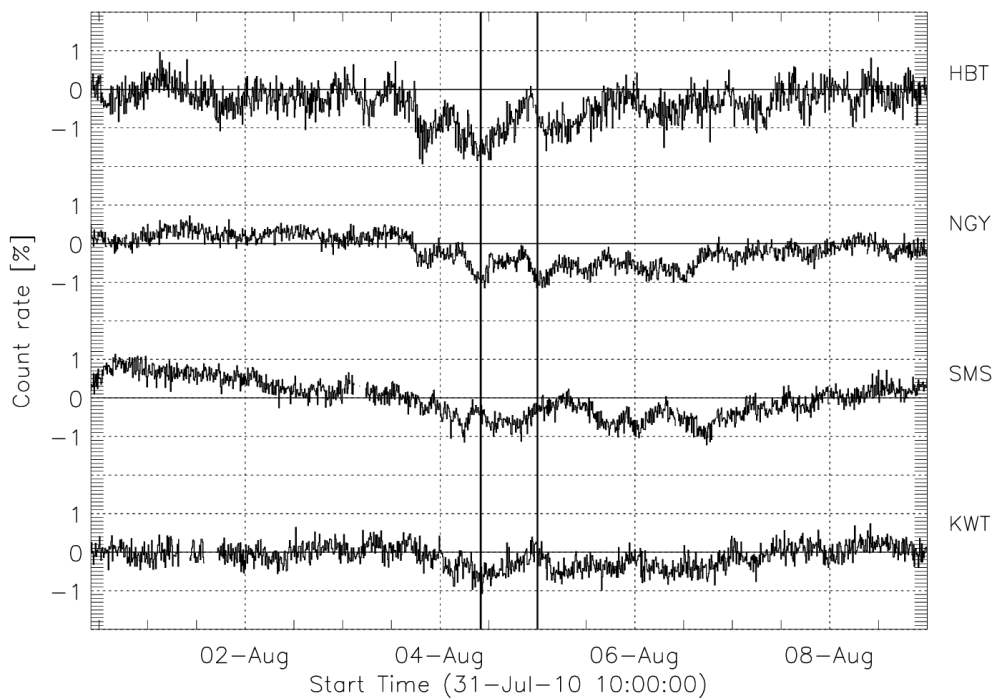


Figure 6.45 - The cosmic ray count rate observed by the vertical directional channels of the GMND during the MC on 2010/08/04.

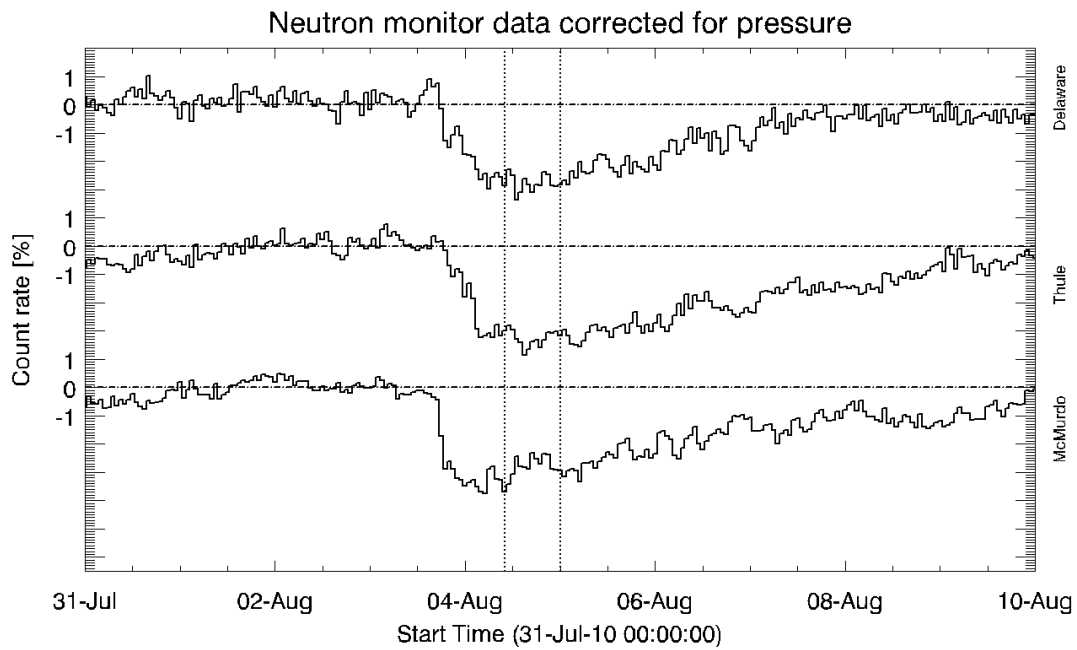


Figure 6.46 - The cosmic ray decrease observed by three different neutron monitors (Delaware, Thule and McMurdo) during the MC on 2010/08/04.

There is an isotropic decrease observed by the GMDN starting on 2010/08/03, in close timing to the shock. The CR recovery phase back to the level before the shock starts on 2010/08/06. In between those periods (during the MC observation), the isotropic level is kept basically unchanged, see Figure 6.47. Therefore, it is not possible to apply the cosmic ray cylinder model in the magnetic cloud observation in the interplanetary medium.

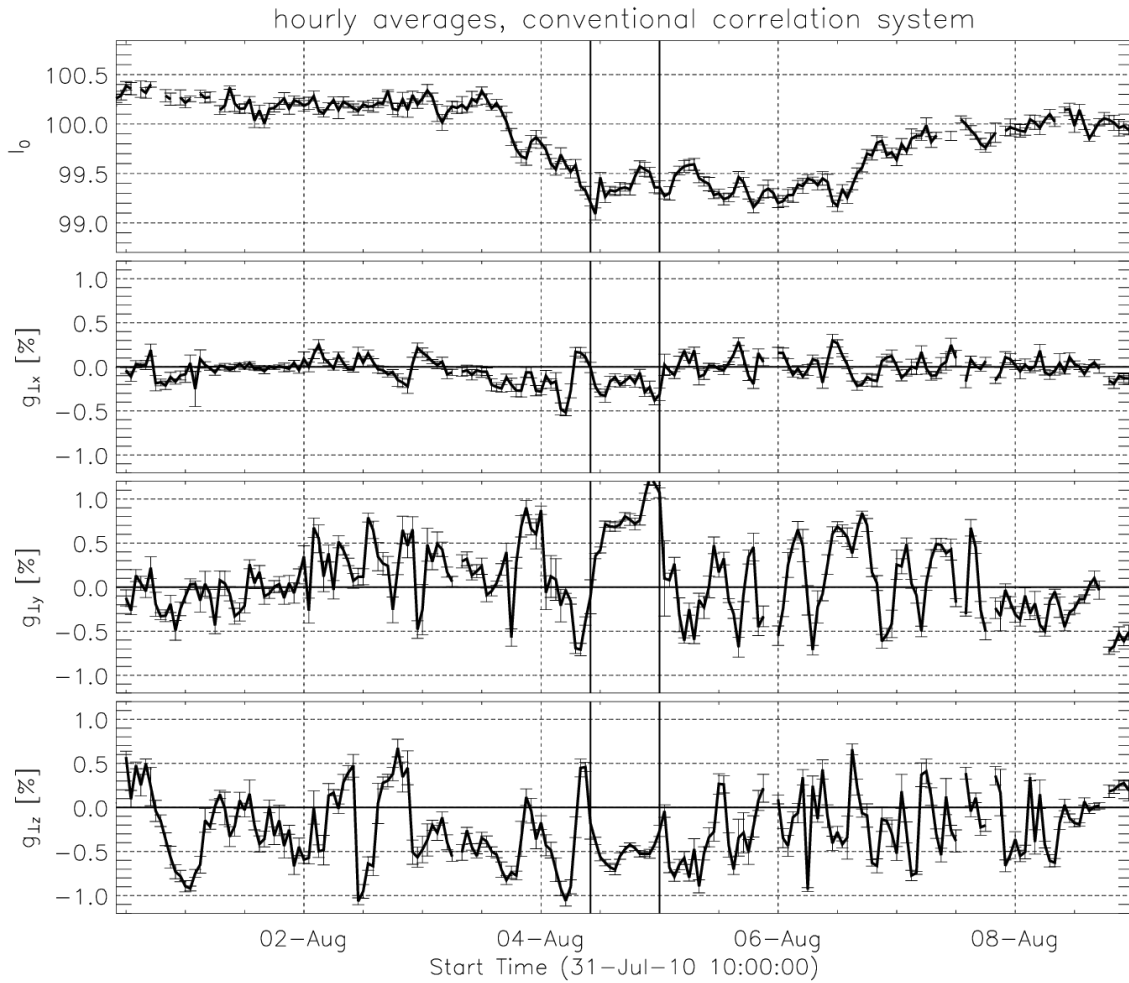


Figure 6.47 - The isotropic cosmic ray intensity and the orthogonal components of the cosmic ray fractional gradient during the MC period on 2010/08/04.

Although we cannot apply we CRC model, the direct inspection of the orthogonal components of the gradient may give us some idea of the position of the MC. We calculated the anisotropy components perpendicular and parallel to the IMF and found that the former is significantly higher than the later during the MC period. From Figure 6.47, one can notice that during the MC period the "y" and "z" components of the gradient have a pronounced and stable behavior for approximately 12 hours. The "z" component is negative and suggests a cosmic ray depleted region located mainly above the ecliptic plane. The "y" component is positive, suggesting the cosmic ray depleted region to be located westward of the Earth-Sun line.

6.6.3 The origins in the solar corona

We identified two halo CMEs in the LASCO-C3 data from 2010/07/30 to 2010/08/02. By checking the angular position of these events in COR2A and COR2B, we can affirm that both are earthward directed. The first one has small angular width and the second one is wider, brighter, and faster than the first. The results from the application of CORSET to the two CMEs are shown in Figure 6.48, Figure 6.49 and Figure 6.50.

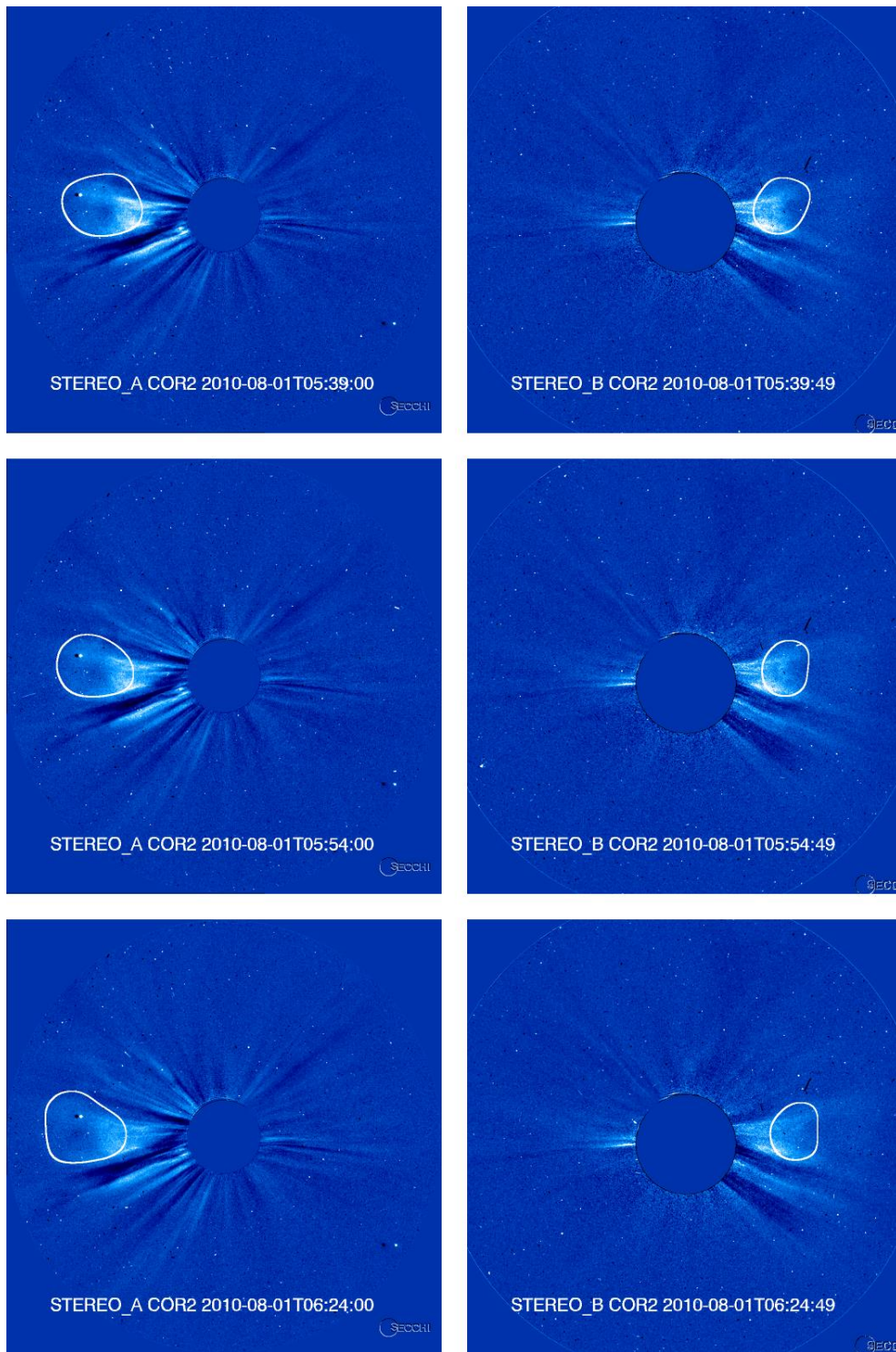


Figure 6.48 - The first earthward CME observed on 2010/08/01 on COR2A (left column) and COR2B (right column) FOVs.

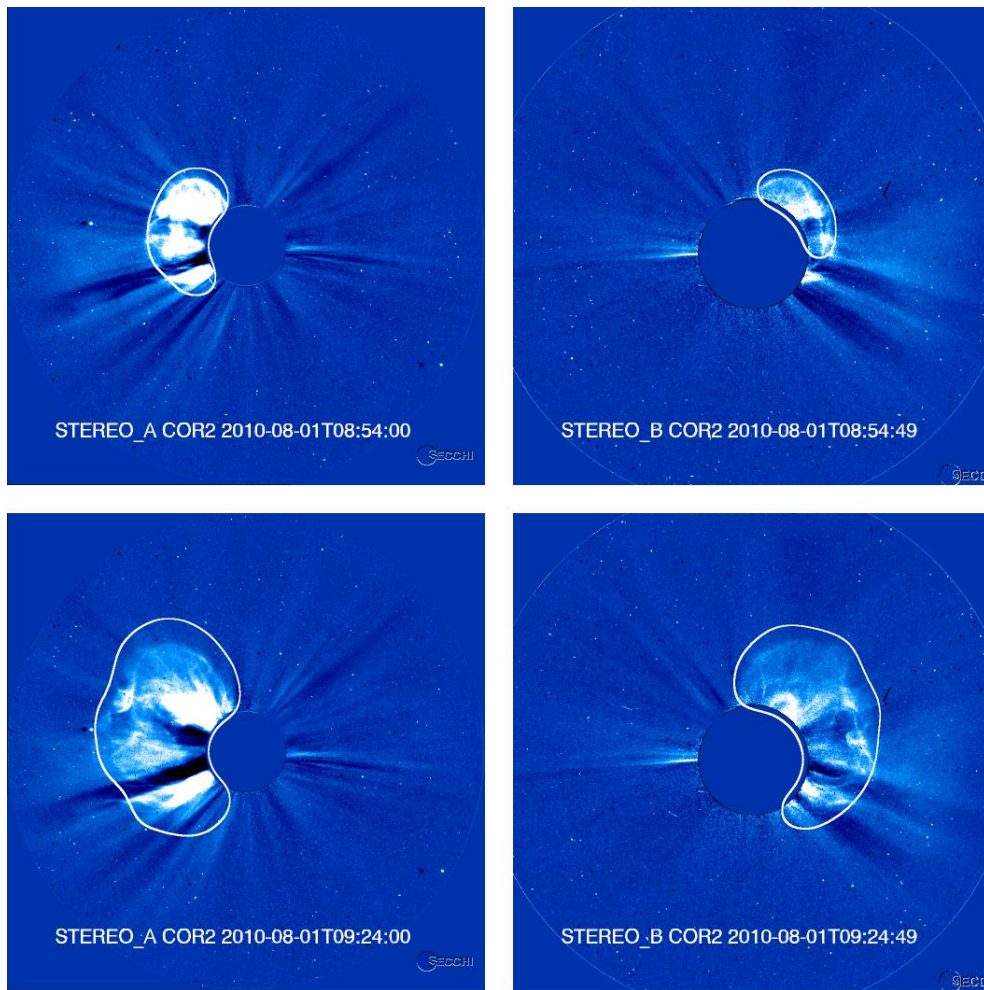


Figure 6.49 - The second earthward CME observed on 2010/08/01 on COR2A (left column) and COR2B (right column) FOVs. In this Figure, only the first two frames tracked by CORSET are shown.

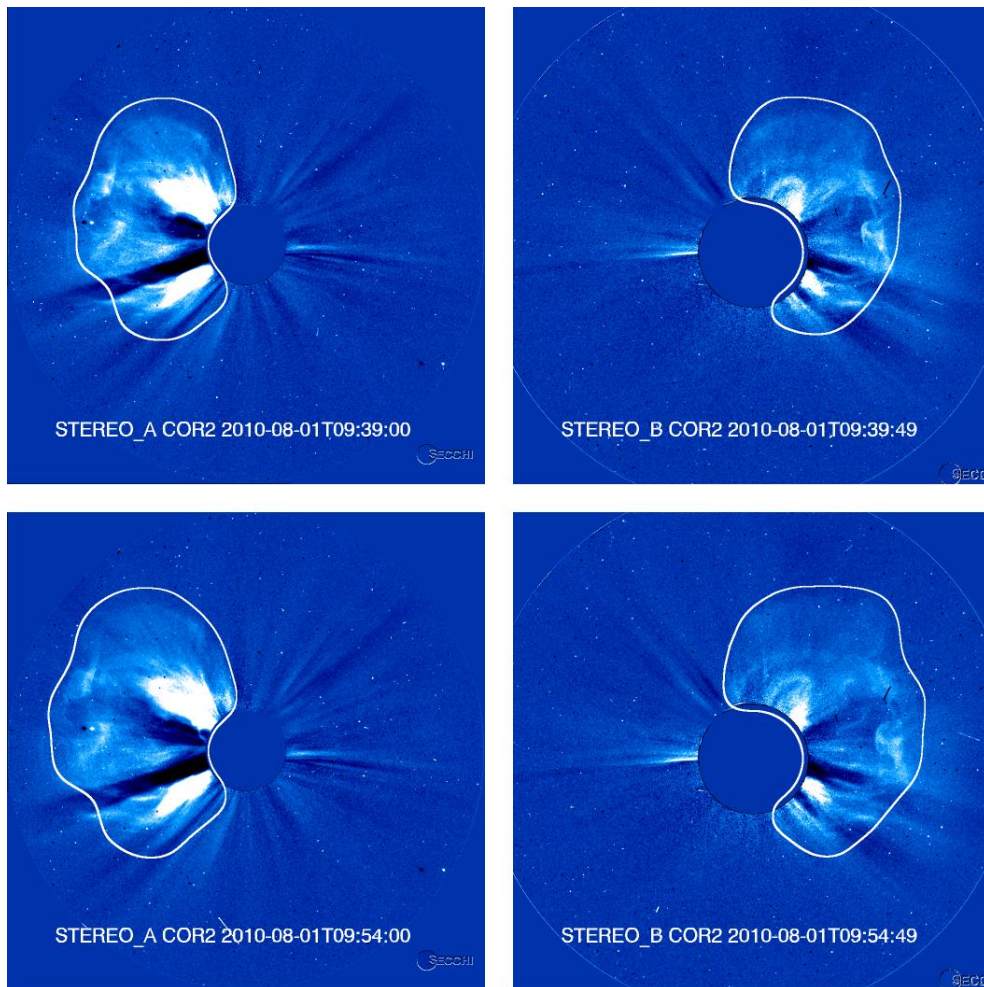


Figure 6.50 - The second earthward CME observed on 2010/08/01 on COR2A (left column) and COR2B (right column) FOVs. In this Figure, only the last two frames tracked by CORSET are shown.

A previous work from Liu et al. (2012) reported three CMEs directed toward the Earth in association to this MC (Figure 6.51) but we tracked only two CMEs in this Thesis: the second and third one. We do not interpret that the first CME is a halo or partial halo but rather a limb event. Due to the wider angular range it covers on COR2B than on LASCO-C3, the direction of propagation is closer to STEREO B than to the Earth. We tracked it using CORSET but we were not able to perform the triangulation due to the different angular ranges it has in COR2A and COR2B: while the later was tracked on the north part of the coronagraph image, the former was tracked on the east portion.

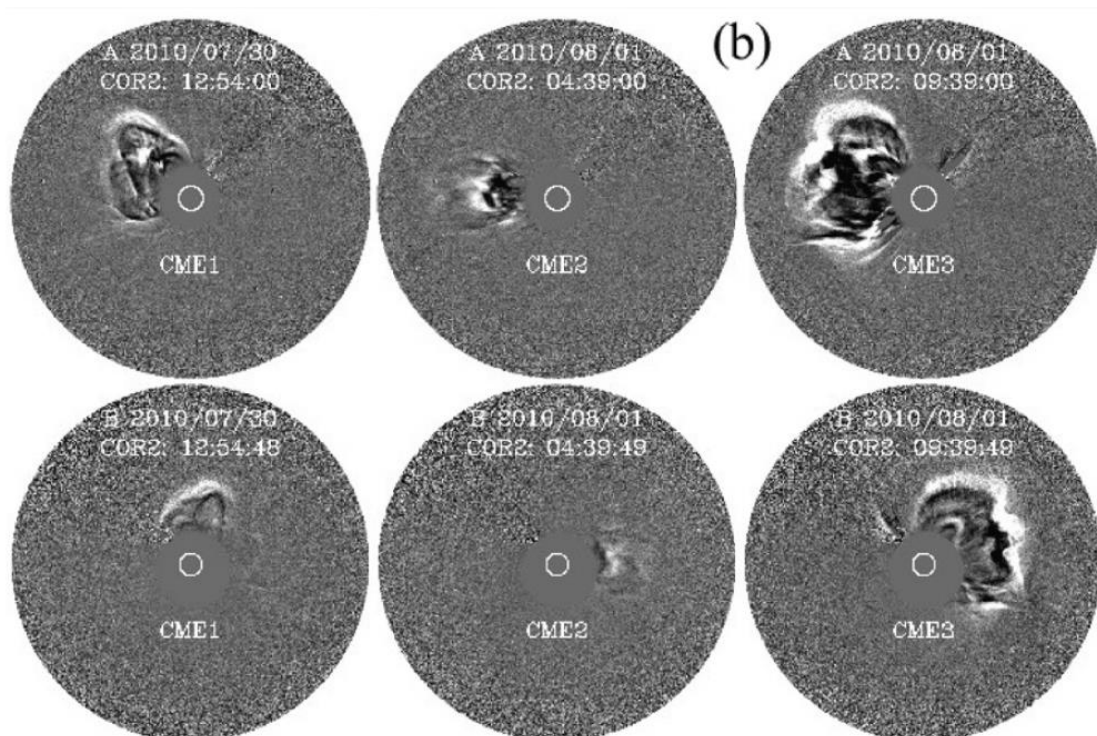


Figure 6.51 - The three earthward directed CMEs identified by a previous study. Source: Liu et al. (2012)

The results from the application of CORSET3D are shown in Figure 6.52, Figure 6.53 and Table 6.13. Both CMEs ejected approximately toward Earth analyzed here are directed eastward of the Sun-Earth line (i.e., at the positive “y” GSE direction) and northward of the ecliptic plane.

The last CME, which is considerably faster, may interact with the previous one. We believe that the second CME on 2010/08/04 is the source of the MC structure observed on 2010/08/04 and that the first CME is the cause of the structure observed right before.

The comparison of the results found here and in previous references using different methods is shown in Table 6.14. For the CME #1, the speed calculated by CORSET3D is significantly smaller than the calculated by the other method. One explanation for the difference is the shorter time windows used when calculating CORSET3D. The direction of propagation of this CME, however, is in quite good agreement among all the methods. For the CME #2, the speed calculated has a very good agreement but there is a considerable difference in the direction of propagation. In the results from CORSET3D, the latitude and longitude are closer to zero.

According to Temmer et al. (2012), the first CME is originated in a small active region (NOAA 11094) located at longitude -14° and latitude 14° . For the second CME, the origin is another

active region (NOAA11092) located at longitude -35° and latitude -20° . Notice that the position of the active region of the second event is northward and eastward of the first. This trend is kept in the CME analyzed here by many different methods, as listed in Table 6.14, except for CORSET3D. One can notice that the direction of propagation of both CMEs derived from Temmer et al. (2012) and Liu et al. (2012) is closer to the solar source than the results from CORSET3D.

If we suppose that the CME will keep the direction of propagation we derived here, the results here are in agreement with the analysis of the cosmic ray gradient that indicated a CRC region located mainly northward and eastward of the Earth.

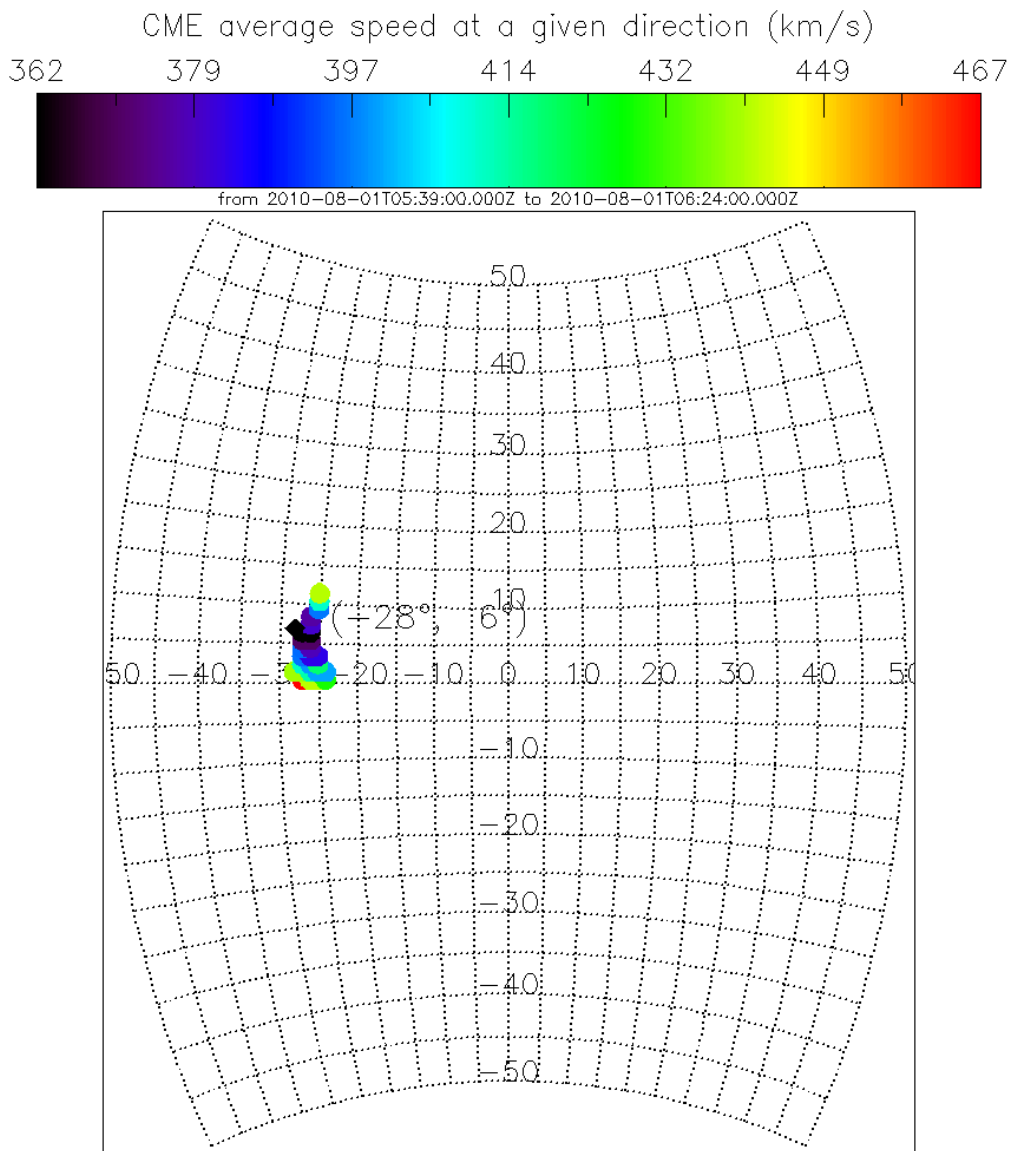


Figure 6.52 - The radial speed of the CME front as a function of latitude and longitude (in HEEQ coordinate system). This Figure corresponds to the first earthward CME observed on 2010/08/01. The black diamond indicates the center of the CME front.

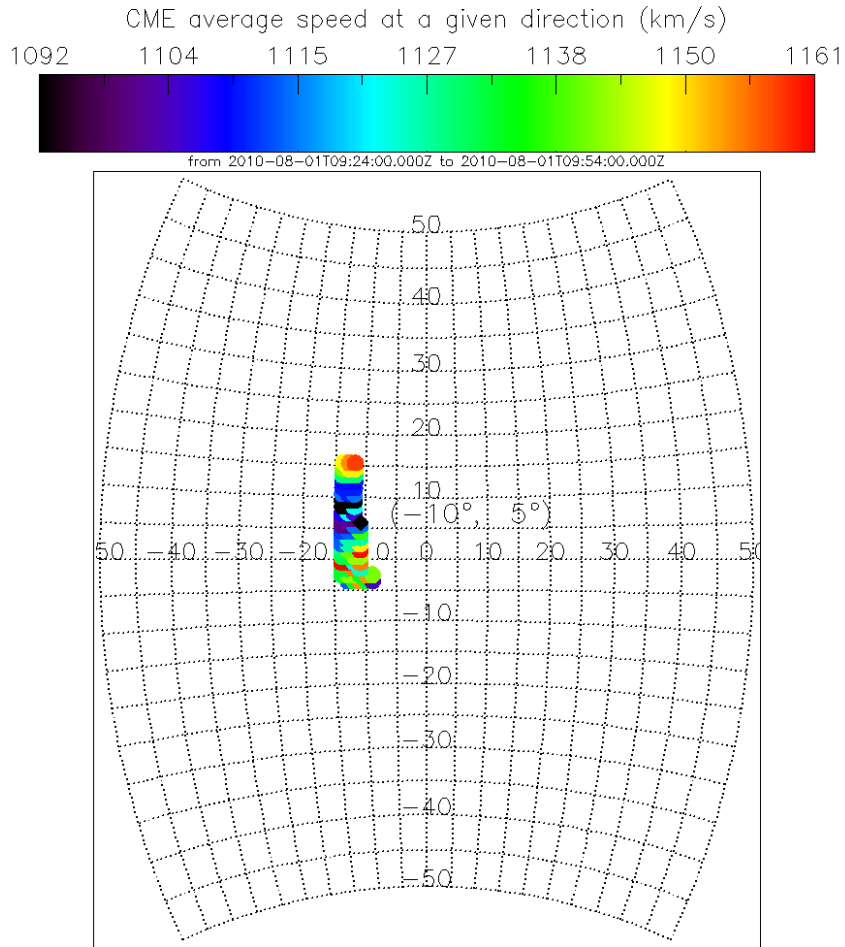


Figure 6.53 - The radial speed of the CME front as a function of latitude and longitude (in HEEQ coordinate system). This Figure corresponds to the second earthward CME observed on 2010/08/01. The black diamond indicates the center of the CME front.

Table 6.13 - Kinematic parameters of the two earthward directed CMEs observed on 2010/08/01. The angles shown here are given in HEEQ coordinate system.

Parameter	CME #1 2010/08/01	CME #2 2010/08/01
Minimum and maximum latitudes	[0°, 14°]	[-4°, 16°]
Minimum and maximum longitudes	[-33°, -23°]	[-15°, -7°]
Group speed v_g averaged over time	404±29 km/s	1126±19 km/s
Central direction of the CME averaged over time (longitude)	-28°	-11°
Central direction of the CME averaged over time (latitude)	7°	6°
Minimum value of $\bar{v}_r(\theta_j, \phi_k)$	362 km/s	1092 km/s
Maximum value of $\bar{v}_r(\theta_j, \phi_k)$	467 km/s	1161 km/s
Group speed as a function of time $v_g(t_{i+1})$	[438, 402] km/s	[1052, 1201] km/s
Maximum error of the triangulation	0.1 solar radii	0.1 solar radii

Table 6.14 - Comparison of the direction and de-projected speed of the two earthward CMEs observed on 2010/08/01 derived using different methods (in HEEQ coordinates).

Method	CME #1			CME #2			FOV
	Speed (km/s)	Longitude	Latitude	Speed (km/s)	Longitude	Latitude	
CORSET3D	404±29	-28° [-33°, -23°]	7° [0°, 14°]	1126±19	-11° [-15°, -7°]	6° [-4°, 16°]	COR2
GCS (Temmer et al., 2012)	650±150	-20±10°	9±5°	1160±200	-28±5°	20±5°	COR1 and COR2
Triangulation (Liu et al., 2012)	732±350	-21±9°	-	1138±550	-20±5°	-	COR2 and HI1
Triangulation ^(*) (Liu et al., 2012)	-	[-28°, -22°]	-	-	[-16, -24°]	-	COR2

6.7 The magnetic cloud observed on 2011/03/30

6.7.1 The interplanetary medium

The ICME catalog suggests a MC event beginning on 2011/03/29 at 03:00 and ending on 2011/03/31 04:00. We inspected the interplanetary magnetic field and plasma parameters data during this period (Figure 6.54). As expected for a MC, the magnetic field increases from about 5 nT to 14 nT and the plasma beta is close to 0.1. One can see that the beta parameter keeps this low value up to the half 2011/04/01, many hours later than the period suggested by the ICME catalog. The magnetic field magnitude also has high intensity (close to 10 nT) after the period. Taking into account the beta parameter and the magnetic field intensity, we would rather consider a much wider period to be part of the MC. The continuous vertical lines in Figure 6.54 indicate this period. The period originally proposed by the catalog as well as the extended period suggested here are both used to perform the cosmic ray analysis and are discussed in Section 6.7.3. Although we see some rotation of the direction of the magnetic field, its orthogonal components behavior is not smooth at all times. The rotation is seen mainly in the “z” component. The temperature is low and the solar wind speed does not reach 400 km/s.

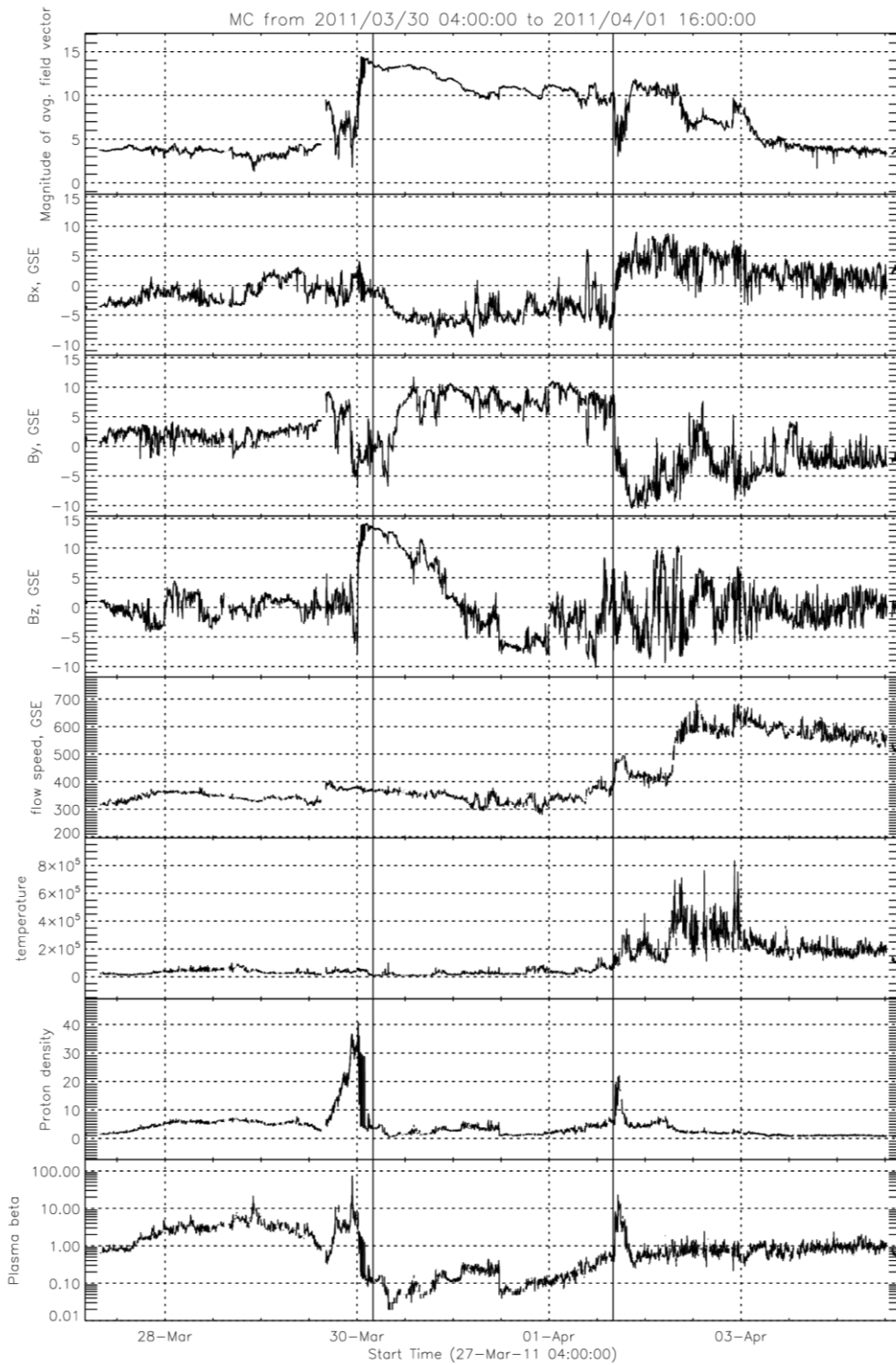


Figure 6.54 - The interplanetary magnetic field and plasma parameters during a MC observed on 2011/03/30.

There is a shock on 2011/03/28 at about 18:00, approximately ten hours before the magnetic cloud. It should be noticed that there is a sector boundary at about 17:00 UT on 2011/04/01 when the IMF changes from away sector (angle between 90° and 180°) to toward sector (angle between 270° and 360°). The previous sector boundary was on 2011/03/22. Beyond these structures, there is no observation of any other that could modulate cosmic ray.

6.7.2 The origins in the solar corona

When searching for CMEs responsible for this ICME, we found two candidate halo events. One is an earthward ejected on 2011/03/25 and it is visible in both coronagraphs from 7:24 UT to 14:24 UT. This CME is very weak and slow, and it is quite difficult to visually separate it from the background. There is a second CME on 2011/03/26 but it is ejected away from the Earth. Beyond these two CMEs, there are no other halo or semi-halo events reported by the CDAW catalog. Moreover, there is no data gap in neither COR nor LASCO instruments. In this way, we can be sure that the CME on 2011/03/25 must be the solar origin of the MC studied here. A previous result from Colaninno (2012) confirms our conclusion.

The CME was tracked by CORSET from 09:39 to 12:24 and the results are shown in Figure 6.55 and Figure 6.56. One can notice that this event has a very low brightness and it rises in both coronagraphs FOV with very low speed. The default set of parameters was not able to track it and we tested many other possible parameters here. Due to the low brightness, the texture of the CME and the texture of the background become similar in this example. The solution adopted was a sample area for the CME in the latest frame where the CME is visible and defining $Q = 0$ (COR2A) and $Q = 14$ (CORB). On COR2A FOV, CORSET selected only part of the CME and ignored a significant part of it. Since in this analysis we are interested only in the front part of the CME, we understand that the result is acceptable.

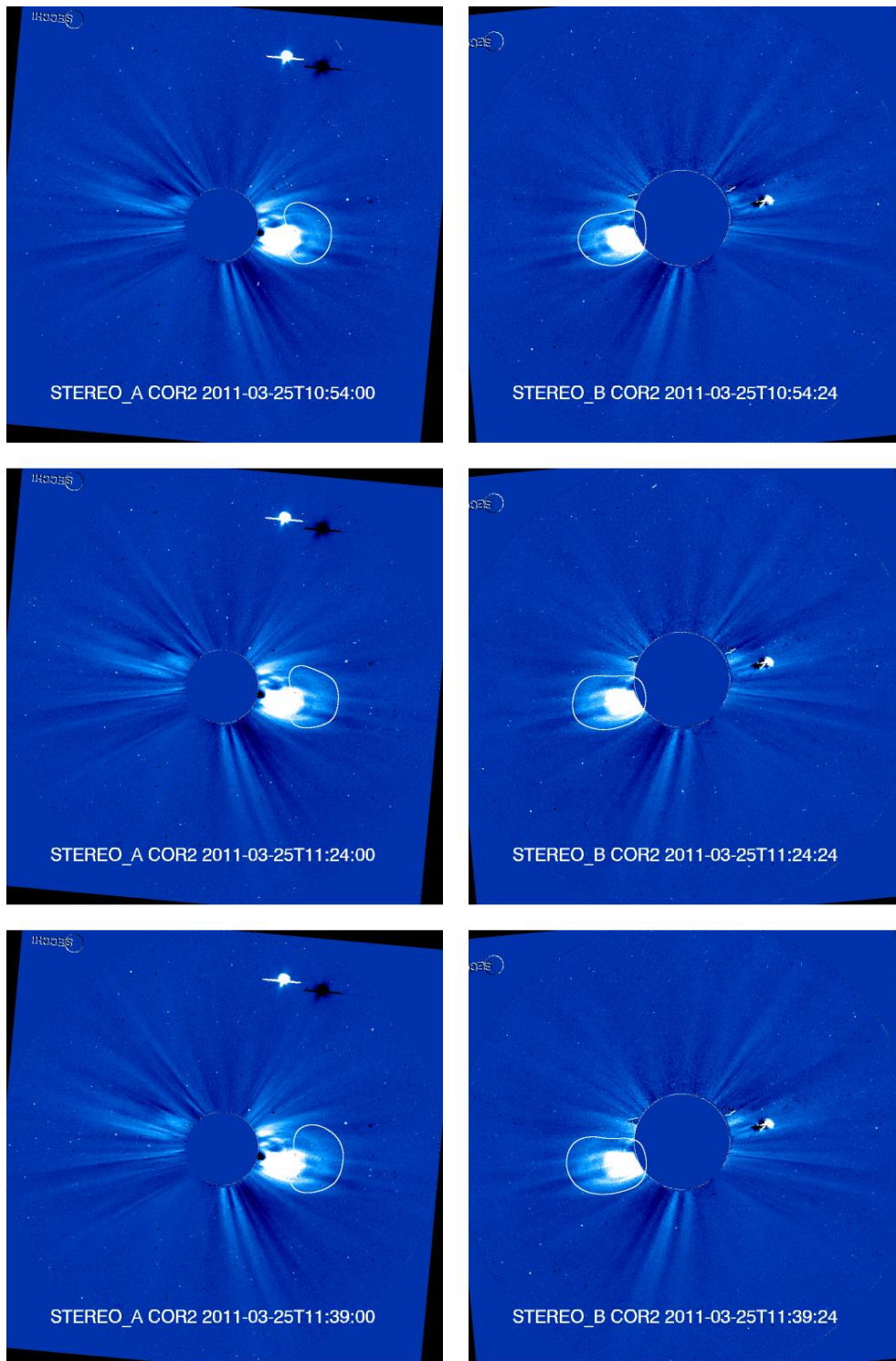


Figure 6.55 - The CME observed on 2011/03/25 on COR2A (left column) and COR2B (right column) FOVs. In this Figure, only the first three frames are shown.

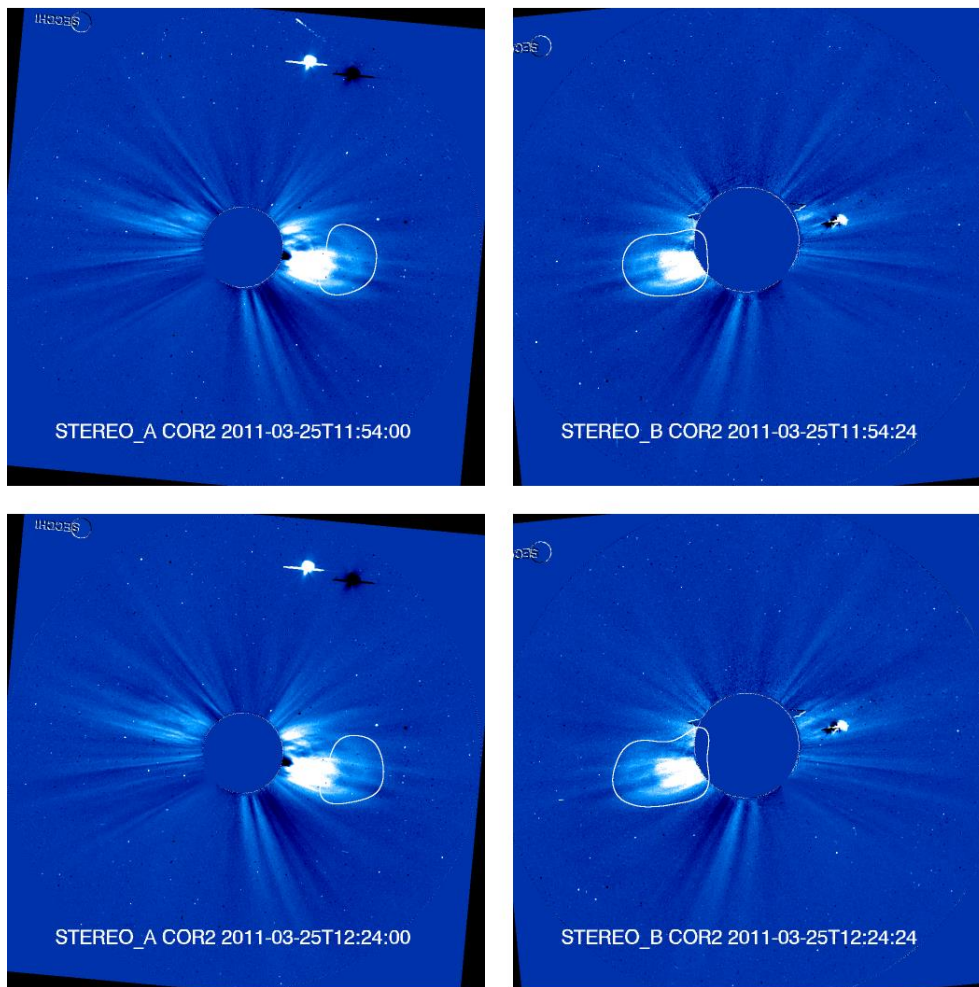


Figure 6.56 - The CME observed on 2011/03/25 on COR2A (left column) and COR2B (right column) FOVs. In this Figure, only the last two frames are shown here, the remaining are shown in Figure 6.55.

According to the results from CORSET3D, the average speed is 180 km/s with average direction of propagation of 3° of longitude and -3° of latitude in HEEQ coordinates. The map of radial speed distribution is shown in Figure 6.57 and summarized in Table 6.15. Taking into account the error ranges of the angles, this result shows that the CME is basically centered in the Sun-Earth line but the speed is higher on the east portion of the front.

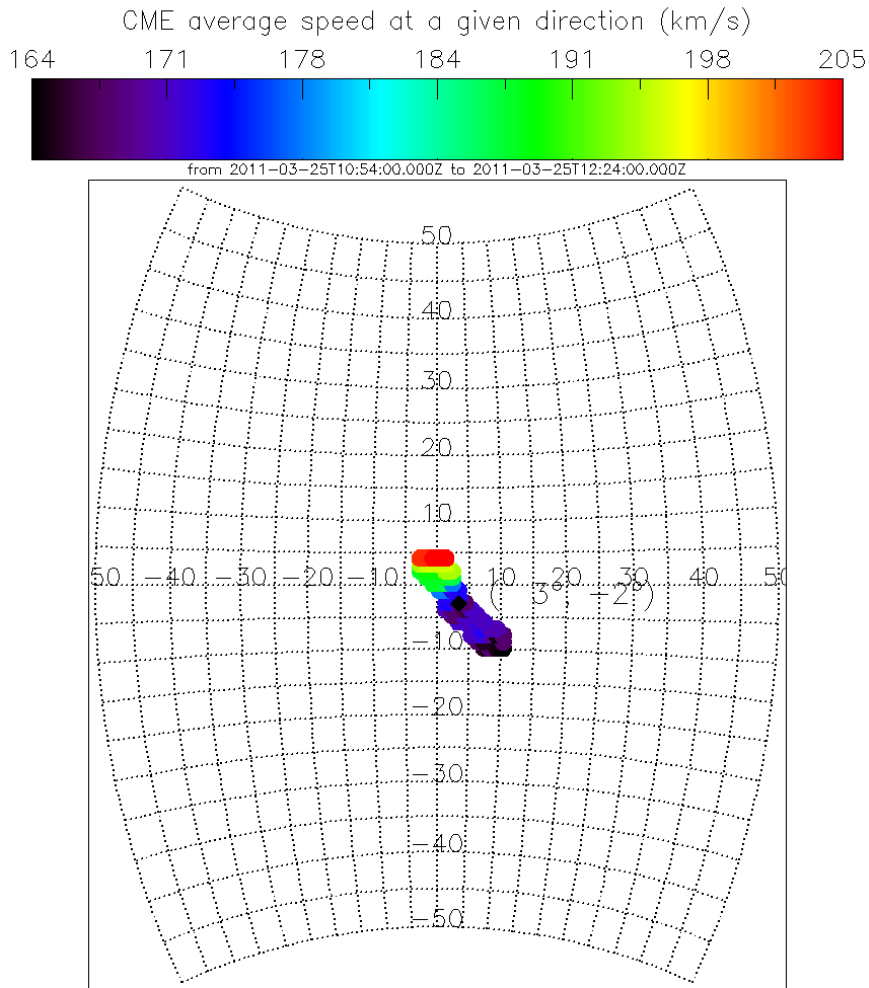


Figure 6.57 - The time average radial speed of the CME front observed on 2011/03/25 as a function of latitude and longitude (in HEEQ coordinate system). The black diamond indicates the center of the CME front.

Table 6.15 - Kinematic parameters of the CME on 2011/03/25. The angles shown here are given in HEEQ coordinate system.

Parameter	Result
Minimum and maximum latitudes	$[-11^\circ, 5^\circ]$
Minimum and maximum longitudes	$[-10^\circ, 17^\circ]$
Group speed v_g averaged over time	178 ± 12 km/s
Central longitude	3°
Central latitude	-3°
Minimum value of time average radial speed $\overline{v_r}(\theta_j, \phi_k)$	164 km/s
Maximum value of time average radial speed $\overline{v_r}(\theta_j, \phi_k)$	205 km/s
Group speed as a function of time $v_g(t_{i+1})$	$[200, 201, 10, 170]$ km/s
Maximum error of the triangulation	0.0 solar radii

This CME was also studied by Colaninno (2012) using the GCS model. At 10 solar radii, the longitude and latitude found are -27° and 3° , respectively (in HEE coordinates). Converting CORSET3D results to HEE, the longitude is 3° and the latitude is -2° . The difference found here for the longitude is very significant and much higher than the error estimates of Mierla et al. (2010) that are within 10° of each other. One possible source of the error for this event is the low brightness of the CME that makes both the analysis on CORSET and GCS more difficult. Other point is that the longitude and latitude found here correspond to the central portion of the CME front line. As the map of radial speed suggests (Figure 6.57), the fastest moving part of the structure is not correspondent to its central position. If we considered the fastest part, the longitude found would be more eastward. Other possible explanation for the disagreement between results is a superposition of another CME on the GCS analysis. A set of three frames were used: one shows the CME at about 10 solar radii, the second at 20 solar radii and the last one at 50. On the last frame, the current CME is superposed by another halo CME ejected on the first hours of 2011/03/26 on LASCO-C3 FOV. On COR2A and COR2B there is no superposition since the projections are located in opposite sides, approximately 180° from each other. This event is also aligned with the Earth-Sun line but it is directed away from the Earth. Since the analysis of the GCS model is done by visual inspection, the superposition might bias adjustments of the GCS parameters that are done by visually inspection.

Colaninno (2012) derived the tridimensional speed using multiple polynomial functions from Wood et al. (2009). The average speed found in the first 8 hours after the ejection was found to be 46.7 km/s. The speeds projected on the coronagraphs FOV calculated in this Thesis and in previous works are indicated in Table 6.16.

Table 6.16 - The speed of the CME observed on 2011/03/25 on the COR2 A and COR2 B coronagraphs.

Reference	COR2 A Speed	Time range	COR2 B Speed	Time range
This Thesis	158 [118-158] km/s	[03:39-15:24]	202 [140-202] km/s	[09:39-12:24]
Colaninno (2012)	100 km/s	-	142 km/s	-
CACTus	No CME found		235 [178-297] km/s	[07:24-15:24]
SEEDS	199 km/s		171 km/s	

6.7.3 The cosmic ray observations and modeling

The cosmic ray count rate observed by vertical directional channels of the GMDN seems to have a significant daily variation before the MC and it has an apparent decrease is about 1% during it (Figure 6.58). For the neutron monitors used in this Thesis, the decrease ranges between 2% and 3% (Figure 6.59).

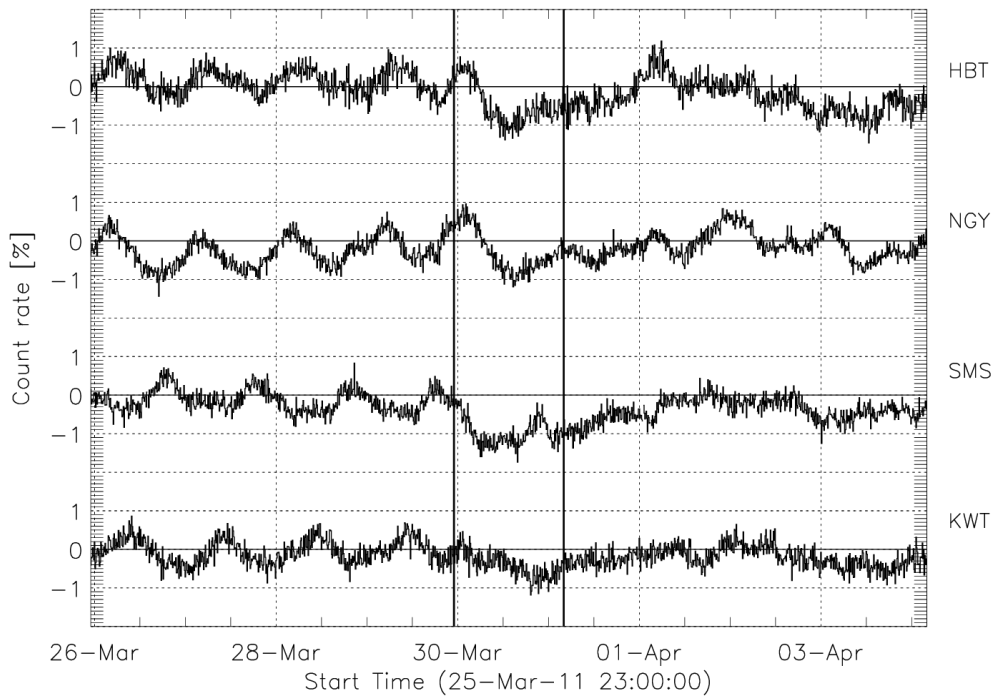


Figure 6.58 - The cosmic ray decrease observed by the vertical directional channels of the GMND during the MC on 2011/03/29. The vertical continuous lines correspond to the MC period suggested by the ICME catalog.

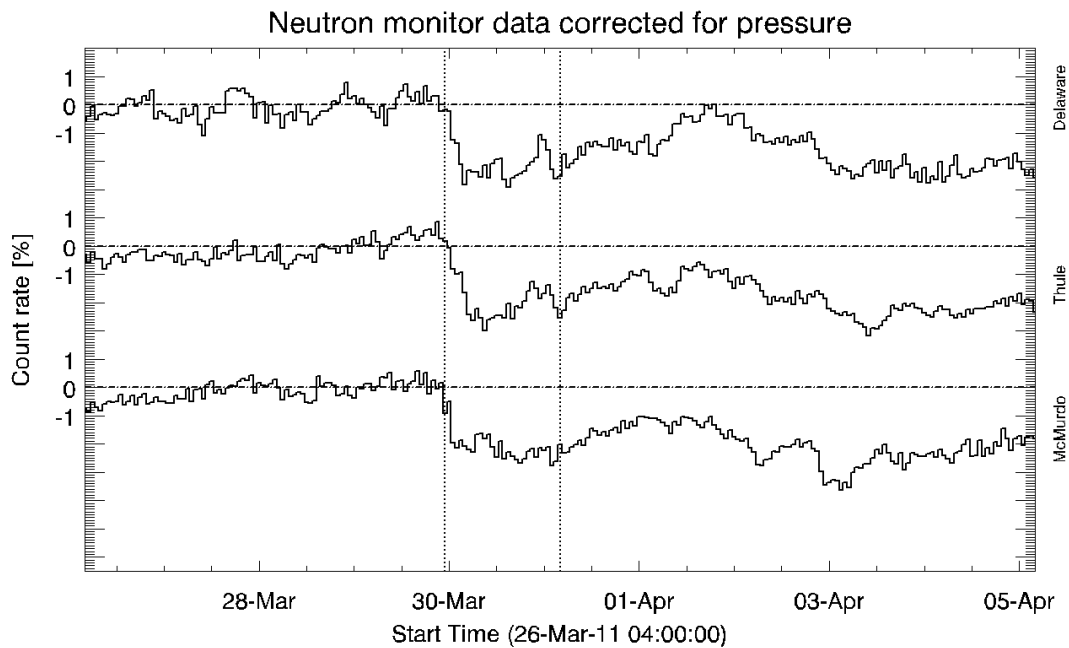


Figure 6.59 - The cosmic ray decrease observed by three different neutron monitors (Delaware, Thule and McMurdo) during the MC on 2011/03/29. The vertical continuous lines correspond to the MC period suggested in the ICME catalog.

We compared the intensity of the parallel and perpendicular components of the anisotropy in the eight days before and after the MC period. In the days before the MC, there is a daily variation in the cosmic ray count rate that corresponds mainly to an anisotropy parallel to the interplanetary magnetic field. From 2011/03/29 on, the component of the anisotropy perpendicular to the IMF becomes significantly higher than the component parallel to it. One exception happens on the first hours of 2011/03/30 and it lasts a few hours.

Considering that the cosmic rays were modulated by a MC with similar time ranges suggested by the catalog, i.e., extending up to the first hours of 2011/03/30, the cosmic ray cylinder model was tested using many possible combinations of periods slightly different from each other. Our objective with this is testing how sensitive the model is to small period changes. The starting point was set at 2:00 UT, 3:00 UT or 4:00 UT; the ending point at 2011/03/30 23:00 UT or 2011/03/30 0:00 UT. The results of any pair of tests changes less than the difference between results shown in Table 6.17 for the new and conventional correlation systems derived using identical periods. Among the periods tested, the residue is minimum for the one shown in Table 6.17. The observed cosmic ray data and the results from the modeling are shown in Figure 6.60.

For the remaining cases, it extends up to 0.014 for the conventional correlation system and up to 0.017 for the new correlation system.

Table 6.17 - Parameters of the cosmic ray cylinder model of the MC observed on 2010/03/30.

Parameter	Conventional correlation system	New correlation system	Conventional correlation system	New correlation system
Beginning of the analysis period	2011/03/30 04:00:00		2011/03/30 04:00	
End of the analysis period	2011/03/30 23:00:00		2011/04/01 02:00	
Time with minimum cosmic ray isotropic intensity	15:00	16:00	22:00 (2011/03/30)	22:00 (2011/03/30)
Amplitude of cosmic ray isotropic intensity decrease	0.5 %	0.5 %	0.4%	0.4%
Larmor radius (AU)	0.02	0.02	0.06	0.08
Latitude (degrees, GSE)	36°	48°	16°	18°
Longitude (degrees, GSE)	127°	130°	158°	140°
Impact distance (AU)	-0.11	-0.11	-0.03	-0.01
κ_0 (dimensionless)	44	46	246	215
Cylinder radius (AU)	0.12	0.11	0.09	0.13
Cylinder radius expansion speed (AU/hour)	-0.004	-0.004	0.001	0.001
Residue	0.012	0.015	0.014	0.013
Position at the beginning [GSE coordinates, AU]	[0.15, 0.13, -0.02]	[0.14, 0.12, 0.00]	[0.03, 0.06, 0.02]	[0.07, 0.08, 0.02]
Position at the end [GSE coordinates, AU]	[0.02, 0.09, -0.08]	[0.00, 0.09, -0.06]	[-0.05, -0.06, -0.08]	[-0.11, -0.10, -0.07]

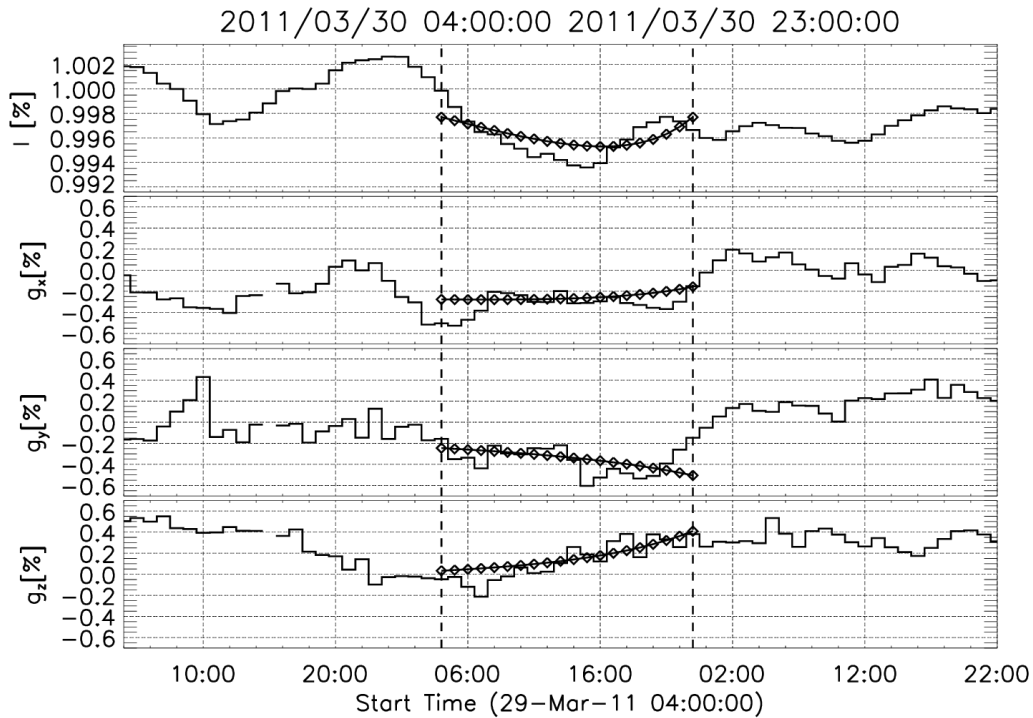


Figure 6.60 - The observation and modeling of cosmic ray depleted region associated to the magnetic cloud in 2011/03/30 using the conventional correlation system. The stair plot is the observed data and the line with diamonds is the modeling of the cosmic ray depleted region. The first panel, from top to bottom, shows the isotropic CR intensity. The remaining three plots show the orthogonal components of the fractional cosmic ray density gradient in the GSE coordinate system.

Other possibility is considering that the cosmic rays were modulated by a flux rope structure on a wider MC period proposed in Section 6.7.1 according to the observation of the beta parameter. From this period, we decided to remove a few hours at its end to avoid possible modulation of the cosmic ray observations by the sector boundary. Even though, the period used in the current analysis is more than two times longer than the one indicated in the second and third columns of Table 6.17. To distinguish the shorter and longer periods, hereafter we refer them as SP and LP, respectively. The comparison of the observed and modeled data is shown in Figure 6.61 and the parameters derived are listed in the last two columns of Table 6.17. The cylinder modelled is shown in Figure 6.62.

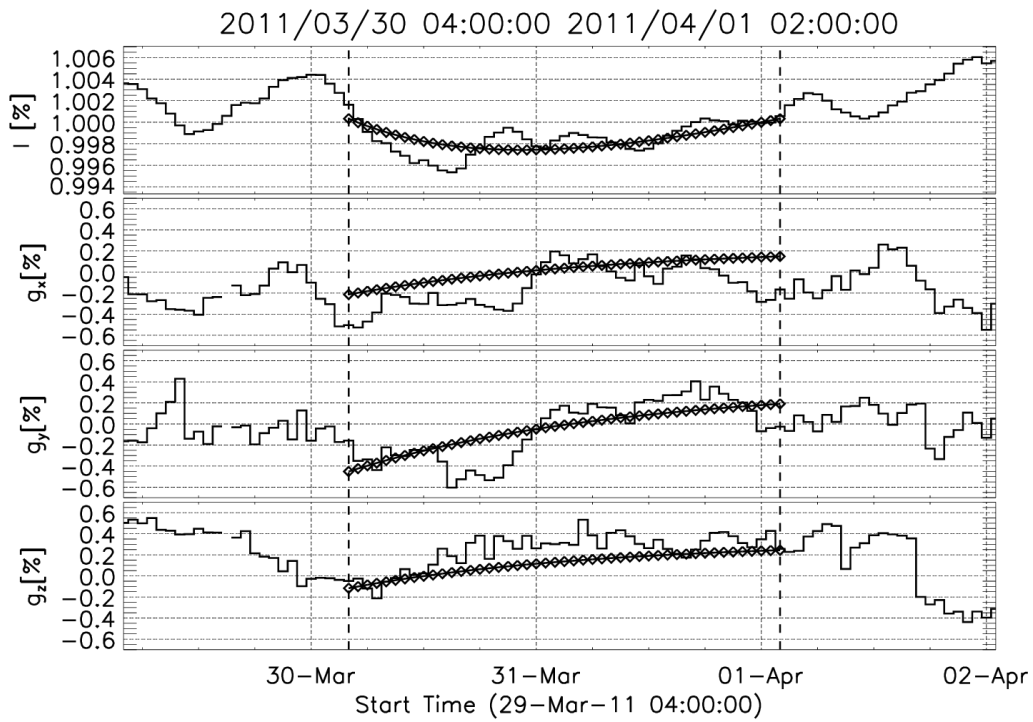


Figure 6.61 - The observation and modeling of cosmic ray depleted region associated to the magnetic cloud in 2011/03/30 using the conventional correlation system. The stair plot is the observed data and the line with diamonds is the modeling of the cosmic ray depleted region. The first panel, from top to bottom, shows the isotropic intensity. The remaining three plots show the orthogonal components of the fractional cosmic ray density gradient in the GSE coordinate system.

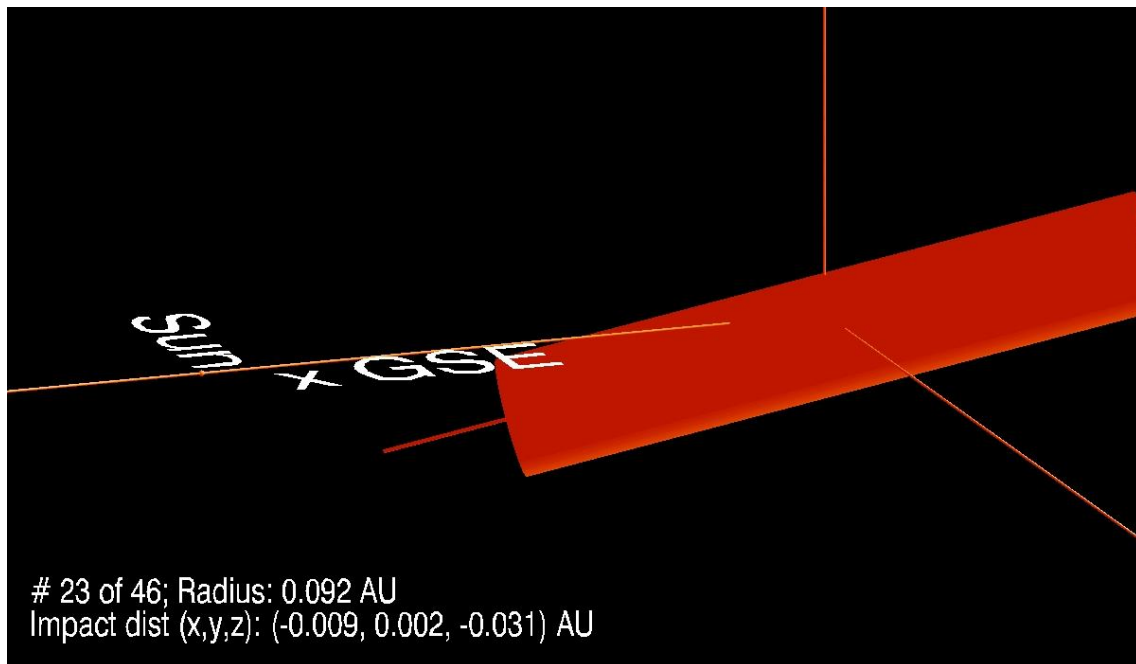


Figure 6.62 - A tridimensional representation of the cylinder derived from CRC model on 2011/03/31 at 03:00 UT. The Earth is located in the origin of the GSE coordinate system (represented by the three axis). The cylinder modelled seems to reproduce the long term trends of the observed data reasonably well. The diameter found is 0.2 AU, a size that is consistent with theoretical expectations. Comparing the two scenarios of the CRC model, there is one important difference between the results: while the cylinder is expanding when using the LP, it is shrinking in the results from the SP. Taking into account the interplanetary magnetic field intensity time profile, one can notice a trend to a decrease as time passes (see section 6.7.1). This suggests a magnetic flux rope expanding with time. Therefore, the longer CRC model is probably more appropriate. Colaninno (2012) studied this magnetic cloud using the Elliptical Flux Rope (EFR) model. This is shown in Figure 6.63 by the green projections. The axis of the ellipse found for this case are 0.04 AU and 0.01 AU, quite small for a flux rope. The same author used the GCS model to estimate the size of the MC close to the Earth and found a structure one order of magnitude larger (radius of 0.4 AU). This is shown in Figure 6.63 by the blue and black curves.

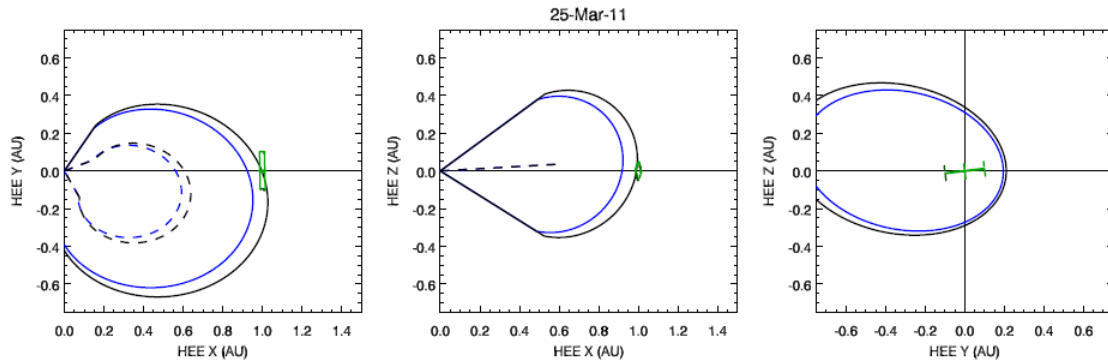


Figure 6.63 - The projection of the GCS model (represented in blue and black) and elliptical flux rope model (in green). For the former, the blue outline is the maximum measured height. The black outline is the model projected to the height when the front crosses Earth. The dashed line is the axis at the center of the cavity. Source: Colaninno (2012).

One can also notice that the cylinder found by the expanding flux rope model is lying in the HEE X-Y plane (which is the ecliptic plane) basically perpendicular to the Sun-Earth line. The CRC model found a cylinder whose axis forms 36° and 16° degrees with the ecliptic for the SP and LP, respectively. The GCS structure is located mainly in the east side of the Earth (negative “y” in HEE, positive “y” in GSE coordinate system). The longitude found by the CRC model ranges from 90° to 180° and indicates that the portion of the cylinder on east side arrived before at Earth then the portion on the west side. In this way, the results using different methodologies and data tend to agree. From the CRC modelling data, one can notice that the “y” component of the observed gradient is centered in zero before the modeling period starts and it is negative during the MC up to 2011/03/31. The CRC model from the SP resulted in a MC located mainly in the positive “y” direction, that is, in the dusk side of the Earth (closer to STEREO B than to STEREO A). The values can be seen in the last row of Table 6.17. When using the LP, the position lies in the positive “y” direction on the first hours and latter moves to the negative direction. This can be interpreted as the east portion of the cylinder arriving first and the portion located westward arriving later.

In order to compare the orientation angles, we also performed the MVA using both SP and LP. The latitudes and longitudes found are indicated in Table 6.18. The method was also performed using a time offset of up to two hours before and after the beginning of the time windows used. In this way, the MVA was calculated 25 times for each case. The average plus or minus one standard deviation is indicated in the Table 6.18. In this event, all the MVA calculations resulted

in $\lambda_2/\lambda_3 > 2$. The MVA result does not agree with the EFR model results when using the SP: both the latitude and longitude changes more than 50° . For the LP, the difference between the EFR and MVA reduced significantly and it is less than 20° for each angle. When comparing the MVA and the CRC model, the LP also produces smaller differences between the results: the latitude found is the same and the longitude changes less than 40° .

Table 6.18 - Results of the minimum variance analysis (MVA) using SP and LP.

	Shorter MC period	Longer MC period
Latitude (single MVA)	56°	16°
Latitude (multiple MVA)	$53\pm 4^\circ$	$16\pm 3^\circ$
Longitude (single MVA)	81°	107°
Longitude (multiple MVA)	$76\pm 16^\circ$	$107^\circ\pm 4$

Another significant difference between the CRC model using the SP and LP is on the Larmor radius. Considering the electromagnetic Lorentz force, a 60 GV particle traveling on a magnetic field of 10 nT will have Larmor radius equal to 0.13 AU. On the other hand, the model using the SP found a Larmor radius that corresponds to a magnetic field intensity of 20 nT. The maximum IMF intensity observed is 14 nT. The difference found here can be explained by the fact that the IMF observed in situ might not be correspondent to the central axis of the cylinder where its magnetic field is maximum, i.e., there is some displacement between the cylinder central axis and the Earth. On the other hand, the Larmor radius found by the CRC model using the SP corresponds to a magnetic field of 60 nT, more than four times higher than the maximum observed.

6.8 The magnetic cloud observed on 2011/05/28

Although the ICME catalog reports a MC type “two” on 2011/05/28, from our analysis we did not find any earthward directed CME from 2011/05/23 to 2011/05/27. There are two partial halo CMEs but both were directed away from the Earth.

This period does not have clear signatures of a magnetic cloud, for example: a) the plasma beta parameter is always much higher than 0.1; b) the magnetic field is not smooth inside the period, especially in the first half. This is shown in Figure 6.64.

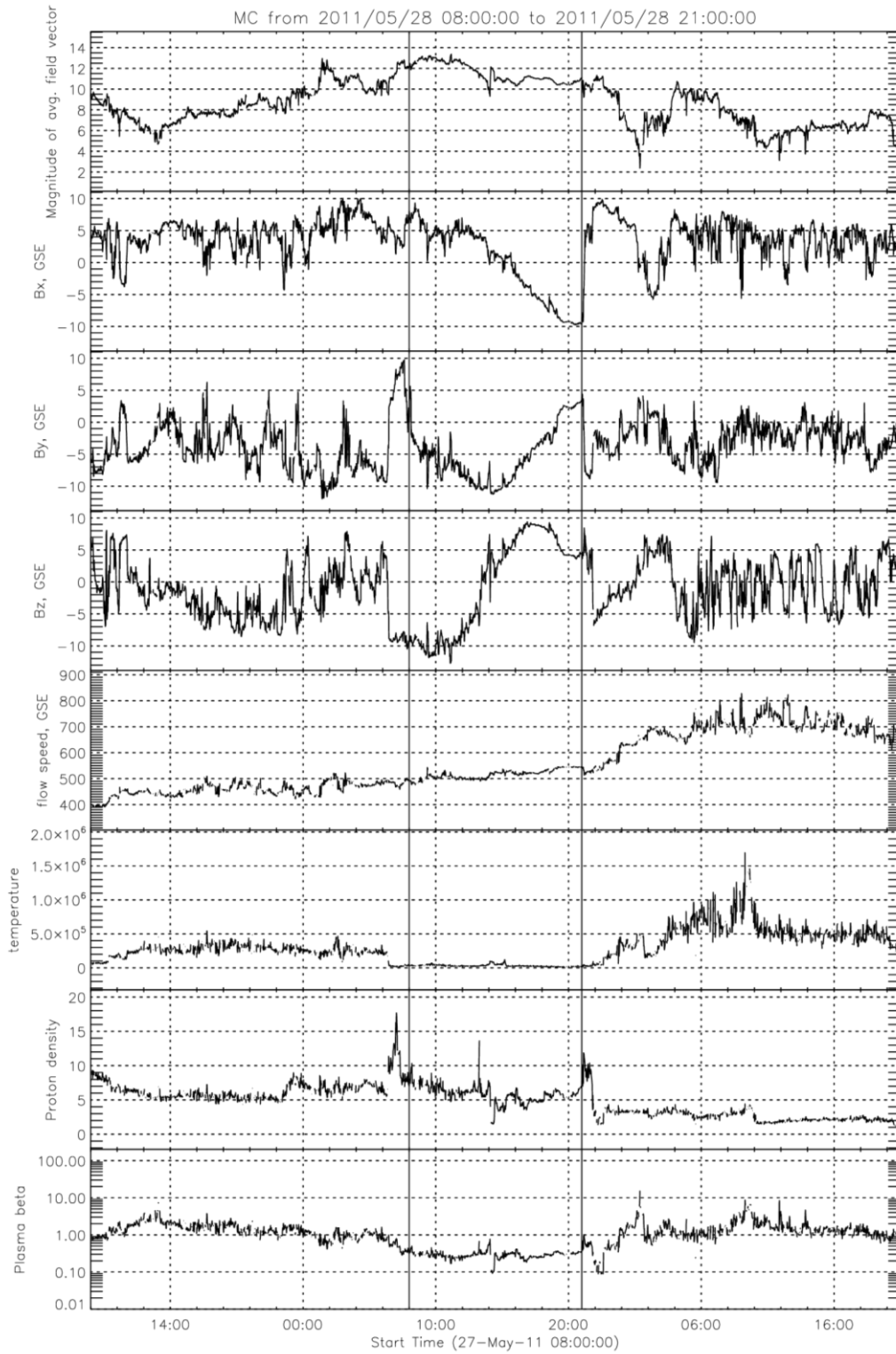


Figure 6.64 - The interplanetary magnetic field and plasma parameters during a MC observed on 2011/05/28.

There is a sector boundary on 2011/05/26 right after 12:00 UT. Notice that the magnetic field changes quickly from an angle between $[90^{\circ}\text{-}180^{\circ}]$ GSE to $[270^{\circ}\text{-}360^{\circ}]$ GSE. This corresponds to a change from the away sector to toward sector. This sector polarity is kept, at least, until the end of the month. This change happens about 2 days before the MC period.

Neither the cosmic ray count rate observed neither by muon detectors nor neutrons monitors do have a significant common modulation during this period (Figure 6.65 and Figure 6.66). The cosmic ray omnidirectional intensity does not decrease during this period and the “x” component of the gradient does not have the signature of an approaching CME. This is in agreement with our conclusion that there is no CME ejected toward the Earth.

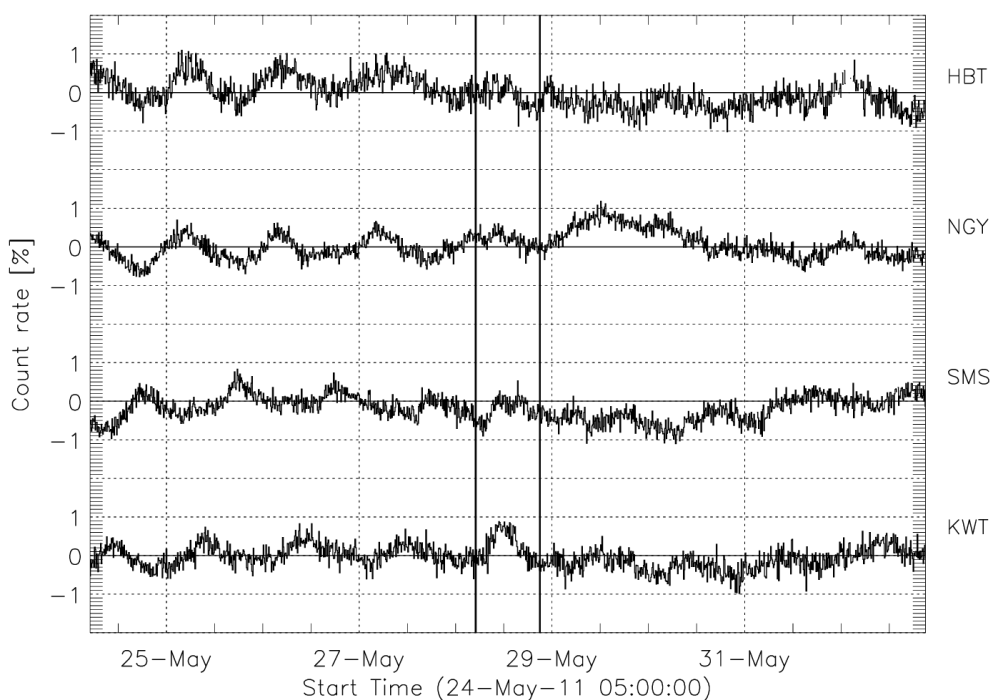


Figure 6.65 - The cosmic ray decrease observed by the vertical directional channels of the four muon detectors of the GMND during the MC on 2011/05/28.

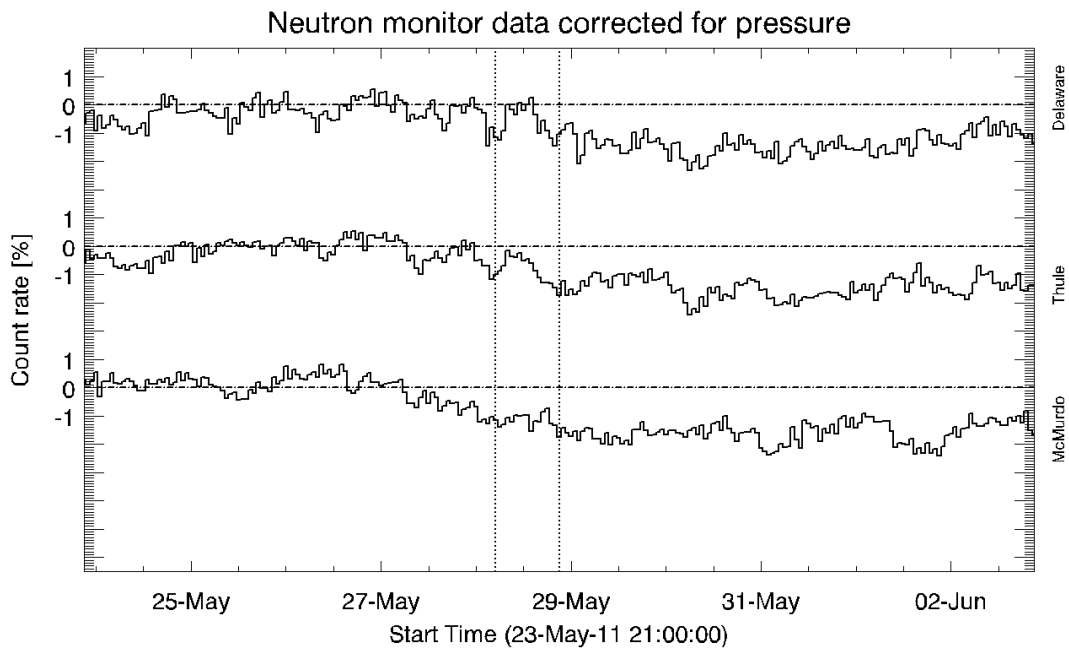


Figure 6.66 - The cosmic ray decrease observed by three different neutron monitors (Delaware, Thule and McMurdo) during the MC on 2011/05/28.

The isotropic component of the cosmic ray intensity do not have any decrease associated to the MC period (Figure 6.67). There is, however, a significant increase after the MC period of approximately 0.5%. The variations with maximum amplitude in the cosmic ray gradient are observed in the “y” component. This behavior might suggest some structure following the rotation of the Sun, like a sector boundary.

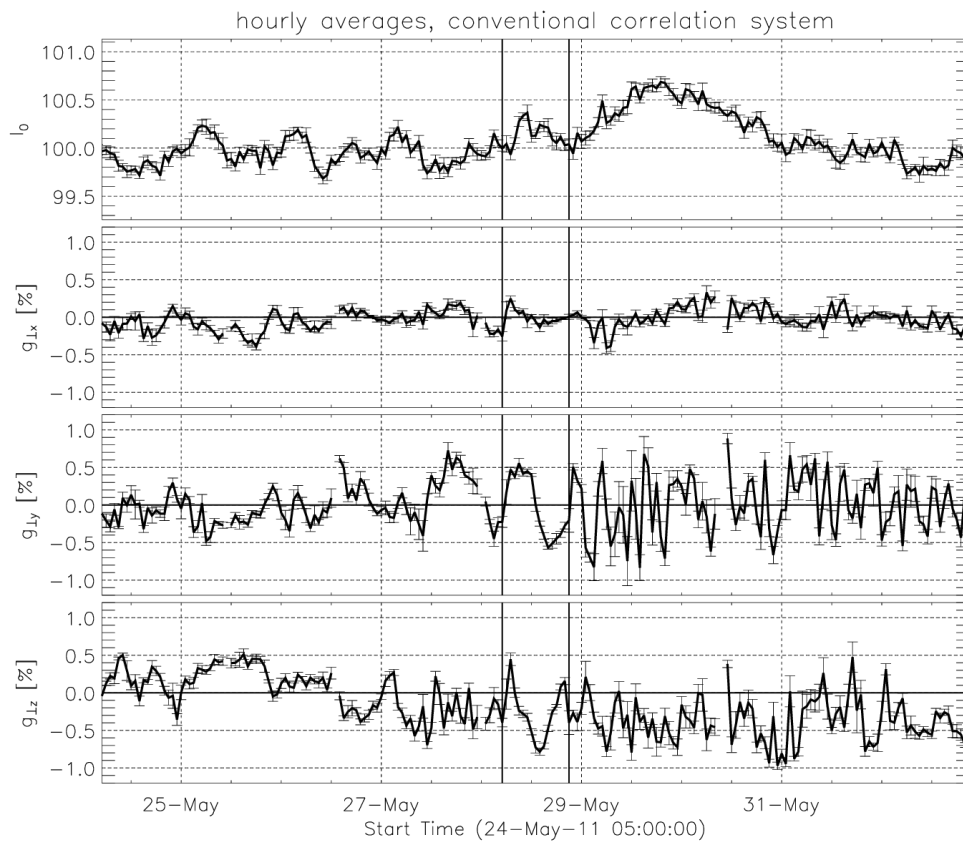


Figure 6.67 - The cosmic ray gradient and omnidirectional intensity observed by the GMDN during a MC observed on 2011/05/28.

6.9 The magnetic cloud observed on 2011/09/10

6.9.1 The origins in the solar corona

We inspected the CMEs ejected from 2011/09/05 to 2011/09/09 using a similar methodology than described in previous events. In this case, four earthward CMEs were observed.

The first CME was tracked on 2011/09/06 from 3:24 to 4:59 on the COR2 FOV. The result from the application of CORSET is shown in Figure 6.68. One can notice that another CME is observed in all frames shown here toward north (bottom part of each coronagraph image shown here). This northward CME is especially visible on COR2A FOV where its brightness is higher than in COR2B. For both coronagraphs, we set $Q = 14$. Even though it is hard to identify the transition line between one CME and the other, we understand that the area selected by CORSET is

appropriate. According to the results from CORSET3D, this CME has origins at high latitude, with longitude close to zero and speed of ~ 500 km/s.

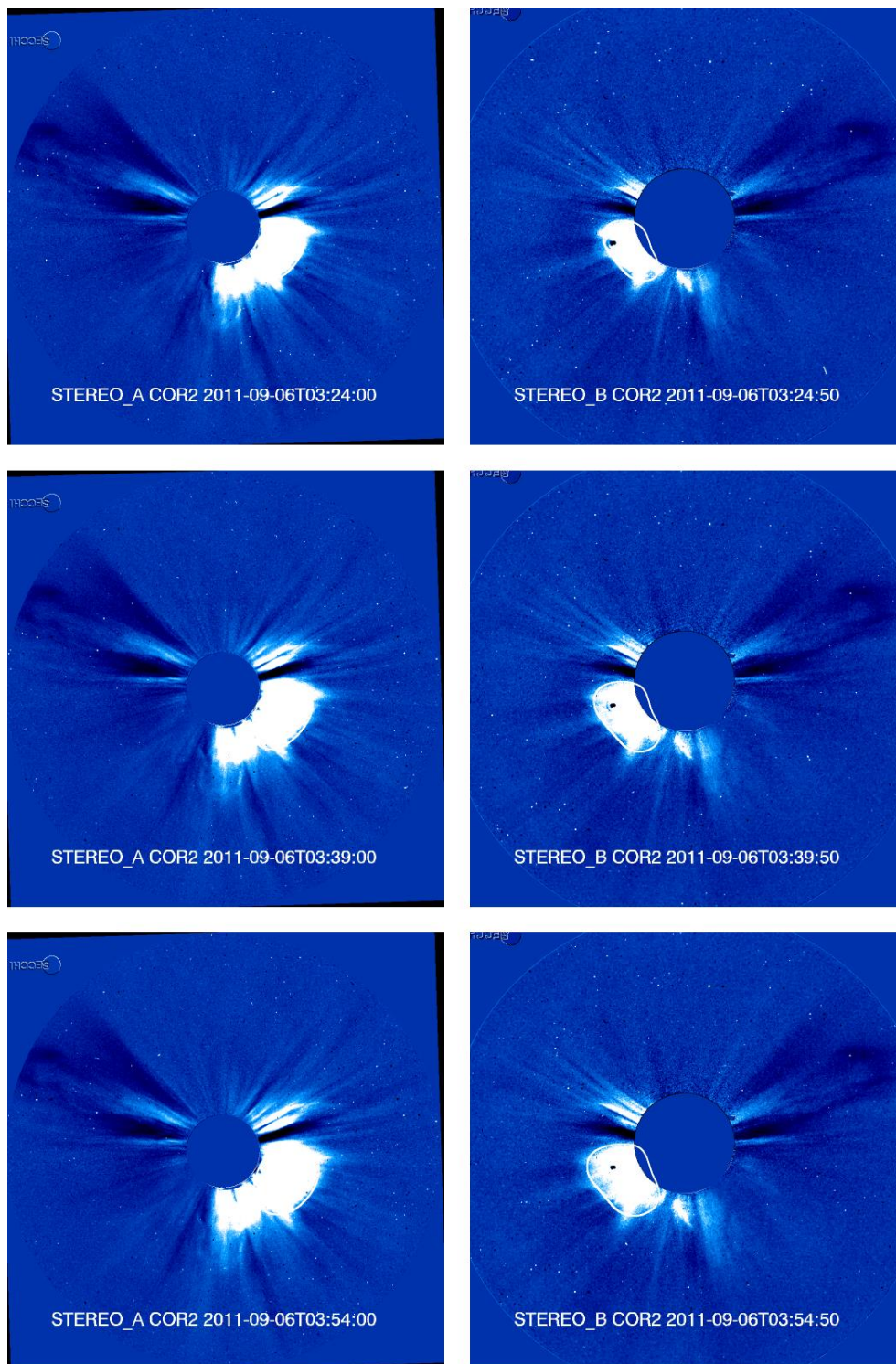


Figure 6.68 - The first earthward CME observed on 2011/09/06 on COR2A (left column) and COR2B (right column) FOVs.

The second CME was tracked from 2011/09/06 23:24 to 2011/09/07 00:24 using the default expansion factor $Q = 4$. The result from the CME tracking by CORSET is shown in Figure 6.69.

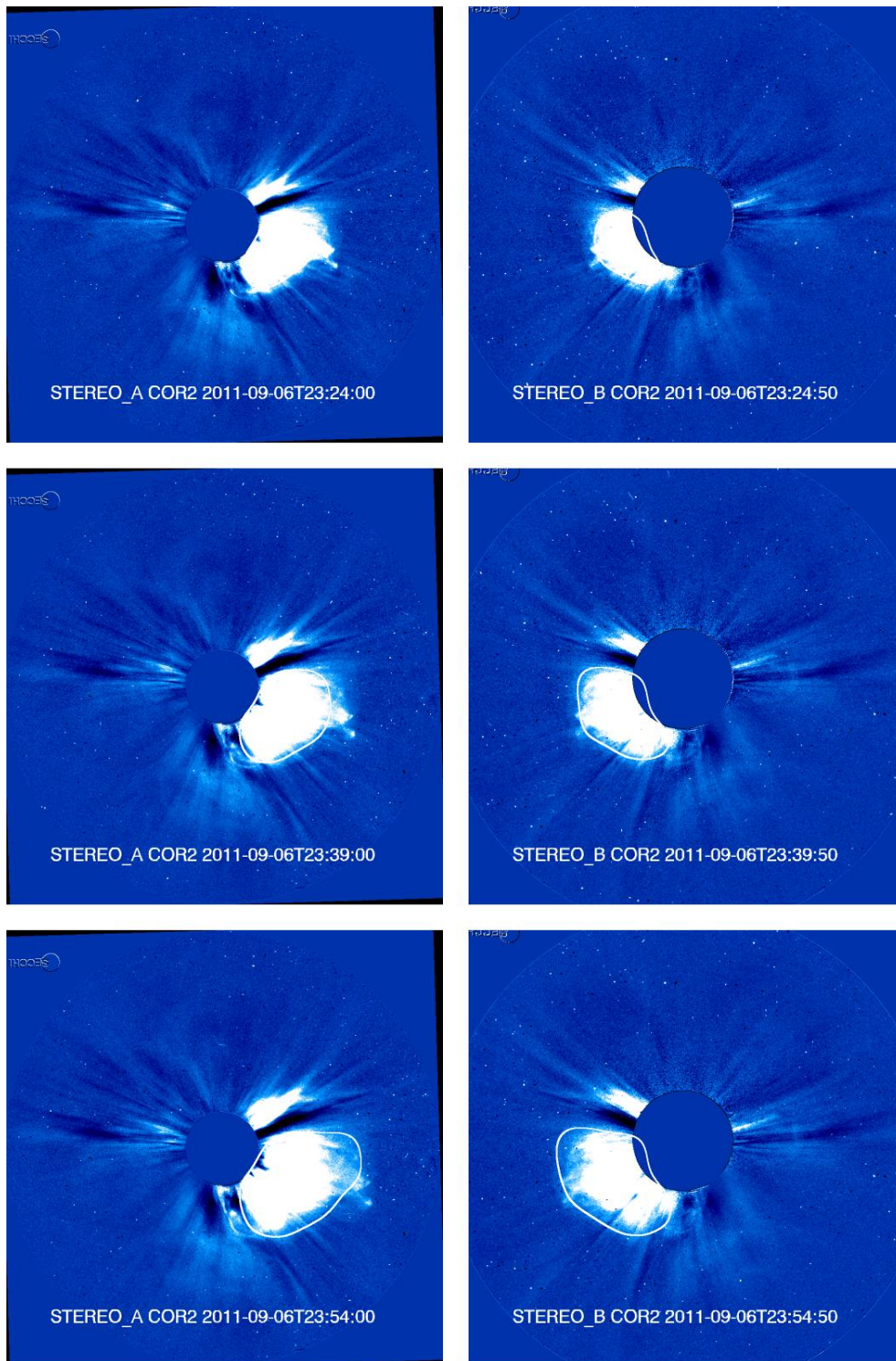


Figure 6.69 - The second earthward CME observed on 2011/09/06 on COR2A (left column) and COR2B (right column) FOVs.

The third CME was tracked from 2011/09/07 23:54 to 2011/09/08 1:24 and using expansion factor $Q = 10$. Its propagating direction is close to 30 degrees of latitude and longitude (Figure 6.70). One can notice that all the coronagraph images from this CME have a dark region. This is due to the base image subtracted from each image were a previous CME was visible and bright enough to produce this dark region. The CME on the background is not directed toward the Earth and is excluded from our analysis.

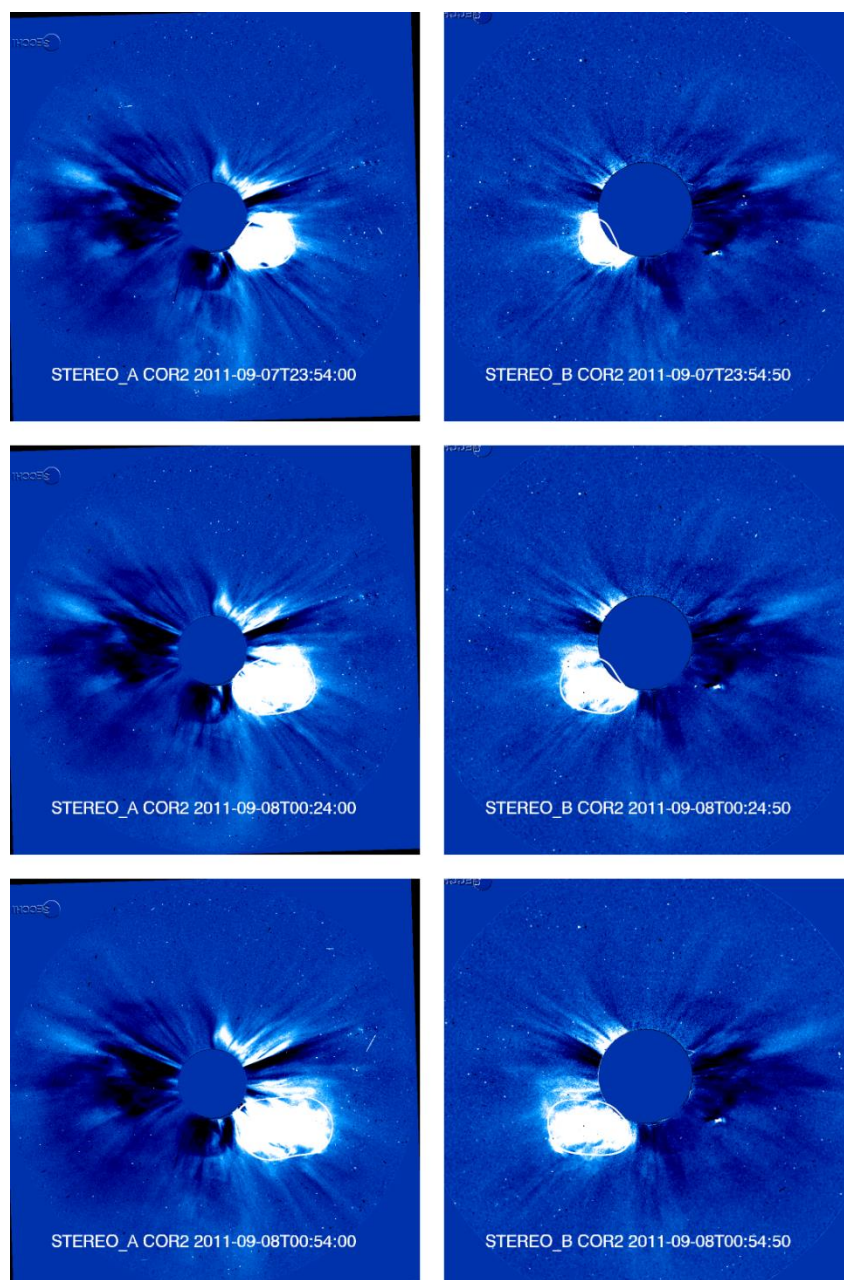


Figure 6.70 - The CME observed on 2011/09/08 on COR2A (left column) and COR2B (right column) FOVs.

The fourth CME was tracked on 2011/09/09 from 9:24 to 11:24 using $Q = 14$ (Figure 6.71 and Figure 6.72). This CME is seen brighter on the COR2A FOV than in the COR2B, suggesting that its propagation direction should be closer to the former than to the latter. The same hypothesis is suggested by the images from LASCO C3, which shows a CME directed mainly westward of the Earth-Sun line. The result found by triangulation is 30 degrees of longitude and -2 degrees of latitude, confirming our expectations of the westward propagation. The instantaneous speed is decreasing as a function of time from 461 to 269 km/s, and the average speed during the tracking period from 09:24 to 11:24 is 376 km/s, a rather slow CME.

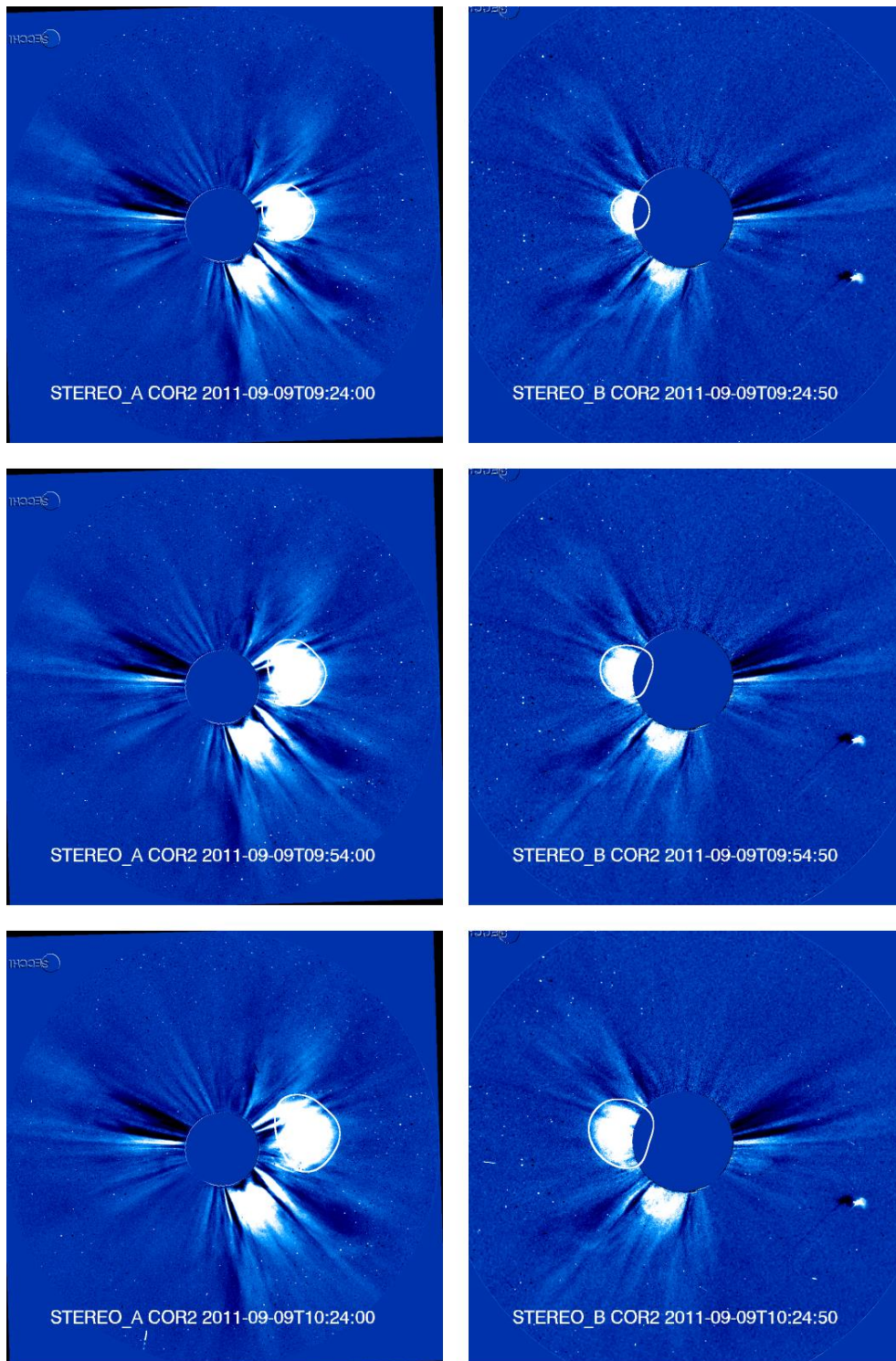


Figure 6.71 - The CME observed on 2011/09/09 on COR2A (left column) and COR2B (right column) FOVs. In this Figure only the first three frames are shown.

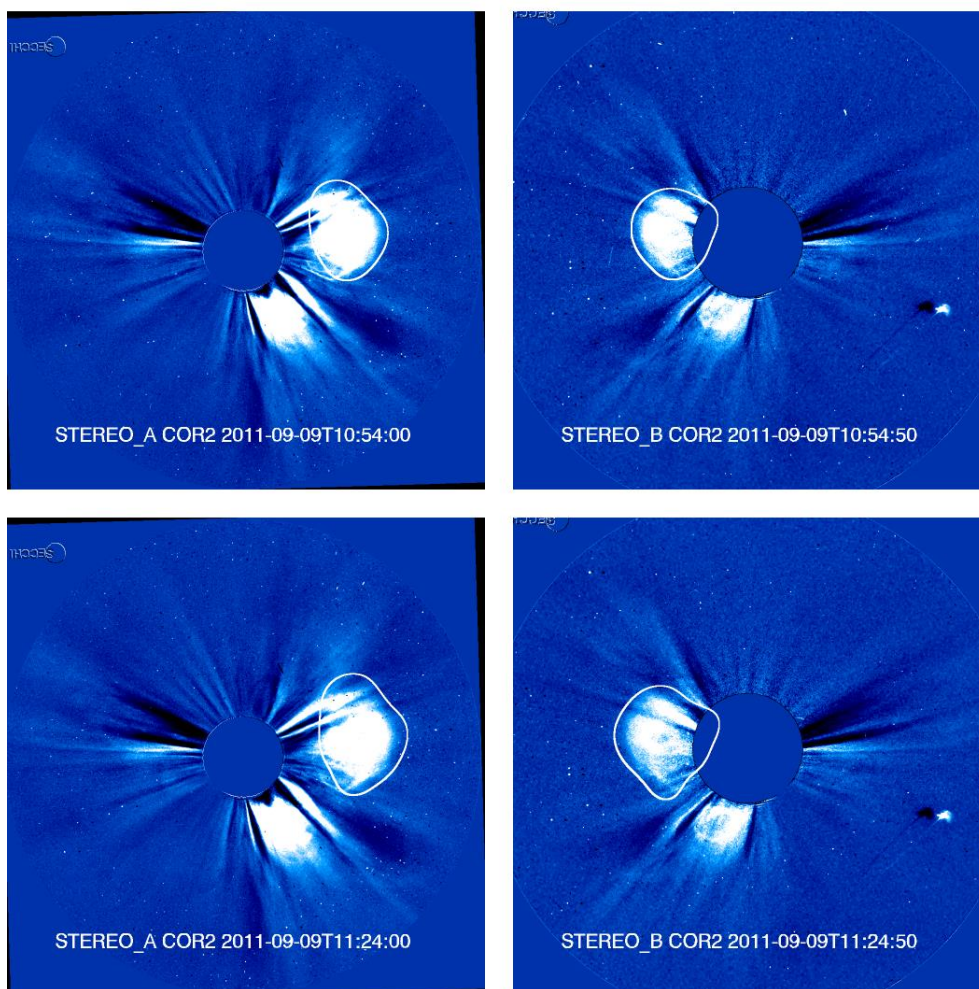


Figure 6.72 - The CME observed on 2011/09/09 on COR2A (left column) and COR2B (right column) FOVs. In this Figure only the last two frames are shown.

The main characteristics of the four CMEs tracked by CORSET3D are listed in Table 6.19. Among the four CMEs studied here, the CME #2 is the one extending closer to the coordinates $(0^\circ, 0^\circ)$. The remaining CMEs are distant from this coordinate in at least one of its coordinates. In the CME# 1 and #3, the latitude does not get closer to zero. In the CME #4, the longitude is distant from zero. Therefore, the CME #2 is more likely to be observed in situ near the Earth.

Comparing the speed of the four events, notice that the #2 is considerably faster than the CME #1 ejected approximately 20 hours before. Depending on the acceleration and/or deceleration of these CMEs beyond the outside limit of COR2 FOV, they may interact with each other. If the speeds are kept constant, the collision will be approximately 20 hours after the CME #2 ejection 0.4 AU distant from the Sun.

Table 6.19 - Kinematic parameters of the four CME ejected toward Earth from 2011/09/06 to 2011/09/09. The angles shown here are given in HEEQ coordinate system.

Parameter	CME #1	CME #2	CME #3	CME #4
First frame tracked	2011/09/06 03:24	2011/09/06 23:24	2011/09/07 23:54	2011/09/09 09:24
Last frame tracked	2011/09/06 03:54	2011/09/07 00:24	2011/09/08 01:24	2011/09/09 11:24
Minimum and maximum latitudes	[28°, 38°]	[5°, 62°]	[19°, 41°]	[-13°, 8°]
Minimum and maximum longitudes	[3°, 10°]	[-2°, 28°]	[8°, 41°]	[24°, 42°]
Group speed v_g averaged over time	435±6 km/s	861±39 km/s	570±13 km/s	372±18 km/s
Central longitude	6°	13°	25°	33°
Central latitude	33°	33°	30°	-2°
Minimum time averaged radial speed $\bar{v}_r(\theta_j, \phi_k)$	423 km/s	794 km/s	538 km/s	339 km/s
Maximum time averaged radial speed $\bar{v}_r(\theta_j, \phi_k)$	447 km/s	1086 km/s	592 km/s	399 km/s
Group speed as a function of time $v_g(t_{i+1})$	[452,417] km/s	[915, 1065, 836] km/s	[592, 572, 482] km/s	[278, 375, 372, 458] km/s
Maximum error of the triangulation	< 0.1 solar radii	0.2 solar radii	0.2 solar radii	0.1 solar radii

6.9.2 The interplanetary medium and the cosmic ray modulation

According to the ICME catalog, this MC event starts at 2011/09/10 03:00 UT and it ends at 2011/09/10 15:00 UT. The analysis of the interplanetary medium is unfavorable due to data gaps (Figure 6.73). From the information available, this event does not strictly follow the definition of a magnetic cloud: the beta parameter is significantly higher than 0.1 and the IMF magnitude does not have a smooth behavior.

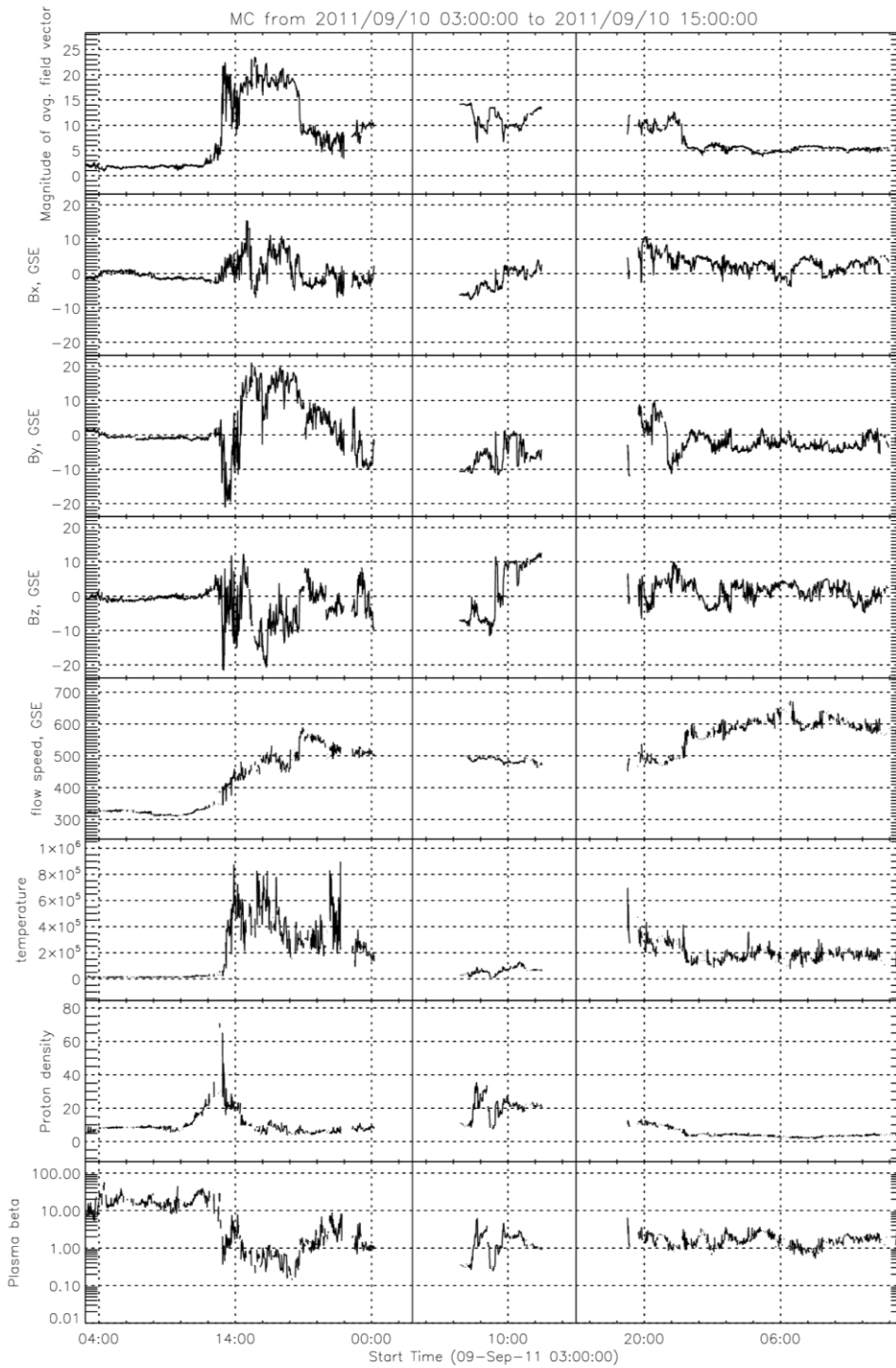


Figure 6.73 - The interplanetary magnetic field and plasma parameters during a MC observed on 2011/09/10.

Inspecting the longitude of the IMF (not shown here), we found a sector boundary in close timing to this MC. From 2011/09/03 to 2011/09/08 the longitude of the IMF lies in the angular range from 90° to 180° (GSE coordinates), a typical behavior of a away sector. From 2011/09/10 on, the longitude ranges mainly from 270° to 360° , a toward sector.

This event might have a superposition of more than one ICME since four CMEs were ejected toward the Earth during a period of a few hours. In special, the CME #2 had higher speed than the CME #1 and there is a possibility that they CME #2 overtook CME #1 in the interplanetary medium before reaching the Earth.

6.9.3 The cosmic ray observations

The vertical directional channels of the GMDN show a count rate decrease during this event (Figure 6.74). The cosmic rays observed by the three neutron monitors used in this Thesis do also have a common decrease of at least 2% during the magnetic cloud period (Figure 6.75).

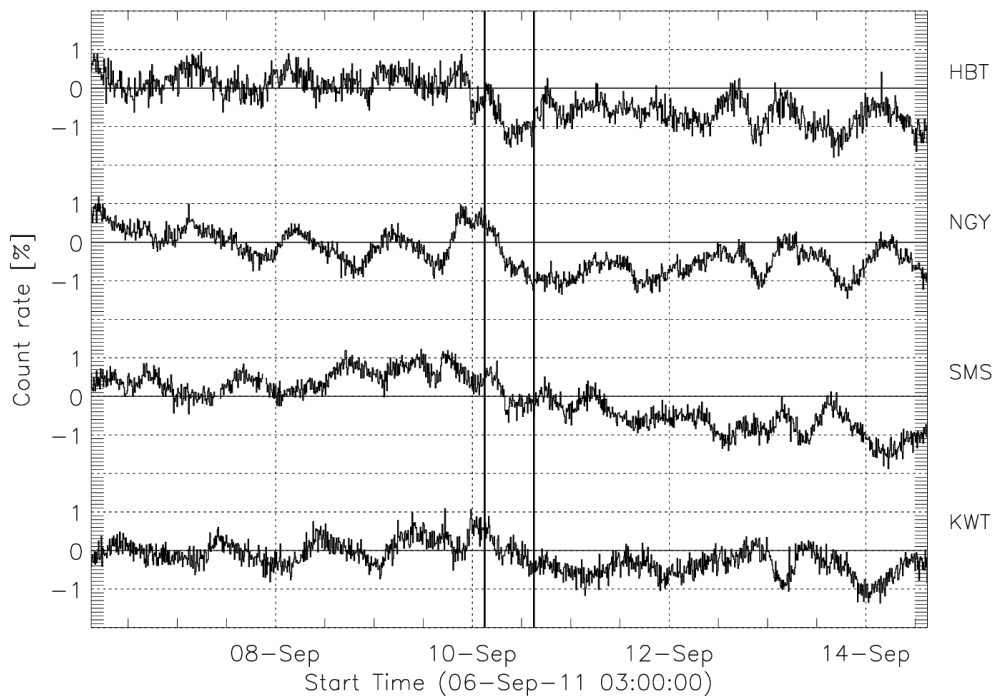


Figure 6.74 - The cosmic ray count rate observed by the vertical directional channels of the four muon detectors of the GMND during the MC on 2011/09/10.

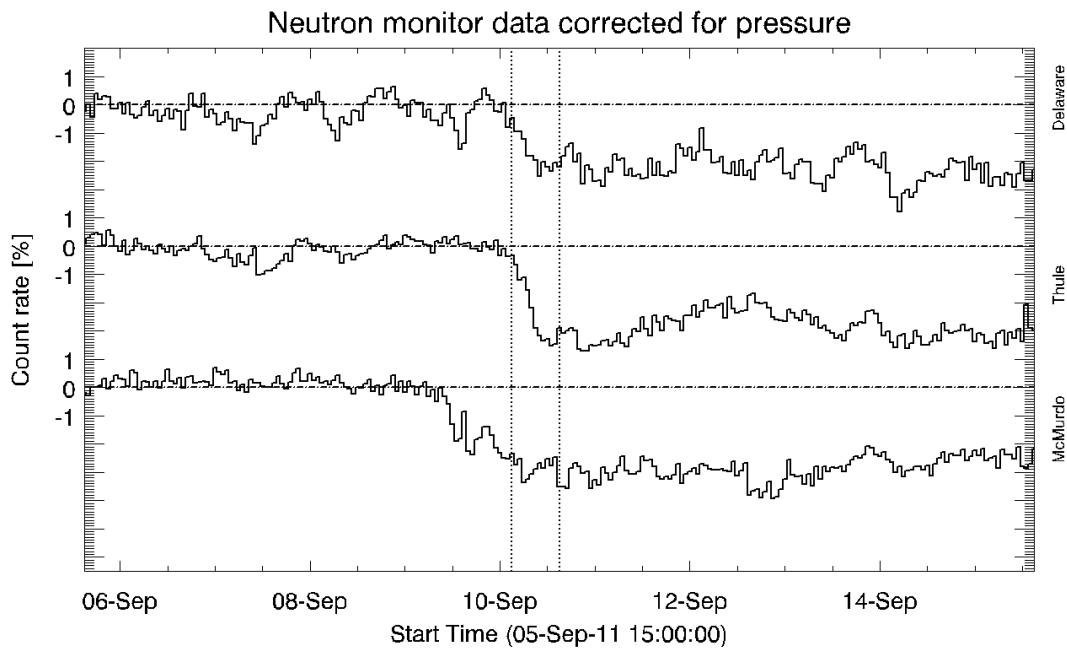


Figure 6.75 - The cosmic ray decrease observed by three different neutron monitors (Delaware, Thule and McMurdo) during the MC on 2011/09/10.

There is a decrease of about 1% in the cosmic ray density observed by the GMDN (Figure 6.74). The anisotropy in this period is basically perpendicular to the IMF, except during a short period of 3 hours starting at 00:00 2011/09/10. Despite of this, the cosmic ray cylinder model is not suitable because the isotropic intensity decrease is not followed by an increase back to the level registered before the decrease started.

The cosmic ray gradient is also unfavorable in this event due to some hours with missing IMF data. From the information available (Figure 6.76), one can notice a significant negative “z” cosmic ray gradient of about 1% during the passage of the MC on the Earth. This suggests a cosmic ray depleted region crossing above the ecliptic plane.

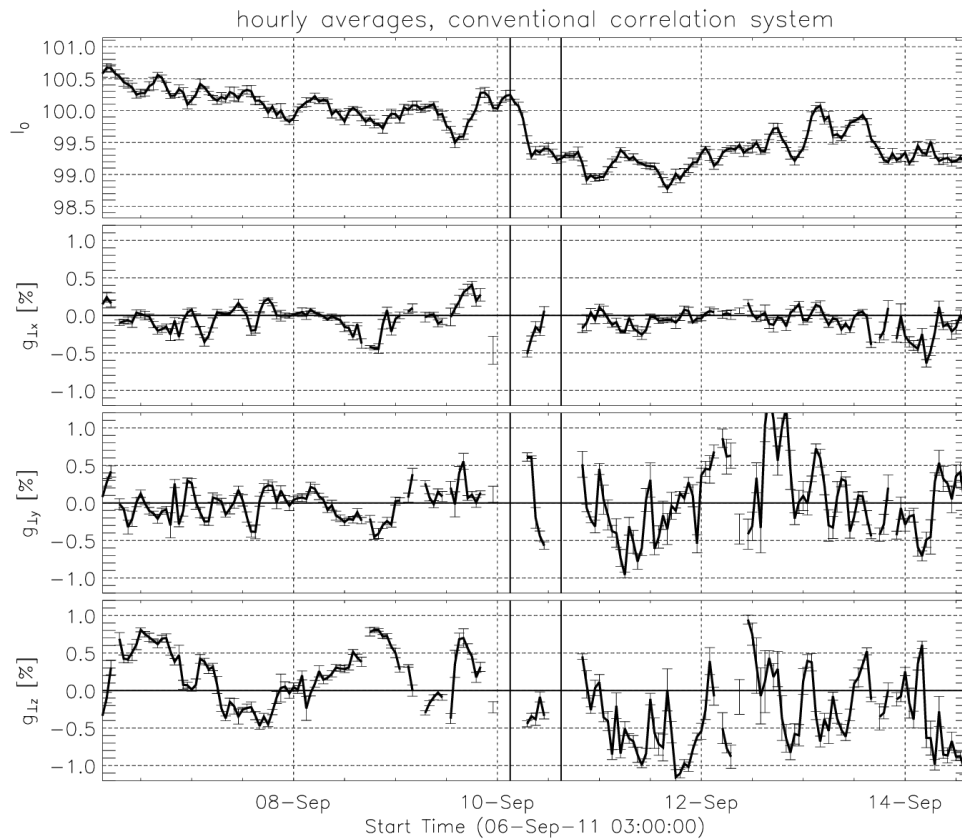


Figure 6.76 - The cosmic ray isotropic intensity and orthogonal components of the gradient during the period of the MC (indicated by the vertical lines) observed on 2011/09/10.

According to conclusions from Section 6.9.1, all CMEs have significantly positive latitudes and the resulting ICME should also be located mainly above the ecliptic plane. So, the overall latitude of propagation deduced from coronagraph observations agrees with the overall position of the cosmic ray depleted region deduced from GMDN data.

6.10 The magnetic cloud observed on 2011/09/17

6.10.1 The interplanetary medium

The MC observed on 2011/09/17 is shown in Figure 6.77. This event is a reasonable example of the MC because:

- the plasma beta parameter is close to 0.1 in large part of the MC period;
- the proton density is low;

- the IMF is quite smooth inside the MC when compared to the period before it;
- the orthogonal components of the IMF suggest some sort of rotation, especially in the “y” and “z” components.

The period of the MC was chosen by visual inspection using the IMF and beta parameter as a reference. Except for a sheath region observed a few hours before the MC (also shown in Figure 6.77), there is no other interplanetary structure observed in the interplanetary medium in the period up to four days before or after the MC.

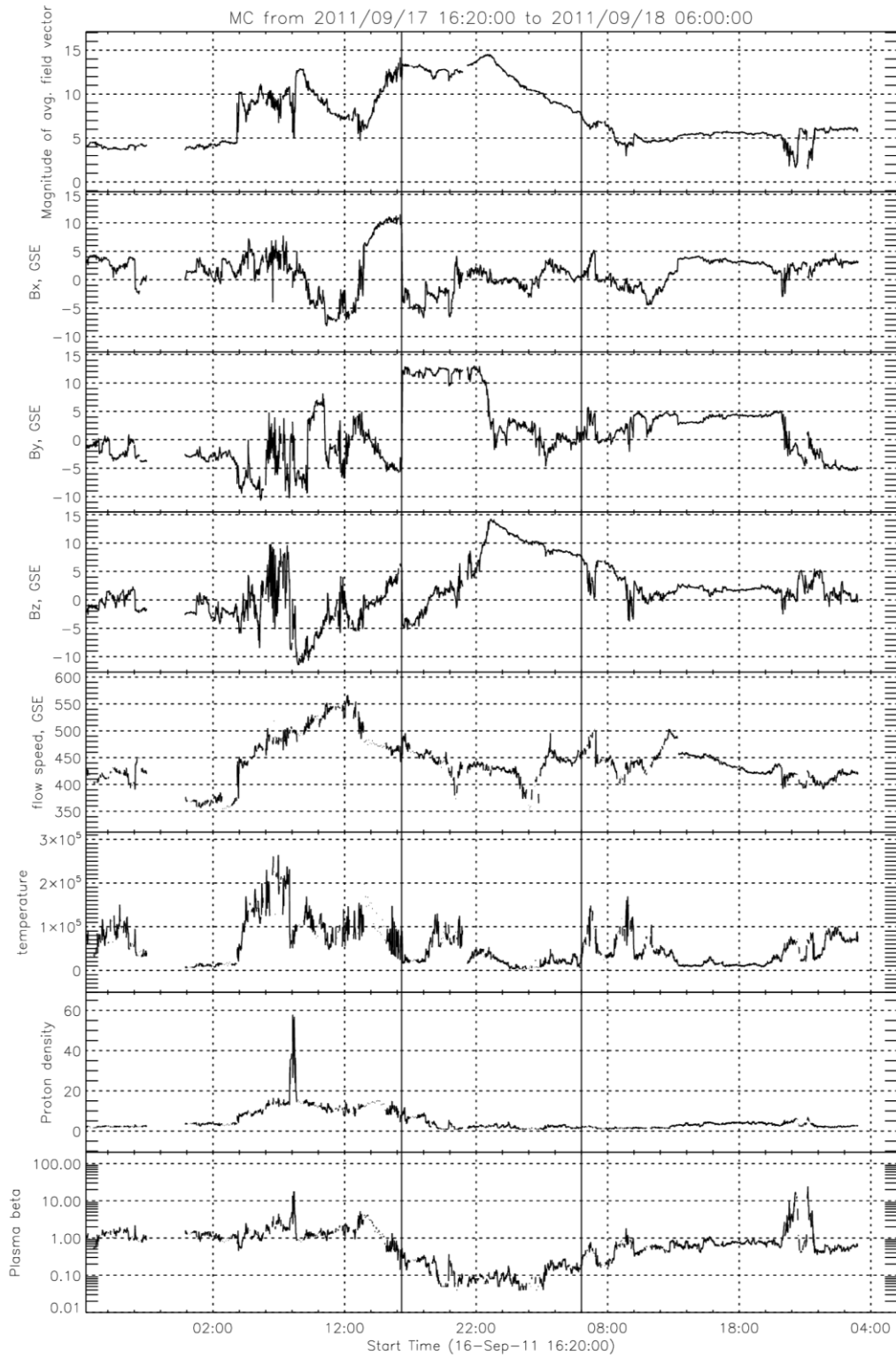


Figure 6.77 - The interplanetary magnetic field and plasma parameters during a MC on 2011/09/17. The vertical lines indicate the magnetic cloud timing.

6.10.2 The origins in the solar corona

We inspected LASCO-C3 images from 2011/09/13 to 2011/09/16 and we found only one halo CME. Inspecting the angular range of this CME on the COR2AB data, we concluded that it must be Earthward directed. We tracked it using CORSET with $Q = 4$ in both COR2 coronagraphs and the results are shown in Figure 6.78, Figure 6.79 and Figure 6.80. To our assessment, the front of the CME is satisfactorily identified but there is a lateral excess on the area included as part of the CME in both coronagraphs. This is clear mainly in the last frames. Since we are not studying the angular extension of the CME here, this problem will probably not affect the radial speed calculated close to the central portion of the CME front.

The map of the CME radial speed is shown in Figure 6.81 and the summary of the radial speed is listed in Table 6.20. It is clear that this CME is directed northward and westward of the Earth. Direct observation of the CME angular range on LASCO-C3 FOV supports our conclusion of the overall direction of propagation.

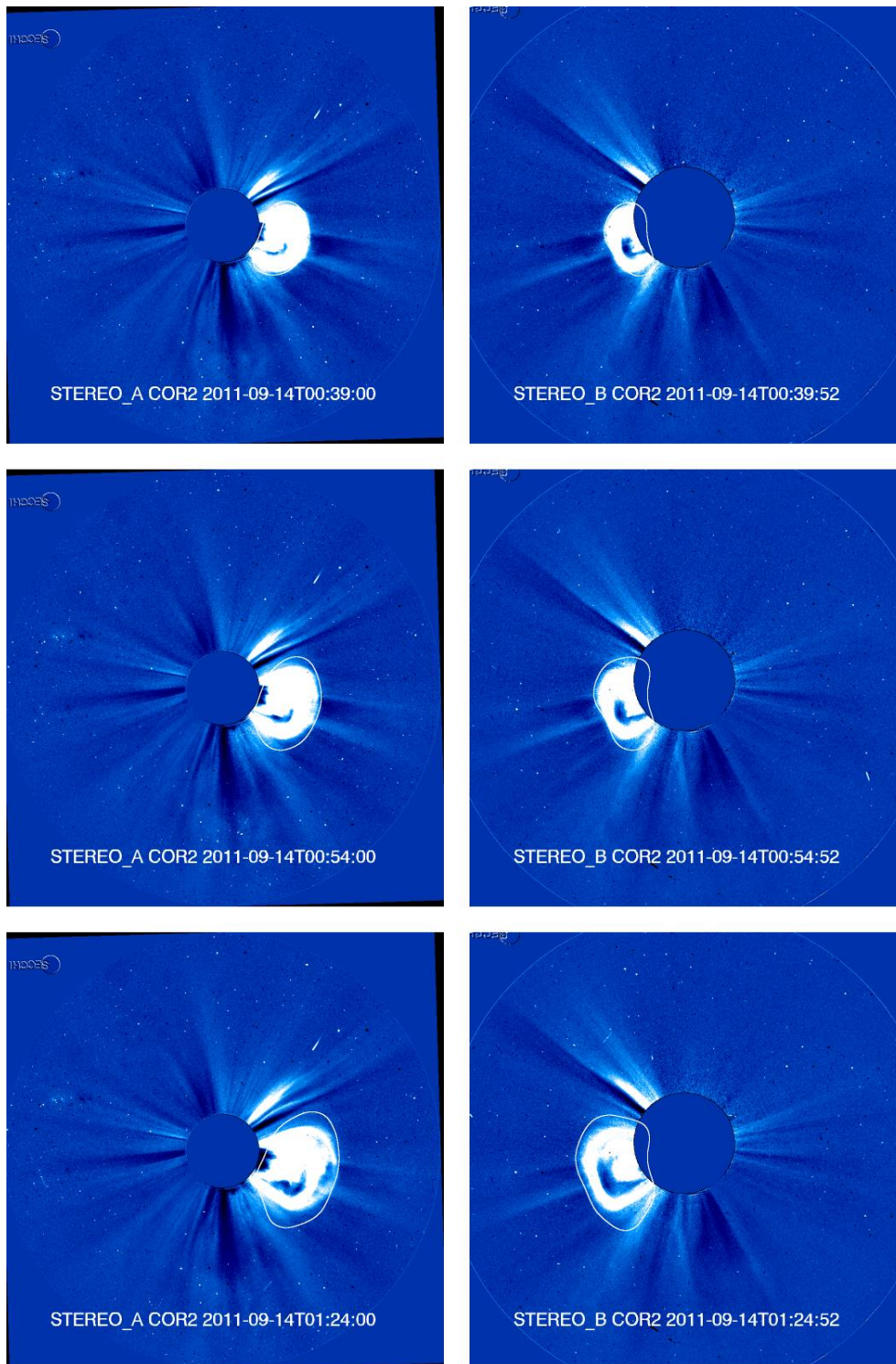


Figure 6.78 - The CME observed on 2011/09/14 in COR2A (left column) and COR2B (right column) FOVs. Only the first three frames are shown here. Notice that the images are rotated to the stereo baseline and that the north of the image is approximately pointing toward the bottom of the image.

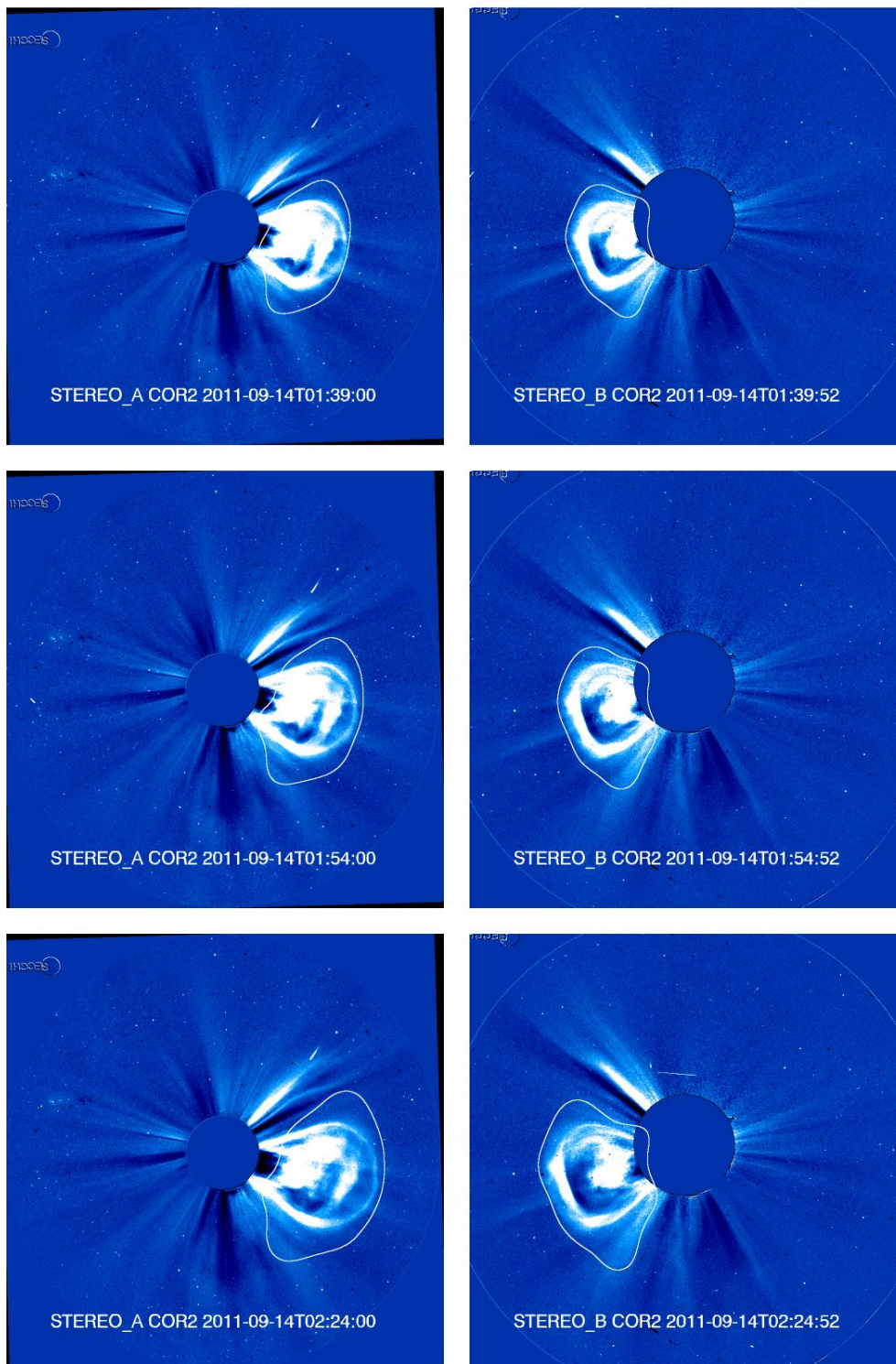


Figure 6.79 - The CME observed on 2011/09/14 in COR2A (left column) and COR2B (right column) FOVs. Only the fourth, fifth and sixth frame are shown here. Notice that the images are rotated to the stereo baseline and that the north of the image is approximately pointing toward the bottom of the image.

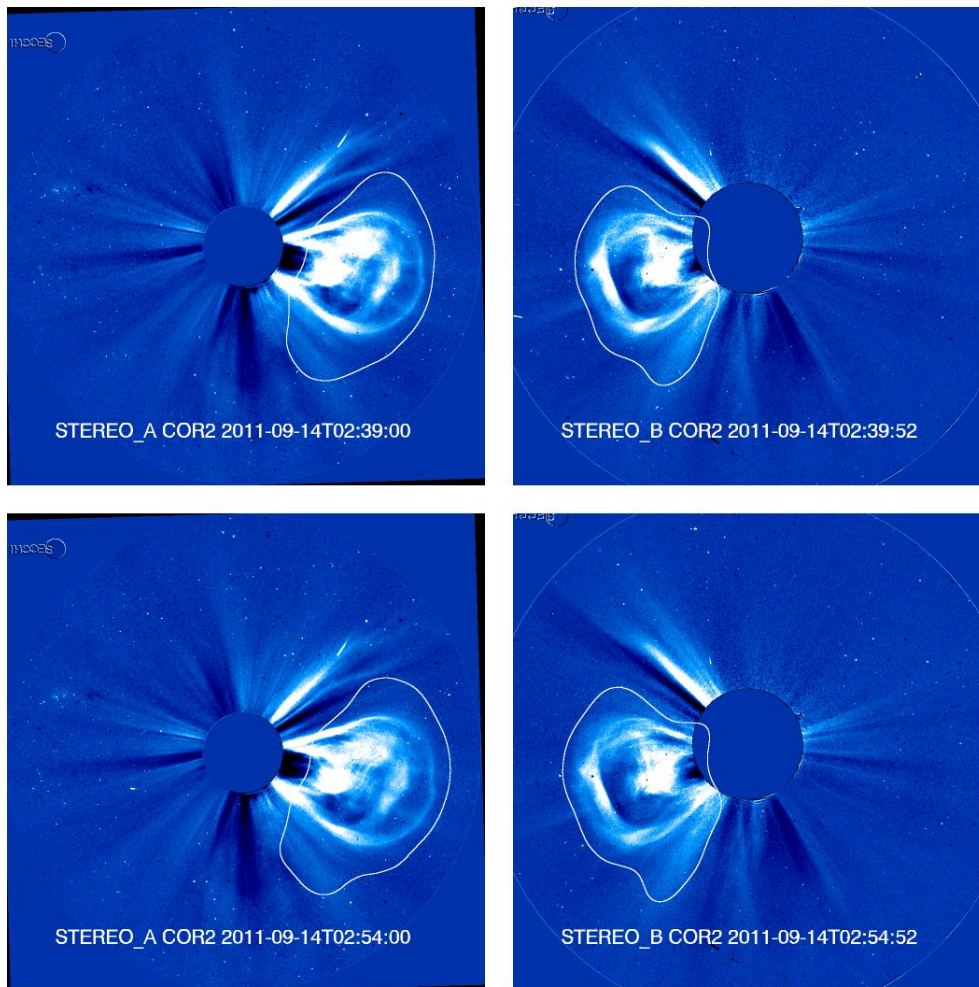


Figure 6.80 - The CME observed on 2011/09/14 in COR2A (left column) and COR2B (right column) FOVs. Only the last two frames are shown here. Notice that the images are rotated to the stereo baseline and that the north of the image is approximately pointing toward the bottom of the image.

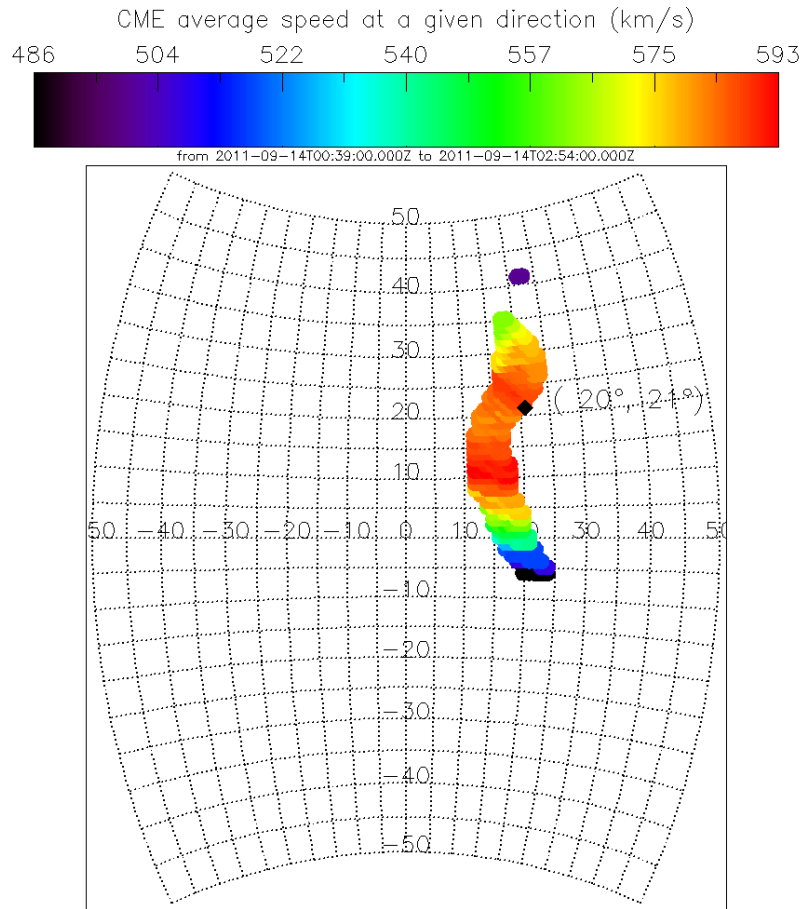


Figure 6.81 - The radial speed of the CME front observed on 2011/09/14 as a function of latitude and longitude (in HEEQ coordinate system). The black diamond indicates the center of the CME front.

Table 6.20 - Kinematic parameters of the CMEs on 2011/09/14. The angles shown here are given in HEEQ coordinate system.

Parameter	Result
Minimum and maximum latitudes	$[-7^\circ, 49^\circ]$
Minimum and maximum longitudes	$[8^\circ, 34^\circ]$
Group speed v_g averaged over time	571 ± 26 km/s
Central direction of the CME averaged over time (longitude)	21°
Central direction of the CME averaged over time (latitude)	21°
Minimum value of $\overline{v_r}(\theta_j, \phi_k)$	486 km/s
Maximum value of $\overline{v_r}(\theta_j, \phi_k)$	593 km/s
Group speed as a function of time $v_g(t_{i+1})$	$[584, 545, 601, 604, 460, 605, 555]$ km/s
Maximum error of the triangulation	0.2 solar radii

6.10.3 The cosmic ray observations and modeling

The cosmic ray count rate observed by the vertical directions of the GMDN are shown in Figure 6.82. Notice that there is no common decrease in the cosmic ray density inside the MC period. The neutron monitor data is shown in Figure 6.83 and their count rate have a decrease up to 2%.

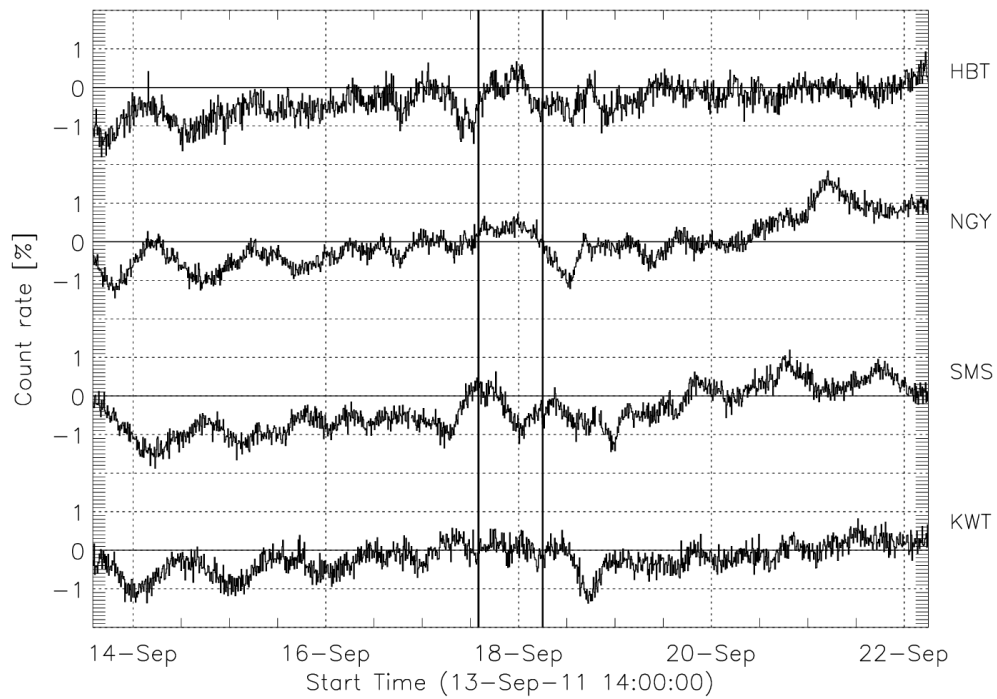


Figure 6.82 - The cosmic ray decrease observed by the vertical directional channels of the four muon detectors of the GMND during the MC on 2011/09/17.

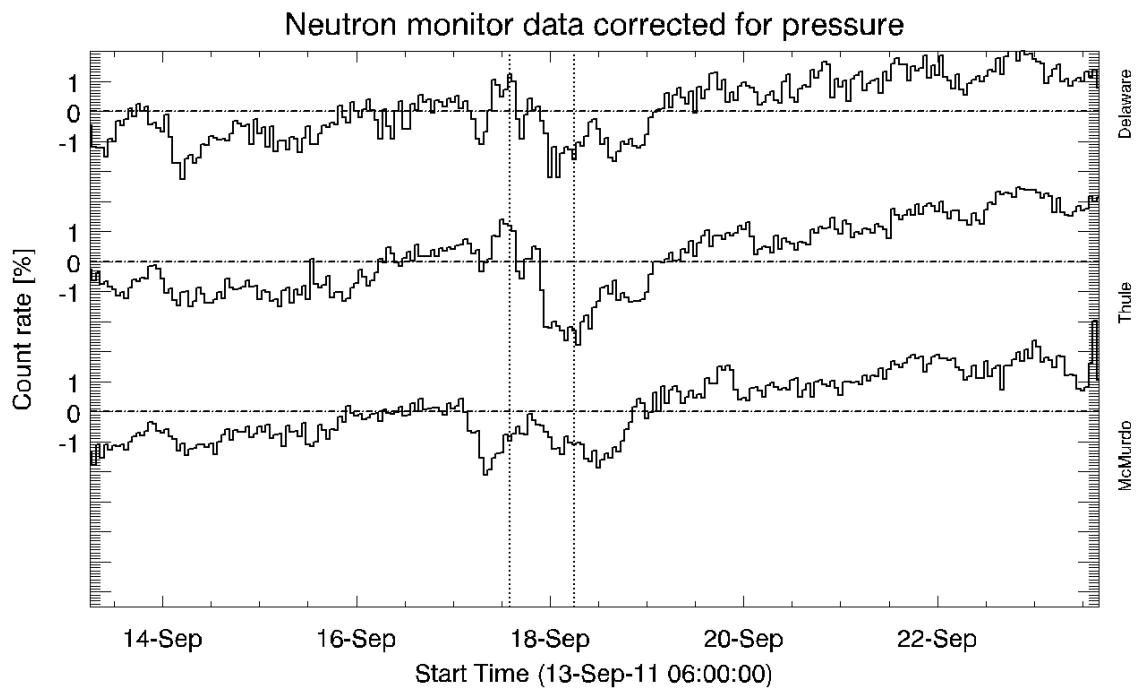


Figure 6.83 - The cosmic ray decrease observed by three different neutron monitors (Delaware, Thule and McMurdo) during the MC on 2011/09/17.

There is no isotropic cosmic ray decrease observed by the GMDN during this MC and the CRC model cannot be used here, see Figure 6.84. The component of the cosmic ray anisotropy perpendicular to the IMF is dominant but the time profile of the “x” component of the gradient does not show any signature of the interplanetary structure approaching the Earth.

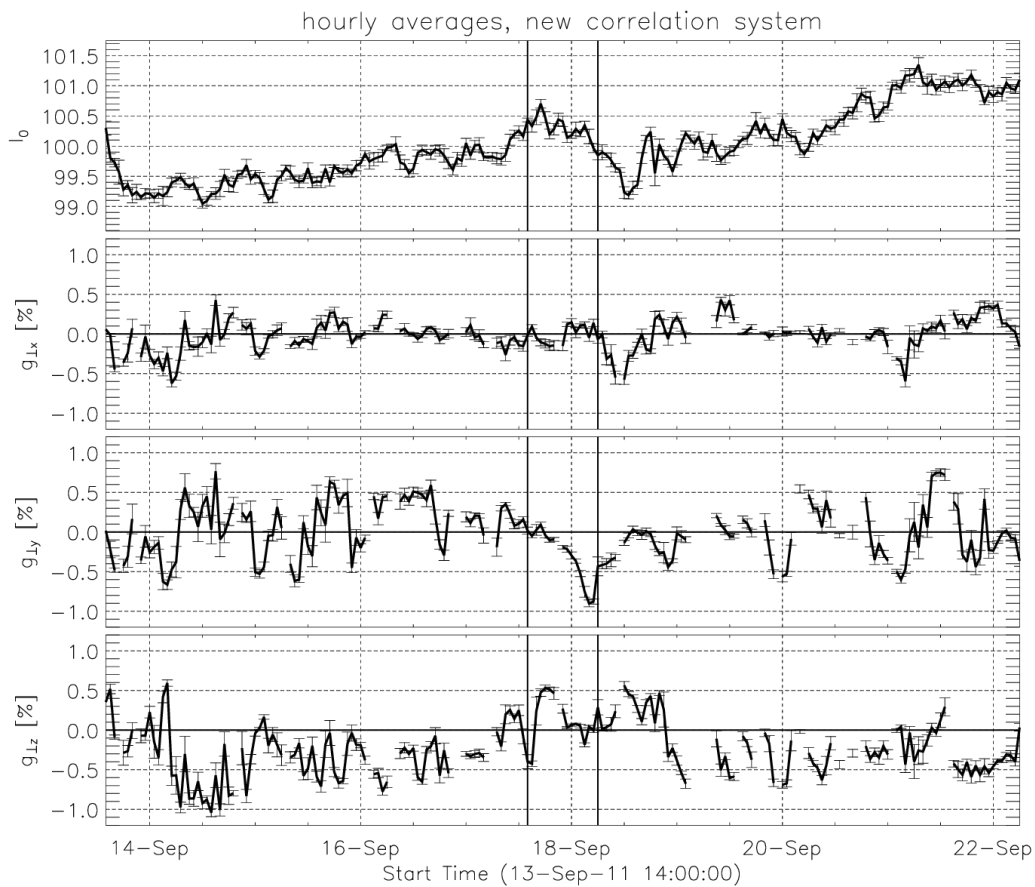


Figure 6.84 - The cosmic ray isotropic intensity and orthogonal components of the gradient during the period of the MC (indicated by the vertical lines) observed on 2011/09/17.

6.11 The magnetic cloud observed on 2011/10/06

6.11.1 The interplanetary medium

According to the ICME catalog, there are three ICMEs in close timing to the MC observed on 2011/10/06, starting at about 7:36 on 2011/10/05 (Table 6.21). In principle, we were interested in studying only the events with MC quality index equal to two and therefore only the second ICME is of our primary interest here (see explanation about the quality index in Table 6.21). However, the interval between one event and the other is less than 24 hours. Distinguishing the effect of each one on both cosmic ray and interplanetary data is not straightforward. Consequently, we need to do this study taking into account all the three ICMEs.

Table 6.21 - The list of three consecutive ICMEs on the beginning of October 2011. Source: ICME catalog from Richardson and Cane.

#	Disturbance	ICME start	ICME end	MC quality index
1	2011/10/05 07:36	2011/10/05 10:00	2011/10/05 22:00	1: "the ICME shows evidence of a rotation in field direction, but lacks some other characteristics of a magnetic cloud"
2	2011/10/06 12:00	2011/10/06 12:00	2011/10/06 23:00	2: "the ICME has the clear features of a magnetic cloud"
3	2011/10/07 02:00	2011/10/07 02:00	2011/10/07 17:00	0: "the ICME is not a reported magnetic cloud, and lacks most of the typical features of a magnetic cloud"

Beyond the ICMEs, there is a shock at the beginning of the first ICME. Therefore, the search for Earthward directed CMEs needs to be done in the period from 5 to 1 days before the beginning of the first ICME, that is, from 2011/09/30 to 2011/10/04 (section 6.11.2). The sector polarity before the set of ICMEs is neither a clear toward nor away sector. From 2011/10/07 on, the polarity is toward the Sun (mainly in the range from 270° to 360°).

The period of the MC is shown in Figure 6.85 (disturbance #2). During the MC period, the IMF intensity has less oscillations. The magnetic field maximum intensity is ~ 12 nT and it is almost constant during this period. From the orthogonal components of the IMF, we can identify some hints of rotation in both "y" and "z" components. The rotation shown probably does not exceed 90° degrees since the "y" and "z" components do not change signal. The solar wind speed is almost constant and has magnitude of ~ 370 km/s. The temperature is never higher than 0.5 MK. The beta parameter, which should be 0.1 according to the criteria of MC, is always higher than 0.3. In summary, this MC does not have all the signatures of a MC although there are indications of rotation in the IMF. The two remaining ICMEs identified by the catalog are much more distant from the definition of the MC because the magnetic field has significant oscillations, and the orthogonal components do not show clear rotation. The last ICME has a remarkably low IMF magnitude of ~ 5 nT.

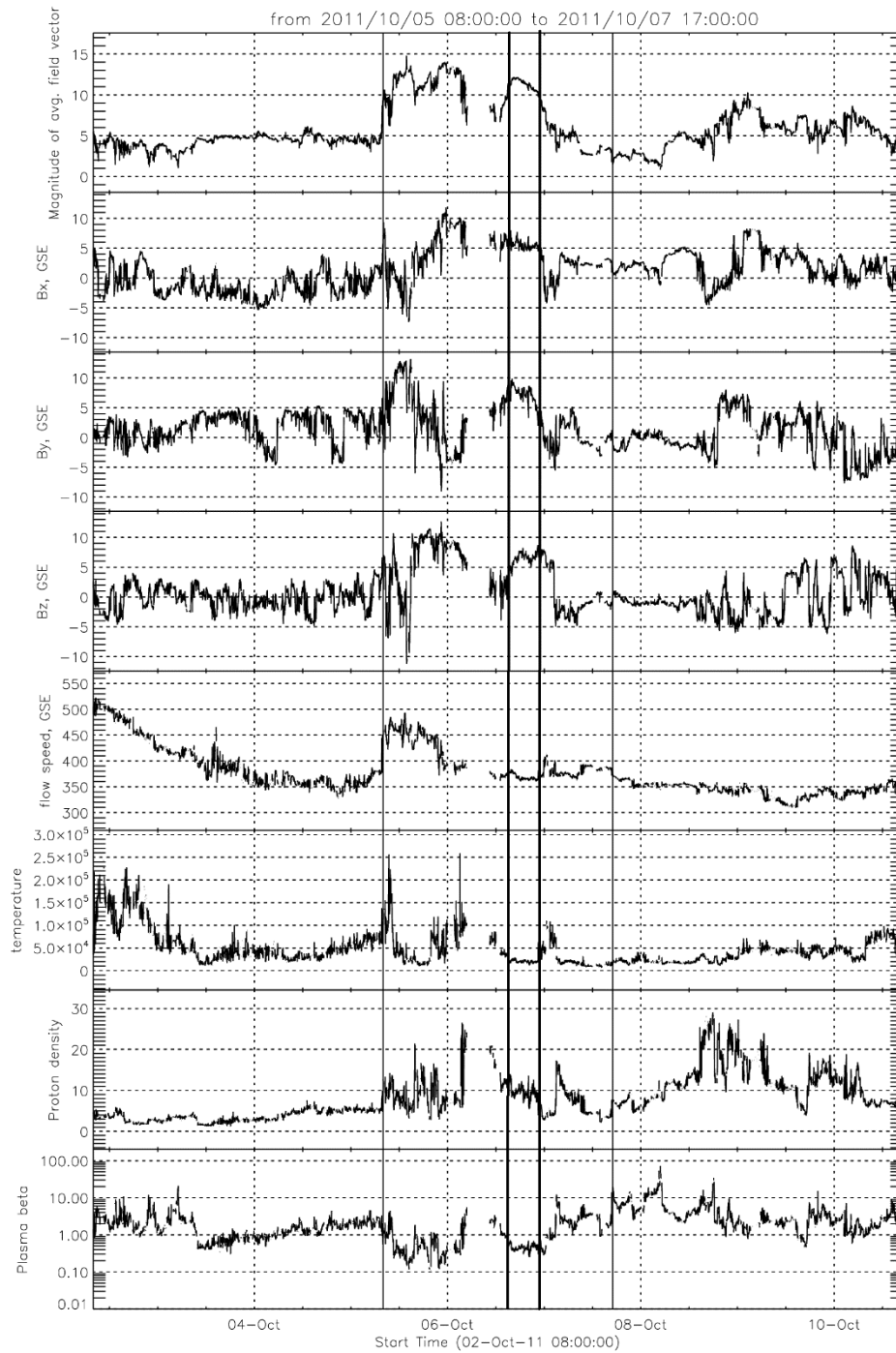


Figure 6.85 - The interplanetary magnetic field and plasma parameters during a MC on 2011/10/06. Within the thin vertical lines, there are three interplanetary structures. The thick vertical lines indicate the MC timing (disturbance #2).

6.11.2 The origins in the solar corona

We carefully analyzed all the CMEs between 2011/09/30 and 2011/10/06 observed by the three spacecraft in order to identify those directed toward the Earth.

On 2011/09/30 there is a slow northward CME starting at about 2:00 UT in the LASCO-C3 FOV. In close timing, COR2B FOV has a CME in the northeast quadrant and COR2A FOV in the northwest quadrant. These combined observations indicate a CME ejected on the backside of the Sun, away from the Earth.

On 2011/10/01 there is a small CME seen in both COR2A and COR2B in close timing, starting just a few minutes before and directed slightly toward north. The CME is potentially a source of any ICME observed close to the Earth and we tracked it with CORSET in both COR2A and COR2B from 11:39 to 13:54. Unfortunately it was not possible to distinguish one CME from the other in the images from COR2A using both $Q = 4$ and $Q = 16$. On COR2B both CMEs were selected using $Q = 16$ but only the desired CME was selected using $Q = 4$. It is surprising that the same set of parameters ($Q = 4$) did not produce the same results when comparing COR2A and COR2B. One hypothesis is that the difference of brightness (and texture) between the two CMEs is much higher on COR2B when compared to COR2A. We also ran CORSET using $Q = 0$ but the result was a region with progressively decreasing area without any consistency with the CME definition. As we need to keep consistency between the structures selected in both COR2A and COR2B to perform a reliable triangulation, we adopted the result with $Q = 16$. Notice that in this scenario, although a significant part of the area selected is not part of the desired CME and the width of the area selected is not consistent, the front part of the desired CME is not affected by the adjacent CME. The results of the CME tracking is shown in Figure 6.86, Figure 6.87 and Figure 6.88.

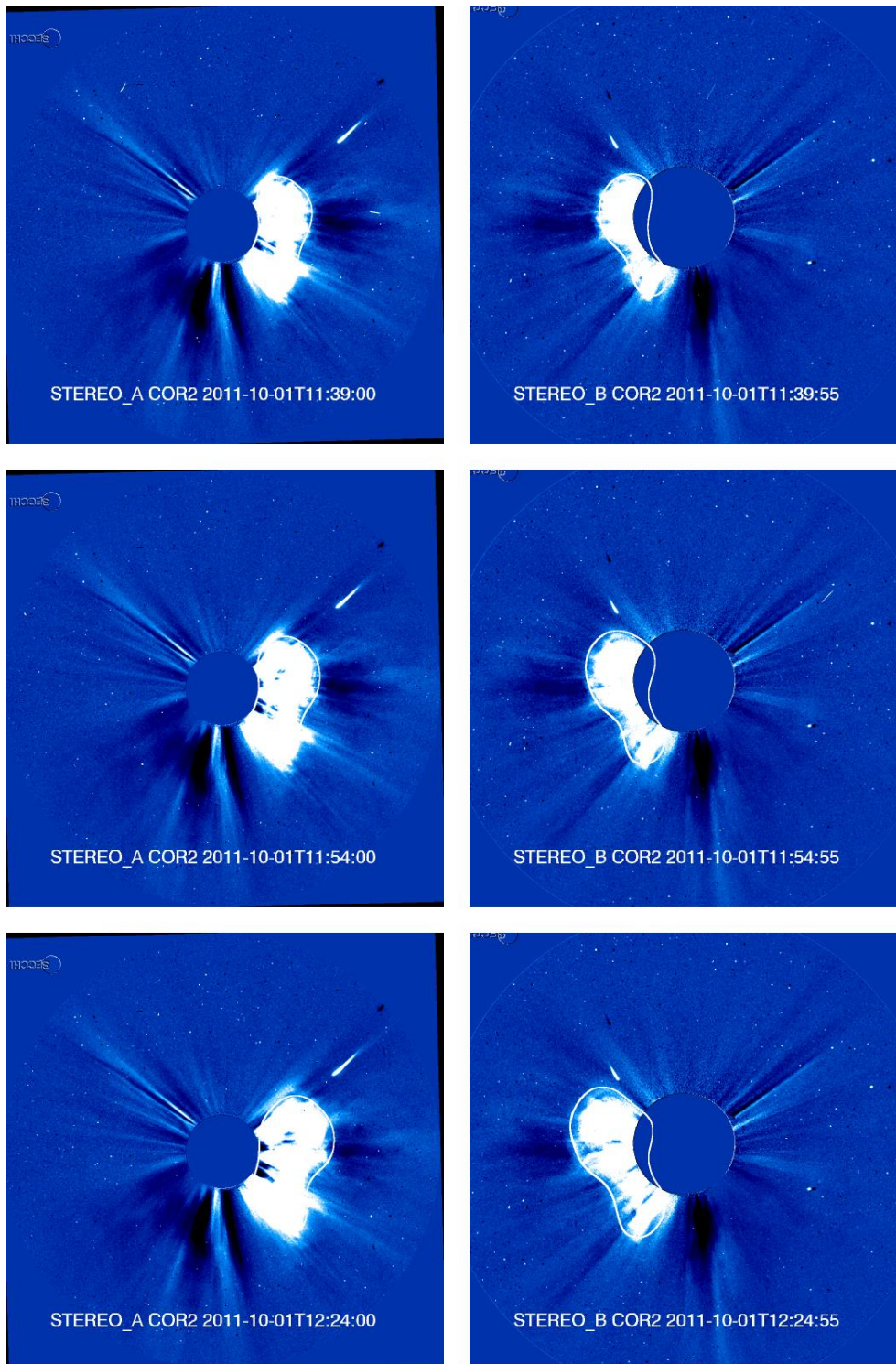


Figure 6.86 - The CME observed on 2011/10/01 in COR2A (left column) and COR2B (right column) FOVs. Only the first three frames are shown here. Notice that the images are rotated to the stereo baseline and that the north of the image is approximately pointing toward the bottom of the image. Notice the presence of the another CME (located slightly northward) included in the boundary found by CORSET.

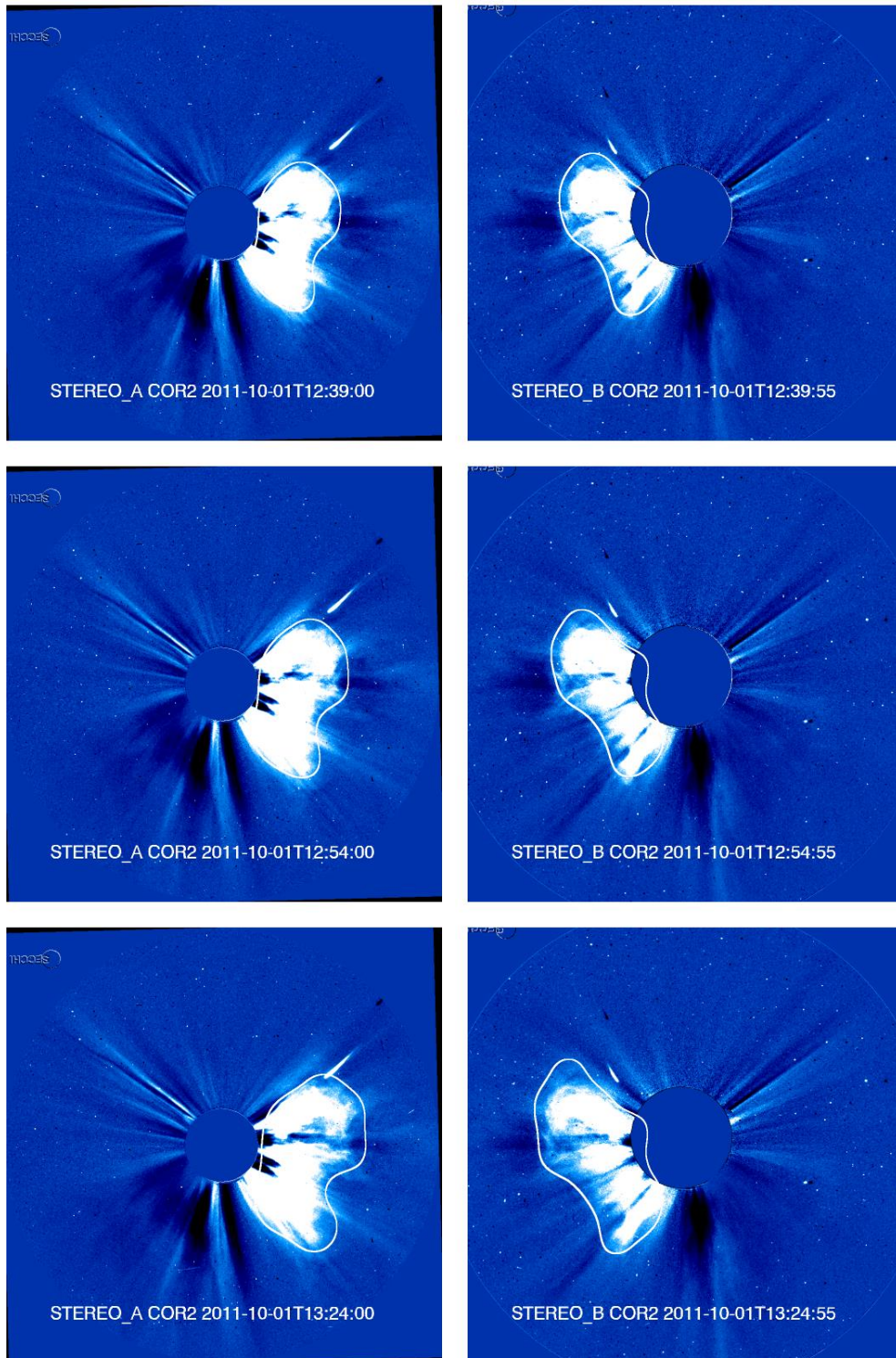


Figure 6.87 - The CME observed on 2011/10/01 in COR2A (left column) and COR2B (right column) FOVs. Only the fourth, fifth and sixth frames are shown here. Notice that the images are rotated to the stereo baseline and that the north of the image is approximately pointing toward the bottom of the image.

There is another CME located slightly northward of the CME we are interested, but it is hard to distinguish them in the frames shown here.

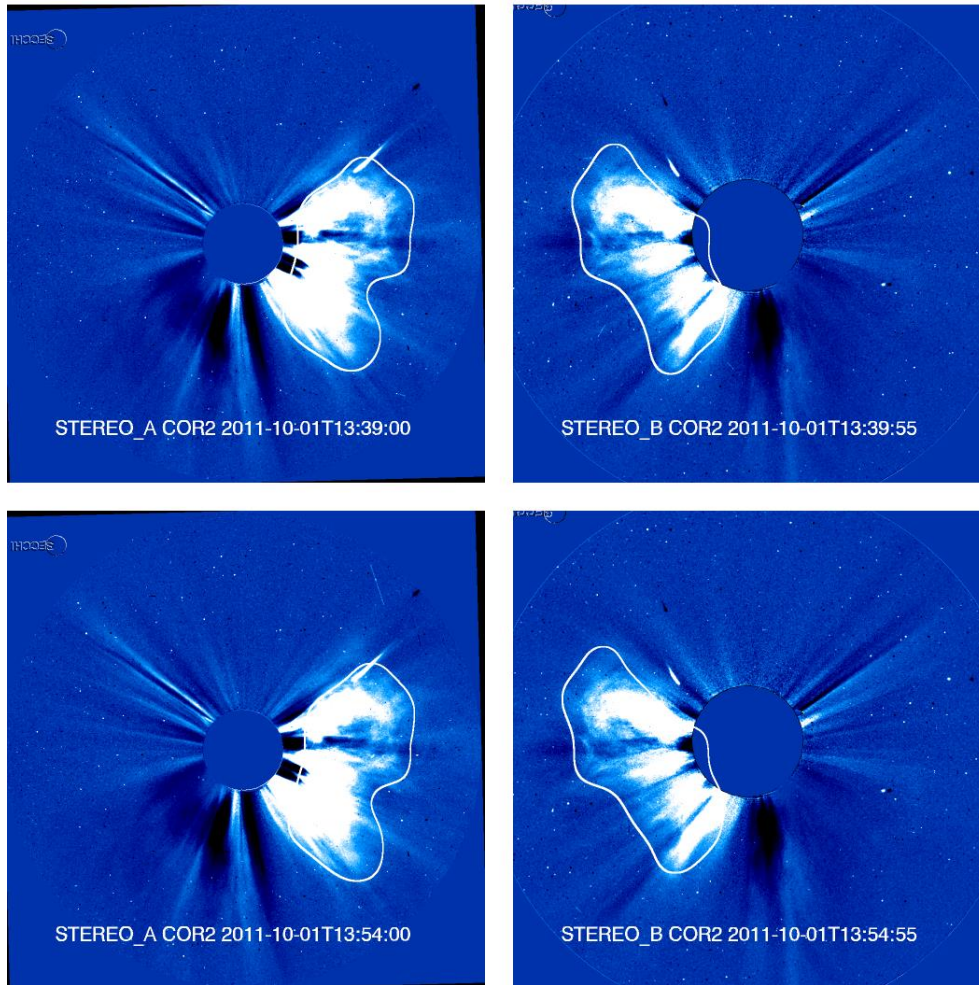


Figure 6.88 - The CME observed on 2011/10/01 in COR2A (left column) and COR2B (right column) FOVs. Only the seventh and eighth frames are shown here. Notice that the images are rotated to the stereo baseline and that the north of the image is approximately pointing toward the bottom of the image. There is another CME located slightly northward of the CME we are interested, but it is hard to distinguish them in the frames shown here.

At the end of 2011/10/01, there is another CME seen as halo for both COR2A and COR2B and as semihalo on LASCO-C3 FOV. This CMEs is also not earth-directed, it is directed toward STEREO B or STEREO A. This CME is certainly not responsible for any ICME observed close to the Earth by ACE and/or WIND.

On 2011/10/02, there is an earthward CME visible in both COR2 coronagraphs from 01:54 UT to 05:24 UT. The base image for this event is contaminated by the previous halo CME observed less than 3 hours before. By the time this CME is ejected, the halo CME is not very bright but still

present close to the outermost part of the coronagraph. By using the default parameter $Q = 4$ this CME was tracked with reasonable result (Figure 6.89 and Figure 6.90).

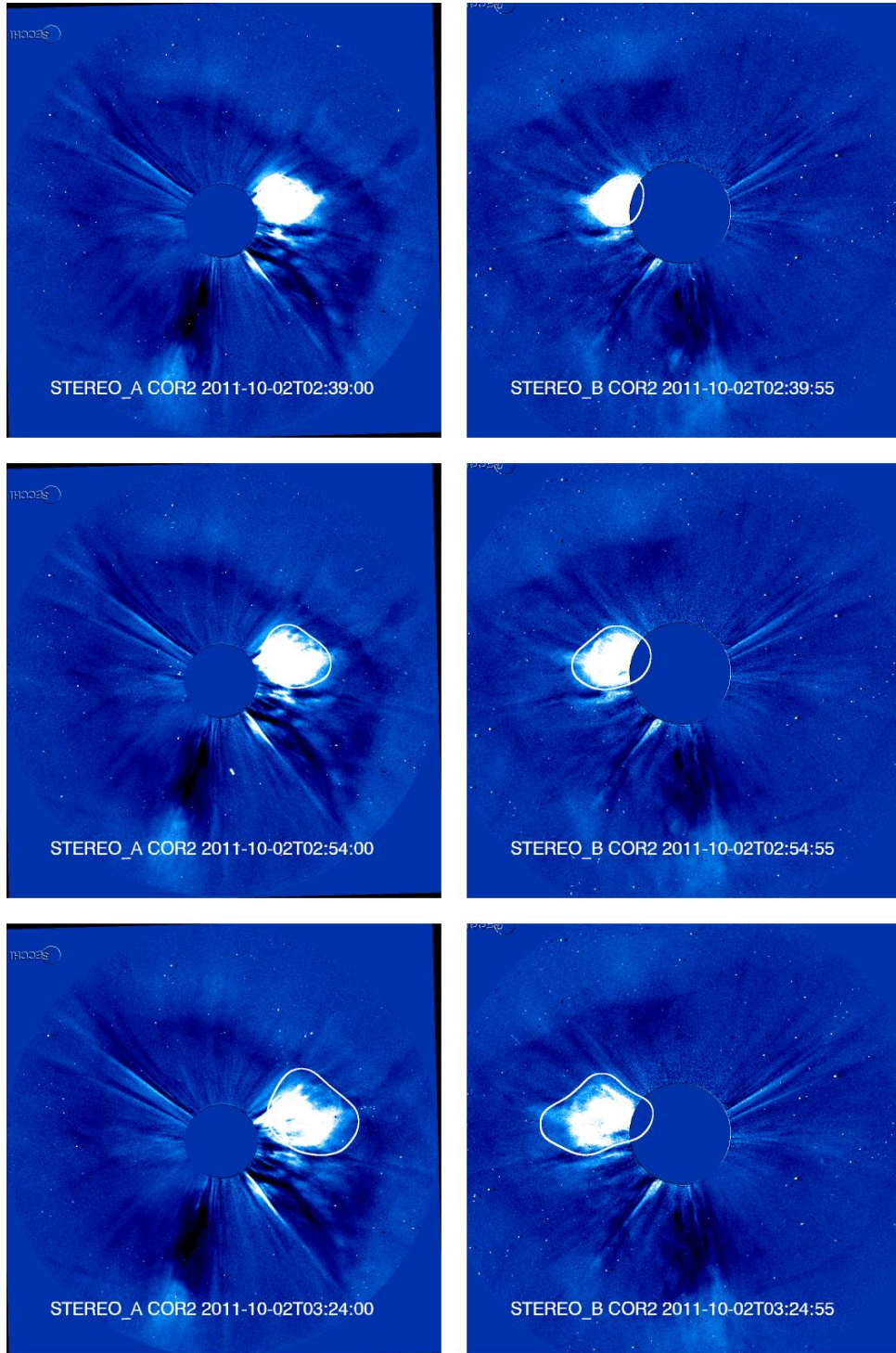


Figure 6.89 - The CME observed on 2011/10/02 in COR2A (left column) and COR2B (right column) FOVs. Only the first three frames are shown here. Notice that the images are rotated to the stereo baseline and that the north of the image is approximately pointing toward the bottom of the image.

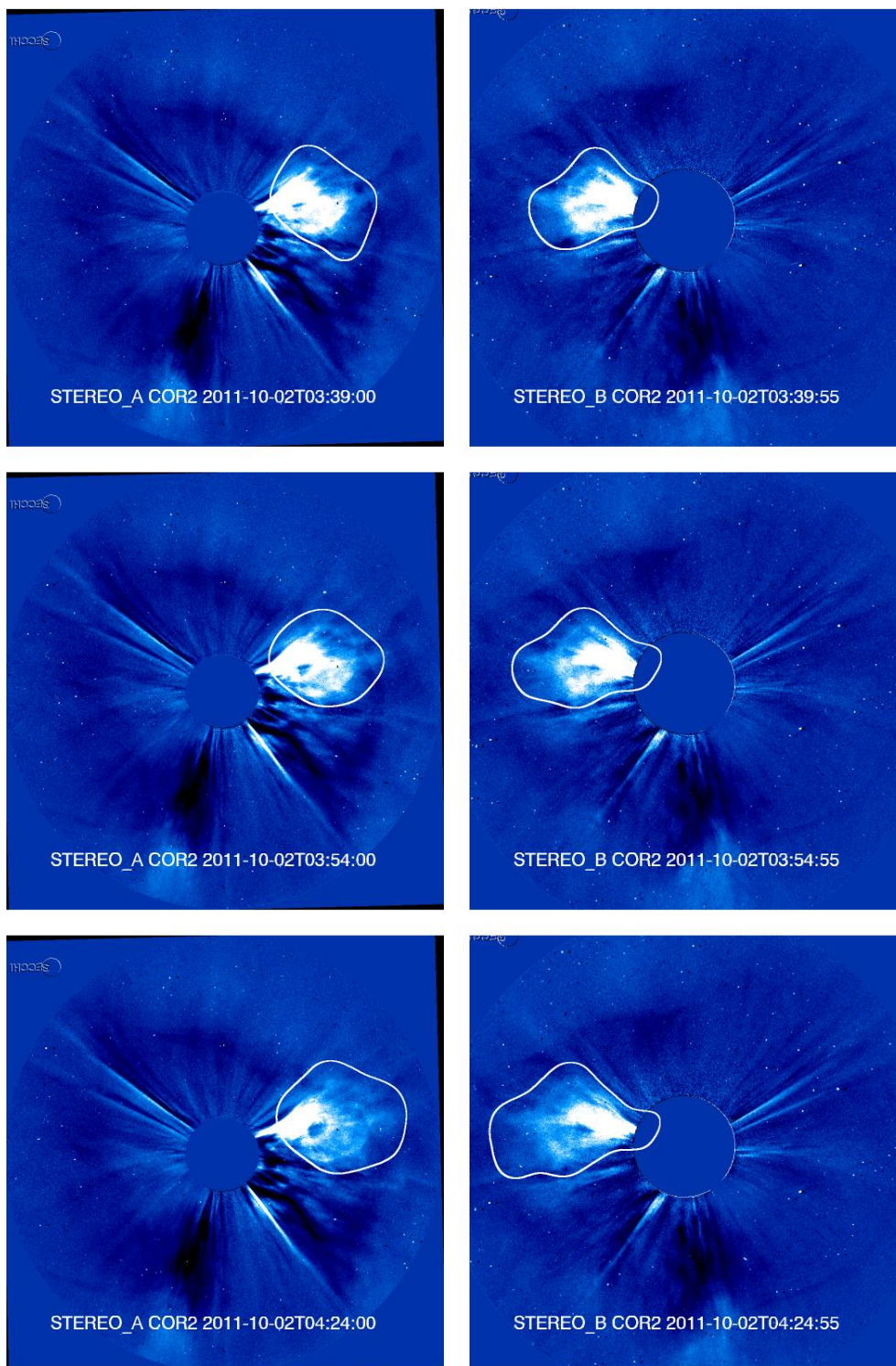


Figure 6.90 - The CME observed on 2011/10/02 in COR2A (left column) and COR2B (right column) FOVs. Only the last three frames are shown here. Notice that the images are rotated to the stereo baseline and that the north of the image is approximately pointing toward the bottom of the image.

On 2011/10/03 at about 3:00 UT, there is a CME on COR2A FOV extending from north to east and on COR2B from north to west. Although this CME is not ejected in the direction away from the Earth, this CME is seen as a narrow limb on LASCO-C3 FOV and therefore it is hard to suppose it will hit the Earth.

The following day, there is one full halo CME observed by LASCO/C3. This event is very bright and easy to identify. Although there is some data gaps in COR2A and COR2B, the CME was observed simultaneously at a single frame on both STEREO coronagraphs and, thanks to this, we concluded that it is directed away from the Earth.

On the period from 2011/10/05 to 2011/10/06, there is no CME possibly directed toward the earth since none of the CMEs is seen as a semi-halo in the LASCO-C3 FOV.

To wrap up, among all the CMEs ejected in this period, we can affirm that there are only two Earthward directed, as specified in Table 6.22. The map of the distribution of the radial speed is shown in Figure 6.91 and Figure 6.92.

Table 6.22 - The Earthward CMEs observed in association to the MC event on 2011/10/06.

First appearance on LASCO-C2 FOV	Relative time	First frame tracked on COR2AB FOV	Last frame tracked on COR2AB FOV	Average speed on COR2AB FOV
2011/10/01 09:36	0 h	10:54	13:54	491 km/s
2011/10/02 03:00	16 h	02:39	03:39	782 km/s

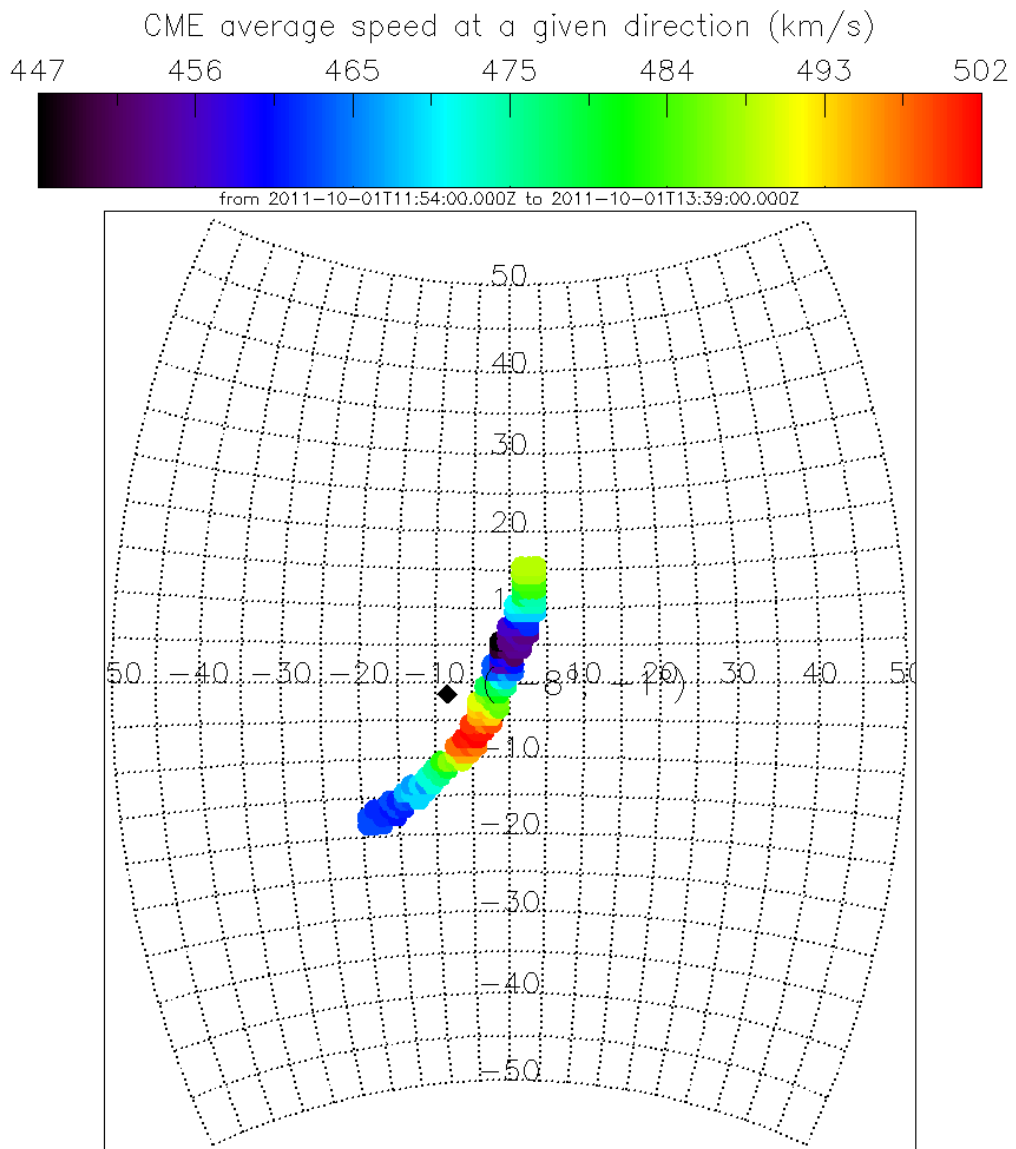


Figure 6.91 - The radial speed of the CME front observed on 2011/10/01 as a function of latitude and longitude (in HEEQ coordinate system). The black diamond indicates the center of the CME front.

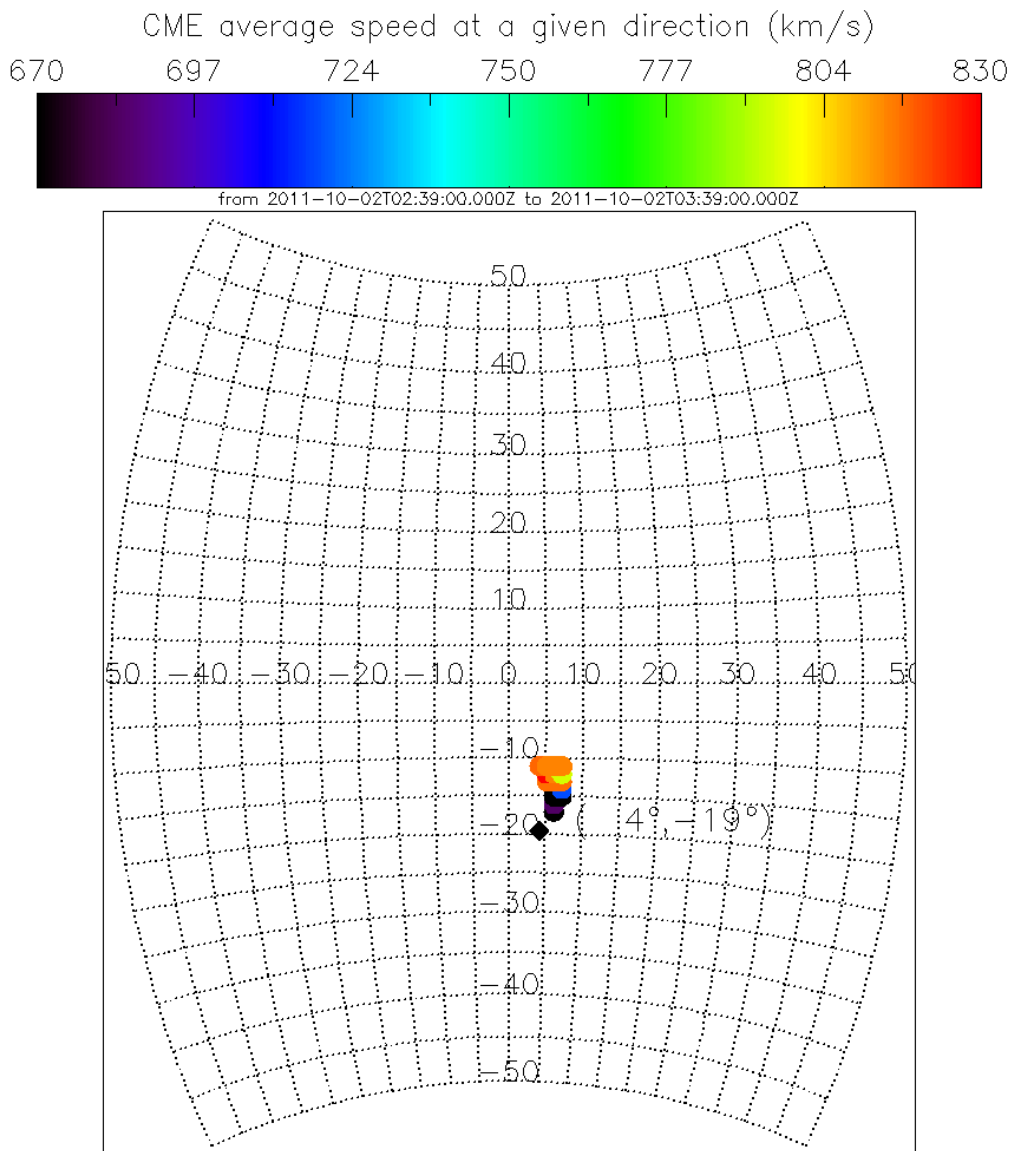


Figure 6.92 - The radial speed of the CME front observed on 2011/10/02 as a function of latitude and longitude (in HEEQ coordinate system). The black diamond indicates the center of the CME front.

The speed of propagation of the two Earthward directed CMEs was estimated using CORSET3D and is given in Table 6.23. The second CME, ejected approximately 16 hours later than the first, had a much higher speed than the first. Since the propagation direction of both is similar, they probably interacted. The time passed since the first CME ejections until the shock arrival at Earth is 93 hours. Considering the path from the Sun to the Earth, the first CME had an average speed of 448 km/s and the second 541 km/s. It means that on average, both CMEs were decelerated.

Table 6.23 - Kinematic parameters of the CMEs on 2011/10/01 and 2011/10/02. The angles shown here are given in HEEQ coordinate system.

Parameter	Result for CME1	Result for CME2
Minimum and maximum latitudes	[-19°, 16°]	[-29°, -11°]
Minimum and maximum longitudes	[-21°, 4°]	[-2°, 11°]
Group speed v_g averaged over time	474±15 km/s	765±68 km/s
Central direction of the CME averaged over time (longitude)	-8°	4°
Central direction of the CME averaged over time (latitude)	-2°	-20°
Minimum value of $\bar{v}_r(\theta_j, \phi_k)$	447 km/s	670 km/s
Maximum value of $\bar{v}_r(\theta_j, \phi_k)$	502 km/s	830 km/s
Group speed as a function of time $v_g(t_{i+1})$	[410, 476, 459, 478, 609] km/s	[862, 612, 846] km/s
Maximum error of the triangulation	0.2 solar radii	< 0.1 solar radii

6.11.3 The cosmic ray observations

Both cosmic ray muon and neutron monitor data show a count rate decrease on 2011/10/05 in close timing to the beginning of the first ICME and the interplanetary shock. While the muon detectors have a decrease ranging from 1% to 2%, the neutrons monitor have a decrease of more than 2% (Figure 6.93 and Figure 6.94).

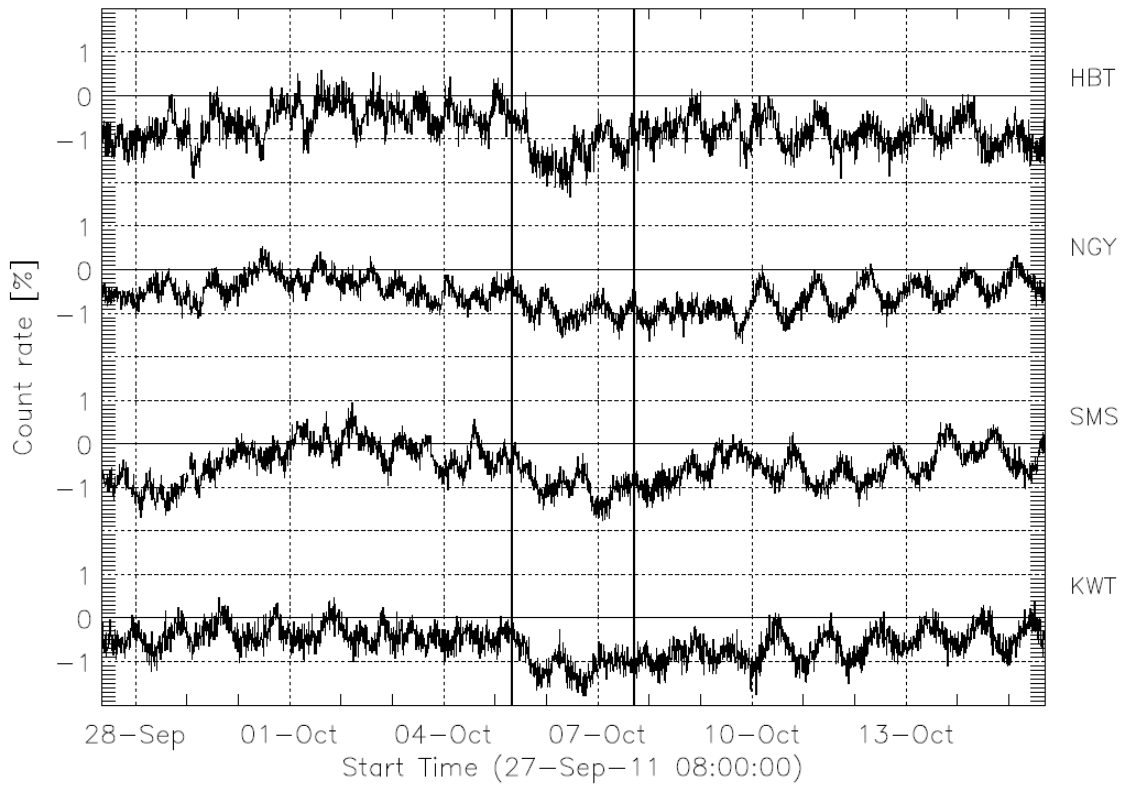


Figure 6.93 -The cosmic ray decrease observed by the vertical directional channels of the four muon detectors of the GMND during the MC on 2011/10/06.

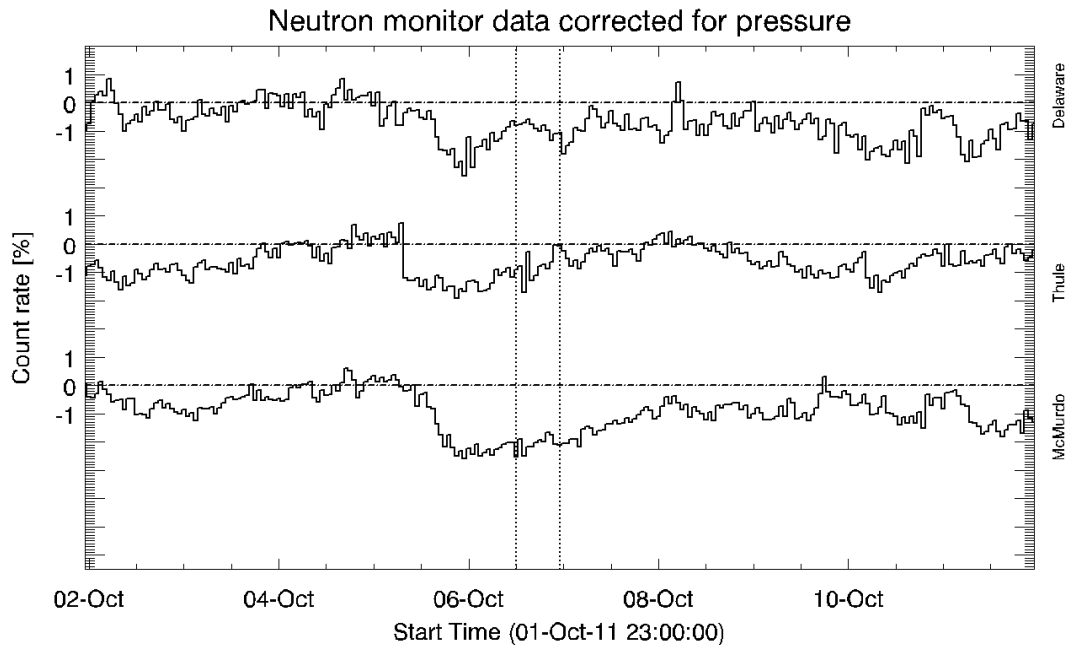


Figure 6.94 - The cosmic ray decrease observed by three different neutron monitors (Delaware, Thule and McMurdo) during the MC on 2011/10/06.

The isotropic cosmic ray intensity and the fractional gradient are shown in Figure 6.95. There is some significant intensity decrease in close timing to the beginning of the first ICME but it does not happen during the magnetic cloud period (second half of 2011/10/06). Therefore, it is not possible to use the cosmic ray cylinder model in this example. The CRC model can neither be applied to the ICME because the decrease on the cosmic ray intensity is not followed by an increase back to a similar level observed before the ICME beginning. Since the CRC model was developed for the scenario of a single MC arriving to the Earth, changes in the model are probably necessary if someone intends to use it when two or more interplanetary structures are arriving to the Earth in close timing to each other.

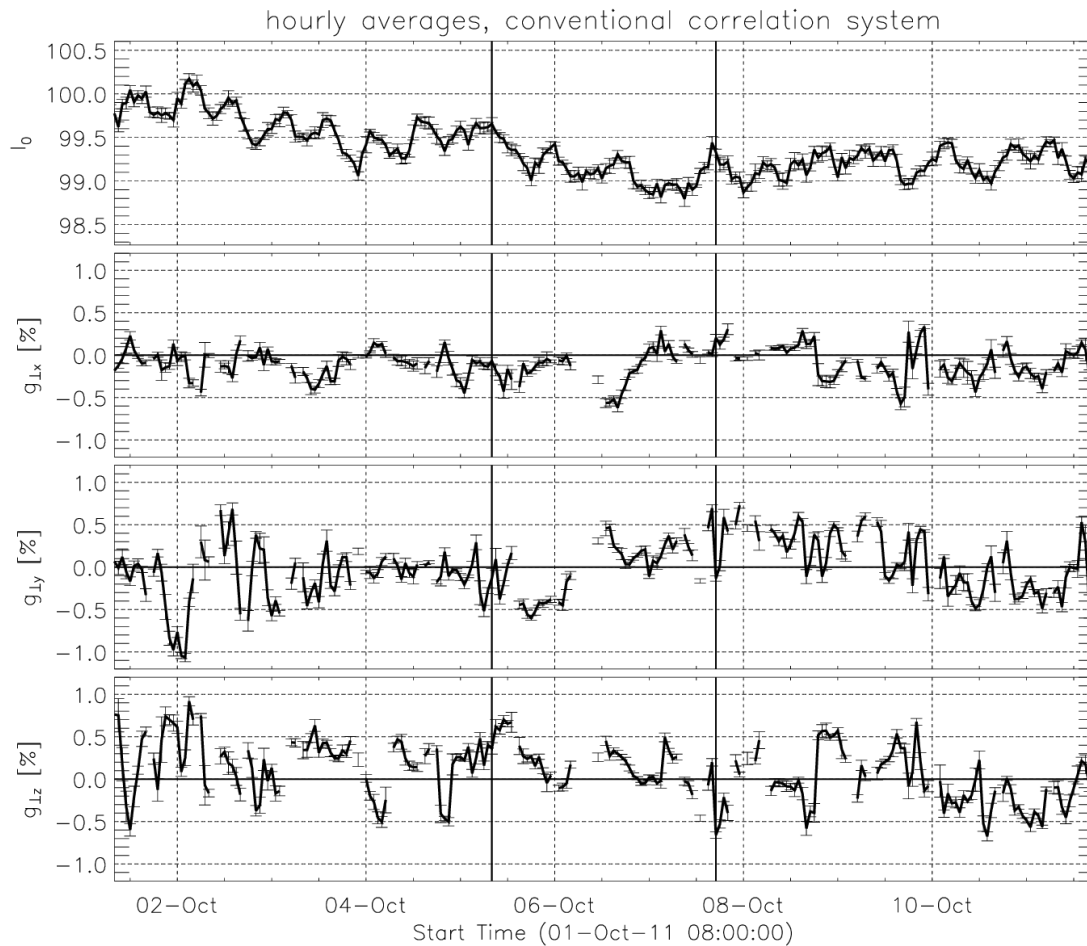


Figure 6.95 - The cosmic ray isotropic intensity and orthogonal components of the gradient during the period of the MC and two other interplanetary structures. The vertical lines indicate the period since the beginning of the first structure until the end of the last one.

6.12 The magnetic cloud observed on 2011/10/24

6.12.1 The interplanetary medium

During the MC period, the IMF magnitude ranges from 20 nT to 24 nT, the highest among the MC studied in this Thesis. Its orthogonal components “y” and “z” suggests a rotation of the IMF. The solar wind speed ranges from 550 km/s to 450 km/s. The temperature is always lower than 0.2 MK inside the MC period, although it is much higher in the period right before the MC. The beta parameter is close to 0.1 and is never higher than 0.2 (Figure 6.96).

There is an interplanetary shock observed in front of the MC on 2011/10/24 between 16:00 UT and 18:00 UT. Right after that, the IMF, density, temperature and flow speed increases significantly. This period is a sheath region. Up to at least 4 days before and after the MC, there is no indication of sector polarity changing and the IMF direction is toward the Sun.

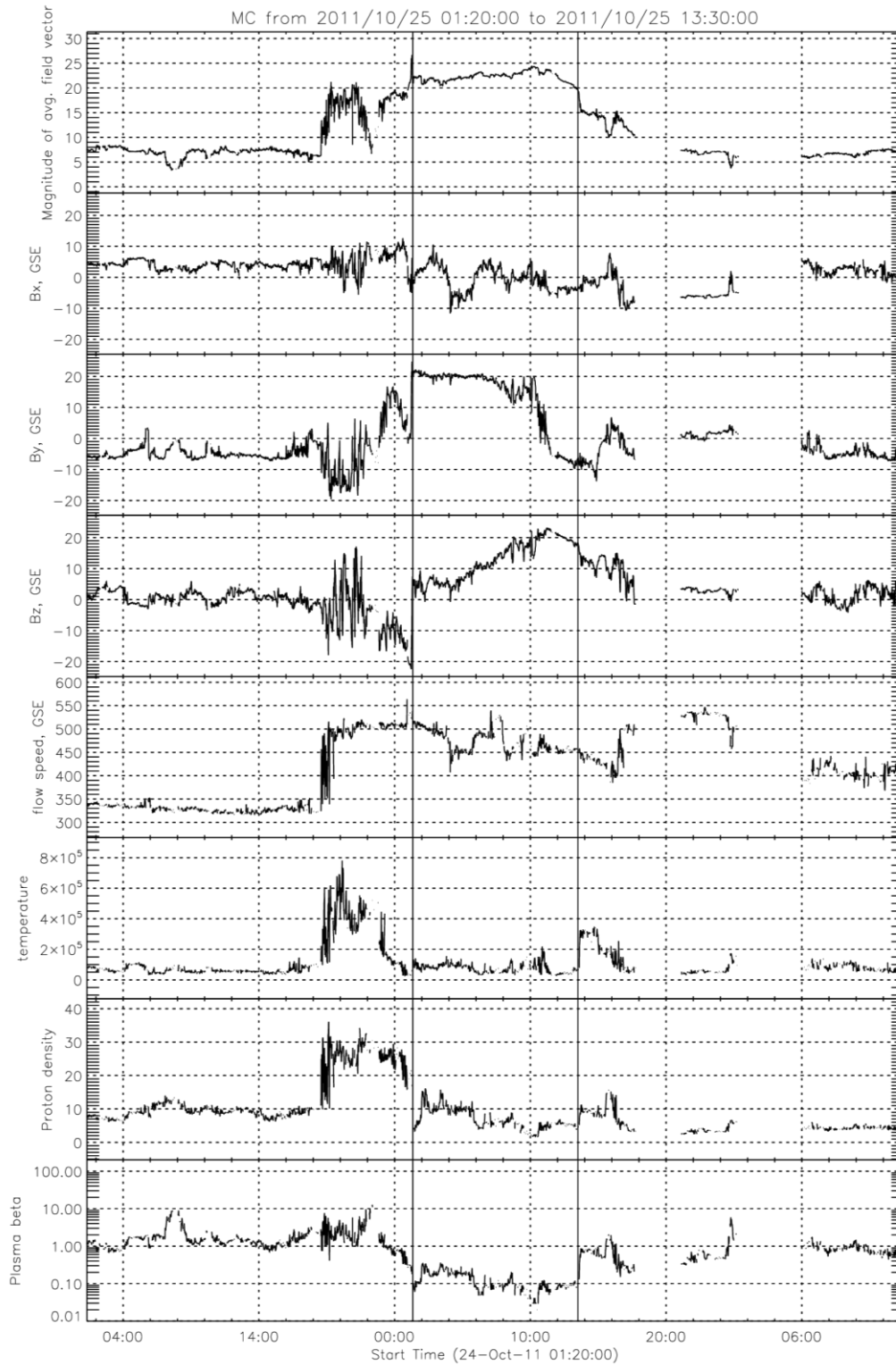


Figure 6.96 - The interplanetary magnetic field and plasma parameters during a MC on 2011/10/25.

6.12.2 The origins in the solar corona

On 2011/10/19 and 2011/10/20, two CMEs were observed on LASCO-C3 FOV but neither of them are halo nor partial halo. On 2011/10/22, there are two halo CMEs seen on LASCO-C3 FOV. The first one was observed on the first hours of the day and, according to COR2, it must be directed toward the Earth. The second CME is seen as a semi-halo by LASCO-C3 and as a halo on STEREO. Therefore, it is directed toward STEREO and at least 90° distant from the Earth. There is also a small and tenuous CME basically at the same time than the Earthward halo CME. On 2011/10/23, there is no halo CME in the LASCO FOV that could be directed toward the Earth.

Therefore, on the period from 2011/10/19 to 2011/10/23, there is only one earthward CME and it must be the coronal origin of the MC observed on 2011/10/25. An article published independently from this Thesis also found the same conclusion (MÖSTL et al., 2014). Other authors referred in previous section in this Chapter, such as Liu et al. (2012), Lugaz et al. (2012) and Colaninno (2012), did not study this CME.

The results of the application to CORSET to this CME are show in Figure 6.97 and Figure 6.98. The presence of other two CMEs in close angular range complicated the analysis. They were ejected just a few hours before the Earthward CME. They were seen on COR2 FOV from the last hour of 2011/10/21 on. One has at least 45° of width and was ejected southward (top part of each coronagraph image). It is seen as a darker region because it reached the outside part of the COR2 FOV before the first hour of 2011/10/22, when images were used to construct a base image. The remaining CME is very narrow ($< 30^\circ$) and was ejected toward north (bottom part of each figure). Due to the background subtraction, this CME is seen in the Figure 6.97 and Figure 6.98 as a black region plus a front bright. It is quite difficult to distinguish the latter CME from the earthward CME, especially on the last frames because the front part of both are aligned and, as a consequence, it is hard to decide whether the region selected by CORSET covers the CME completely or missed its part close to the northward CME. To our understanding, the selection of the CME front is self-consistent between STEREO A and STEREO B and it is consistent on time. For the expansion factor, we used $Q = 4$ but a very similar result was derived using $Q = 10$ or $Q = 14$.

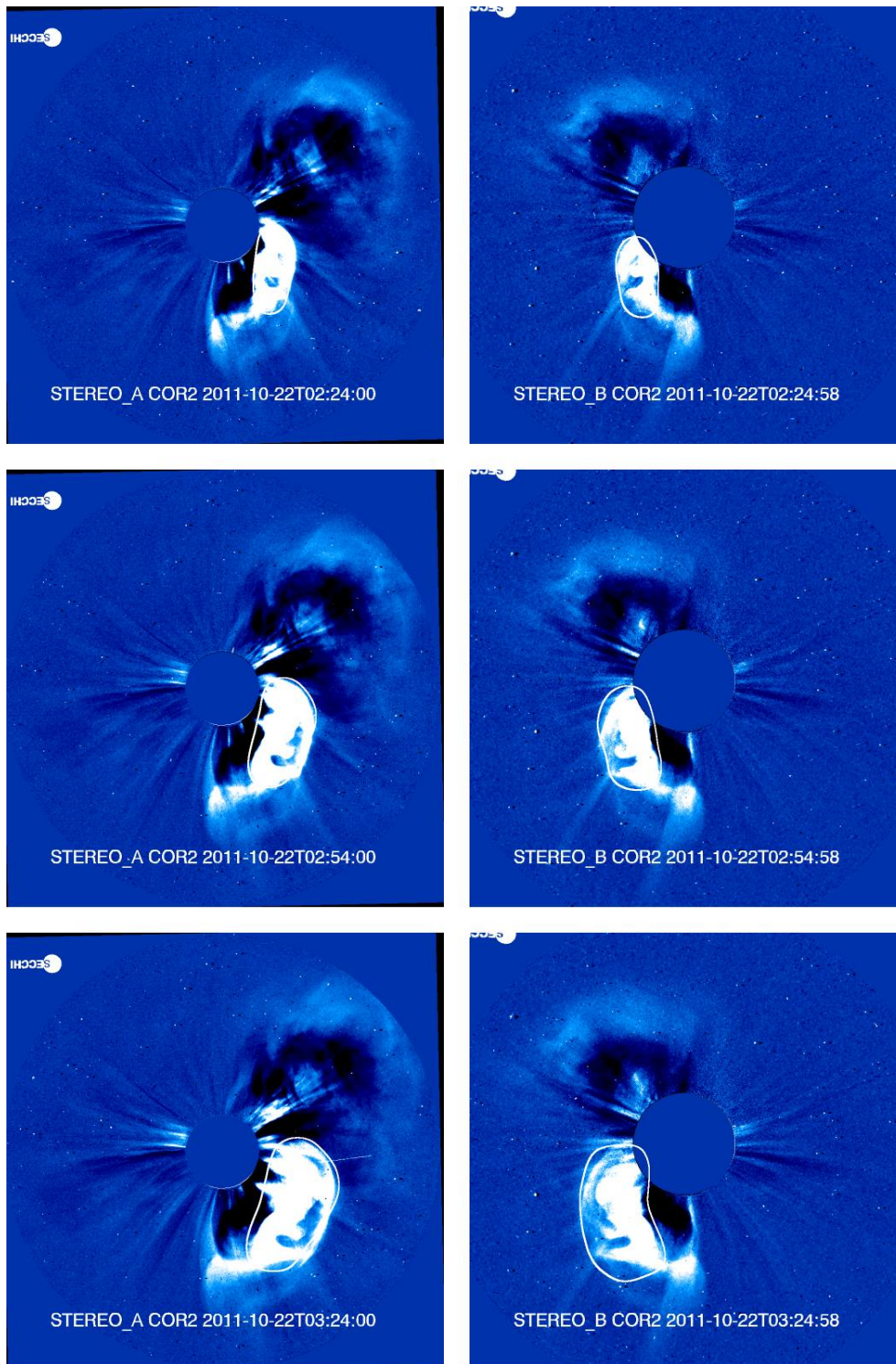


Figure 6.97 - The CME observed on 2011/10/22 in COR2A (left column) and COR2B (right column) FOVs. Only the first three frames are shown here. Notice that the images are rotated to the stereo baseline and that the north of the image is approximately pointing toward the bottom of the image.

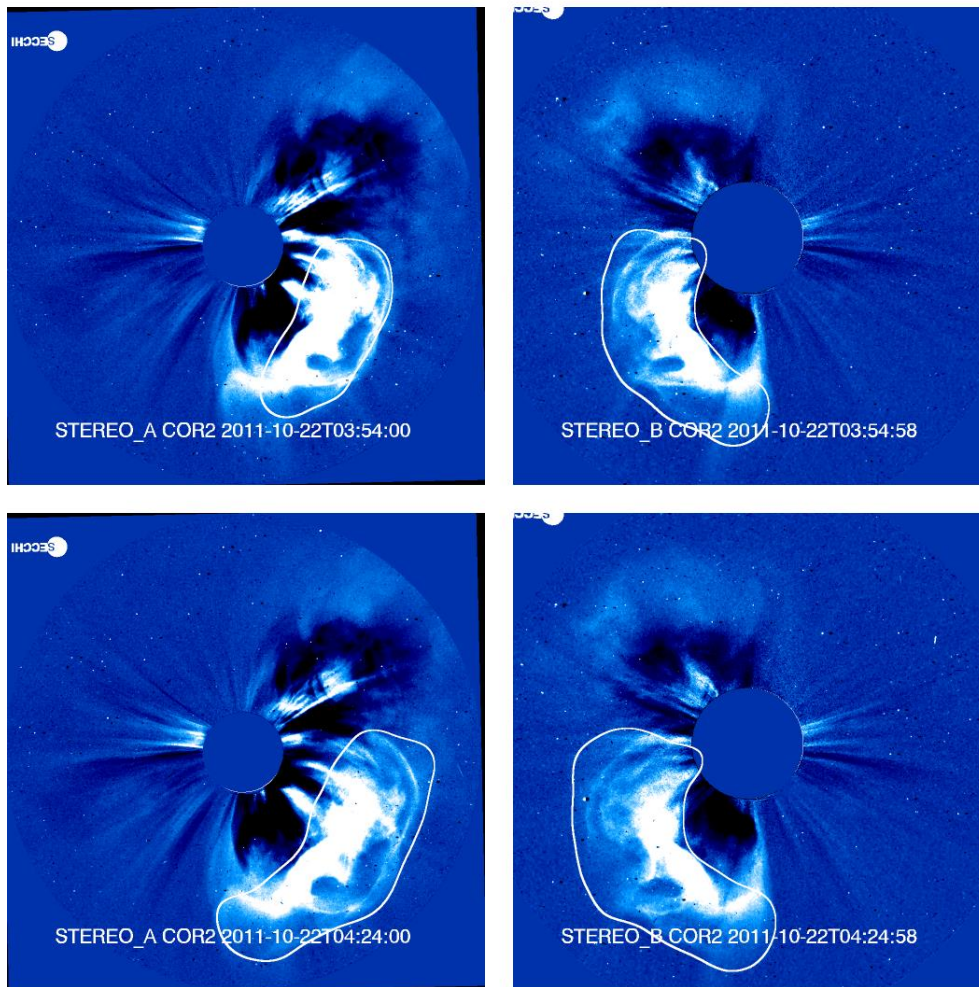


Figure 6.98 - The CME observed on 2011/10/22 in COR2A (left column) and COR2B (right column) FOVs. Only the last two frames are shown here. Notice that the images are rotated to the stereo baseline and that the north of the image is approximately pointing toward the bottom of the image.

The radial speed of the CME projected in the coronagraph FOVs is shown in Figure 6.99 and Figure 6.100. The de-projected radial speed of the CME is shown in Figure 6.101 and Table 6.24. Notice that it is located basically above the ecliptic plane and propagating basically aligned with the Sun-Earth line.

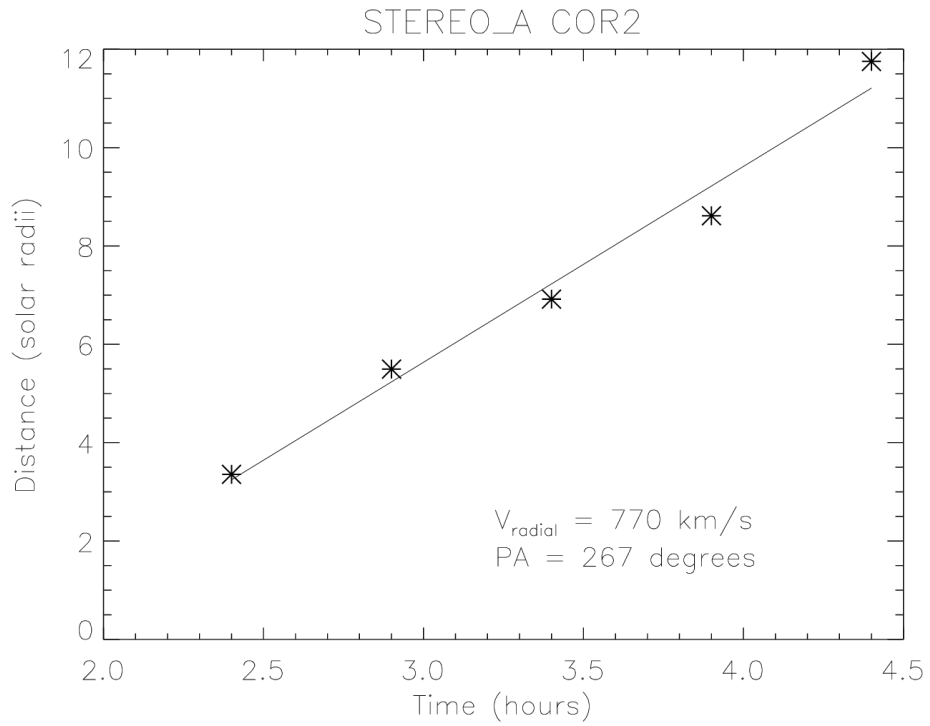


Figure 6.99 - The height-time profile of the CME on 2011/10/22 on the COR2A FOV for the fastest moving position angle. A linear fit is shown and the speed calculated in indicated. This CME was tracked by CORSET from 02:24 UT to 04:24 UT.

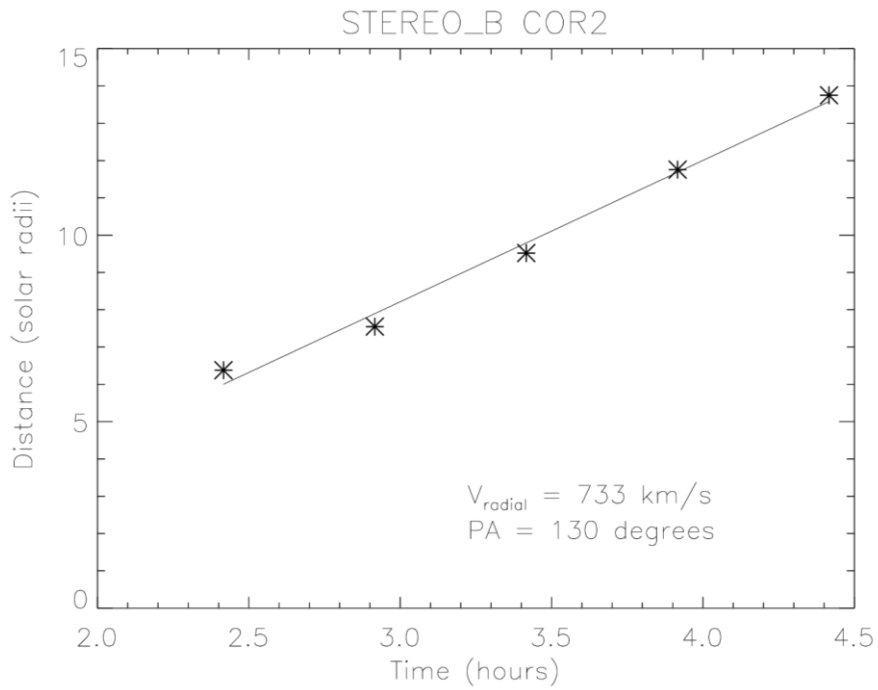


Figure 6.100 - The height-time profile of the CME on 2011/10/22 on the COR2B FOV for the fastest moving position angle. A linear fit is shown and the speed calculated in indicated. This CME was tracked by CORSET from 02:24 UT to 04:24 UT.

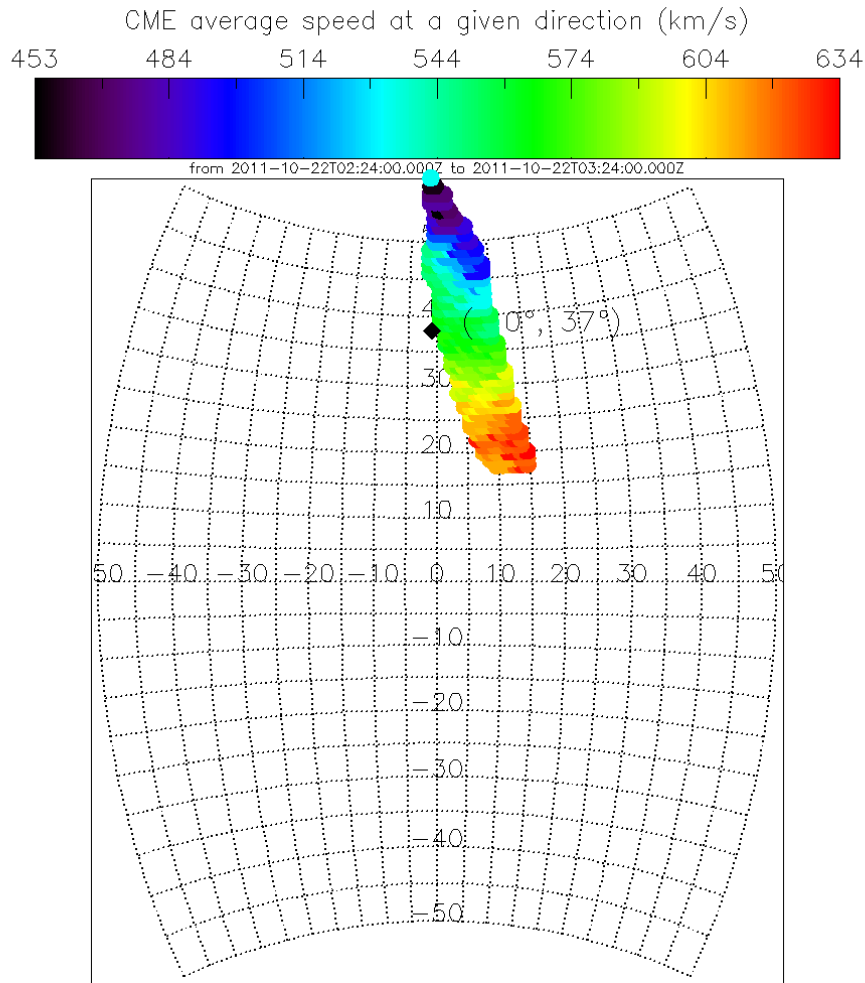


Figure 6.101 - The radial speed of the CME front as a function of latitude and longitude (in HEEQ coordinate system). The black diamond indicates the center of the CME front.

Table 6.24 - Kinematic parameters of the CME on 2011/10/22. The angles shown here are given in HEEQ coordinate system.

Parameter	Result
Minimum and maximum latitudes	[17°, 59°]
Minimum and maximum longitudes	[-18°, 16°]
Group speed v_g averaged over time	563±44 km/s
Central direction of the CME averaged over time (longitude)	-1°
Central direction of the CME averaged over time (latitude)	38°
Minimum value of $\bar{v}_r(\theta_j, \phi_k)$	453 km/s
Maximum value of $\bar{v}_r(\theta_j, \phi_k)$	634 km/s
Group speed as a function of time $v_g(t_{i+1})$	[479, 627] km/s
Maximum error of the triangulation	0.2 solar radii

6.12.3 The cosmic ray observations and modeling

The cosmic ray count rate has a decrease associated to this MC observed by all detectors of the GMDN (Figure 6.102). The decrease has an amplitude close to 2%, the biggest cosmic ray density decrease observed during MC periods from January 2008 to December 2011. The decrease starts a few hours before the shock at about 14 UT, approximately 4 hours before the beginning of the sheath region observation by OMNI. As for neutron monitors, the decrease ranges from 4% to more than 5% (Figure 6.103).

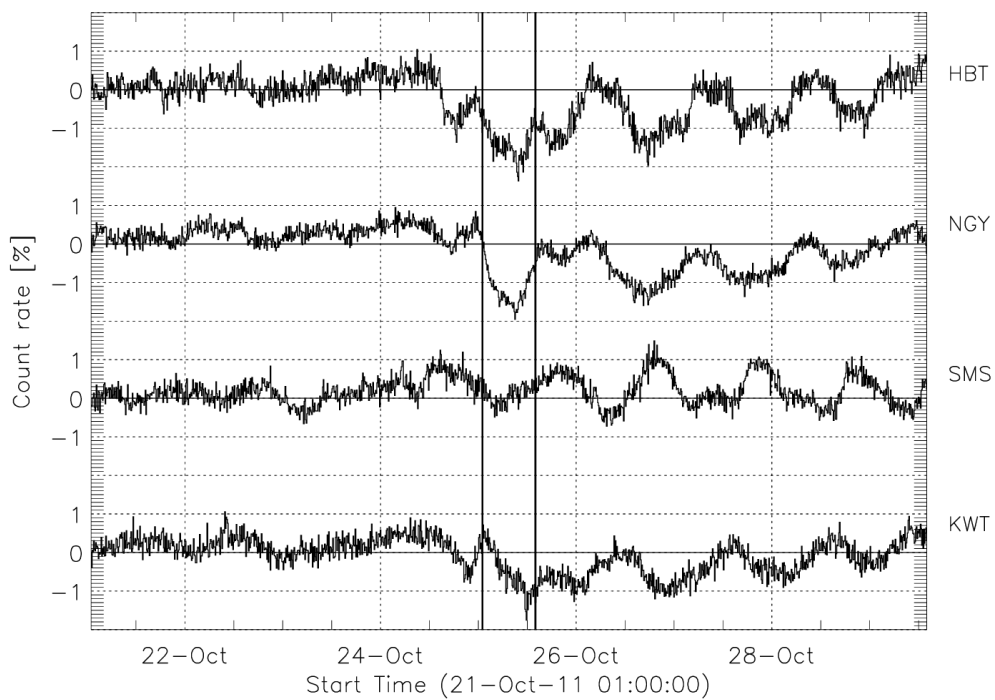


Figure 6.102 - The cosmic ray decrease observed by the vertical directional channels of the four muon detectors of the GMND during the MC on 2011/10/25.

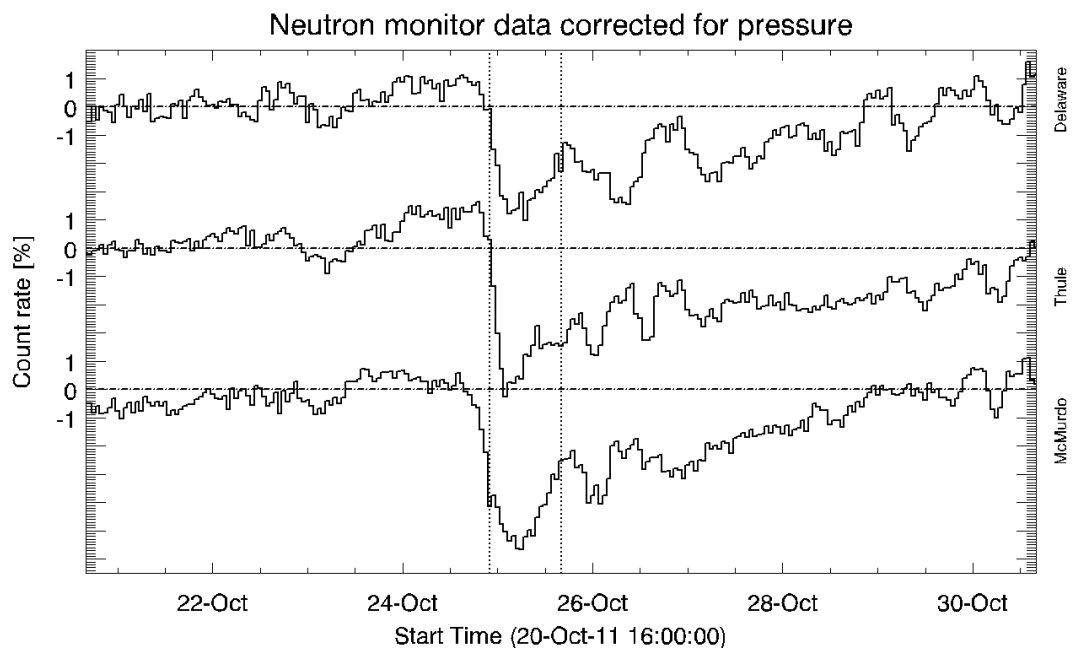


Figure 6.103 - The cosmic ray decrease observed by three different neutron monitors (Delaware, Thule and McMurdo) during the MC on 2011/10/25.

After the MC period, the four GMDN detectors show a pronounced daily variation that was not present before the MC. At the end of the month there is another modulation of the cosmic ray due to some interplanetary structure which increases the interplanetary magnetic field intensity to more than 10 nT.

There is a considerable contribution from the parallel anisotropy in this event, especially in the “y” component on the first half of the MC. This contribution may be produced by the shock reported a few hours before the MC starts. This contribution, however, is smaller than the component of the anisotropy perpendicular to the IMF.

The results from the application of the cosmic ray cylinder model are shown in Table 6.25, Figure 6.104 and Figure 6.105. The tridimensional representation of the cylinder modelled is shown in Figure 6.106. We have chosen a different period from 1 UT to 15 UT, i. e., we included two extra hours at the end of the MC period because doing so the isotropic intensity is basically at the same level at the beginning and end of the period. We used the model independently with data from the conventional and new correlation system and the residue of the data fit is smaller when using the former data (see Table 6.25).

Table 6.25 - Parameters of the cosmic ray cylinder model of the MC observed on 2011/10/25.

Parameter	Conventional correlation system	New correlation system
Start period of analysis	2011/10/25 01:00:00	
End period of analysis	2011/10/25 15:00:00	
Time with minimum cosmic ray isotropic intensity	07:20:00	08:20:00
Minimum cosmic ray isotropic intensity	-2%	-1.8%
Larmor radius (AU)	0.0091	0.0177
Latitude (degrees, GSE)	19°	28°
Longitude (degrees, GSE)	16°	20°
Impact distance (AU)	-0.02	-0.02
κ_0 (dimensionless)	55	86
Cylinder radius (AU)	0.04	0.05
Cylinder radius expansion speed (AU/hour)	0.00	0.00
Residue	0.015	0.016
Position at the beginning [GSE coordinates, AU]	[0.02, 0.00, -0.04]	[0.03, -0.01, -0.05]
Position at the end [GSE coordinates, AU]	[-0.02, 0.04, 0.01]	[-0.02, 0.04, 0.02]

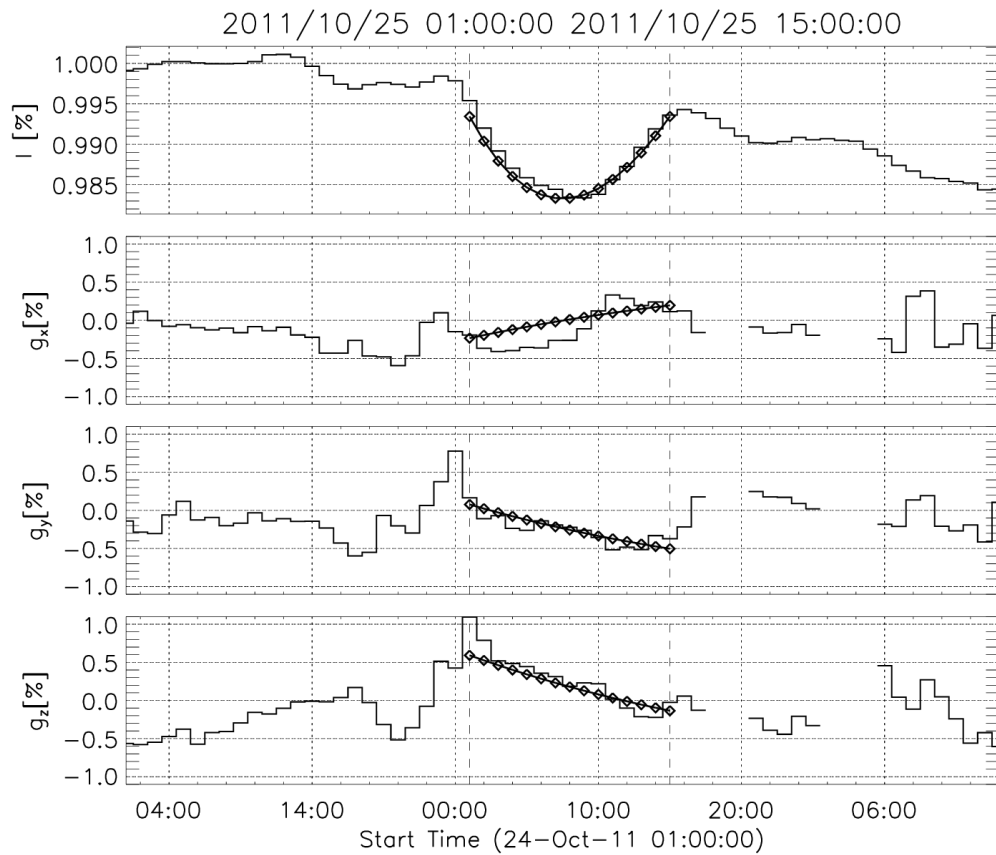


Figure 6.104 - The observation and modeling of cosmic ray depleted region associated to the magnetic cloud in 2011/10/25 using data from the conventional correlation system. The stair plot is the observed data and the line with diamonds is the modeling of the cosmic depleted region. The first panel, from top to bottom, shows the isotropic intensity. The remaining three plots show the orthogonal components of the fractional cosmic ray density gradient in the GSE coordinate system. The two vertical dashed lines correspond to the beginning and the end of the cosmic ray depleted region chosen by eye. These timings are indicated on top of the plot.

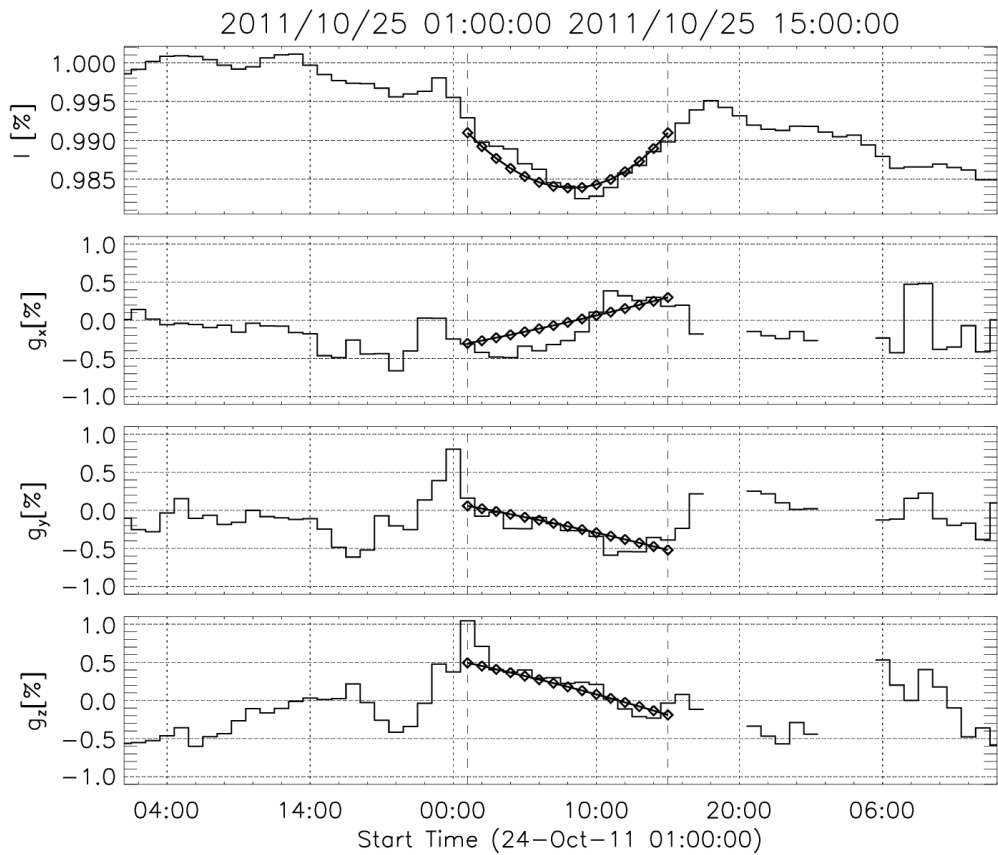


Figure 6.105 - The observation and modeling of cosmic ray depleted region associated to the magnetic cloud in 2011/10/25 using data from the new correlation system. The stair plot is the observed data and the line with diamonds is the modeling of the cosmic ray depleted region. The first panel, from top to bottom, shows the isotropic intensity. The remaining three plots show the orthogonal components of the fractional cosmic ray density gradient in the GSE coordinate system. The two vertical dashed lines correspond to the beginning and the end of the cosmic ray depleted region chosen by eye. These timings are indicated on top of the plot.

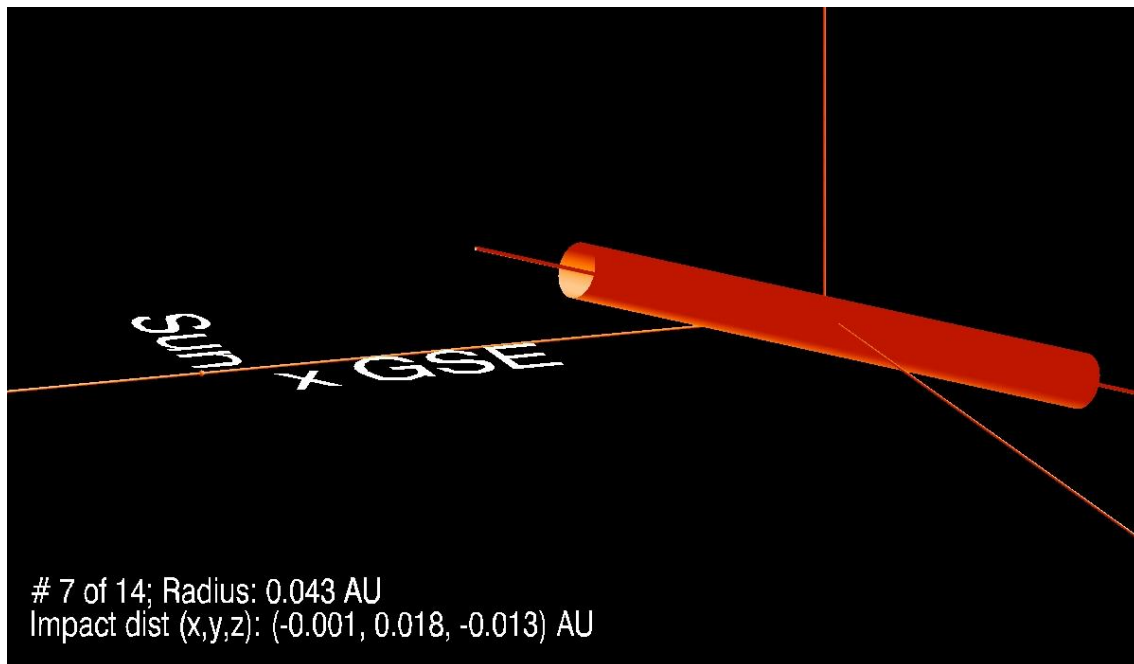


Figure 6.106 - A tridimensional scale model of the cylinder derived from CRC model on 2011/10/25 at 08:00 UT using the conventional correlation system. The actual cylinder length used in the model is infinite. The Earth is located at the origin of the GSE coordinate system (represented by the three axes).

In both cases (when we use the conventional and new correlation system), the portion of the cosmic ray cylinder close to the Earth is moving toward the negative “x” GSE direction (in other words, from the Sun to the Earth) and toward the positive “y” GSE direction (somehow following Parker spiral pattern).

The minimum variance analysis (MVA) was also performed for the same magnetic cloud period. The result was an angle of 73° of latitude and 74° of longitude for its axis using the same period. Using an offset of the period up to two hours before and after the original boundaries of the MC, 25 combinations of periods are possible and all of them have $\lambda_2/\lambda_3 > 2$ and were used to calculate the MVA statistics. The result for the latitude is a mean of 66° and a standard deviation of 9°; for the longitude, the mean is 78° and the standard deviation is 33°. Notice that the MVA is very sensitive to the boundaries of the period to be analyzed. To our understanding, the most appropriate period for the MVA analysis starts at 01 UT and ends at 13 UT because the field clearly rotates approximately 180° in the maximum variance axis. In this case, the latitude found is 62° and the longitude is 60°. If the beginning and/or the end of the magnetic cloud period used in the MVA analysis is changed to more than 2 hours, the difference in the latitude and longitude

increase dramatically. If we take into account the standard deviation, the result of the MVA does not agree with the result from the cosmic ray cylinder analysis.

In order to assess the effect of this difference in the angle when comparing the observed cosmic ray data with the expected data, we ran the cosmic ray cylinder model in a further test: we imposed the latitude and longitude found by the MVA to the cosmic ray cylinder model and we kept the remaining parameters of the model free. The period was kept the same than shown in Table 6.25. The result is shown in Figure 6.107. When comparing to the results with the angle as a free parameter, there are differences in the four time profiles but it is much more evident on the “z” component of the gradient, which changed significantly and does not agree with the actual data observed in the latter case. There is an expressive increase in the radius from 0.04 AU to 0.09 AU. The residue has increased from 0.015 AU to 0.023 AU.

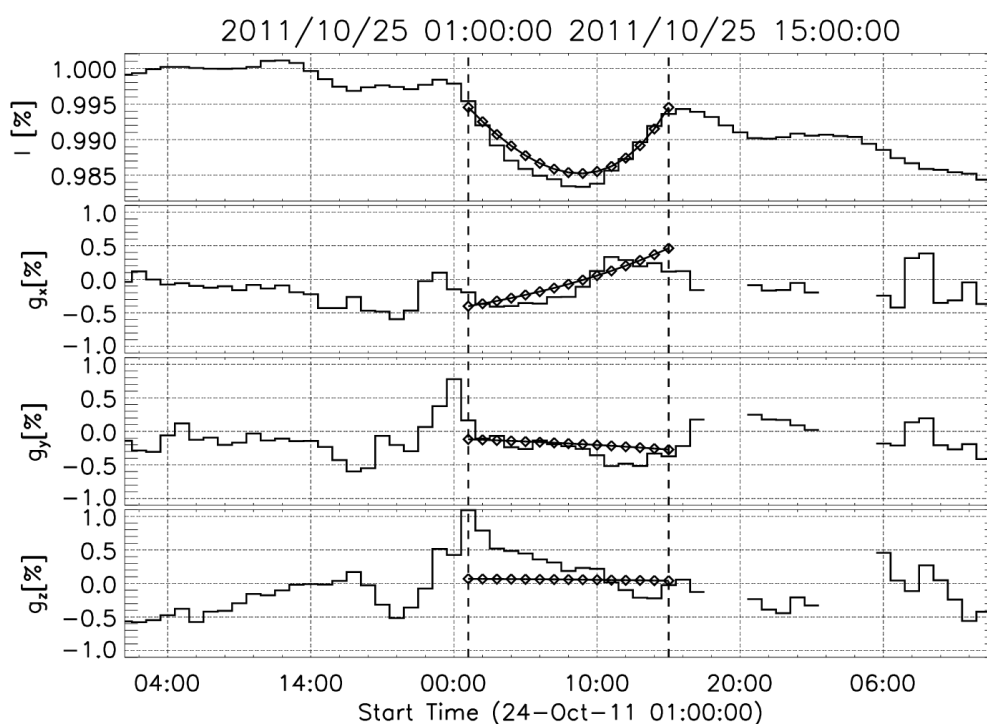


Figure 6.107 - The observation and modeling of cosmic ray depleted region associated to the magnetic cloud in 2011/10/25 using data from the conventional correlation system and imposing the latitude and longitude angles found by the MVA analysis. The stair plot is the observed data and the line with diamonds is the modeling of the cosmic ray depleted region. The first panel, from top to bottom, shows the isotropic intensity. The remaining three plots show the orthogonal components of the fractional cosmic ray density gradient in the GSE coordinate system. The two vertical dashed lines correspond to the beginning and the end of the cosmic ray depleted region chosen by eye. These timings are indicated on top of the plot.

The flux rope was expected to be located mainly northward the ecliptic plane given its original ejection direction which is more than 10 degrees in HEEQ coordinates. The cosmic ray depleted region, however, is located mainly below the ecliptic plane.

6.13 The magnetic cloud observed on 2011/11/07

The magnetic cloud reported by the ICME catalog on 2011/11/07 is shown in Figure 6.108. This is not a good example of MC due to the following reasons: 1) the IMF rotation is not smooth and not very clear; 2) the duration is about 6 hours, a quite short period for a MC; 3) the plasma beta parameter, although smaller inside the MC period than outside, is much higher than 0.1. There are no other ICMEs reported in close timing and there is a sector boundary on 2011/11/06, about one day before then MC period.

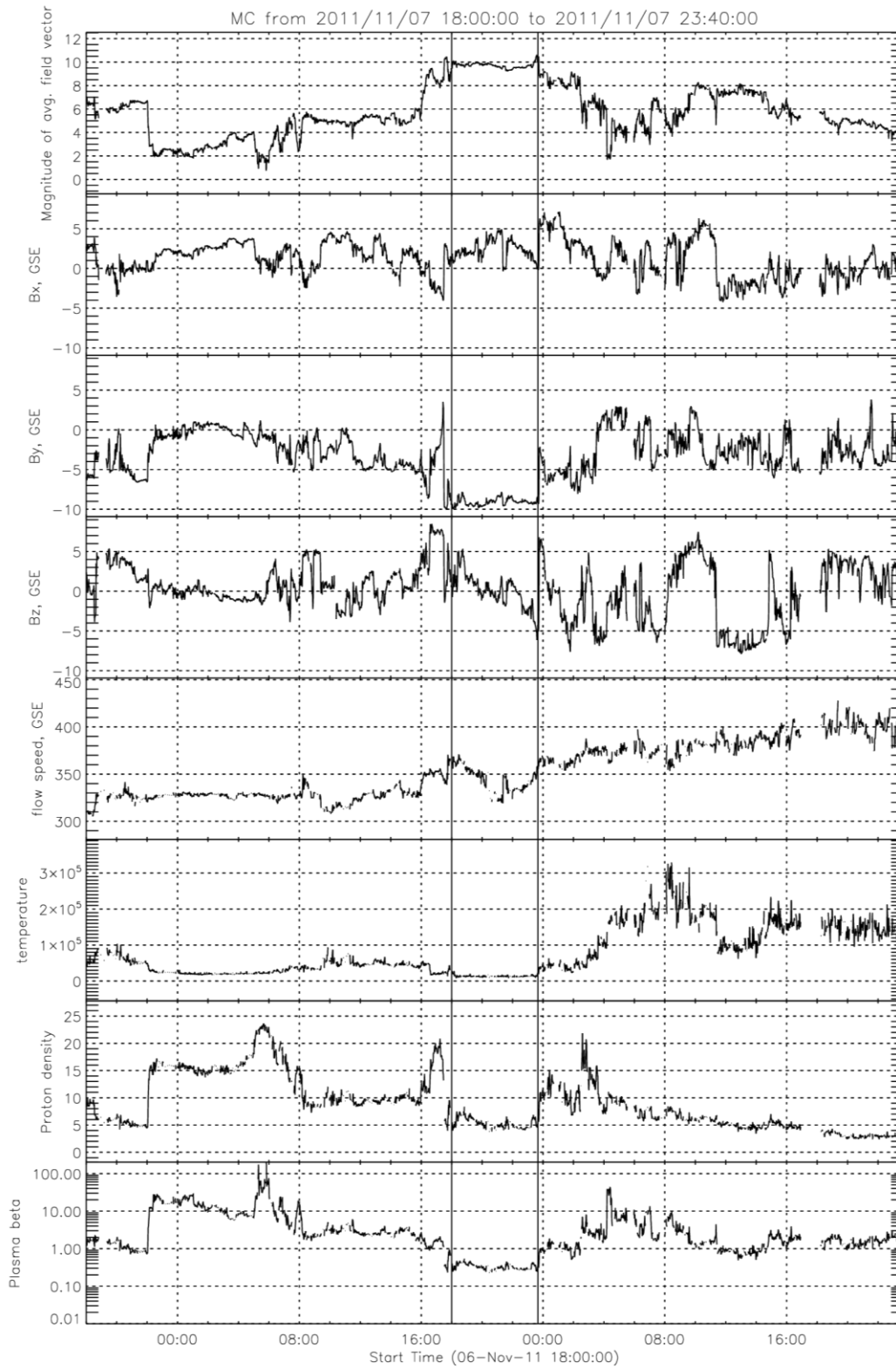


Figure 6.108 - The interplanetary magnetic field and plasma parameters during a MC at 2011/11/07.

We inspected images from solar corona in the period from 2011/11/02 to 2011/11/06 in order to find possibly earth-directed CMEs. According to the CDAW CME catalog (YASHIRO et al., 2004) and our own inspections of LASCO-C3 and COR2 data, there are two halo CMEs in this period. One was at 2011/11/03 23:30 and the other at 2011/11/04 01:25. By observing the CME position on COR2 FOV, we can dismiss that the first CME was Earthward directed. We also used the Sunloop method and confirmed that it is directed away from the Earth. The second CME, by its turn, was directed neither toward nor away from the Earth according to observations from COR2. Using Sunloop, we found that its propagation direction was toward STEREO B. During that period, STEREO B is more than 90° behind the Earth in its trajectory around the Sun. It is very unlikely (if not impossible) that a CME directed to STEREO B could be observed close to the Earth.

There is no CME directed Earthward that could be the solar source of the MC according to our observations on LASCO-C3 and COR2 FOV. One possibility is that this interplanetary structure considered a MC is actually not an ICME (neither a MC) and it is the result of sector boundary or a stream-interaction region. The IMF magnitude of 10 nT is frequently observed during sector boundaries and this possibility cannot be discarded (GOSLING, 2010).

There is no clear decrease in the vertical directional channels of the four muon detectors of the GMDN (Figure 6.109). The same can be said for the neutron monitors used here (Figure 6.110). The cosmic ray model cannot be applied here because there is no isotropic decrease observed in this period (Figure 6.111).

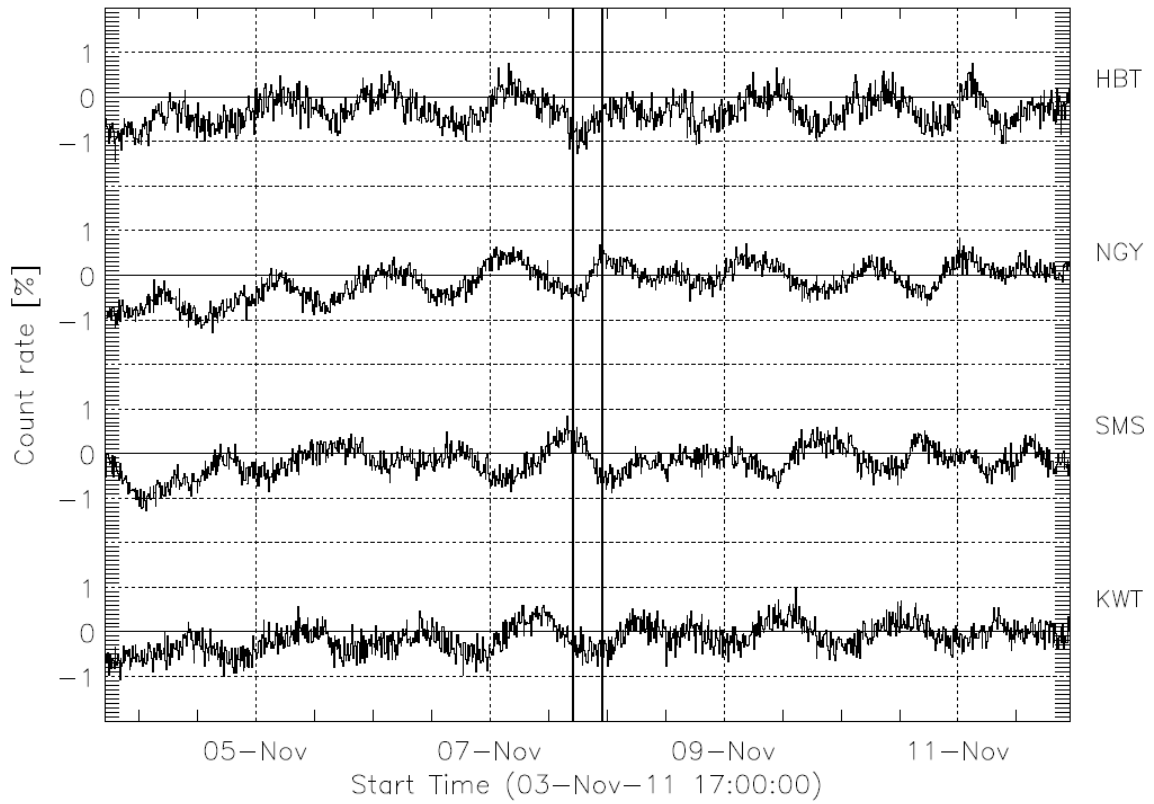


Figure 6.109 - The cosmic ray count rate observed by the vertical directional channels of the four muon detectors of the GMND during the MC at 2011/11/07. The two vertical continuous lines indicate the beginning and end of the MC.

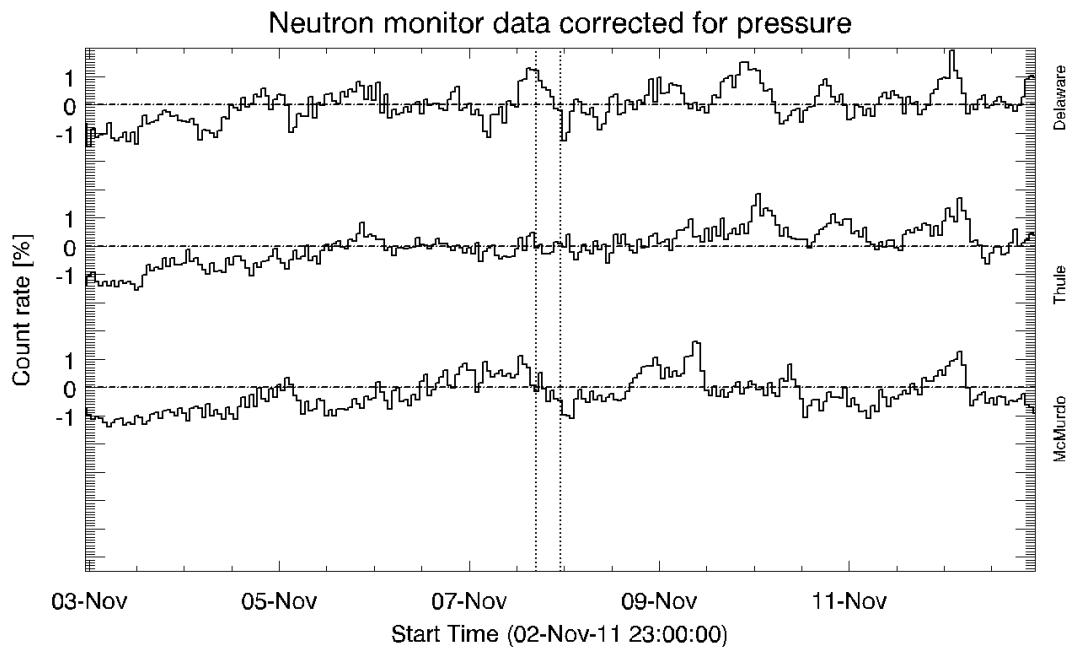


Figure 6.110 - The cosmic ray count rate observed by three different neutron monitors (Delaware, Thule and McMurdo) during the MC on 2011/11/07. The two vertical dashed lines indicate the beginning and end of the MC.

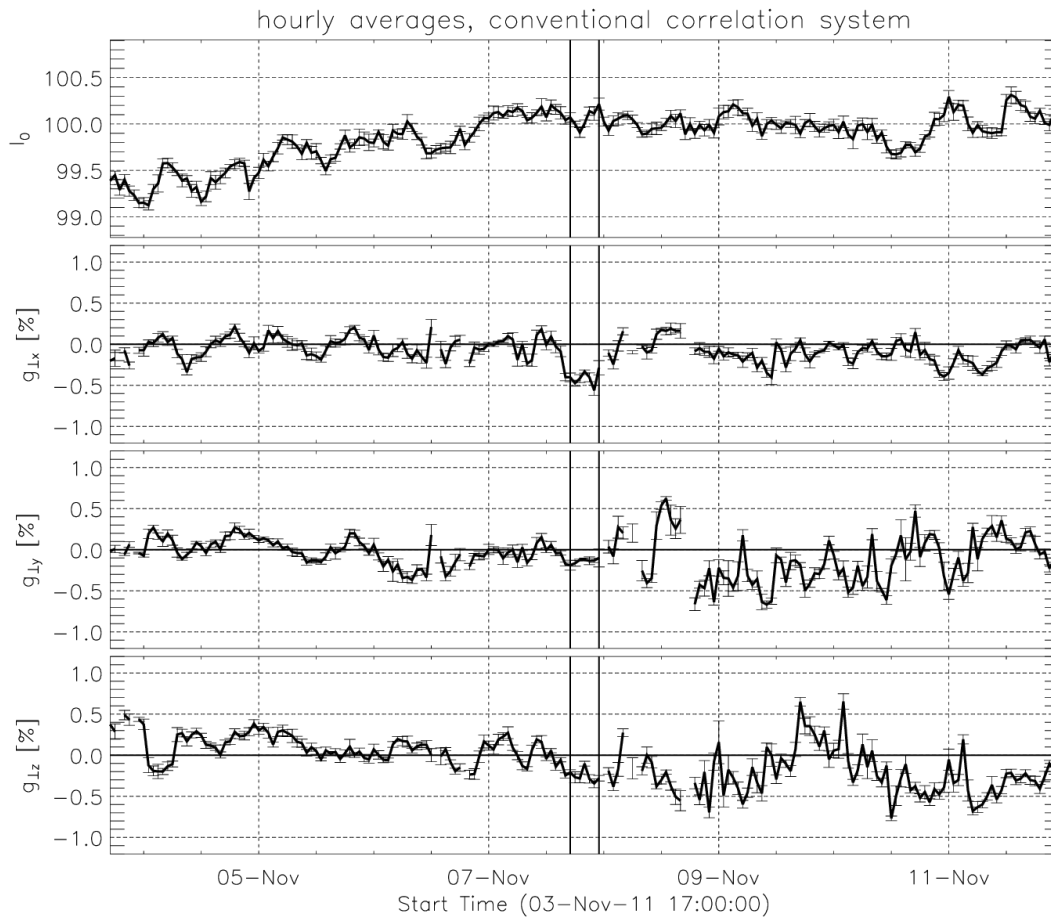


Figure 6.111 - The isotropic cosmic ray intensity and the orthogonal components of the cosmic ray fractional gradient during the MC period on 2011/11/07.

6.14 The magnetic cloud observed on 2011/11/29

6.14.1 The interplanetary medium

The magnetic cloud observed on 2011/11/29 has its interplanetary magnetic field and plasma parameters shown in Figure 6.112. This event does not show many of the signatures that can be identified in a good magnetic cloud event:

- 1) the interplanetary magnetic field does not show a smooth rotation inside the MC period;
- 2) the temperature increases in the second half of the period;
- 3) the density is very high;

4) there is a decrease in the magnetic field intensity inside approximately the middle of the structure;

5) the beta parameter, although being lower than in the interplanetary medium, is higher than 0.1;

6) the duration of the MC is less than six hours, while magnetic clouds frequently are observed for more than 12 hours. This duration is deduced from MC transit speed and the radial size of the MC that is ~ 0.25 (KLEIN, BURLAGA, 1982) when they are close to the Earth.

The MC period indicated in the Figure 6.112 was selected taking into account the beta parameter and the variation of the IMF magnitude. The original MC period from the ICME catalog ranges from 2011/11/29 00 UT to 2011/11/29 08:00. There is a shock reported a few hours before the magnetic cloud beginning on 2011/11/28 at 22 UT. Before the shock the IMF had a toward sector polarity for at least 5 days. From 2011/11/29 on, the IMF is in an away sector. Therefore, this MC lies on a lateral side of an IMF sector.

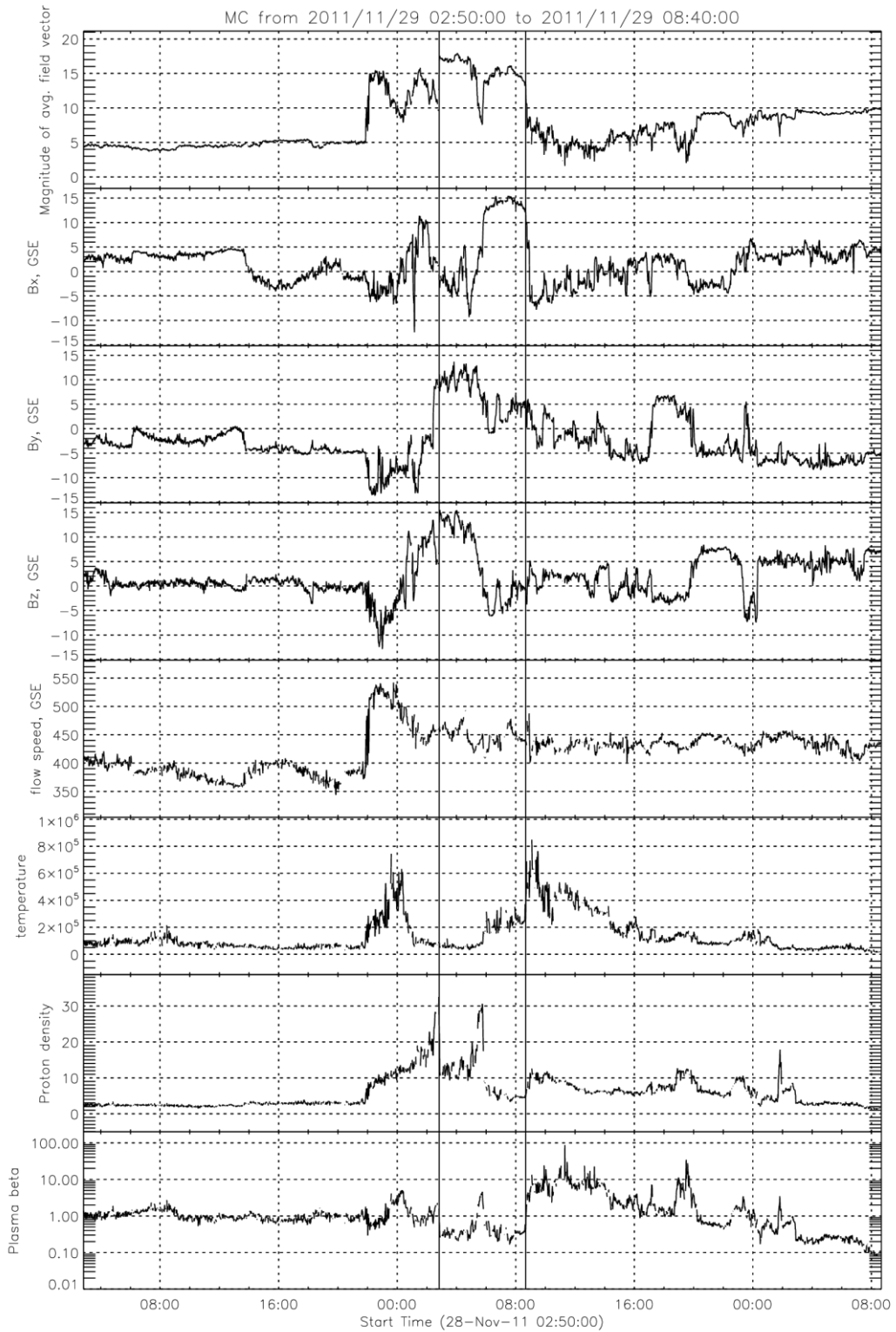


Figure 6.112 - The interplanetary magnetic field and plasma parameters during a MC on 2011/11/29.

6.14.2 The cosmic ray observations

The cosmic ray count rate of the vertical directional channels of each muon detector of the GMDN is shown in Figure 6.113. There is no clear decrease associated to this MC. After it, there is a clear daily variation observed in all detectors. As for the neutron monitors, there is a decrease observed by the detectors starting during the MC with an amplitude of about 1% (Figure 6.114). This decrease lasts for a period longer than the MC observed in the interplanetary medium and ends on 2011/12/01.

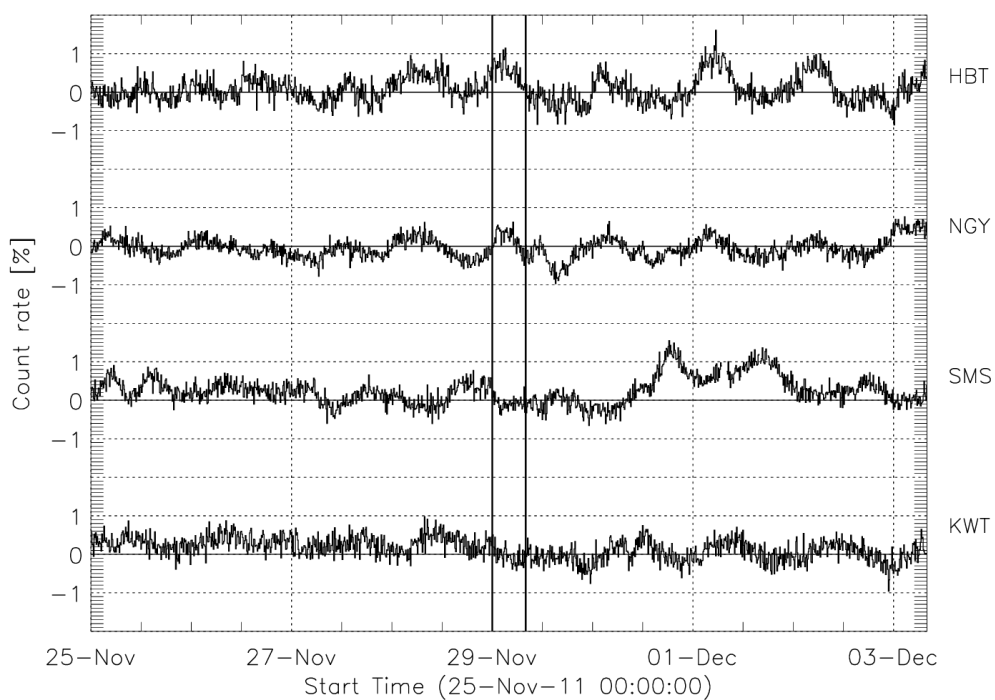


Figure 6.113 - The cosmic ray count rate observed by the vertical directional channels of the four muon detectors of the GMND during the MC on 2011/11/29. The vertical lines indicate the period of the magnetic cloud.

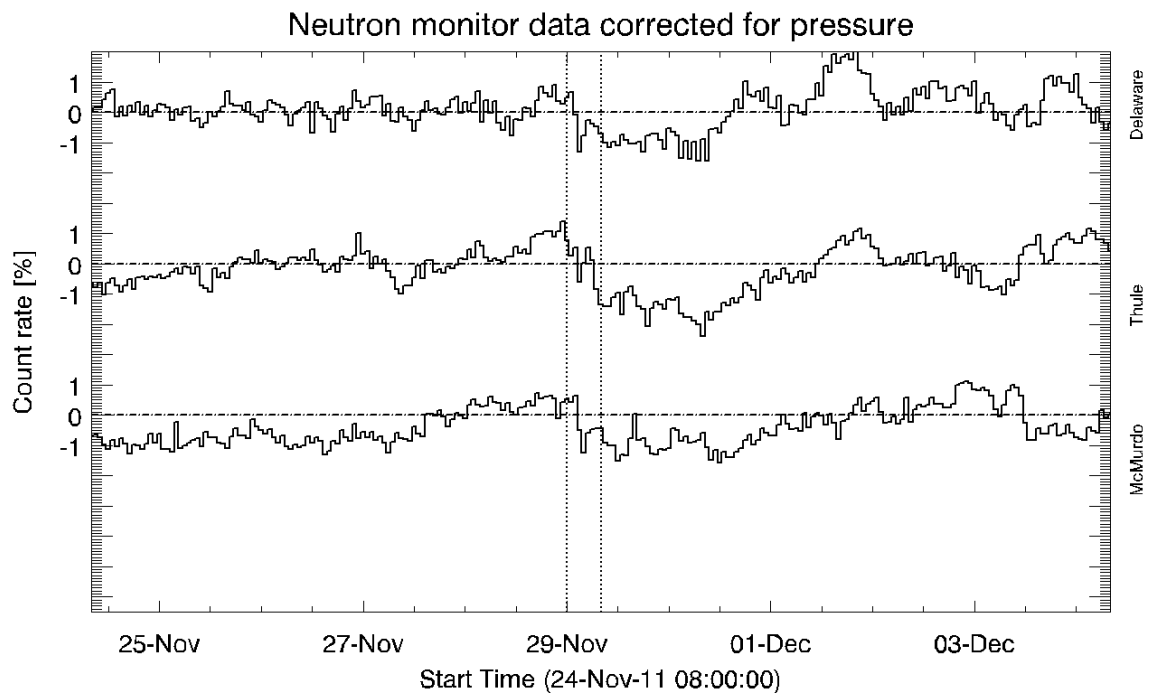


Figure 6.114 - The cosmic ray count rate observed by three different neutron monitors (Delaware, Thule and McMurdo) during the MC on 2011/11/29.

In this MC period, the isotropic intensity does not have the appropriate MC signature (Figure 6.115). The time-profile of the “x” component of the gradient suggests a structure approaching the Earth. However, the parallel anisotropy is higher than the perpendicular component on the second half of the magnetic cloud period. Since there is no isotropic cosmic ray intensity decrease during the magnetic cloud period and the anisotropy parallel to the IMF is higher, it is impossible to use the cosmic ray cylinder model.

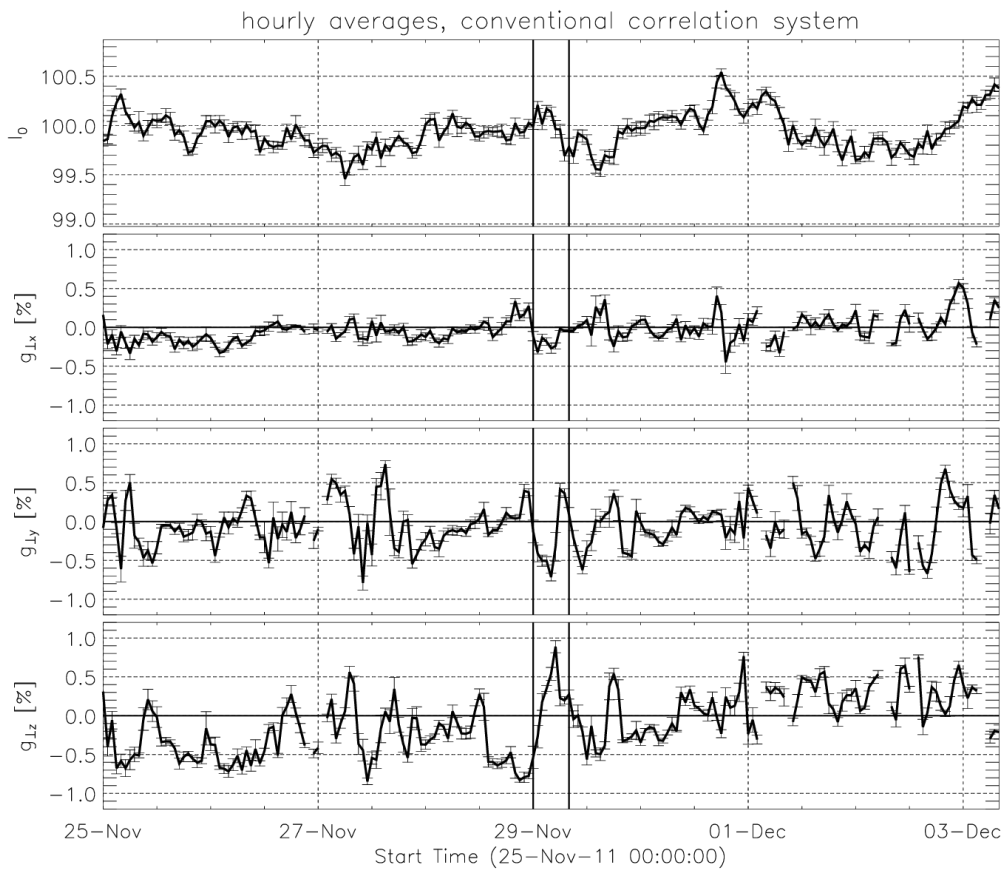


Figure 6.115 - The isotropic cosmic ray intensity and the orthogonal components of the cosmic ray fractional gradient during the MC period on 2011/11/29. The error bars indicate the error calculated from the six data points calculated using integration time of 10 minutes.

6.14.3 The origins in the solar corona

According to the CDAW SOHO catalog (YASHIRO et al., 2004), there are two halo events observed in the period before the MC. The observation of the first halo CME on LASCO-C2 FOV starts at 2011/11/26 7:11 and of the second CME at 2011/11/27 14:00. We inspected the position angle of these CMEs on the COR2 FOV and concluded that only the first is Earthward directed and the second one is directed away from the Earth. Therefore, the CME observed on 2011/11/26 must be the solar origin of the magnetic cloud observed on 2011/11/29.

The results of the CME on 2011/11/26 tracked by CORSET is shown in Figure 6.116. We tried different expansion factors and the result was not in agreement with the CME definition because the area selected was too high on the last frames ($Q = 4$) or a significant part of the CME region was not selected ($Q = 12, 16$). Finally, using the experience from previous events, we set $Q =$

0 because the CME kept a high brightness until it reaches of outer limit of the coronagraph. For the foreground model (explained in Section 4.4), we used a sample region in the third frame. If we used a sample region in the first frame and kept $Q = 0$, parts of the CME would not be included in the segmentation of the second and third frames. In principle, the CME was tracked in four frames (from 07:54 UT to 08:54 UT), but the last frame was removed when the triangulation was performed, because the result structure selected in COR2A and COR2B was apparently different from each other. In the remaining frames, to our understanding, the front of the CME selected is consistent with its definition. The lateral sides segmented by CORSET for this CME apparently are not consistent on time on COR2B because the area selected on the last frames extends excessively. Since we are not using the width of the CME in this analysis, this problem does not affect the calculation of the speed.

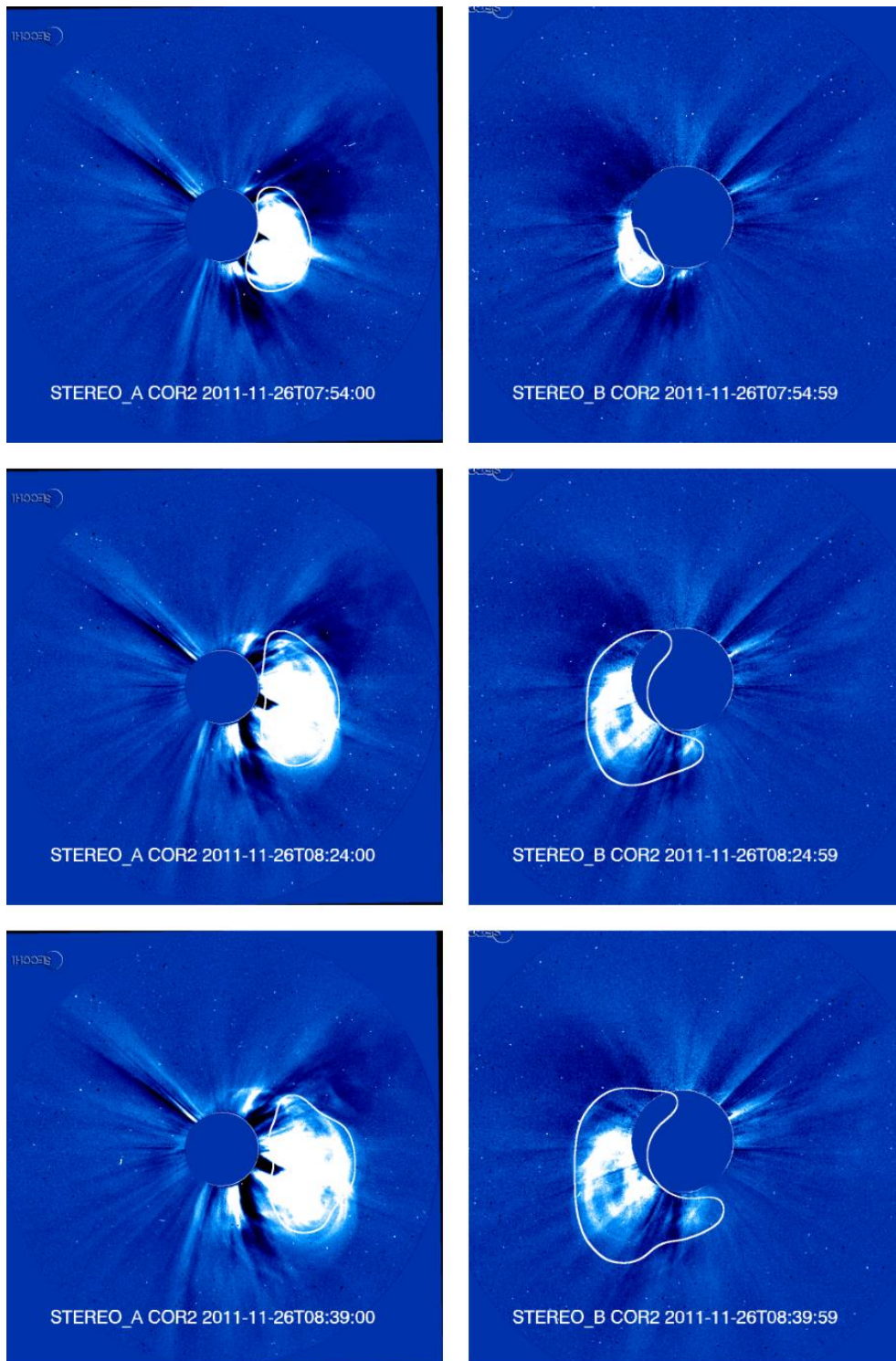


Figure 6.116 - The CME observed on 2011/11/26 in COR2A (left column) and COR2B (right column) FOVs. Notice that the images are rotated to the stereo baseline and that the north of the image is approximately pointing toward the bottom of the image.

The radial speeds calculated projected in each coronagraph FOV are shown in Figure 6.117 and Figure 6.118. The tridimensional speed map is shown in Figure 6.119 and it is summarized in Table 6.26. We tried to make the map also using the second and third frame but the error was too high. Therefore, it was constructed using only the first two frames.

This CME is quite fast (more than 800 km/s) on the coronagraph FOV but its interplanetary counterpart has a significantly lower speed (~450 km/s). The angular position of the partial halo CME on LASCO-C2 FOV suggests that its propagation is westward of the Sun-Earth line. Moreover, the CME is brighter on COR2A FOV than on COR2B suggesting that it is closer to COR2A and propagating westward of the Sun-Earth line. The direction of propagation from CORSET3D confirms these expectations. Unfortunately the cosmic ray cylinder model could not be performed and we cannot deduce the CRC position because the anisotropy is mainly parallel to the IMF.

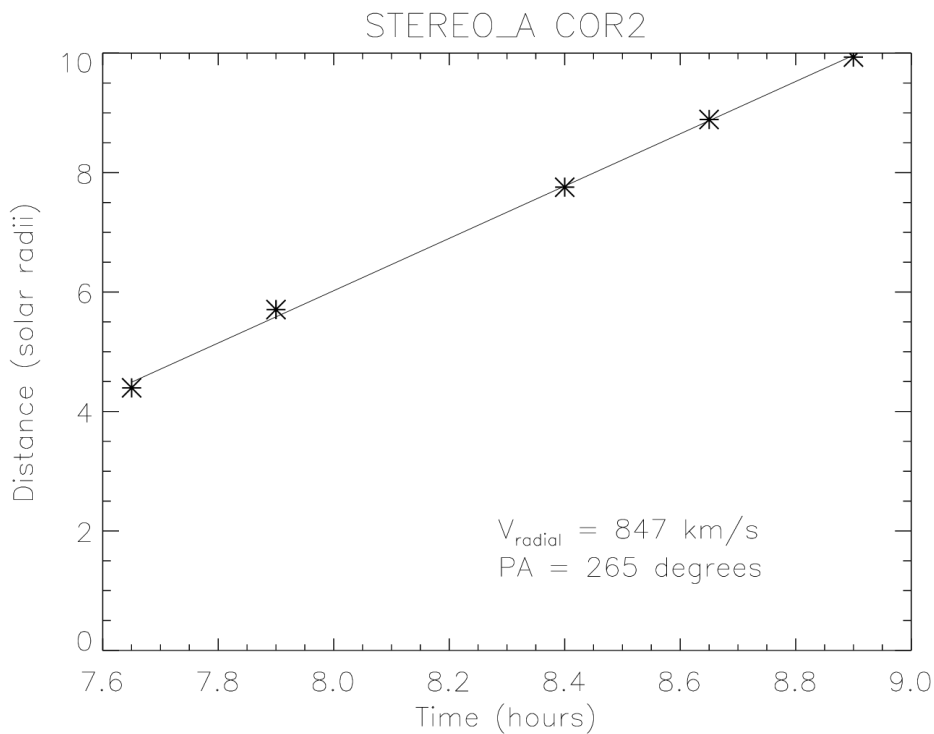


Figure 6.117 - The height-time profile of the CME on 2011/11/26 in the COR2A FOV for the fastest moving position angle. A linear fit is shown and the speed calculated is indicated. This CME was tracked by CORSET from 07:39 UT to 08:54 UT.

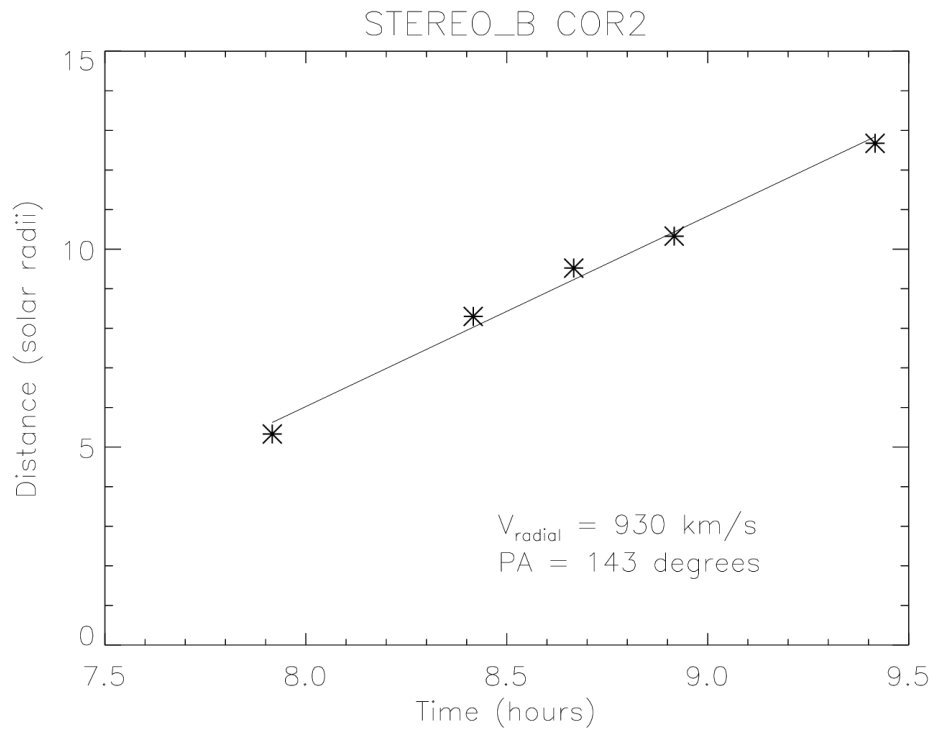


Figure 6.118 - The height-time profile of the CME on 2011/11/26 on the COR2B FOV for the fastest moving position angle. A linear fit is shown and the speed calculated is indicated. This CME was tracked by CORSET from 07:54 UT to 09:24 UT.

To our knowledge, there is no previous studies about this CME. In particular, this event is not included in any of the references previously cited in this Thesis such as Colaninno (2012) and Möstl et al. (2014).

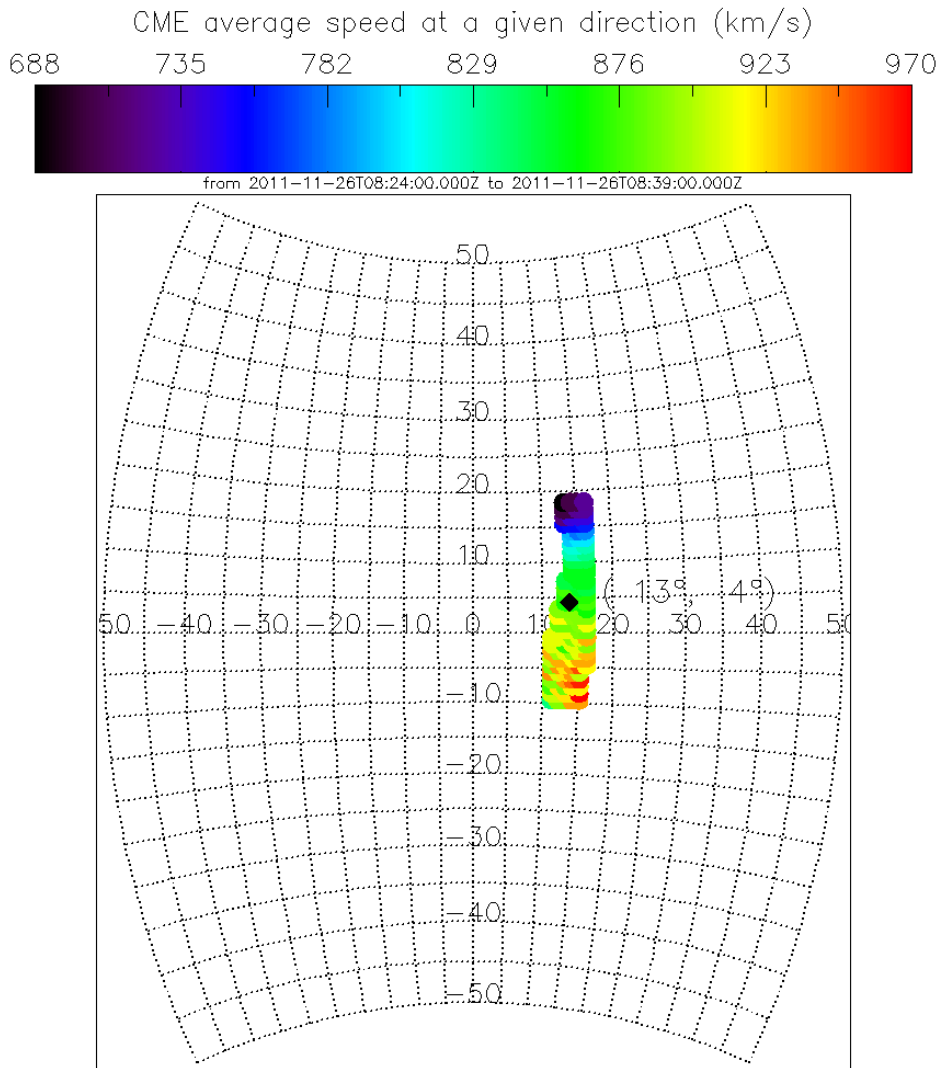


Figure 6.119 - The radial speed of the CME front as a function of latitude and longitude (in HEEQ coordinate system). The black diamond indicates the center of the CME front.

Table 6.26 - Kinematic parameters of the CME on 2011/11/26. The angles shown here are given in HEEQ coordinate system.

Parameter	Result
Minimum and maximum latitudes	[-10°, 19°]
Minimum and maximum longitudes	[11°, 17°]
Group speed v_g averaged over time	868±65 km/s
Central longitude of the CME averaged over time	13°
Central latitude of the CME averaged over time	4°
Minimum value of $\bar{v}_r(\theta_j, \phi_k)$	688 km/s
Maximum value of $\bar{v}_r(\theta_j, \phi_k)$	970 km/s
Group speed as a function of time $v_g(t_{i+1})$	[868] km/s
Maximum error of the triangulation	< 0.1 solar radii

7 DISCUSSION OF THE RESULTS

In Chapter 6, a detailed analysis of each of the 14 magnetic cloud observed between 2008 and 2011 was done. In this Chapter, we compare results from different events and discuss the overall trends.

7.1 Earthward directed CMEs observed

We determined the direction of propagation of CMEs observed from one to five days before the magnetic cloud observation close to the Earth. The results are summarized in Table 7.1 (events from 2008 to 2010) and Table 7.2 (events from 2011). The number of earthward directed CMEs found in each case is written in the fourth column. Other information about the CMEs already introduced in Chapter 6 (such as number of frames observed, CME group speed, longitude and latitude) are reproduced in these tables. According to the analysis done here, for 6 events among 14, there is only one CME directed toward the Earth and the magnetic cloud was therefore caused by only one CME. These events are highlighted in green. There is no earthward directed CME observed in three cases: #2, #8 and #13 (rows highlighted in blue). In other three events, two earthward CMEs were found in association to the magnetic cloud. In one case, four CMEs were directed toward the Earth. The MCs associated with more than one earthward directed CME are highlighted in yellow. The last three columns introduce topics not explored in Chapter 6. The observed travel time (third column from right to left in the tables) is the difference (in days) between the time of the first CME tracking in COR2 FOV using CORSET3D and the ICME beginning date. The estimated travel time (second column from right to left in the tables) corresponds to the CME travel time from the first observation on the COR2 FOV until it reaches the Earth supposing that the CME group speed is kept constant in the entire trajectory. The last column is the difference between the estimated and observed travel time. This difference is omitted in the cases that have more than one earthward directed CME.

Table 7.1 – MCs (observed from 2008 to 2010) and characteristics of corresponding CMEs

Event ID	ICME beginning date	CRC model	Number of Earthward CMEs	First frame of the CME tracked by CORSET3D	Last frame of the CME tracked by CORSET3D	CME group speed (km/s)	Longitude (HEEQ)	Latitude (HEEQ)	Observed travel time (days)	Estimated travel time (days)	Difference
1	2008/12/17 04:40	yes	1	2008/12/12 11:07	2008/12/17 13:37	357	4	4	4.73	4.86	0.13
2	2009/02/04 00:00	no	0	-	-	-	-	-	-	-	-
3	2010/04/05 13:00	no	1	2010/04/03 10:39	2010/04/03 11:54	982	0	-31	2.10	1.77	-0.33
4	2010/04/12 02:00	no	1	2010/04/08 05:24	2010/04/08 06:39	590	7	-5	3.86	2.94	-0.92
5	2010/05/28 21:00	yes	2	2010/05/23 18:54	2010/05/23 20:39	394	2	3	5.09	4.41	-
				2010/05/24 15:39	2010/05/24 16:24	610	6	3	4.22	2.85	-
6	2010/08/04 10:00	no	2	2010/08/01 05:39	2010/08/01 06:24	404	-28	7	3.18	4.30	-
				2010/08/01 09:24	2010/08/01 09:54	1126	-11	6	3.02	1.54	-

Table 7.2 – MCs (observed in 2011) and characteristics of corresponding CMEs

Event ID	ICME beginning date	CRC model	Number of Earthward CMEs	First frame of the CME tracked by CORSET3D	Last frame of the CME tracked by CORSET3D	CME group speed (km/s)	Longitude (HEEQ)	Latitude (HEEQ)	Observed travel time (days)	Estimated travel time (days)	Difference
7	2011/03/30 04:00	yes	1	2011/03/25 10:54	2011/03/25 12:24	178	3	-3	4.71	9.75	5.04
8	2011/05/28 08:00	no	0	-	-	-	-	-	-	-	-
9	2011/09/10 03:00	-	4	2011/09/06 03:24	2011/09/06 03:54	435	6	33	3.98	3.99	-
				2011/09/06 23:24	2011/09/07 00:24	861	13	33	3.15	2.02	-
				2011/09/07 23:54	2011/09/08 01:24	570	25	30	2.13	3.05	-
				2011/09/09 09:24	2011/09/09 11:24	372	33	-2	0.73	4.67	-
10	2011/09/17 16:20	no	1	2011/09/14 00:39	2011/09/14 02:54	571	21	21	3.65	3.04	-0.61
11	2011/10/05 08:00	no	2	2011/10/01 11:54	2011/10/01 13:39	474	-8	-2	3.84	3.66	-
				2011/10/02 02:39	2011/10/02 03:39	765	4	-20	3.22	2.27	-
12	2011/10/25 01:20	yes	1	2011/10/22 02:24	2011/10/22 03:24	563	-1	38	2.96	3.08	0.13
13	2011/11/07 18:00	no	0	-	-	-	-	-	-	-	-
14	2011/11/29 02:50	no	1	2011/11/26 08:24	2011/11/26 08:39	868	13	4	2.77	2.00	-0.77
Mean (from 2008 to 2011)						595	5	7	3.37	3.54	0.38
Standard deviation (from 2008 to 2011)						243	14	18	1.06	1.85	1.94

7.2 Overall analysis of CORSET3D tracking results for each CME

In this Thesis, 17 CMEs were tracked in both COR2A and COR2B FOVs, so CORSET was applied 34 times. In any CME, the user of CORSET needs to define, among other parameters such as the set of frames to be used, the expansion parameter Q . Any integer number from 0 to 16 can be chosen, in principle. In agreement with previous results from Braga et al. (2013) done for CMEs observed by LASCO, setting the expansion parameter at 4 works for most of the cases. In the analysis done here, the first test of CME tracking for all cases was setting the expansion parameter to this value. When the results produced were not consistent to the CME definition, a new test was performed with a different value of the parameter. In 15 cases (44% of the cases), the expansion parameter used was kept at 4. In 8 cases (24%), $Q = 0$ was adopted. Notice that using $Q = 0$ or $Q = 4$ produced consistent CME tracking results in almost 75% of the cases. The remaining parameters used were 14 (5 cases, 15%), 8, 10 and 16 (each one used 2 times, 6% of the cases). The results also suggest that CMEs that are very tenuous and very similar texture to the background are sometimes not tracked correctly using $Q = 4$ nor $Q = 0$. When $Q = 0$, the sample region to estimate the CME texture must be taken from one of the last frames tracked by CORSET, never from the first frame. It is interesting to notice that in Braga et al. (2013) none of the 57 CMEs studied was tracked using parameter $Q = 0$ and it was adopted here after trying many other values of Q from the reference (such as 8, 10, 14 and 16) without proper results.

The frames properly tracked by CORSET3D sometimes do not take into account the full CMEs path until the end of the coronagraph FOV. This is one possible limitation of the methodology when compared to the manual inspection and identification of CMEs. In some events, the CME frames close to the outside limit of the coronagraph FOV are not easily segmented from the background and CORSET did not produce good results. The remaining individual frames (considered to be in good agreement with the CME definition) were all shown in Chapter 6 and were used to calculate the speed in three dimensions. When a CME is very fast (for instance, speeds higher than 1000 km/s) the number of frames available in the coronagraph FOV will be lower than the average number indicated above and the application of CORSET will be limited to short time period. The average number of CME frames tracked in each cases is 4.82.

In order to assess the reliability of the results derived from CORSET3D, CMEs were compared to previous works as much as possible. Events observed in 2008, 2009, 2010 and the first CME from

2011 were compared to results from similar kinematical parameters derived by Liu et al. (2011), Lugaz et al. (2012), Colanino (2012) and Lugaz (2010). They are summarized in Table 7.3. For the remaining events observed after March 2011, we did not find any reference using simultaneous observation from two coronagraphs and stereoscopy. These events are listed in Table 7.4.

Following the results from Mierla et al. (2011), we considered the difference in the direction of propagation significant when latitude or longitude differs by more than 10 degrees. Among 8 events, 3 of them have significant differences in the propagation direction when we compared the results from CORSET3D with previous works. One possible reason for the differences is the presence of an adjacent CME, i. e., another CME not necessarily earthward directed observed at least on COR2A or COR2B in close timing and/or position to the earthward directed CME. This is the case of the CMEs observed on 2010/05/24 and 2010/08/01 (second event). On the event on 2011/03/25, Colanino (2012) mixes up two different CMEs (the earthward directed CME plus another later event). In the remaining 5 events from Table 7.3, there is no significant difference in the direction of propagation derived by CORSET3D and previous works.

When comparing the speed derived using CORSET3D with previous works, among the 8 events from Table 7.3, 2 of them have significant difference. We considered the difference in speed significant when it is higher than 100 km/s. This value was arbitrarily chosen as approximately 15% of the average CME speeds found here (595 km/s).

Table 7.3 - Parameters used when tracking each CMEs using CORSET that were compared to previous works.

CME observation date	Number of frames tracked by CORSET3D	Expansion parameter (Q) on COR2A FOV	Expansion parameter (Q) on COR2B FOV	Adjacent CME	Comparison with previous works
2008/12/12	6	0	0	No	no significant difference in speed nor direction of propagation
2010/04/03	5	4	4	No	no significant difference in speed nor direction of propagation
2010/04/08	6	4	4	No	significant difference in speed, no significant difference in the direction of propagation
2010/05/23	6	4	8	No	no significant difference in speed nor direction of propagation
2010/05/24	3	4	4	Yes	no significant difference in speed, significant difference in the direction of propagation
2010/08/01 (I)	3	8	0	No	significant difference in speed, no significant difference in the direction of propagation
2010/08/01 (II)	4	0	0	Yes	no significant difference in speed, significant difference in the direction of propagation
2011/03/25	5	0	14	No	no significant difference in speed, significant difference in the direction of propagation

Table 7.4 - CME tracked by CORSET3D in this Thesis that could not be compared to previous works.

CME observation date	Number of frames tracked	Expansion parameter (Q) on COR2A FOV	Expansion parameter (Q) on COR2B FOV	Adjacent CME
2011/09/06	3	14	14	Yes
2011/09/07	3	4	4	No
2011/09/08	3	10	10	Yes
2011/09/09	5	14	14	No
2011/09/14	8	4	4	No
2011/10/01	8	16	16	Yes
2011/10/02	6	4	4	Yes
2011/10/22	5	4	4	Yes
2011/11/26	3	0	0	No

7.3 Results from cosmic ray observation

The anisotropy was perpendicular to the IMF during the 13 of the 14 MC periods, as expected by Bieber & Evenson (1999). This condition needs to be satisfied for us to apply the CRC model.

The cosmic ray cylinder model was tested for all 14 MCDs studied here but the results are acceptable in only 4 cases. The MCs to which to CRC was successfully applied are indicated in the third column of Table 7.1 and Table 7.2. Hereafter, we will refer the four events as CRC events. In the remaining cases, the CR decrease is too small or it does not happen during the MC period but some hours before or after it. Among the 14 MCs, the OMNI data had gaps during the MC period in one event and the cosmic ray gradient could not be calculated. In three cases, there is no CME observed and the event does not fully satisfy the MC criteria. In the remaining 10 cases, most of the events that we cannot apply the CRC model are caused by more than one CME ejected toward the Earth.

There are seven MCs caused by only one CME (namely, #1, #3, #4, #7, #10, #12, #14) and the CRC model could be applied to 3 of them. The remaining case to which the CRC model was applied is caused by two CMEs. One of them was found to be deflected away from the Earth (LUGAZ et al., 2012). In this way, the interplanetary magnetic field and plasma parameters observed close to the Earth are probably caused by only one CME.

One common feature among the CRC events is the average beta parameter observed during the MC period: it is not higher than 0.2. For example, on #4 (which is not a CRC event) the average beta parameter is close to 1 during the MC period and on #1 (a CRC event) beta is close to 0.1. Moreover, among events with low average beta (close to 0.1), the CRC model could not be applied to only one event. From the studies done here, events that had better agreement with the MC criteria are more likely to be successfully studied by the CRC model.

Furthermore, sometimes the decrease is observed before or after the MC due to the cosmic ray modulation by a shock and/or a sheath region. In these circumstances, the CRC model is also not appropriate. In two of the CRC events, there is no shock nor sheath observed.

The cylinder radius found for the CRC events ranges from 0.04 to 0.09 AU at the central hour of the model application (see details in Section 3.9). The smaller cylinder was found for event #12 and the largest for #7. As a function of time, the cylinder radius is shrinking in two cases (#1 and #5) at radii of -0.002 and -0.001, respectively. In one event, there is expansion (#7) and in the remaining, the cylinder radius is kept constant at all times. As already discussed in Section 6.1.2, a CRC shrinking does not necessarily indicate that the magnetic flux (and MC) is also shrinking. As time passes, cosmic ray populate the flux rope in a way that close to its outside boundary the density becomes similar to outside it. This hypothesis here is supported by the results from the simulation performed by Kubo & Shimazu (2010). Their results suggest that the cosmic ray populates first the region closer to the outer boundary and, after this, the density in the innermost region starts increasing.

We also compared the results of the MC orientation (latitude and longitude of the MC cylinder axis) from the CRC model and the MVA. In two cases, there is a bad agreement in latitude and longitude between the CRC model and the MVA analysis. These cases were observed on 2010/05/28 (#5) and on 2010/10/24 (#12). One possibility is that other structures present in the interplanetary medium in close timing also modulated the cosmic ray observed by the Global Muon Detector Network and not only the MC. In the first case, there are two earthward directed CMEs interacting with each other and there is shock observed ahead of the MC. In the second case, we identified shock/sheath region ahead of the MC. Moreover, in this event only (when compared to the remaining analyzed by the CRC model) the CME propagation direction is significantly above the ecliptic plane (more than 30° of latitude in HEEQ coordinates).

7.4 Comparing the properties of CMEs and corresponding ICMEs

The de-projected (tridimensional) speeds deduced from CORSET3D ranges from 178 km/s to 1126 km/s while the solar wind speed range from 350 km/s to 800 km/s during MCs studied. While slow CMEs tend to be accelerated, the fast ones are decelerated. This trend has been reported by many studies both using CMEs speeds projected on LASCO FOV (SHEELEY et al., 1999; YASHIRO et al., 2004) as well as in de-projected speeds studies using observations from SECCHI (COLANINNO, 2012; MÖSTL et al., 2014).

The position of the MC can be deduced from the direction of the gradient vector: the gradient vector will be opposite directed to the region of minimum cosmic ray density. The cosmic ray region of minimum density will correspond to the central region of the magnetic cloud. Notice that this can be deduced even when we are not able to determine the CRC model if the following conditions are satisfied: (i) the cosmic ray anisotropy is deduced; (ii) the information of the interplanetary magnetic field direction is available and (iii) the anisotropy direction is basically perpendicular to the IMF direction.

If we consider that the CME propagated only radially away from the Sun, the position of the MC will depend only on the direction of the propagation of the CME. We deduced the tridimensional (de-projected) CME group speed and compared it with the position deduced from the cosmic ray gradient.

Events #2, #8 and #13 do not have any earthward directed CME identified. In the #14 the anisotropy is not clearly perpendicular to the IMF direction and the gradient calculated does not necessarily correspond to the most significant fraction of the structure. There are 10 remaining cases to investigate the relation between CME and CRC position.

In the following events, there is agreement between results from CRC and CORSET3D:

- #1: structure is above the ecliptic plane;
- #5: the longitudinal position of the CME agrees with the cosmic ray cylinder observation but there is no clear trend in the latitude;
- #7: the portion of the CME that is further away from the Sun is in the eastside of the Sun-Earth line and the CRC is observed first in the same semi space;

- #9: all the four CMEs lie in the region above the ecliptic plane and the cosmic ray gradient is negative, suggesting a CRC above the ecliptic plane; there is no clear trend in the longitude.

In the following events, there is a clear disagreement:

- #3: the cosmic ray minimum density is above the ecliptic plane but the CME direction is clearly below it;

- #10: the latitudinal position suggested by the CRC and the observation from the CME disagree: while the latter is clearly above the ecliptic plane, the former suggests a structure below it. There is also a disagreement in the longitude;

- #12: the CME position is clearly above the ecliptic plane, but the CRC is clearly below it. There is no clear trend in the longitude.

In one case (#6), there is a partial agreement and partial disagreement between position deduced from CORSET3D and CRC results: their latitudinal position agrees but the longitudinal disagrees. The two earthward directed CMEs are located eastward of the Sun-Earth line and above the ecliptic plane.

In two cases (#4 and #11), there is no clear agreement nor disagreement. In the first one, the cosmic ray minimum density region is above the ecliptic plane but the CME is basically centered in the ecliptic plane). In the second event, the two CMEs are located in different position and, from the analysis done, there is no clear way to understand which one produced modulation in the cosmic ray.

Although speed and position of MC and corresponding CME are compared in this Thesis, there is no comparison of orientation of both structures since we are not assuming any physical or geometrical model of the CME. Some authors assume a magnetic flux rope model for the CME and then compare the orientation found from coronagraph data in the solar corona and with in situ data from the MC (COLANINNO, 2012). Since CORSET3D is a methodology that does not impose any geometric or physical constraint, it is out of the scope of Thesis adopting a model for the CME such as the magnetic flux rope. One advantage that CORSET3D brings us is the possibility of studying the radial speed of the CME in any portion of its front.

From the radial speed distribution of the 17 CME fronts analyzed, we concluded that 11 of them have significantly higher speeds on the portion closer to the solar equator (latitude zero) than on the remaining portions: #1, #3, #4, #5 (1st CME), #6 (1st CME), #7, #11 (2nd CME), #12, #9 (1st CME), #9 (2nd and 3rd CMEs). A further investigation is necessary to decide whether this trend is an artifact of the methodology or whether it has a physical explanation. If the first possibility is discarded, one physical explanation is that particularly near solar minimum, many CMEs tend to deflect toward the solar equator (PLUNKETT et al., 2001). One reason for the deflection is an asymmetrical expansion when its portion close to the pole is blocked by something else in the solar corona (WANG et al., 2011).

8 CONCLUSIONS

From 2007 onwards, we had the first opportunity to simultaneously observe the solar corona by remote sensing from three different viewpoints thanks to the combination of the SOHO and STEREO missions. Combining those observations with in situ data of the interplanetary medium, CMEs and related ICMEs can be studied in more details than ever before.

We started the analysis from a list of MCs and studied the conditions in the interplanetary medium using solar wind magnetic and plasma in situ data. Among the 14 events observed from 2008 to 2011, the maximum IMF intensity ranges from 9 nT to 24 nT and the average solar wind speed is ~ 450 km/s. Some events reported as MCs by the ICME catalog (RICHARDON; CANE, 2010) did not follow all its criteria: the beta parameter was higher than 0.1 (sometimes close to 1), and the IMF did not show a smooth behavior.

Knowing the MC timing, we inspected coronagraph observations to identify the CMEs that caused them in a period up to 5 days before. In three events, we did not identify any earthward CME. To our understanding, these events are possibly the result of a stream-interaction region. Other three events had two CMEs ejected toward the Earth in such a way that the second one ejected in each case was faster than the first. As a result, the second CME interacted with the first in its propagation between the Sun and the Earth. In only one case, four CMEs were ejected toward the Earth and two of them probably interacted.

We developed a new method to estimate the CME speed and direction using simultaneous observation of two coronagraphs from different viewpoints. This method was named CORSET3D and results from the combination of CORSET (for tracking the CME projection in each coronagraph) and Sunloop (for doing triangulation and tie-pointing analysis). The CME results do not depend on visual inspection for tie-pointing identification. Hence, CORSET3D allows 3D reconstruction of the time evolution of the whole CME leading edge in an objective way. This method provides us information about the instantaneous and average radial speeds of a given CME at any portion of its front. In opposition to the forward fitting methods (such as the GCS), we reconstructed the CME front without any geometric constraint.

We used CORSET3D to track earthward directed CMEs that caused the MCs observed from 2008 to 2011. We used observations from the coronagraph COR2 onboard the twin STEREO spacecraft. Among 20 CMEs, CORSET failed in one event and CORSET3D was discarded in two cases due to

triangulation problems when the separation angle between the two spacecraft was very close to 180° . In a few cases, lateral portions of the CMEs tracked by CORSET were not satisfactorily selected and part of an adjacent CME was also included.

We compared the results derived by CORSET3D, such as de-projected speed and direction of propagation, with previous works using different methodologies whenever possible. Taking into account the extensive comparison of many methods (MIERLA et al., 2010), we considered the differences in direction of propagation significant when they were higher than 10° . No previous references about the 3D propagation direction of CMEs observed in 2011 by STEREO was found. We compared results from the remaining eight CMEs (all of them observed in 2008 and in 2010). For three CMEs, there is a significant difference in the latitude or longitude: the second CME from events #5 and #6 and the CME from event #7. We realized that these three events are superposed to other CMEs on the coronagraph images. In the first two cases, there are previous CMEs on the COR2 FOV that may prevent a proper boundary identification by CORSET or may bias the GCS analysis, which is done by visual inspection. In the third case, the GCS analysis is unfavorable because a CME is observed on LASCO FOV a few hours latter than the studied one.

Since the objective of the present work was studying connections between the phenomena observed in the Sun and the consequences in the interplanetary medium close to the Earth, we also analyzed the cosmic ray observations from the Global Muon Detector Network (GMDN).

After correcting the GMDN data for atmospheric pressure and temperature effects, we computed the isotropic cosmic ray intensity as well as the anisotropy vector following the methodology from Okazaki et al. (2008). During the MC periods analyzed here, the expectations from Bieber & Evenson (1998) were confirmed: the anisotropy tends to be perpendicular to the IMF and, therefore, the drift $B \times \nabla n$ is the source of the anisotropy observed during the MC periods.

When a MC is approaching the Earth, the cosmic ray cylinder model expects a decrease in the isotropic intensity followed by an increase back to a similar level than observed before the beginning of the MC. In spatial terms, the cosmic rays are expected to have gradient component aligned with the Sun-Earth direction with minimum toward the Sun due to the cosmic ray depleted region. As the MC moves in the interplanetary medium approximately radially away from the Sun, it approaches the Earth and the gradient decreases gradually until reaches zero

and the MC has an equal portion away and toward the Sun. The gradient of the cosmic ray density in the plane perpendicular to the Sun-Earth line suggests us the position of the MC in this plane.

The cosmic ray cylinder model was applied to all MC periods and the results were acceptable to four events: #1, #5, #7 and #12. Considering only the 6 events with unique MC/CME relation (#1, #4, #7, #10, #12 and #14), the CRC model was applied in two among six events. In the remaining events, the signatures commented in the previous paragraph are absent and the fitting is not satisfactory. Many MC events did not have any decrease in the CR isotropic intensity observed by the GMDN. In the analysis conducted here, we did not include any limitation in the minimum intensity necessary to perform the CRC analysis, in opposition to the 2% decrease imposed in Kuwabara et al. (2004, 2009). The isotropic decrease observed by the vertical directional channels of the GMDN was smaller than 1% for all the MCs observed between December 2008 and December 2011, except for those on 2010/08/04 and 2011/10/05.

We compared results of the CRC model using the conventional and new correlation systems of the GMDN. Differences in the results were found in some parameters, especially in the orientation of the CRC. The difference extends up to 10° in the latitude and longitude and we believe that the error of the method is at least of this order of magnitude. We also compared orientation deduced by the MVA and CRC. Results from events #1 and #7 are in good agreement but a significant difference (higher than 30 degrees) was found for events #5 and #12.

In all events with anisotropy component perpendicular to the IMF higher than the component parallel to it (including the cases that the CRC model could not be applied), we used the gradient as an indication of the MC central axis position.

Finally, we compare results from the cosmic ray gradient to those deduced from CORSET3D. To our assessment, such comparison has never been done before. A previous work compared results from GCS and EFR but they did not agree for most of the cases (COLANINNO, 2012).

We compared the relative position of the MC in relation to the Earth. We analyzed whether the center of the cosmic ray depleted region was located northward (or southward) of the ecliptic and east (or westward) of the Sun-Earth line. We noticed that many of the events with disagreement have more than one CME visible on the COR2 FOV during the earthward tracking. Part of an adjacent CME was included the region tracked by CORSET in some cases.

A disagreement between results do not necessarily mean error in one or two or the methods compared since we have comparing one structure located close to the Sun with it corresponding located close to the Earth. In some cases the difference may be explained by CMEs deflection (LUGAZ et al., 2012; XIE et al., 2009; NIEVES-CHINCHILLA et al., 2013), non-radial propagation (WANG et al., 2011) or even rotation of CMEs (VOURLIDAS et al., 2011) in its path since they left COR2 FOV until get close to the Earth. Such analysis is out of the scope of this Thesis. The conciliation between the CME-MC properties is necessary if we wish to understand the interplanetary consequences of each CME.

One question that is not fully elucidated is whether the structure observed in the remote sensing data from coronagraphs correspond to the same structure observed in the interplanetary data in situ and the cosmic ray depleted region. Some studies claim that the structure observed in remote sensing data may correspond to the shock ahead of the CME in some cases (VOURLIDAS et al., 2003) and this might be the explanation of the differences found in some of the events studied here.

One would believe that the CRC results would be closer to other methods when the isotropic cosmic ray intensity is higher. The results found here, however, do not support this hypothesis. Event #1 have small cosmic ray isotropic decrease as well as small IMF intensity. Even though, the results derived by the CRC are in good agreement with both the position of the orientation deduced from the MVA analysis and the MC determined from CORSET3D (and other methods using coronagraph data). On the other hand, the event #12 has the highest cosmic ray intensity decrease and highest IMF strength and, in spite of this, their CRC results are different from those deduced from coronagraphic observations and from the MVA analysis.

The cosmic ray data observed by the GMDN may be affected by the sector boundary and by interplanetary shock located ahead of the ICMEs. In many of the events studied here (10 among 14), a sector boundary was reported a few hours ahead or before the MC period. Moreover, MCs are frequently accompanied by an interplanetary shock. The CRC model does not take into account any consideration about shock nor sector boundary. Since shocks are observed ahead of many MCs, any study in this direction could improve the results.

As a suggestion for future work, the application the CRC model can be applied to magnetic cloud observed from 2012 on. Moreover, the model needs to be complemented to include the

modulation of galactic cosmic ray by the interplanetary shocks and sheath region since they are frequently preceding a magnetic cloud.

REFERENCES

- ANDREWS, M. D. A search for CME associated with big flares. **Solar Physics**, v. 218, p. 261-279, 2003.
- BERKOVA, M. D. et al. Temperature effect of the Muon Component and Practical Questions for Considering It in Real Time. **Bulletin of the Russian Academy of Sciences. Physics**, v. 75, n. 6, p. 869-873, 2011.
- BIEBER, J. W.; EVENSON, P. CME Geometry in Relation to Cosmic Ray Anisotropy, **Geophysical Research Letters**, v. 25, n. 15, p. 2955-2958, 1998.
- BILLINGS, D. E. **A guide to the solar corona**, New York: Academic Press, 1966.
- BOBIK, P. et al. Cosmic ray transparency for a medium latitude observatory. **Il Nuovo Cimento C**, v. 26, n. 2, p. 177-189, 2003.
- BONTE, K. et al. Validation of CME detection software (CACTus) by means of simulated data, and analysis of projection effects on CME velocity measurements. **Solar Physics**, v. 270, p. 253-272, 2011.
- BOTELER, D. H.; PIRJOLA, R. J.; NEVANLINNA, H. The effects of geomagnetic disturbances on electrical systems at Earth's surface, **Advances in Space Research**, v. 22, p. 17-27, 1998.
- BRAGA, C. R. **Study of solar-interplanetary-geomagnetic disturbances using data from the Global Muon Detector Network and the LASCO coronagraph**. 2011. 178 p. (sid.inpe.br/mtc-m19/2011/02.07.20.31-TDI). Master Thesis - Instituto Nacional de Pesquisas Espaciais, São José dos Campos, 2011.
- BRAGA, C. R.; DAL LAGO, A.; STENBORG, G. Pseudo-automatic characterization of the morphological and kinematical properties of coronal mass ejections using a texture-based technique, **Advances in Space Research**, v. 51, p. 1949-1965, 2013.
- BRUECKNER, G. E. et al. The Large Angle Spectroscopic Coronagraph (LASCO), **Solar Physics**, v. 162, p. 357-402, 1995
- BURLAGA, L. F. et al. Magnetic loop behind an interplanetary shock: Voyager, Helios and IMP-8 observations. **Journal of Geophysical Research**, v. 86, n. A8, p. 6673-6684, 1981.
- BURLAGA, L. F.; BEHANNON, K. W. Magnetic clouds: voyager observations between 2 and 4 AU. **Solar Physics**, v. 81, n. A2, p. 181-185, 1982.
- BURLAGA, L. F.; LEPPING, R. P.; JONES, J. Global configuration of a magnetic cloud. In: RUSSEL C. T.; PRIEST, E. N.; LEE, L. C. (eds.), **Physics of magnetic flux ropes**, Washington, DC: American Geophysical Union, 1990. v. 58, p. 373-385.

BURLAGA, L. F. **Interplanetary magnetohydrodynamics**. New York, U.S.A.: Oxford University Press, 1995.

CARRINGTON, R. C. Description of a Singular Appearance seen in the Sun on September 1, 1859. **Monthly Notices of the Royal Astronomical Society**, v. 20, p. 13-15, 1859.

COLANINNO, R. **Investigation of the forces that govern the three-dimensional propagation and expansion of Coronal Mass Ejections from the Sun to the Earth**. George Mason University. Fairfax, VA, 145p. 2012.

CREMADES, M. H. **Three-dimensional configuration and evolution of coronal mass ejections**. Ph.D. Dissertation. Fakultät für Physik und Geowissenschaften der Technischen Universität Carolo-Wilhelmina, Braunschweig, Germany, 2005.

DAL LAGO, A. **Estudo de nuvens magnéticas geofetivas no meio interplanetário**. 1999. 122 p. (INPE-7263-TDI/705). Master Thesis (in Portuguese) - Instituto Nacional de Pesquisas Espaciais, São Jose dos Campos, 1999.

DA SILVA, M. R. **Detecção de distúrbios solar-interplanetários combinando observações de satélites e de raios cósmicos de superfície para aplicação em clima espacial**. PhD Dissertation (in Portuguese), Instituto Nacional de Pesquisas Espaciais, São José dos Campos, 2010.

DORMAN, L. I. **Cosmic rays in the Earth's atmosphere and underground**. Dordrecht, The Netherlands: Kluwer Academic Publishers, 2004.

DULDIG, M. Muon observations. **Space Science Review**, v. 93, p. 207-226, 2000.

DUNHAM, D. V. et al. STEREO Trajectory and Manuever Desing. **Johns Hopkins APL Technical Digest**, v. 28, n. 2, 2009.

DUZELLIER, S. Radiation effects on electronic devices in space, **Aerospace Science and Technology**, v. 9, n. 93-99, 2005.

FRIEDLANDER, M. W. **Cosmic ray**. Encyclopedia Britannica Online. Encyclopedia Britannica Inc., n.d. Available at: <http://global.britannica.com/EBchecked/topic/139234/cosmic-ray>. Access on: 2 Jan. 2014.

FUSHISHITA, A. et al. Precursors of the Forbush Decrease on 2006 December 14 observed with the Global Muon Detector Network (GMDN). **The Astrophysical Journal**, v. 715, p. 1239-1247, 2010.

GLEESON, L. J.; AXFORD, W. I. The Compton-Getting Effect, **Astrophysics and Space Science**, n. 2, p. 431-437, 1968

GIACALONE, J. Energetic particle transport. In: SCHRIJVER, C. J.; SISCOE, G.L. (Eds). **Heliophysics: space storms and radiation: causes and effects**. 1. ed. Cambridge, UK: Cambridge University Press, 2010, 447p. ISBN: 978-0521760515.

GONZALEZ, W. D.; TSURUTANI, B. T.; CLÚA DE GONZALEZ, A. L. C. Interplanetary origin of geomagnetic storms. **Space Science Reviews**, v. 88, n. 3, p. 529-562, 1999.

GOPALSWAMY, N. et al. The pre-CME Sun. **Space Sciences Reviews**, v. 123, p. 303-339, 2006.

GOPALSWAMY, N. et al. A catalog of halo coronal mass ejections from SOHO, **Sun and Geosphere**, v. 5, n. 7-16, 2010.

GOSLING, J. T. et al. Direct observations of a flare related coronal and solar-wind disturbance. **Solar Physics**, v.40, n. 2, p. 439-448, 1975.

GOSLING, J. T. et al. Coronal mass ejections and large geomagnetic storms, **Geophysical Research Letters**, v. 17, p. 901-904, 1990.

GOSLING, J. T. The structure and evolution of the three-dimensional solar wind. In: SCHRIJVER, C. J.; SISCOE, G. L. **Heliophysics: evolving solar activity and the climates of the space and earth**. 1. ed. Cambridge, UK: Cambridge University Press, 2010, 495p. ISBN: 978-0521388559.

GOUSSIES, N. et al. Tracking of Coronal White-Light Events by Texture. **Solar Physics**, v. 262, n. 2, p. 481-494, 2010.

HAPGOOD, M. A. Space Physics coordinate transformations: a user guide. **Planetary and Space Sciences**, v. 40, n. 5, p. 711-717, 1992.

HARALICK, R.M., SHANMUGAM, K., DINSTEN, I. Textural features for image classification. **IEEE Transactions on Systems, Man and Cybernetics**, v. SMC3, p. 610-621, 1973.

HAYES, A. P.; VOURLIDAS, A.; HOWARD, R. A. Deriving the electron density of the solar corona from the inversion of total brightness measurements. **The Astrophysical Journal**, v. 548, p. 1081-1086, 2000.

HOGSON, R. On a curious Appearance seen in the Sun, **Monthly Notices of the Royal Astronomical Society**, v. 20, p. 15-16, 1859.

HOWARD, R. A. et al. The observation of a coronal transient directed at Earth, **The Astrophysical Journal**, v.263, n. 2L, p. 101-104, 1982.

HOWARD, R. A. et al. Coronal mass ejections 1979-1981. **Journal of Geophysical Research**, v. 90, p. 8173-8191, 1985.

HOWARD, R. A. et al., Observations of CME from SOHO/LASCO, In: CROOKER, N., JOSELYN, J.A., FEYNMAN, J. (Eds)., **Coronal mass ejections**, Washington, DC, American Geophysical Union, v. 99, p. 17-26, 1997.

HOWARD, R. A. et al. Sun Earth Connection Coronal and Heliospheric Investigation (SECCHI), **Space Science Reviews**, v. 136, p. 67-115, 2008.

HU, Q.; SONNERUP, B. U. O. Reconstruction of magnetic clouds in the solar wind: Orientations and configurations, **Journal of Geophysical Research**, v. 107, n. A7, p. SSH 10-1-SSH10-10, 2002.

ILLING, R. M.; HUNDHAUSEN, A. J. Disruption of a coronal streamer by an eruptive prominence and coronal mass ejection. **Journal of Geophysical Research**, v.91, n. A10, p. 10951-10960, 1986.

INHESTER, B. Stereoscopy basics for the STEREO mission, arxiv.org/pdf/astro-ph/0612649.pdf, 2006.

JOKIPII, J. R. Cosmic Rays. In: SUESS, S. T.; TSURUTANI, B. T. (eds.) **From the Sun: auroras, magnetic storms, solar flares, cosmic rays**. Washington (DC), USA: American Geophysical Union, 2000. ISBN: 0-87590-292-8.

JOKIPII, J. R. The heliosphere and cosmic rays. In: SCHRIJVER, C. J.; SISCOE, G. L. (eds.) **Heliophysics: evolving solar activity and the climates of the space and Earth**. 1. ed. Cambridge, UK: Cambridge University Press, 2010, p. 495. ISBN: 978-0521388559.

KANE, R. P. Mechanism of the Diurnal Anisotropy of Cosmic Radiation. **Journal of Geophysical Research**, v. 79, n. 10, p. 1321-1331, 1974.

KLEIN, L. W.; BURLAGA, L. F. Interplanetary magnetic clouds at 1 AU. **Journal of Geophysical Research**, v. 87, p. 613-624, 1982.

KUBO, Y.; SHIMAZU, H. Effect of finite Larmor radius on cosmic-ray penetration into an interplanetary magnetic flux rope, **The Astrophysical Journal**, v. 720, p. 853-861, 2010.

KUWABARA, T. et al. Geometry of an interplanetary CME on October 29, 2003 deduced from cosmic rays. **Geophysical Research Letters**, v. 100, p. L19803, 2004.

KUWABARA, T. **Uchū-sen myūon kansoku nettowāku o mochiita wakusei-kan kūkan jōran no kenkyū**. PhD Thesis (in Japanese), Shinshu University, Matsumoto, Japan, 2005.

KUWABARA, T. et al. Determination of interplanetary coronal mass ejections geometry and orientation from ground-based observations of galactic cosmic rays. **Journal of Geophysical Research**, v. 114, n. A05109, 2009.

LIEWER, P. C. et al. Stereoscopic Analysis of the 19 May 2007 Erupting Filament, **Solar Physics**, v. 256, p. 57-72, 2009

LIEWER, P. C. et al. Stereoscopic analysis of STEREO/SECCHI data for CME trajectory determination, **Journal of Atmospheric and Solar-Terrestrial Physics**, v. 73, p. 1173-1186, 2011.

LIU, Y. et al. Geometric triangulation of imaging observations to track coronal mass ejections. **The Astrophysical Journal Letters**, v. 710, p. L82-L87, 2010.

LIU, Y. et al. Reconstructing coronal mass ejections with coordinated imaging and in situ observations: global structure, kinematics, and implications for space weather forecasting, **The Astrophysical Journal**, v. 722, p. 1762-1777, 2010.

LIU, Y. et al. Solar source and heliospheric consequences of the 2010 April 3 coronal mass ejection: a comprehensive view. **The Astrophysical Journal**, v. 734, n. 84, 2011.

LIU, Y. D. et al. Interactions between coronal mass ejections viewed in coordinated imaging and in situ observations. **The Astrophysical Journal Letters**, v. 746, L15, 7 PP. 2012.

LOOP, C.; ZHANG, Z. Computing Rectifying Homographies for Stereo Vision, **Proceedings of IEEE Conference on Computer Vision and Pattern Recognition**, v.1, p. 125-131, 1999.

LUGAZ, N. Accuracy and Limitations of Fitting and Stereoscopic Methods to Determine the Direction of Coronal Mass Ejections from Heliospheric Imagers Observations, **Solar Physics**, v. 267, p. 411-429, 2010.

LUGAZ, N. et al. The deflection of the two interacting coronal mass ejections of 2010 May 23–24 as revealed by combined in situ measurements and heliospheric imaging. **The Astrophysical Journal**, v. 759, p.68, 13 pp., 2012.

MARUBASHI, K. Interplanetary magnetic flux ropes and solar filaments. In: N. CROOKER, N.; JOSELYN, J.; FEYMAN, J. (eds.) **Coronal mass ejections**, Geophysics Monograph Series, v. 99, pp. 147– 156, American Geophysical Union, Washington, D. C., 1997.

MCCRACKEIN, K. G., RAO, U. R; SHEA, M. A. The trajectory of cosmic ray in a high simulation of geomagnetic field. v. 77, **Massachusetts Institute of Technology**, Cambridge, 1962.

MCDONALD, F. B. Integration of neutron monitor data with spacecraft observations: A historical perspective, **Space Science Reviews**, v. 93, p. 263-284, 2000.

MENDONÇA, R. R. S. et al. Continuous analysis and meteorological effects study of the cosmic ray intensity images generated by the Global Muon Detector Network. In: INTERNATIONAL COSMIC RAY CONFERENCE (ICRC), 33., 2013, Rio de Janeiro. **Proceedings...** Rio de Janeiro: International Union of Pure and Applied Physics (IUPAP), 2013. 1 DVD.

MIERLA, M. et al. On 3D Reconstruction of Coronal Mass Ejections: I Method description and application to SECCHI-COR Data, **Solar Physics**, v. 259, p. 123-141, 2009.

MIERLA, M. et al. On the 3-D reconstruction of Coronal Mass Ejections using coronagraph data, **Annales Geophysicae**, v. 28, p. 203–215, 2010.

MINNAERT, M. On the continuous spectrum of the corona and its polarization, **Zeitschrift für Astrophysik**, v. 1, p. 209-236, 1930.

MORAN, T. G.; DAVILA, J. M. Three-Dimensional Polarimetric Imaging of Coronal Mass Ejections, **Science**, v. 305, p. 66-70, 2004.

MORAN, T. G.; DAVILA, J. M.; THOMPSON, W. T. Three-dimensional polarimetric coronal mass ejection localization tested through triangulation, **The Astrophysical Journal**, v. 712, p. 453-458, 2010.

MÖSTL, C. et al. Connecting speeds, directions and arrival times of 22 coronal mass ejections from the Sun to 1 AU. **The Astrophysical Journal**, v. 787, n. 2, p. 199, 2014.

MUNAKATA, K. et al. On the Cross-Field Diffusion of Galactic Cosmic Rays into an ICME, **Advances in Geosciences**, v. 2, n. 9, p. 115-124, 2006.

NAGASHIMA, K. Three-dimensional cosmic ray anisotropy in interplanetary space. Part I - Formulation of Cosmic Ray Daily Variation produced by Axis-Symmetric Anisotropy. **Report of Ionosphere and Space Research in Japan**, v. 25, N. 3, p. 189-211, 1971.

NAGASHIMA, K.; UENO, H. Three-dimensional cosmic ray anisotropy in interplanetary space. Part II -General Expression of Annual Modulation of Daily Variation by Frequency Modulation Method and its Application to the Modulation due to Earth's Revolution around Sun. **Report of Ionosphere and Space Research in Japan**, v. 25, N. 3, p. 212-241, 1971.

NAGASHIMA, K. et al. Three-dimensional cosmic ray anisotropy in interplanetary space. Part III - Origin of Cosmic Ray Solar Semi-Diurnal Variation. **Report of Ionosphere and Space Research in Japan**, v. 26, N. 1-2, p. 1-30, 1971.

NAGASHIMA, K.; UENO, H.; FUJIMOTO, K.; FUJII, Z.; KONDO, I. Three-dimensional cosmic ray anisotropy in interplanetary space. Part IV - Origin of Solar Semi Diurnal Variation. **Report of Ionosphere and Space Research in Japan**, v. 26, N. 1-2, p. 31-68, 1971.

NIEVES-CHINCHILLA, T. et al. Inner heliospheric evolution of a "stealth" CME derived from multi-view imaging and multipoint in situ observations. I. Propagation to 1 AU. **The Astrophysical Journal**, v. 779, n. 1, p. 55, 13 pp., 2013.

OKAZAKI, Y. et al. Drift effects and the cosmic ray density gradient in a solar rotation period: First observation with the global muon detector network (GMDN). **The Astrophysical Journal**, v. 681, p. 693-707, 2008.

OKAZAKI, Y. **Three dimensional anisotropy and density gradient of galactic cosmic rays measured by Global Muon Detector Network**. PhD Thesis, Department of Geophysics, Tohoku University, Sendai, Japan, 2008.

OLMEDO, O. et al. Solar eruptive event detection system (SEEDS). **Bulletin of the American Astronomy Society**. v. 37, p. 1, p. 1342-1343, 2005.

OLMEDO, O. et al. Automatic detection and tracking of coronal mass ejections in coronagraph time series. **Solar Physics**, v. 248, p. 485-499, 2008.

OTAOLA, J. A; VALDÉS-GALICIA, J. F. **Los rayos cósmicos: mensajeros de las estrellas**. Cidade do México: Fondo de Cultura Económica, 1992.

- PARKER, E. N. The passage of energetic charged particles through interplanetary space, **Planetary and Space Sciences**, v. 13, p. 9-49, 1965.
- PLUNKETT, S. P. et al. Solar source regions of coronal mass ejections and their geomagnetic effects, **Journal of Atmospheric and Solar-Terrestrial Physics**, v. 63, n. 5, p. 389-402, 2001
- RICHARDSON, I. G.; CANE, H. V. Near-Earth Interplanetary Coronal Mass Ejections During Solar Cycle 23 (1996 – 2009): Catalog and Summary of Properties. **Solar Physics**, v. 264, p. 189-237, 2010.
- ROBBRECHT, E.; BERGHMANS, D. Automated recognition of coronal mass ejections (CMEs) in near-real-time data. **Astronomy & Astrophysics**. v. 425, p. 1097-1106, 2004.
- ROCKENBACH, M. et al. Global Muon Detector Network Used for Space Weather Applications. **Space Science Reviews**, v. 182, p. 1-18, 2014.
- ROLLETT, T. et al. Constraining the Kinematics of Coronal Mass Ejections in the Inner Heliosphere with In-Situ Signatures, **Solar Physics**, v. 276, p. 293-314, 2012.
- SAGISAKA, S. Atmospheric effects on cosmic-ray muon intensities at deep underground depths, **Il Nuovo Cimento C**, v. 9, n. 4, p. 809-828, 1986.
- SHEELEY, N. R. et al. Continuous tracking of coronal outflows: two kinds of coronal mass ejections. **Journal of Geophysical Research**, v.104, n. A11, p. 24739-24767, 1999.
- ST. CYR, O. C. et al. Properties of coronal mass ejections: SOHO LASCO observations from January 1996 to June 1998. **Journal of Geophysical Research**, v. 105, n, A8, p. 18169-18185, 2000.
- TEMMER, M. et al. Characteristics of kinematics of a coronal mass ejection during the 2010 August 1 CME–CME interaction event, **The Astrophysical Journal**, v. 749, n. 57, 2012.
- THERNISIEN, A. F. R.; HOWARD, R. A.; VOURLIDAS, A. Modeling of Flux Rope Coronal Mass Ejections. **The Astrophysical Journal**, v. 652, p. 763-773, 2006.
- THERNISIEN, A.; VOURLIDAS, A.; HOWARD, R. A. Forward Modeling of Coronal Mass Ejections Using STEREO/SECCHI Data, **Solar Physics**, v. 256, p. 111-130, 2009.
- THOMPSON, W. T. Coordinate systems for solar image data, **Astronomy and Astrophysics**, v. 449, p. 791-803, 2006.
- TRUCCO, E., VERRI, A. **Introductory techniques for 3-d computer vision**. Prentice Hall, ISBN 13:9780132611084, 1998.
- VOURLIDAS, A.; HOWARD, R. A. The proper treatment of coronal mass ejection brightness: a new methodology and implications for observations. **The Astrophysical Journal**, v. 642, p. 1216-1221, 2006.

VIEIRA, L. R. et al. Near 13.5-day periodicity in Muon Detector data during late 2001 and early 2002, **Advances in Space Research**, v. 49, p. 1615-1622, 2012.

VRISNAK, B. et al. Propagation of interplanetary coronal mass ejections: The drag-based model. **Solar Physics**, v. 285, n. 1-2, p. 295-315, 2013.

VOURLIDAS, A. et al. Direct detection of a coronal mass ejection–associated shock in large angle and spectrometric coronagraph experiment white-light images, **The Astrophysical Journal**, v. 598, p. 1392-1402, 2003.

VOURLIDAS, A. et al. Comprehensive analysis of coronal mass ejection mass and energy properties over a full solar cycle, **The Astrophysical Journal**, v. 722, p. 1522-1538, 2010.

VOURLIDAS, A. et al. The First Observation of a Rapidly Rotating Coronal Mass Ejection in the Middle Corona, **The Astrophysical Journal**, v. 733, n. L23, 2011.

VOURLIDAS, A. et al. How Many CMEs Have Flux Ropes? Deciphering the Signatures of Shocks, Flux Ropes, and Prominences in Coronagraph Observations of CMEs, **Solar Physics**, v. 284, p. 179-201, 2013.

VOURLIDAS, A.; HOWARD, R. The proper treatment of coronal mass ejection brightness: a new methodology and implications for observations, **The Astrophysical Journal**, v. 642, p. 1216-1221, 2006.

WANG, Y. et al. Statistical study of coronal mass ejection source locations: Understanding CMEs viewed in coronagraphs, **Journal of Geophysical Research**, v. 116, n. A04104, 2011.

WOOD, B. E. et al. Comprehensive Observations of a Solar Minimum Coronal Mass Ejection with the Solar Terrestrial Relations Observatory, **The Astrophysical Journal**, v. 694, p. 707-717, 2009.

YASHIRO, S. et al. A catalog of white light coronal mass ejections observed by the SOHO spacecraft, **Journal of Geophysical Research**, v. 109, A07105, 2004.

YASUE, S. et al. Design of a Recording System for a Muon Telescope Using FPGA and VHDL. In: INTERNATIONAL COSMIC RAY CONFERENCE, 28., 2003, Tsukuba, Japan. **Proceedings...** Tsukuba: International Union of Pure and Applied Physics (IUPAP), 2003. p. 3461-3464.

XIE, H. et al. On the Origin, 3D Structure and Dynamic Evolution of CMEs Near Solar Minimum, **Solar Physics**, v. 259, p. 143-161, 2009.